

CENTRE FOR BIOLOGICAL ENGINEERING  
CHEMICAL ENGINEERING  
LOUGHBOROUGH UNIVERSITY  
SEPTEMBER 2015

# **Incorporating primary human renal proximal tubule cells into a hollow fibre bioreactor in the development of an *in vitro* model for pharmaceutical research**

---

by

**Maaria Ginai**

A thesis submitted to  
Loughborough University  
for the degree of

**Doctor of Philosophy**

© Maaria Ginai (2015)

## Abstract

Current *in vitro* cellular methods utilised in drug metabolism and pharmacokinetic (DMPK) studies during drug development do not provide the 3D structure and functions of organs found *in vivo*, such that resulting *in vitro-in vivo* extrapolation (IVIVE) may not always accurately reflect clinical outcome. This highlights the need for the development of new dynamic *in vitro* cell models to aid improvement of IVIVE. The aim of this project was to incorporate characterised primary renal cells within a hollow fibre bioreactor for use in DMPK studies investigating renal clearance.

Fluorescence based assays were developed to assess the functionality of three drug transporters involved in the renal transport of pharmaceutical compounds: P-gp, BCRP and OCT2. The developed assays were then applied alongside transporter visualisation and genetic expression assays to characterise primary human proximal tubule cells over a series of population doublings. Cells at a population doubling of 5 demonstrated the best transporter activity whilst allowing cells to be expanded *in vitro*.

Polysulfone (PSF) based membranes, which are widely used in dialysis components were developed by blending additives to improve renal cell attachment and culture. The membranes exhibited a characteristic porous internal structure with smooth skin layers on the surface, and were able to be sterilised via autoclaving due to their high thermal stability. PSF blended with polyvinylpyrrolidone (PVP) was the most hydrophilic with cell metabolic activity similar to standard tissue culture plastic.

The production of hollow fibres of varying thicknesses and properties from the PSF and PVP blend yielded a marked difference in renal cell attachment and long term viability. Fibres incorporated into glass casings to produce the single hollow fibre bioreactors (HFBs) were able to be sterilised by autoclaving whilst remaining intact. Due to the variation of fibre integrity within the batch, many fibres exhibited tears within the HFBs. This ultimately led to cell depletion within the fibre over the culture period; however, intact fibres demonstrated an increase in cell growth towards the end of the culture period under flow conditions. These results demonstrate the progress made towards a small scale *in vitro* renal model incorporating characterised primary renal cells to aid the improvement of IVIVE in DMPK research.

**Keywords:** DMPK; Proximal tubule cells; Drug transporters; Polysulfone; Hollow fibre bioreactors; Bioartificial kidney device; *In vitro* cell model

## Acknowledgments

My PhD has been both a major challenge and a valuable learning curve, and would feel incomplete without the acknowledgement of the people who have supported me through it.

Appreciation and thanks go to my supervisors at Loughborough, Dr Karen Coopman and Professor Chris Hewitt. They have provided valuable academic support whilst allowing me to pursue the avenues of interest throughout my project independently. Their guidance and trust have allowed me to become the independent researcher that I am today.

I had heard that having an industrial sponsor, whilst beneficial may also be a burden. However, I have nothing but praise for my supervisors at AstraZeneca. Although it was a turbulent time throughout my project with the changeovers at the company, Dr Rob Elsby ensured that there was minimal disruption to my work whilst also providing the practical and theoretical knowledge and support that I needed for my project. Immense thanks goes to him, and although he is not at AZ any longer, I hope he is finding success in his pursuits. Gratitude also goes to Dr Katherine Fenner, who took on the project after the initial guidance from Dr Dominic Surry, and has supported me until completion. Gaining an insight into the industrial setting during my placement was hugely beneficial, if not a bit daunting at first. I would therefore like to thank Charles 'Chazzle' Crawford for providing a source of (continuous) laughter throughout my time there.

I am grateful to the Biotechnology and Biological Sciences Research Council (BBSRC) for the financial support and opportunity that they have provided. I have also been given the opportunity to be aligned with the Engineering and Physical Sciences Research Council (EPSRC) Doctoral Training Centre in Regenerative Medicine. This has allowed me to build a great network of friends and colleagues throughout my project. In particular, I would like to thank Dr Paul Roach, who was good enough to reply to my numerous emails and provide invaluable guidance on the chemical aspects of my work.

My time at the Centre for Biological Engineering would not have been as enjoyable as it has without my colleagues and friends here. Thanks to Andy for providing a much

needed keen eye over my chapters (and the 'witty' comments scribbled on my drafts), Emma for the help with various areas of my project whilst doing her own, Juan who was my imaging Guru within the CBE for the first few years of my project, Chan for being a great desk neighbour (but hopeless organiser) and Nat (Chuckles) for the laughs and Zumba sessions. I would also like to thank Andreea for supporting me throughout my time at Loughborough, reading through my chapters (whilst balancing working and being a mum) and tolerating my endless rants about work. Although I haven't known them from the beginning, Preeti and Matt must get a mention and thanks. It's amazing how friendships can grow over a short space of time, and hopefully we will remain as close in the future.

The completion of this project could not have been done without Petra and Tudor. They provided me with a place to stay through the final months of my PhD, but gave me so much more than that. Their support and advice with work, personal issues and cooking me dinner has made them like a second family to me and I am so grateful to them.

Finally I must acknowledge one of the most important things to me, my family. Although we don't always get along, there has never been a dull moment with my sisters Ayesha and Farah and I thank them for their support through my time at Loughborough. Last but certainly not least I must thank my mum and dad. They have been a great source of inspiration, support, help, and love through these past 25 years, and more so through my PhD. I am eternally grateful to them and I hope that I have and continue to make them proud.

## Published work

### Peer reviewed papers

M. Ginai, R. Elsbay, C. J. Hewitt, D. Surry, K. Fenner, and K. Coopman, "The use of bioreactors as in vitro models in pharmaceutical research," *Drug Discov. Today*, vol. 18, no. 19–20, pp. 922–935, Oct. 2013. <http://dx.doi.org/10.1016/j.drudis.2013.05.016>

### Conference presentations

13<sup>th</sup> – 14<sup>th</sup> September 2011, HealthTech and Medicine KTN and IChemE Biochemical Engineering subject group, Young researchers meeting. London, UK. *Development of primary and/or embryonic stem cell derived human renal cells to study drug elimination and the creation of a bioartificial kidney in order to model drug-drug interactions*

18<sup>th</sup> April 2013, EPSRC Doctoral Training Centre Cross Cadre Conference. Loughborough, UK. *Development of primary human renal cells to study drug elimination and the creation of a bioartificial kidney in order to model drug-drug interactions*

17<sup>th</sup> February 2014, Health and Wellbeing Conference. Loughborough, UK. *Development of primary human renal cells to study drug elimination and the creation of a bioartificial kidney in order to model drug-drug interactions*

8<sup>th</sup> – 11<sup>th</sup> September 2014, Future Investigators in Regenerative Medicine. Girona, Spain. *Assessment of drug transport and disposition functions of primary human renal proximal tubule cells in 2D culture in the development of a bioartificial kidney to model drug-drug interactions*

## Contents

Abstract.....	i
Acknowledgments .....	iii
Published work.....	v
Peer reviewed papers .....	v
Conference presentations .....	v
Contents.....	vi
List of Figures .....	xiii
List of Tables .....	xviii
Abbreviations.....	xx
Chapter 1.....	1
1.1. General Background .....	2
1.2. Thesis objectives .....	7
Chapter 2.....	10
2.1. Introduction .....	11
2.2. Review of the literature .....	13
2.2.1. Drug screening processes within the pharmaceutical industry .....	13
2.2.2. Renal transporter mechanisms of action .....	18
2.2.2.1. ABC transporters .....	18
2.2.3. Methods for renal drug transporter functionality assessment <i>in vitro</i> .....	24
2.2.4. Conclusion.....	28
2.3. Materials and methods.....	31
2.3.1. Chemicals, reagents, consumables and equipment.....	31
2.3.2. Cell lines .....	31

2.3.3. Cryopreservation and cell resuscitation .....	31
2.3.4. Medium formulation.....	31
2.3.5. Monolayer Culture .....	32
2.3.6. Cell counting .....	35
2.3.7. Monolayer integrity assessment .....	35
2.3.8. Bidirectional Transport Assay- P-gp Assessment.....	36
2.3.9. Fluorescence assays to assess transporter functionality .....	38
2.4. Results.....	41
2.4.1. Rhodamine 123 assay development in MDCKII and MDCK-MDR1 cells .....	41
2.4.2. P-gp functionality assessment in MDCK-MDR1 cells using Calcein-AM .....	51
2.4.3. OCT2 functionality in HEK-OCT2 cells using ASP+ .....	56
2.4.5. BCRP functionality in MDCK-BCRP cells using Hoechst 33342 .....	59
2.5. Chapter discussion and conclusion.....	65
2.5.1. Discussion .....	65
2.5.2. Conclusion.....	66
Chapter 3.....	67
3.1. Introduction .....	68
3.2. Review of the literature .....	69
3.2.1. Renal physiology .....	69
3.2.2. Cell sources for 2D models of the kidney .....	79
3.2.3. Conclusion.....	82
3.3. Materials and methods.....	83
3.3.1. Cell Lines .....	83
3.3.2. Cryopreservation and Cell Resuscitation.....	83
3.3.3. Medium Formulation.....	83
3.3.4. Monolayer Culture.....	83

3.3.5. Cell counting- Aquadin orange and propidium iodide exclusion (automated cell counts) .....	85
3.3.6. Fluorescence assays to assess transporter functionality .....	85
3.3.7. Transwell Coatings and monolayer integrity analysis .....	87
3.3.8. Immunostaining procedure and analysis.....	88
3.3.9. RT-PCR and preparation.....	89
3.4. Results.....	92
3.4.1. Transporter expression on hPTCs .....	92
3.4.2. Transporter functionality in hPTC.....	103
3.4.3. hPTC growth on porous surfaces.....	110
3.5. Chapter discussion and conclusion.....	114
3.5.1. Discussion .....	114
3.5.2. Conclusion.....	115
Chapter 4.....	116
4.1. Introduction .....	117
4.2. Review of literature .....	119
4.2.1. Biomaterial surface features desirable for cell growth.....	119
4.2.2. Materials used for renal replacement devices and potential therapies .....	122
4.2.3. Methods of membrane production.....	129
4.2.4. Conclusion.....	130
4.3. Materials and methods.....	131
4.3.1. Formulation.....	131
4.3.2. Membrane generation.....	131
4.3.3. Wettability .....	132
4.3.4. Surface chemistry .....	132
4.3.5. Surface topography.....	132

4.3.6. Membrane and fibre imaging .....	132
4.3.7. Membrane sterilization .....	133
4.3.7.1. Immersion in IMS .....	133
4.3.7.2. Incubation with antibiotic/antimycotic solution .....	133
4.3.7.3. Autoclaving and sterility testing .....	133
4.3.8. Cell viability assay- Presto blue.....	134
4.4. Results.....	135
4.4.1. Predicted chemistries and structures of polymer blends.....	135
4.4.2. Membrane wettability .....	138
4.4.3. Surface chemistry analysis.....	140
4.4.4. Membrane topography.....	142
4.4.5. Membrane structure.....	145
4.4.7. Membrane preparation and cell viability .....	147
4.4.7.1. Membrane sterilisation.....	147
4.4.7.2. Cell attachment and viability on membranes .....	150
4.5. Chapter discussion and conclusion.....	152
4.5.1. Discussion .....	152
4.5.2. Conclusion.....	153
Chapter 5.....	154
5.1. Chapter introduction .....	155
5.2. Review of literature .....	156
5.2.1. Bioreactors in tissue engineering .....	156
5.2.2. Existing bioartificial kidneys.....	164
5.2.3. Engineering a hollow fibre bioreactor .....	167
5.2.4. Conclusion.....	170
5.3. Materials and methods.....	171

5.3.1. Hollow fibre production.....	171
5.3.2. Fibre porosity measurements.....	171
5.3.3. Surface topography.....	172
5.3.4. Module assembly, sterilisation and disassembly .....	172
5.3.5. Hydraulic permeability.....	172
5.3.6. Module integrity assessment.....	173
5.3.7. Fibre seeding- static culture .....	175
5.3.8. Cell viability assay- Presto blue.....	175
5.3.9. Cell visualisation- Live/ dead staining.....	175
5.3.10. Bioreactor seeding and cell cultivation .....	176
5.3.11. Spent medium analysis .....	176
5.4. Results.....	179
5.4.1. Fibre structure after sterilisation.....	179
5.4.2. Physical characteristics of the fibres .....	181
5.4.3. Module sterilisation .....	183
5.4.4. Module integrity assessment.....	185
5.4.5. Long term cell viability on fibres in static conditions .....	187
5.4.6. Cell performance in the hollow fibre bioreactors .....	190
5.5. Chapter discussion and conclusion.....	193
5.5.1. Discussion .....	193
5.5.2. Conclusion.....	194
Chapter 6.....	195
6.1. Summary .....	196
6.2. Discussion.....	201
6.3. Conclusions .....	203
6.4. Further Work.....	205

Chapter 7.....	209
Appendices.....	242
1. List of Equipment .....	243
2. List of Equations .....	244
2.1. Equation 1: Cell Counting and viability .....	244
2.2. Equation 2: Population Doublings .....	244
2.3. Equation 3: Transepithelial electrical resistance (TEER $\Omega/\text{cm}^2$ ) .....	244
2.4. Equation 4: Apparent Permeability ( $P_{\text{app}} \times 10^6/\text{cm}^2$ ) .....	245
2.5. Equation 5: Efflux Ratio.....	245
2.6. Equation 6: Fibre porosity (%) .....	245
2.7. Equation 7: Volumetric water flux ( $\text{m}^3/\text{m}^2 \cdot \text{s}$ ) .....	245
2.8. Equation 8: Hydraulic permeability ( $\text{Pa m}^3/\text{m}^2 \cdot \text{s}$ ).....	245
3. Development of MDCKII cell growth in transwells .....	246
4. Rhodamine 123 transport in MDCK-MDR1 and MDCKII cells.....	247
5. Calcein-AM efflux in the presence of P-gp inhibitors in MDC-MDR1 cells .....	249
6. Calcein-AM degradation and its effect on fluorescence.....	250
7. Hoechst 33342 concentration assessment for efflux assay.....	252
8. RPTEC growth profile .....	255
9. RNA integrity assessment .....	256
10. Calcein-AM efflux assay in RPTECs at various population doublings.....	257
11. Hoechst 33342 efflux assay in RPTECs at various population doublings.....	259
12. RPTEC culture in transwell plates.....	261
13. Presto Blue assay calibration curves.....	262
14. Membrane sterilisation.....	263
15. Membrane sterilisation images .....	265
16. Bioreactor setup.....	266

---

17.	Hydraulic permeability .....	266
18.	Surface topography of hollow fibres.....	268
19.	Module sterilisation .....	269
20.	Cell performance in hollow fibre bioreactors .....	270

---

## List of Figures

**Figure 1:** The development of BAKs for clinical and research uses

**Figure 2:** Project methodology representation

**Figure 3:** Diagram of the structures and functions of ABC transporters

**Figure 4:** Diagrams of the structures and functions of OCT2 and MATE1 transporters

**Figure 5:** Bidirectional transport assay schematic

**Figure 6:** Schematic of uptake transporter assays

**Figure 7:** LY permeation values and apparent permeabilities of Rho123 in Run 1 through MDCKII cell monolayers

**Figure 8:** LY permeation values apparent permeabilities of Rho123 in Run 2 through MDCKII monolayers

**Figure 9:** The LY permeation percentages and apparent permeabilities of Rho123 at the higher concentration range through MDCKII and MDCK-MDR1 cell monolayers

**Figure 10:** The LY permeation percentages and apparent permeabilities of Rho123 at the lower concentration range through MDCKII and MDCK-MDR1 cell monolayers

**Figure 11:** Calcein-AM fluorescence in MDCK-MDR1 cells in the presence and absence of the P-gp inhibitors

**Figure 12:** The native fluorescence of Calcein-AM alongside P-gp and BCRP inhibitors

**Figure 13:** Calcein-AM fluorescence in MDCK-BCRP cells in the presence and absence of P-gp and BCRP inhibitors

**Figure 14:** The ASP<sup>+</sup> uptake in HEK-OCT2 cells at a range of concentrations in the presence and absence of OCT2 inhibitors

**Figure 15:** Hoechst 33342 fluorescence at a range of concentrations in MDCK-BCRP cells in the presence and absence of BCRP inhibitors

**Figure 16:** Fluorescence of Hoechst 33342 in MDCK-BCRP cells in the presence and absence of BCRP

**Figure 17:** The native fluorescence Hoechst 33342 alongside P-gp and BCRP inhibitors

**Figure 18:** Fluorescence of Hoechst 33342 in MDCK-MDR1 cells in the presence and absence of P-gp inhibitors

**Figure 19:** Structure of the kidney showing the 3 main sections and the structure and function of the nephron

**Figure 20:** Structure of the PTC: the arrangements of proteins comprising the intercellular compartment and the location of drug transporters

**Figure 21:** The comparative gene expression of P-gp, OCT2, BCRP and MATE1 on RPTECs over 9 population doublings compared to Pd=0

**Figure 22:** RPTECs stained for BCRP at Pds 0, 5, 7 and 9

**Figure 23:** RPTECs stained for MATE1 at Pds 0, 5, 7 and 9

**Figure 24:** RPTECs stained for MRP2 at Pds 0, 5, 7 and 9

**Figure 25:** RPTECs stained for OAT3 at Pds 0, 5, 7 and 9

**Figure 26:** RPTECs stained for OCT2 at Pds 0, 5, 7 and 9

**Figure 27:** RPTECs stained for P-gp at Pds 0, 5, 7 and 9

**Figure 28:** Calcein-AM fluorescence in RPTECs at Pd 0, 5, 7 and 9 in the presence and absence of P-gp inhibitors

**Figure 29:** ASP<sup>+</sup> uptake in RPTECs at Pd 0, 5, 7 and 9 in the presence and absence of OCT2 inhibitors

**Figure 30:** Hoechst 33342 fluorescence in RPTECs at Pd 0, 5, 7 and 9 in the presence and absence of BCRP inhibitors

**Figure 31:** Percentage LY permeation and TEER readings of RPTECs cultured on coated or uncoated transwells

**Figure 32:** Percentage LY permeation of uncoated and coated PCT transwells without cells

**Figure 33:** Mechanisms of protein adsorption and cell attachment on hydrophilic and hydrophobic surfaces

**Figure 34:** Structures of polymer membranes commonly used for haemodialysis, BAK devices and renal cell growth applications

**Figure 35:** The predicted reaction mechanisms of PSF, PSF+PVP and PSF+ (malonic) acid

**Figure 36:** Water contact angles on the top and bottom sides of the 4 flat sheet membranes

**Figure 37:** XPS spectra of PSF, PSF+PVP, PSF+MA and PSF+GA membranes

**Figure 38:** AFM images of the tops and bottoms of PSF, PSF+PVP, PSF+MA and PSF+GA membranes

**Figure 39:** SEM images of the top, bottom and cross sections of PSF, PSF+PVP, PSF+MA and PSF+GA

**Figure 40:** SEM images of the tops and bottoms of PSF, PSF+PVP, PSF+MA and PSF+GA membranes after sterilisation

**Figure 41:** Cell performance on the top and bottom of the flat sheet membranes shown by Presto blue percentage reduction and cell recovery

**Figure 42:** The idealised arrangement of fibre bundles comprised of Krogh cylinder units in a HFB

**Figure 43:** Schematic of the extrusion rig used to produce the PSF+PVP hollow fibres

**Figure 44:** Schematic of the single HFB layout and image of the setup

**Figure 45:** SEM images of the 3 batches of PSF+PVP hollow fibres

**Figure 46:** Medium samples from sterilised modules incubated on TCP and spread plates to assess the efficiency of sterilisation methods

**Figure 47:** The pressure drop and LY permeation after 24 hours under high flow post sterilisation to assess module integrity

**Figure 48:** The Presto Blue reduction by RPTECs cultured on each PSF+PVP fibre batch and the equivalent cell number over 8 days in culture

**Figure 49:** Images of RPTECs on the exterior of the PSF+PVP fibres using live/dead staining

**Figure 50:** The Presto Blue reduction and spent medium analysis of RPTECs over 8 days in culture under flow conditions

**Figure 51:** Development of MDCKII growth in transwell plates

**Figure 52:** TEER values of MDCKII and MDCK-MDR1 monolayers before and after the application of Rho123 in the bidirectional transport assay in the range of 1 $\mu$ M-100 $\mu$ M

**Figure 53:** TEER values of MDCKII and MDCK-MDR1 monolayers before and after the application of Rho123 in the bidirectional transport assay in the range of 10nM-2000nM

**Figure 54:** Calcein-AM fluorescence in MDCK-MDR1 cells over 71 cycles in the presence and absence of the P-gp inhibitors Ketoconazole, Verapamil and Quinidine

**Figure 55:** Calcein-AM fluorescence in MDCK-MDR1 cells over 71 cycles in the presence and absence of the P-gp inhibitors Ketoconazole, Verapamil and Quinidine indicating degradation of the Calcein-AM

**Figure 56:** Hoechst 33342 fluorescence in the range of 1 $\mu$ M-20 $\mu$ M in MDCK-BCRP cells over 71 cycles in the presence and absence of the BCRP inhibitors Novobiocin and Ko143

**Figure 57:** 20 $\mu$ M Hoechst 33342 fluorescence in MDCK-BCRP cells over 71 cycles in the presence and absence of the BCRP inhibitors Novobiocin and Ko143

**Figure 58:** The growth profile of RPTECs over 16 days on TCP

**Figure 59:** The RNA integrity of samples extracted from RPTECs at Pds 0, 5, 7 and 9

**Figure 60:** Calcein-AM fluorescence in RPTECs at Pds 0, 5, 7 and 9 over 71 cycles in the presence and absence of the P-gp inhibitors Ketoconazole, Verapamil and Quinidine

**Figure 61:** Hoechst 33342 fluorescence in RPTECs at Pds 0, 5, 7 and 9 over 71 cycles in the presence and absence of the BCRP inhibitors Novobiocin and Ko143

**Figure 62:** LY permeation through RPTECs cultured on transwells under static and agitated conditions

**Figure 63:** Calibration curve equating Presto Blue reduction with cell number

**Figure 64:** The optical densities of nutrient broth incubated with flat sheet membranes after sterilisation with 70% IMS, Antibiotics/Antimycotics and autoclaving

**Figure 65:** Spread plate images of nutrient broth incubated with flat sheet membranes after sterilisation with 70% IMS, Antibiotics/Antimycotics and autoclaving

**Figure 66:** SEM images of flat sheet membranes after sterilisation with 70% IMS, Antibiotics/Antimycotics and autoclaving

**Figure 67:** Layout of the incubation chamber designed for HFB setup

**Figure 68:** The surface topography of the exterior and interior of each fibre batch

**Figure 69:** Images of medium incubated in modules after sterilisation with 70% IMS and autoclaving

**Figure 70:** The Presto Blue reduction and spent medium analysis of the batch 2 module demonstrating fibre integrity

---

## List of Tables

**Table 1:** Profiling assays employed to investigate DDI potential of CDs

**Table 2:** Properties of renal transporters clinically relevant in *in vivo* drug interactions

**Table 3:** Selected probe substrates and inhibitors for renal drug transporters

**Table 4:** Culture conditions for the various cell types used on different plates

**Table 5:** Rho123 dilutions in DMSO to get 100x solutions for the production of varying concentrations of Rho123 with DMSO at 1% (v/v)

**Table 6:** Inhibitor concentrations used and their IC<sub>50</sub> profiles for the transporter functionality assays

**Table 7:** Dilutions of ASP<sup>+</sup> and H33342 in DMSO for 200x stock solutions to produce the range of working solutions for ASP<sup>+</sup> and H33342

**Table 8:** ECM proteins present throughout the kidney

**Table 9:** The filtration, reabsorption and excretion rates of nutrients and electrolytes in the kidney, the percentage of filtrate reabsorbed in the proximal tubule and their transport mechanisms

**Table 10:** Culture conditions for the various cell types used on different plates

**Table 11:** Modified Krebs buffer component concentrations

**Table 12:** List of primary antibodies to selected transporters and fluorescent secondary antibodies and fluorophores used in RPTEC immunostaining

**Table 13:** Analysis settings for transporter fluorescence quantification

**Table 14:** The name of the primers and identification designated by Life technologies

**Table 15:** Properties of membranes commonly used for haemodialysis, BAK devices and renal cell growth applications

**Table 16:** Amounts of solvent and polymer used in the generation of PSF based dope solutions

**Table 17:** Parameters of the polymer surfaces

**Table 18:** Properties of bioreactors in tissue engineering

**Table 19:** Process parameters and sizes of 3 batches of PSF+PVP hollow fibres

**Table 20:** Components used in the assembly of the HFBs

**Table 21:** Physical characteristics of the 3 fibre batches

**Table 22:** The transmembrane pressure, water flux and hydraulic permeability of modules incorporating batch 2 fibres

---

## Abbreviations

$\alpha$ SMA- Alpha smooth muscle actin

A-B- Apical to basolateral

ABC- ATP binding cassette

ADH- Anti-diuretic hormone

ADME-Tox- Absorption, distribution, metabolism, excretion- Toxicology

AFM- Atomic force microscopy

ALP- Alkaline phosphatase

ANOVA- Analysis of variance

AO- Aquadin orange

ARF- Acute renal failure

ASP<sup>+</sup>- 4-(4-(dimethylamino)styryl)-*N*-methylpyridinium

ATP- Adenosine triphosphate

B-A- Basolateral to apical

BAK- Bioartificial kidney

BAL- Bioartificial Liver Device

BBB- Blood Brain Barrier

BBM (AP)- Brush border membrane (apical)

BCRP- Breast cancer resistance protein

BLM- Basolateral membrane

BLSS- Bioartificial Liver Support System

BRECS- Bioartificial Renal Epithelial Cell System

BSA- Bovine serum albumin

BSC- Biosafety cabinet

C- Carbon

CA- Contact angle

Ca<sup>2+</sup>- Calcium

Calcein-AM- Calcein- Acetoxymethyl

CD- Candidate drug

CKD- Chronic kidney disease

Cl<sup>-</sup> Chloride

CNS- Central nervous system

CYP- Cytochrome P450

DAPI- 4'6-Diamidino-2-phenylindole

DC- Dicarboxylate

DDIs- Drug-drug interactions

DEAE- Dimethylaminoethyl

DI- Deionised water

DMEM- Dulbeccos modified eagle medium

DMPK- Drug metabolic and pharmacokinetic

DMSO- Dimethyl sulfoxide

DNA- Deoxyribonucleic acid

ECM- Extracellular matrix

ECS- Extracapillary space

EIPS- Evaporation induced phase separation

ELAD- Extracorporeal Liver Assist Device

ER- Efflux ratio

EVAL- Ethyvinylalcohol

FBS- Fetal bovine serum

FC- Fullcure

FDA- Food and Drugs Administration

FEGSEM- Field emission gun scanning electron microscope

GA- Glutaric acid

GBM- Glomerular basement membrane

H<sup>+</sup>- Hydrogen

H<sub>2</sub>O- Water

H33342- Hoechst 33342

HBSS- Hanks balanced salt solution

HEPES- 4-(2-hydroxyethyl)piperazine-1-ethanesulfonic acid

HFB- Hollow Fibre Bioreactor

HPLC- High performance liquid chromatography

hPTCs- Human proximal tubule cells

HPV16- Human papilloma virus 16

hTERT- human telomerase

HTS- High-throughput screening

IC<sub>50</sub>- half maximal inhibitory concentration

I-ECM- Interstitial extracellular matrix

IMS- Industrial methylated spirit

iPSC- Induced pluripotent stem cells

IVIVE- *In vitro/in vivo* extrapolations

K<sup>+</sup> - Potassium

LC-MS/MS- Liquid chromatography-mass spectrometry/mass spectrometry

L<sub>(p)</sub>- Hydraulic permeability

LY- Lucifer yellow

M-ECM- Mesangial extracellular matrix

MA- Malonic acid

MATE1/2K- Multidrug and toxin extrusion protein 1/2K

MDCK- Manin Darby canine kidney

Mg<sup>2+</sup> - Magnesium

MHC- Major histocompatibility complex

MPP- 1-methyl-4-phenylpyridinium

MRP2- Multidrug resistance protein 2

MSC- Mesenchymal Stem Cell

N- Nitrogen

Na<sup>+</sup> - Sodium

NBD- Nucleotide binding domain

NBD-TMA- *N, N, N*- trimethyl-2-[methyl(7-nitrobenzo[c][1,2,5]oxadiazol-4-yl)amino]ethanamonium

NBE- New biological entity

NCE- New chemical entity

NH<sub>3</sub>- Ammonia

NHE- Sodium/hydrogen exchanger

NIPS- Non-solvent induced phase separation

NMP- 1-methyl-2-pyrrolidinone

NO<sub>3</sub>- Nitrate

O- Oxygen

OA- Organic anion

OAT1/3- Organic anion transporter 1/3

OC- Organic cation

OC- Osteocalcin

OCT2- Organic cation 2

OD- Optical density

P.- Passage

PAH- *p*-aminohippuric acid

PAN- Polyacrylonitrile

P<sub>app</sub>- Apparent permeability

PBS- Phosphate buffered saline

PCT- Polycarbonate

PD- Pharmacodynamic

Pds- Population doublings

PES- Polyethersulfone

PET- Polyester

PFA- Paraformaldehyde

P-gp/MDR1- P-glycoprotein/Multidrug resistance 1

PI- Propidium iodide

PK- Pharmacokinetic

PLGA- Poly(lactic-co-glycolic acid)

PLL- Poly-L-lysine

PMEDAP- 9-(2-phosphonylmethoxyethyl)-2,6-diaminopurine

PMEG- 9-(2-phosphonylmethoxyethyl)guanine

pO<sub>2</sub>- Dissolved oxygen

PPSF- Polyphenylsulfone

PSF- Polysulfone

PT- Proximal tubule

PTCs- Proximal tubule cells

PTH- Parathyroid hormone

PVP- Polyvinylpyrrolidone

PYR- Pyridostigmine bromide

QSAR- Quantitative structure-activity relationship

R<sub>a</sub>- Average roughness

RAD- Renal Assist Device

RC- Regenerated cellulose

REDOX- Oxidation-reduction

REGM- Renal epithelial growth medium

Rho123- Rhodamine 123

$R_{\max}$ - Maximum peak height

RPTECs- Renal proximal tubule epithelial cells

$R_{\text{rms}}$ - Root square mean roughness

RRT- Renal replacement therapy

$R_T$ - Peak-Valley roughness RT-PCR- Real-time Polymerase chain reaction

RWB- Rotating Wall Bioreactor

$R_x\text{-SO}_2$ - Sulfone

S- Sulphur

$\text{SO}_4^{2-}$ - Sulphate

SD- Standard deviation

SEM- Standard error of the mean

SEM- Scanning electron microscopy

SNR- Signal to noise ratio

TBM- Tubular basement membrane

TCP- Tissue culture plastic

TEA- Tetraethylammonium TEER- Transepithelial electrical resistance

TEMA- Triethylmethylammonium

TER- Transepithelial resistance

TIPS- Thermally induced phase separation

TJ- Tight junction

TMD- Transmembrane domain

TMH- Transmembrane spanning helices

TMP- Transmembrane pressure

UPy-U- Ureido-pyridinone-urea

VIPS- Vapor induced phase separation

WCA- Water contact angle

XPS- X-ray photoelectron spectroscopy

ZO-1- Zona occludens 1

# Chapter 1

## Introduction

## 1.1. General Background

The kidneys are primarily responsible for the excretion of waste products such as urea and ammonia from the body through the urine. Alongside this the kidneys also provide a variety of significant secondary functions including homeostatic, endocrine, immune and metabolic processes. The proximal tubule is the main site of action within the kidney in terms of reabsorption of nutrients back into the blood and the secretion of metabolites into the urine, as well as being the main site of drug metabolism within the kidney. Its architecture is distinct, and whilst it is not as complex as the liver, which is the main site of drug metabolism within the body, it does rely on the extensive interconnectivity of parenchymal cells, non-parenchymal cells, extracellular matrix (ECM) proteins and vascular supply. The proximal tubule epithelial cells form the tubule, with the apical side exposed to the tubular lumen and the basolateral side anchored to the non-parenchymal cells and ECM proteins. These proteins also act as a size selective filter for substances and a support network for the closely associated vascular supply. Interaction with these cells results in many of the functions that are associated with the kidney, and in many disease states, the proximal tubule is the main site of injury. In the UK, approximately 5% of all deaths are caused or contributed to by renal diseases. Acute renal failure (ARF) affects approximately 58,000 people with a mortality rate of 7% which is steadily increasing [1]. Approximately 200,000 people are affected annually in the US [2]. ARF is predominantly caused by renal proximal tubule cell injury and necrosis from ischemic or toxic insult [2][3]. Death usually occurs after the development of systemic inflammatory response syndrome or sepsis [3], causing ischemic damage to vital organs and cardiovascular collapse and eventually culminating in Multiple Organ Failure [2]. If a patient survives an episode of ARF, the kidney can regenerate to restore 90-95% of its functional capacity. However, with a non-reversible disease such as chronic kidney disease (CKD), renal function is progressively lost alongside the development of comorbidities such as congestive heart failure, coronary artery disease, hypertension, diabetes and anaemia [4]. Once the patient loses 90% of their renal function, they require transplantation or renal replacement therapies such as chronic dialysis [3]. Although kidney transplantation has significantly decreased mortality and morbidity, the demand for organs outweighs the number available. Only a third of patients on the

waiting list actually received a transplant in the UK [5] whilst in the US less than a fifth of patients received a kidney transplant in 2013 [6]. For many patients, dialysis is the only option of renal replacement therapy (RRT), with the population prevalence for adults of 746 per million population, and an annual increase of approximately 5% per annum since 2007 [7]. However, dialysis only provides a basic and usually intermittent filtration function, and does not provide the homeostatic, metabolic, endocrine and regulatory functions of the native kidney. The number of patients treated for renal diseases alongside the treatments of comorbidities highlights both the need for the more efficient drugs to treat renal diseases, and the development of RRTs with enhanced function compared to conventional dialysis.

Current forms of RRT consist of haemofiltration and haemo or peritoneal dialysis. Haemofiltration utilises an extracorporeal system that filters blood through a semi-permeable membrane using convective forces to remove water and small solutes from the blood. A haemofilter is also used in haemodialysis to produce the dialysate which flows counter current to the blood. Solute diffuse through the membrane along their concentration gradients, allowing some replacement of electrolytes back into the blood. Peritoneal dialysis uses the peritoneal membrane as the semipermeable membrane for the removal of waste from the body. However all forms of RRT lack many functions of the native kidney including drug metabolism and clearance, which may lead to the development of comorbidities in CKD. Examples of drugs that are not removed by RRT include digoxin, tri-cyclics and beta-blockers [8]. Alternative methods of RRT to address these issues have included the development of bioartificial kidney (BAK) devices. These devices utilise renal cells within the device to provide some reabsorption, metabolism and clearance functions of the kidney. From the initial conception of the device by Aebischer *et al* in the 1980's [9], the devices have progressed into various forms of BAK devices that are seen today (see Figure 1). Many of them focus on the need for RRTs, and have subsequently incorporated cell lines [10] or human [11][12] proximal tubule cells within a hollow fibre bioreactor (usually consisting of a haemofiltration cartridge). Although these have been relatively successful, with the model by Humes *et al* progressing onto phase I/IIa clinical trials [11], there are many areas of improvement to be addressed before these devices can be utilised in the clinical setting. In recent years,

with the emergence of 'organ-on-a-chip' technologies and microfluidics, there has been emphasis on creating smaller scale BAKs for use as *in vitro* models. Whilst demonstrating promising results such as the ability to recapitulate the *in vivo* toxicity after exposure to nephrotoxic compounds, the devices need further development and validation [13][14]. Other devices that stray away from the conventional compartmentalisation by renal cells mimicking the *in vivo* architecture include the bioartificial renal epithelial cell system (BRECS) [15]. This device, also created by the Humes group incorporate renal cells on coated discs within a perfusion bioreactor, allowing the culture and cryopreservation of cells within the device. Although the device has also shown promising results, it requires further validation and testing before utilisation as an RRT. Overall, the emergence of BAK devices has seen many forms of device design to address the need for better RRTs, and more recently, the need for *in vitro* models as both a replacement to animal models and as an improvement on the current methods of testing within the pharmaceutical industry. However, there are still many aspects to be addressed an improved on in the development of devices to mimic the native kidney.

The current economic climate is seeing an increase in the demand for cost effective, safe and efficacious new chemical and biological entities (NCE/NBEs) developed over short periods of time, to the detriment of many companies within the pharmaceutical industry. Presently, the process of bringing a new drug to market consumes an average of \$1.3 billion over 12 years [16] [17]. This process spans the identification of the compound and characterisation in pre-clinical testing using *in vitro* methods and *in vivo* animal models, to phase I/II/III clinical trials and regulatory approval to bring the drug to market [17]. There is evidence that many NCE/NBEs which fail late stage human testing do not produce *in vitro* pharmacological and toxicity data predictive of the clinical situation through pre-clinical testing stages. In light of this evidence alongside financial and time costs, there is great interest in in the development of newer and more reliable *in vitro* methods for compound investigation [18]. Current cellular models and cell based assays utilise 2D systems to assess drug transport, metabolism, excretion and the effects of drug-drug interactions (DDIs). However, in the case of renal cells the presence of shear via the fluid flow has shown to be important in the reorganisation of the cytoskeleton and junction complexes of the epithelium, and may improve transport

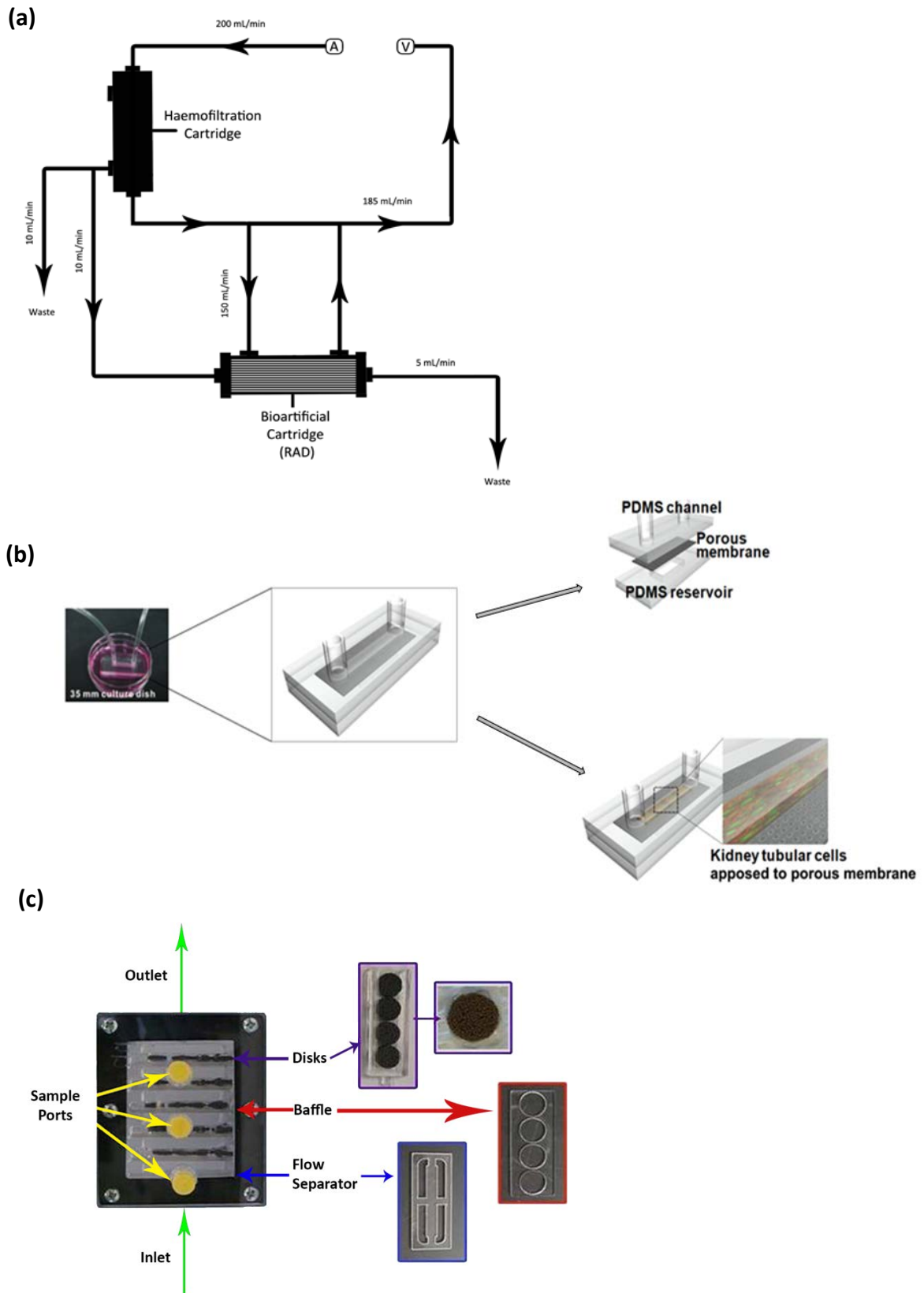


**Figure 1:** The development of BAKs for clinical and research uses: (a) RAD, (b) Kidney on a chip, (c) BRECS. Modified from [14] [15][11]

the transport capacities of the cells [19]. Therefore, the development of 3D dynamic systems will provide an increased similarity to the native architecture of the proximal tubule, which is the main site of activity but also injury in the kidney. 3D *in vitro* models may improve the assessments of drugs before progressing to later stages of testing, thereby reducing the time and monetary investments currently utilised in the clinical testing of drugs that will not be brought to market.

## 1.2. Thesis objectives

To generate *in vitro* models of the kidney to aid pre-clinical testing, many aspects must be addressed. Device functionality is important to ensure cells express the desired transporters for drug screening. As the intention of the model is incorporation into pharmaceutical research the device must be easy to assemble and use, reproducible, cost effective and easy to validate. Existing BAKs are being developed for both clinical and research uses, but have major limitations in the source of cells used and maintenance of cell phenotype over the culture period. This work aims to address these issues by developing a proof of concept model of the proximal tubule. The aim of this work can be defined in four parts, which are summarised in Figure 2.

The first aim of the project is to develop a panel of fluorescence based assays to assess the functionality of the transporters of interest in DMPK studies. These assays provide an easier and more cost effective method of transporter analysis over current assays using radioligands. By employing cell lines overexpressing the transporter of interest, functionality assays were developed for 3 transporters important to renal substrate transport. The application of these assays in multi-transporter systems was also addressed and is detailed in Chapter 2.

The second aim of the project is to determine the transporter capabilities on primary cells over time in *in vitro* culture. The need to ascertain transporter functionality and expression is due to the tendency of primary cells losing functional transporter expression over time. Consequently they have not been widely applied in BAKs. To achieve this aim the fluorescence assays developed previously in cell lines, alongside visualisation and genetic expression were applied to ascertain the preferential doubling of cells to apply within the bioreactor (Chapter 3).

The third aim of the project is to develop porous membranes as an improved renal cell culture substrate without the need for protein coatings and is addressed in Chapter 4. Tailoring polymer blends is beneficial in terms of reducing costs and also increasing the reproducibility of the models. Using polysulfone as a polymer backbone, additives were incorporated to generate flat sheet membranes. These membranes were physically

characterised before renal cell culture to ascertain the appropriate blend for hollow fibre production.

The final aim of the project is to produce hollow fibres, incorporate them into the device and assess cells within the hollow fibre bioreactor. To achieve this aim, fibres of varying thicknesses were produced and assessed both physically and in terms of renal cell performance. Seeded bioreactors were then run under flow conditions for 7 days and cell performance was assessed (Chapter 5).

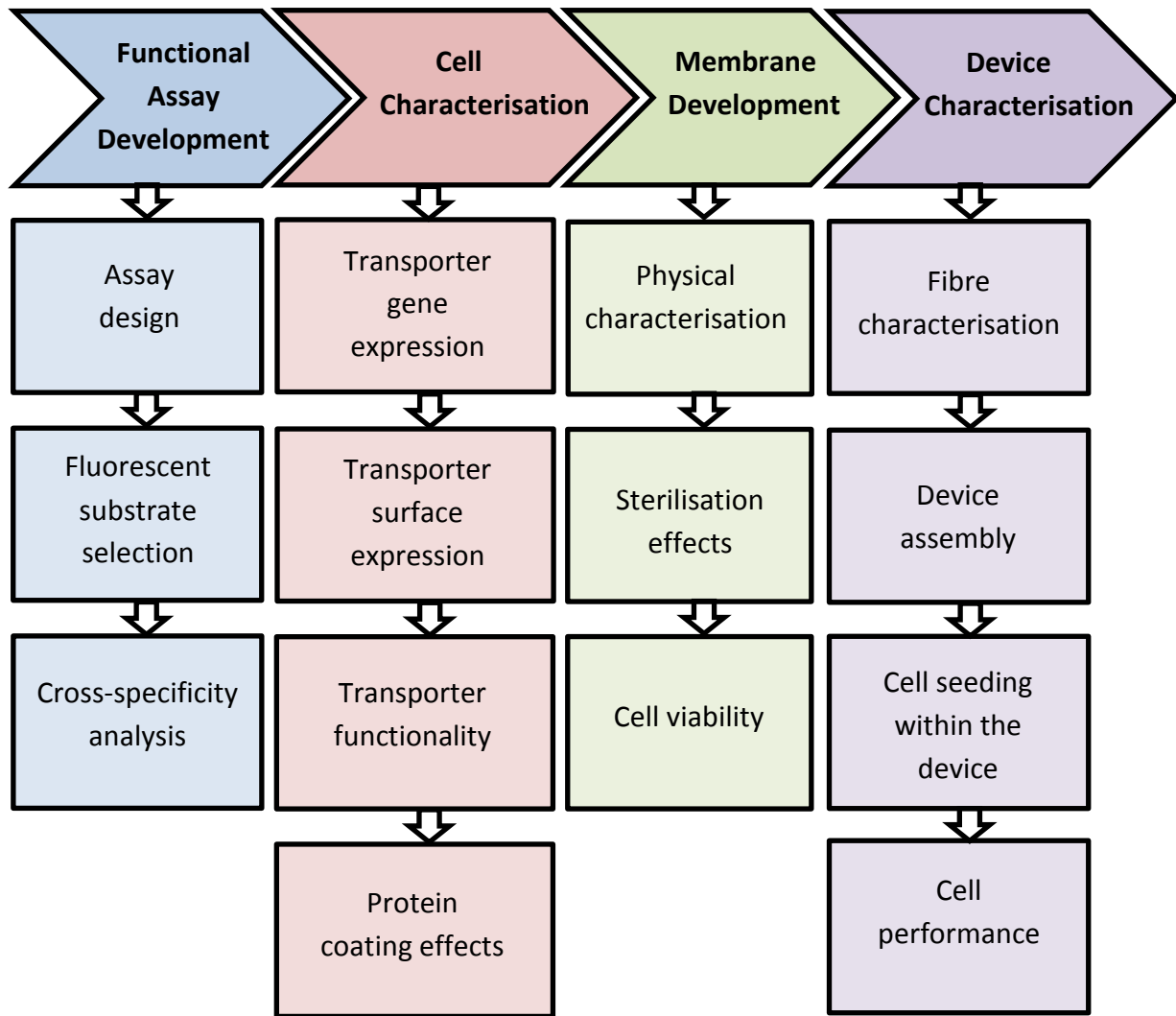


**Figure 2:** Project methodology representation

# Chapter 2

**Fluorescence assay development for  
transporter characterisation**

## 2.1. Introduction

Cellular experimental models are regularly employed in the pharmaceutical industry to assess the impact of potential compounds on cells and organ systems *in vivo*. Cellular models enable the screening of compounds for certain properties and characteristics in the earlier stages of drug development, before progressing successful candidates into the clinic.

However, due to the difficulties of culturing primary cells *in vitro* whilst retaining their native functionality [20], genetically modified or immortalised cell lines are employed as an easier and more cost effective alternative. Cell lines like MDCK-MDR1 are used to overexpress a specific drug transporter for drug interaction studies, whilst the Caco-2 cell line is employed to act as a multifunctional model system when cultured under specific conditions. These cell lines are used throughout the drug metabolic and pharmacokinetic (DMPK) process to screen and eliminate ~99% of compounds initially generated, so it is of great importance that they are representative of cellular functionality *in vivo* [21].

Cells can be cultured as polarised or non-polarised monolayers when modelling epithelia. Polarised monolayers are usually cultured on inserts, exposing both sides of the monolayer to medium and allowing cells to develop apical and basolateral permeability barriers with specialised functions (Figure 2). Polarised cell monolayers also contain tight junction complexes between cells, which restrict the transport of large molecules and allow small (<250 Da) positively charged molecules through the cell barrier *via* paracellular diffusion. The selective permeability of these cells also allows the transport of compounds to be assessed, whether they cross by passive diffusion (paracellular or transcellular movement) or active transport (dependent on transporter activity within the cell [22]). Non-polarised cells adhere to the bottom of tissue culture plates and flasks with only one side of the monolayer exposed to medium. Although these monolayers express functional transporters they lack the apical/ basolateral surfaces found *in vivo* and in polarised cell monolayers [23]. Transport into these cells can only be measured indirectly due to the accumulation of compounds within the cells. Polarised cell monolayers are a preferable epithelial model due to the ability to measure the direct

vectorial transport of compounds, and are routinely cultured when using cell lines due to the ease of maintenance on porous inserts. However, for the extrapolation of absorption, distribution, metabolism, excretion-toxicology (ADME-Tox) data representing the effects of compounds *in vivo*, robust assays to initially assess transporter functionality are also required. Therefore both types of models are utilised in the pre-clinical screening of compounds.

Radioligands are widely used to measure the transport of labelled substrates across cell monolayers in the presence and absence of transporter inhibitors. Radiolabelled compounds have the advantage of being directly quantifiable in high throughput screening techniques (such as scintillation proximity assays) as opposed to methods such as liquid chromatography-mass spectrometry which require additional bioanalytical work up. However, they are costly and require special handling and disposal procedures within a controlled laboratory environment. Fluorescence assays are comparably cheaper, safer and do not generally require extensive training or costly disposal procedures. When assessing non-specific compounds *via* radio or fluorescent labelling, a caveat arises when developing assays for cell models expressing multiple transporters with overlapping substrate specificities. However, this caveat is usually addressed by utilising transporter inhibitors to analyse the specific transporter activity of a fluorescent substrate [24][25].

This Chapter describes the development of fluorescence assays for the efflux transporters P-glycoprotein (P-gp/MDR1) and Breast cancer resistance protein (BCRP), and the uptake organic cation transporter (OCT2) in specific cell lines. These assays will then be used to later characterise primary human proximal tubule cell transporter function (Chapter 3).

## 2.2. Review of the literature

### 2.2.1. Drug screening processes within the pharmaceutical industry

At present, there is a balance within the pharmaceutical industry between the stringent testing of drugs and products against increasing costs and return on investment risks. On average, bringing a new drug to market costs US \$1.3 billion over 12 years with pre-clinical *in vitro* testing consuming approximately half of the total development time [26]. This emphasises the need to improve current screening methods of NCEs/NBEs, many of which fail late stage human testing. The DMPK process encompasses many models and techniques to assess NBEs and NCEs before Phase I clinical trials, which can be split up into 6 waves of testing [21].

#### 2.2.1.1. Wave 0: *In silico* prediction for compound design

*In silico* pharmacology, also known as computation therapeutics or computational pharmacology uses software to capture, analyse and integrate biological and medical data from a variety of sources. The development of computational models and simulations from this data can then be used to predict compounds and entities for specific target sites. The earliest *in silico* methods used quantitative structure-activity relationships (QSARs) to mathematically model biological effects relating to a molecular structure using statistical techniques. Incorporating descriptor-based and rule-based methods alongside knowledge-based approaches have enabled these models to address many biological effects of potential compounds, such as ligand-protein complex formation and ligand metabolism. With the inclusion of virtual ligand screening and affinity profiling to the QSAR models the pharmacological profile of molecules on multiple targets can be predicted [27]. *In silico* predictive methods are therefore valuable in lead molecule selection and optimisation in terms of selectivity, potency and pharmacokinetics i.e. ADME-Tox [28]. The molecules generated in this wave are filtered through the screening cascade (the subsequent waves) to generate lead compounds to submit to clinical trials.

### 2.2.1.2. Wave 1: High throughput assays

From wave 0, thousands of compounds can be generated as candidates for a specific target. It is therefore necessary to identify hit molecules (compounds which exhibit specific activity at the target protein) as efficiently as possible. High throughput screening (HTS) assays are fully automated high volume short delivery time assays which have a throughput of at least 10,000 samples per day and have an approximate hit rate of between one in two hundred and one in a thousand compounds [29]. Through this wave 20-60% of compounds generated from *in silico* predictions can be eliminated. These assays are designed to represent a cost effective screen for a broad range of ADME-Tox properties. Examples of these assays include rat hepatocyte and human microsome assays to assess intrinsic clearance and metabolism, aqueous solubility at physiological pH (7.4), plasma protein binding and lipophilicity *via* LogD measurements [21]. Numerous HTS assays have been developed for different targets, and the appeal of these rapid screening methods is also translating into academia [30]. Through wave 1 most of the chemistry output for the compounds will be evaluated and metabolic stability and key project specific issues will be addressed. Positive hit molecules are then assessed further in terms interactions with more complete biological systems in wave 2.

### 2.2.1.3. Wave 2: High-use project specific assays

High-use project specific assays involve the increased assessment of hit molecules in terms of intrinsic clearance, oral absorption and bioavailability, which further eliminates 30-55% of compounds from the previous wave. Human hepatocytes are a valuable tool for assessing compound pharmacokinetic (PK) properties as they possess a wide range of phase I and phase II metabolising enzymes found within intact cells [31]. The ability to use them readily from a cryopreserved source provides some high throughput capabilities, although not as much so as the liver microsomes employed in the previous wave. Human oral absorption and bioavailability can be initially assessed using the Caco-2 cell line, which when polarised expresses similar morphological and functional characteristics to the intestinal barrier [32]. To investigate *in vivo* clearance, bioavailability and to allow robust *in vitro/in vivo* extrapolations (IVIVE) to be developed compounds are also administered orally and intravenously to small animal models such

as rats and mice. Acquiring acceptable PK data requires many cycles of wave 1 and wave 2 testing, with the integration of DMPK and pharmacodynamic (PD) data allowing the refinement of human dose predictions of the remaining hit molecules [21].

#### 2.2.1.4. Wave 3: Low-use project specific assays

Wave 3 is used for PD testing on approximately 5% of compounds to build confidence in the data acquired in the previous waves. Typically, IVIVE across species and further oral bioavailability assessments are strengthened by conducting canine PK. Reactive metabolite assessments are also carried out to determine the potential toxicities of compound intermediates through metabolism, either by direct modification of cellular proteins or DNA, or adduct formation with proteins critical to cell viability. Liver microsomes or murine models are commonly used to assess adduct formation and generate covalent binding data for compounds *in vitro* and *in vivo* [33][34]. It is important within the drug screening and selection process to address all methods of drug interactions and clearance. As such, individualised models and further assays may be required, especially if metabolism is not the primary route of clearance [21].

#### 2.2.1.5. Wave 4: Profiling assays

Drug-drug interactions (DDIs) are also an important factor to investigate through the DMPK process and approximately 1% of lead compounds are assessed in this wave with the potential to become candidate drugs (CDs). CDs should possess a low PK-based DDI potential to minimise the risks associated with comedication including the effect on the efficacy and/or toxicity of each drug administered compared to when dosed alone. Profiling assays are carried out to address the four most common forms of clinical PK-based DDIs: 1) competitive (reversible) CYP inhibition; 2) mechanism-based/ time dependent CYP inhibition; 3) uptake and efflux transporter inhibition; and 4) CYP induction. A broad range of assays are employed to assess the DDIs of CDs (see Table 1), with data from *in silico* models (lipophilicity, aromaticity, charge type) aiding in the prediction of DDI potential for CDs [35]. Renal clearance (as the secondary site of drug metabolism within the body) is also addressed in this wave through murine and canine clearance studies. Clearance in these models can be predicted by *in silico* analysis as it is most commonly a feature of polar, low LogD compounds due to their low plasma

protein binding and lack of passive permeability. However, although *in vitro* assays for human and animal transporters have been developed, their application for human PK prediction is yet to be fully understood [21].

#### 2.2.1.6. Wave 5: Problem-solving assays

Problem solving assays are employed on approximately 1% of compounds, and in this wave issues such as biotransformation, biliary clearance and the assessment of CD transport by specific drug transporters are addressed. It is essential to understand the biotransformation of compounds and the interactions of their reactive metabolites, especially in the case of pro-drugs, where the metabolite is the active form of the drug. Time-response studies can indicate the presence of these metabolites in circulation assuming an appropriate PD model is available. The biliary clearance of compounds can be a major issue in drug discovery due to the low systemic exposure of CDs from high drug clearance and low bioavailability. Although biliary clearance across species can be difficult to predict, biliary clearance assessment in *in vitro* systems or rat models is recommended before CD nomination. Extensive evaluation of clearance has suggested molecular weight to be a good predictor of biliary clearance in anionic compounds [36]. Biliary clearance involves active secretion from hepatocytes by the adenosine triphosphate (ATP) transporter proteins P-gp, Multidrug resistance protein 2 (MRP2) and BCRP into the biliary canaliculus. However, these transporters are widely distributed throughout the body performing active transport of a wide range of compounds. They are abundant through epithelial systems such as the renal tubules and the CNS as well as the liver, and are therefore useful in the characterisation of CD transport. Cell lines such as MDCK-MDR1 which overexpress P-gp are therefore used to perform permeability studies using the bidirectional transport assay. Efflux ratios (ERs) are used to indicate the active transport of compounds through the cell monolayer, and can be used in earlier phases for risk assessment alongside later phases after validation *in vivo* [21].

**Table 1:** Profiling assays employed to investigate DDI potential of CDs

Clinical DDI	Test systems	Profiling assay utilised	Reference
<b>Competitive (reversible) CYP inhibition</b>	Enzymes, Microsomes, Hepatocytes	Fluorescence: Pro-fluorescent substrate is metabolised to give fluorescent product (High throughput) Luminescence: Pro-luminescent substrate is metabolised to give luminescent product (High throughput) Radiometric: Release of radiolabel on the metabolism of the substrate (Medium throughput) LC-MS/MS: Substrate and metabolites are sorted and quantified. Industry standard (Medium throughput)	[21][35][37]
<b>Mechanism-based/ time dependent CYP inhibition</b>	Enzymes, Microsomes, Hepatocytes	Radiometric: Metabolism of labelled substrate analysed by HPLC based fraction collection/scintillation counting technologies (Low throughput) LC-MS/MS: Substrate and metabolites are sorted and quantified. Industry standard (Medium throughput)	[21][35][37]
<b>Uptake and efflux transporter inhibition</b>	Caco-2 and cell lines overexpressing transporters	Fluorescence and radiometric: Bidirectional transport assay using fluorescent substrates to measure active transport (efflux). Uptake of fluorescent substrate and quantification of intracellular concentration (uptake) (Medium throughput).	[21][35]
<b>CYP induction</b>	Microsomes, Cell lines, Human hepatocytes	Fluorescence and radiometric: The displacement of labelled high affinity nuclear receptor ligands by test compound (Medium throughput)	[21][35][38]

### 2.2.2. Renal transporter mechanisms of action

There are four fundamentally different membrane-bound transporter proteins in existence: ion channels, transporters, aquaporins and ATP-powered pumps [39]. The ATP pumps: P-gp and BCRP, and the transporters: OCT2, OAT1 + OAT3, and MATE1 + MATE2K are of interest when modelling drug transport *in vivo*. To understand the importance of these transporters in renal function, the mechanisms of action and transporter properties should be understood, and are summarised in Table 3.

#### 2.2.2.1. ABC transporters

ATP binding cassette (ABC) transporters are a family of ATP-powered pumps which use the energy from ATP hydrolysis to transport substances across the membranes against their electrochemical gradient (*i.e.* active transport). Both ABC importers (transport of substrate into the cell) and exporters (transport of substrate from the cytoplasm) exist. However, ABC importers have only been found to exist in prokaryotes, whereas ABC exporters are expressed in all kingdoms of life [40]. The structure and mechanism of ABC transporter function are detailed in Figure 3a. The core unit of functional ABC transporters consist of a pair of cytoplasmic ATP-binding cassettes also known as the nucleotide binding domain (NBDs) and a pair of transmembrane domains (TMDs). The NBDs are involved in providing the energy required for substrate transport whilst the TMDs are involved in substrate recognition and translocation across the membrane [41]. The NBD is the conserved domain of these proteins attached to a variety of TMDs which in part make up the subfamilies and variants of the ABC transporters. There are several conserved sequences in this domain, most importantly the P-loops (Walker A motifs) and the LSGGQ motifs located in the RecA-like and helical subdomains respectively (Figure 3c). These motifs are in a head-to-tail arrangement (opposite to each other) leaving the shared interface exposed and available for ATP binding. The wide substrate specificity of ABC transporters is provided by the TMDs, although they all share a common core architecture of 12 transmembrane helices. These helices are intricately woven together rather than being independently aligned and are fused with the NBDs. Coupling proteins connect the separate helices of each monomer in the cytoplasm as is shown in Figure 4d. The cavity between the two monomers of the ABC

transporter is the site of substrate recognition, and is predominantly hydrophilic with little affinity to hydrophobic molecules. Upon binding with ATP, the energy from hydrolysis within the NBDs cause a conformation change of the TMDs in the form of an 'inversion'. The substrate within the TMD cavity is extruded out of the cell, where after the products of ATP hydrolyses are removed and the transporter reverts back to the pre-ATP bound state completing the cycle. It is thought that two molecules of ATP are required for the transport cycle except in cases where the ATP binding site contains mutations which prevent hydrolysis, as is seen in some disease states [40].

There are seven subfamilies of the ABC genes, of which P-gp and BCRP belong to the ABCB and ABCG2 subfamilies respectively. The transporters have some overlapping substrate specificities (see Table 2), but they are different in their dimer structure. P-gp is one of the four full transporters in the ABCB sub-family [39], meaning that the 2 NBD and TMD domains are within a single polypeptide. The hydrophobic nature of the cavity within the TMD gives rise to the alternative name for P-gp, MDR1. In contrast to P-gp, BCRP is one of six reverse half transporters in the ABCG subfamily, with the NBD on the N-terminus and the TMD on the C-terminus of each monomer, functioning as a homodimer [42].

**Table 2:** Properties of renal transporters clinically relevant in *in vivo* drug interactions [43]

Transporter	Gene	Mechanism	Tissue distribution	Function	Membrane localisation in the kidney
<b>P-gp</b>	ABCB1	Primary active	Intestinal enterocyte, kidney proximal tubule, hepatocyte (canalicular), brain endothelia	Efflux	BBM (AP)
<b>OCT2</b>	SLC22A2	OC uniporter	Kidney proximal tubule	Uptake	BLM
<b>OAT1</b>	SLC22A6	DC/OA antiporter	Kidney proximal tubule, placenta	Uptake	BLM
<b>OAT3</b>	SLC22A8	DC/OA antiporter	Kidney proximal tubule, choroid plexus, brain endothelia	Uptake	BLM
<b>BCRP</b>	ABCG2	Primary active	Intestinal enterocyte, kidney proximal tubule, hepatocyte (canalicular), brain endothelia, placenta, stem cells, mammary gland (lactating)	Efflux	BBM (AP)
<b>MATE1</b>	SLC47A1	H <sup>+</sup> /OC antiporter	Liver, kidney proximal and distal tubules	Efflux	BBM (AP)
<b>MATE2</b>	SLC47A	H <sup>+</sup> /OC antiporter	Kidney proximal tubule	Efflux	BBM (AP)

**Abbreviations:** BBM (AP); Brush border membrane (apical), OC; Organic cation, BLM; Basolateral membrane, DC; Dicarboxylate, OA; Organic anion, PMEG; 9-(2-phosphonylmethoxyethyl)guanine, PMEDAP; 9-(2-phosphonylmethoxyethyl)-2,6-diaminopurine

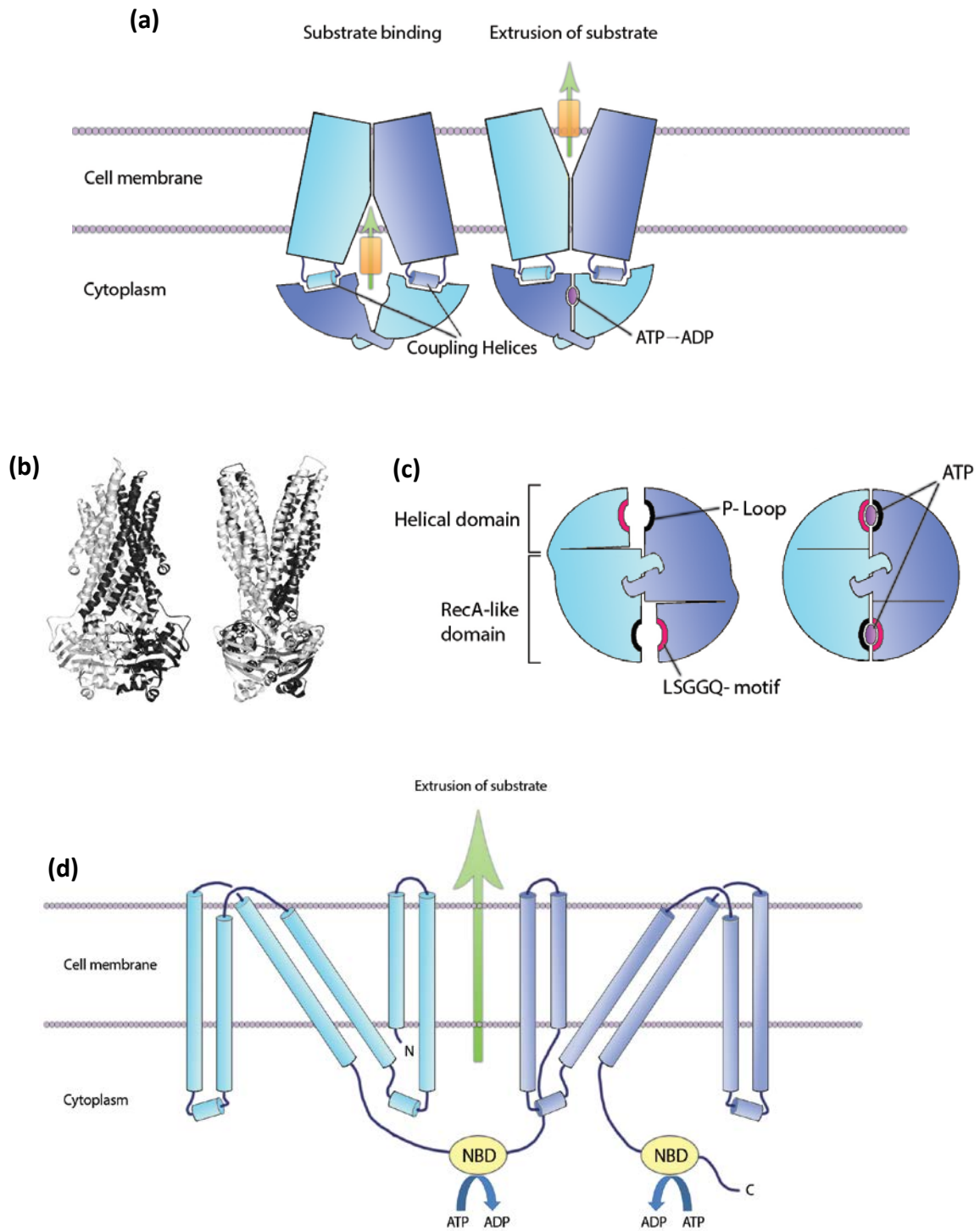


**Figure 3:** Schematic of ABC transporter structure and functions: (a) overview of substrate transport through the homodimeric ABC transporter (b) with ribbon representation of the conformation change of the monomers shown in light and dark grey (side view) (c) the NBD structure in more detail showing ATP binding sites and conserved protein sequences (d) The arrangement of the helices through the membrane (TMD) and in the cytoplasm (NBD) of P-gp (ABCB1). Modified from [40][44]

### 2.2.2.2. SLC gene superfamily transporters

Transporters facilitate the movement of specific substrates across the membrane with or against their concentration gradient. The transport of substrates is considered relatively slow compared to ion channels ( $10^2$  to  $10^4$  s<sup>-1</sup> compared to  $10^8$  s<sup>-1</sup>), with the conformational change of the transporters being fundamental to their function. Many of these transporters belong to the SLC gene superfamily and consist of passive (uniporters or facilitative transporters) and active transporters.

Passive facilitative transporters, as the name implies move the substrate down its concentration gradient one molecule at a time [45][46]. As listed in Table 3, OCT2 is a passive uptake transporter although it has been shown to be sensitive but not dependent on membrane potential and extracellular pH [46]. OCT2 is made up of 12  $\alpha$ -helices spanning the membrane with intracellular C and N termini and a large extracellular loop at transmembrane-spanning helices (TMH) 1 and 2 and a large intracellular loop at TMHs 6 and 7 (see Figure 4a and b). The precise mechanism of uptake by OCT2 however is not fully understood as there are multiple amino acid residue sites proposed for substrate binding [47][48][49].

Active transporters such as the OAT and MATE transporters couple the movement of the substrate against its concentration gradient with another molecule down its concentration gradient. The renal active transporters listed above are antiporters, where the coupled transport of the substrate and molecule are in opposing directions. MATE1 and its interplay with OCT2 is thought to be critical in the vectorial movement of shared substrates (see Table 3) across renal cells [50]. MATE1 is accordingly located on the apical membrane of renal tubular cells and performs efflux of organic cations into the lumen. It is argued whether MATE1 is made up of 12 or 13 helices, of which 12 are functional. The 12 TMHs are arranged in 2 bundles of 6 helices connected by a short cytoplasmic loop between TMH 6 and 7, which form a cavity exposed to the extracellular space [51]. Like OCT2 there are multiple amino acid residues important in MATE1 function distributed throughout the TMHs (Figure 4c and d).

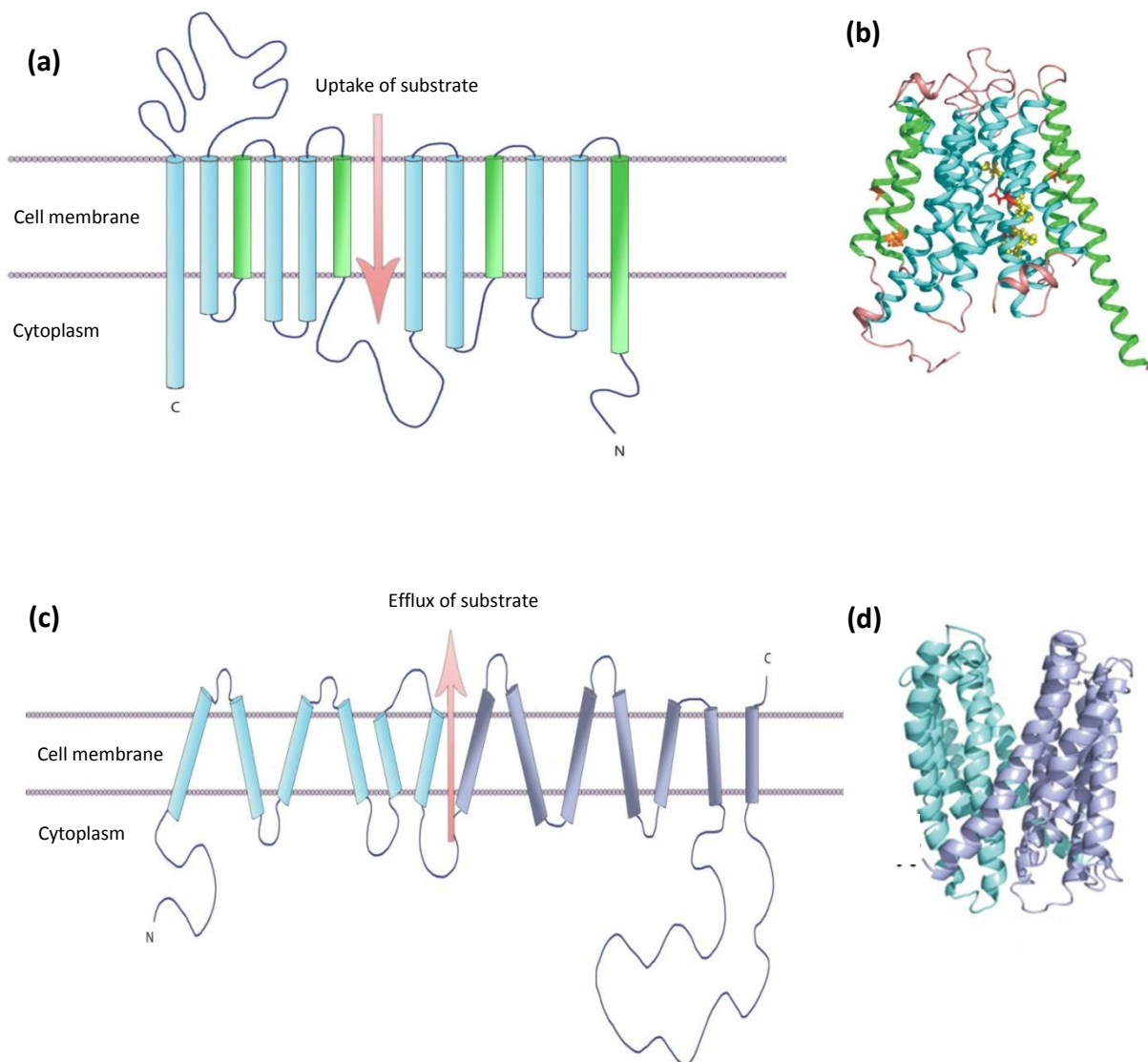


**Figure 4:** Schematic of OCT2 and MATE1 transporter structure and functions: (a) the arrangement of TMHs of the OCT2 uptake transporter with (b) ribbon representation of amino acid residues important to function (red, yellow, orange) and the extracellular and intracellular loops in pink (extracellular loop on top)(side view). Hydrophobic (blue) and hydrophilic (green) TMHs contribute to the structure and function of OCT2 (c) the arrangement of TMHs of the MATE1 efflux transporter with (d) ribbon representation of the 12 functional TMHs. The 6 N-termini TMHs are coloured light blue and the 6 C-termini TMHs are coloured light green. The 13<sup>th</sup> TMH has not been included in the model. Modified from [51][52]

### 2.2.3. Methods for renal drug transporter functionality assessment *in vitro*

As outlined in the previous section, transporter functionality is addressed in the profiling and problem solving assays in the DMPK process (waves 4 and 5). The most common methods employed use cell lines overexpressing the drug transporter of choice (such as MDCK-MDR1 cells), single or double knockout cell lines (such as Caco-2/MDR1 cells) or more physiologically relevant cells expressing multiple transporters (Caco-2 cells). These cells, various culture methods and assays can be employed depending on the transporter type and substrate properties.

#### 2.2.3.1. Polarised monolayer culture

Epithelial cells cultured as non-polarised monolayers on conventional tissue culture plastic exhibit losses of structured polarity, differentiated function and lateral junctions (e.g. tight junction proteins) [23]. However, when cultured on porous inserts the retention of these features enables a physical and biochemical cell barrier to be cultured with the retention of specific functions. In the case of Caco-2 which is widely used for the prediction of the *in vivo* absorption of drugs across the gut wall, polarised monolayers exhibit a well-defined brush border on the apical surface and intercellular proteins [53]. By culturing wild-type and modified epithelial cell lines, efflux transporter functionality such as P-gp and BCRP can be assessed using bidirectional transport assays. These assays use transporter substrates to assess the apparent permeability ( $P_{app}$ ) of the substrate through the monolayer in both apical to basolateral (A-B) and basolateral to apical (B-A) directions (Figure 5). From these permeabilities ERs can be calculated, indicating the transport of the substrate either by active transport or passive diffusion. By using transporter specific inhibitors, the specificity of the substrate can also be investigated.

#### 2.2.3.2. Flat plate culture

For investigating transporter functionality, cell lines can also be cultured on conventional tissue culture plastic as non-polarised monolayers, although the drawbacks for this type of culture are mentioned above. When assessing uptake transporter functionality, lysis assays are performed and the intracellular concentration of the substrate is directly

measured (Figure 6). As with the bidirectional transport assay, in the presence of inhibitors the specificity of the substrate can be established in multi-transporter systems [54].

### **2.2.3.3. Substrates and inhibitors for renal transporters**

In terms of renal transport studies P-gp, BCRP, OCT2, Organic anion transporter 1 and 3 (OAT1 + OAT3), and Multidrug and toxin extrusion proteins 1 and 2 (MATE1 + MATE2K) have all been identified as clinically relevant in *in vivo* drug interactions [43][55]. For most profiling and problem solving assays involving transporter assessment radiolabelled substrates are used and analysed *via* scintillation counting and LC-MS as the industry standard. However as mentioned previously the risks and costs associated with radiolabelled substrates and their safe disposal are high. Fluorescent substrates are currently only utilised in high throughput assays, although they are being developed for incorporation into the testing in the later waves. Due to the wide range of substrate specificities by the multidrug transporters (P-gp and BCRP) it is necessary to apply transporter specific inhibitors to the assays where enhanced transporter expression or multi-transporter cell lines are used. A list of commonly used fluorescent and probe substrates and transporter specific inhibitors are listed in Table 3.

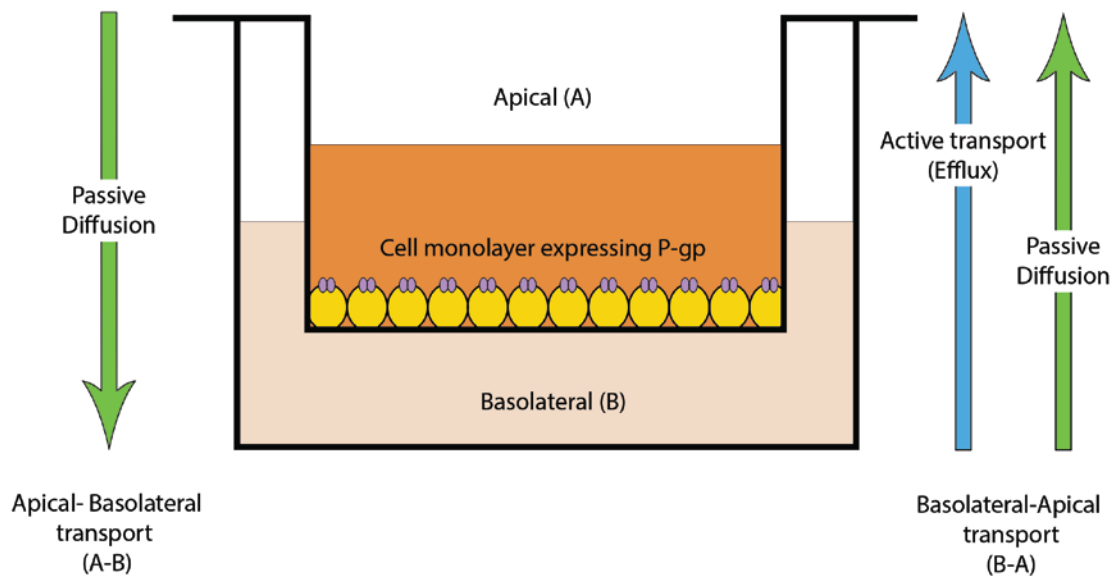
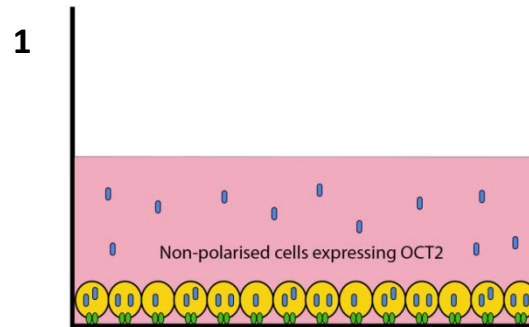
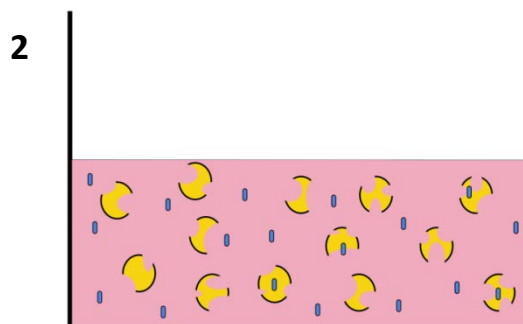


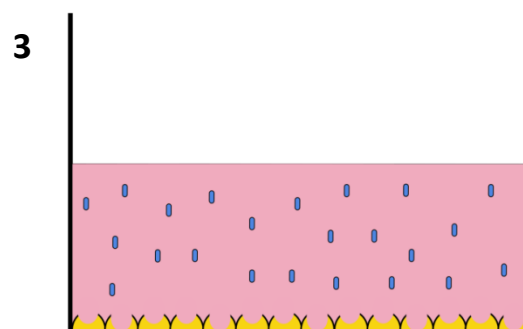
**Figure 5:** Bidirectional transport assay schematic to assess the transport of P-gp substrates through cell monolayers expressing/ overexpressing efflux transporters (P-gp) using the transwell system. Cells are cultured on a porous membrane and exposed to medium on both sides as a polarised monolayer. Substrates are incubated in either the insert (apical) or well (basolateral) chamber as the donor solution. Samples are taken from the receiver chamber (opposing the donor chamber where the test substrate/inhibitor is applied) over time and from this the  $P_{app}$  and Efflux ratio can be calculated. In the presence of inhibitors, efflux of the substrate is reduced resulting in less substrate in the receiver chamber



Cells incubated with pre-incubation  
(inhibitor) and incubation  
(substrate/ substrate + inhibitor)



Cells washed to remove substrate  
and cells lysed to release



Cells pelleted and supernatant  
sampled and analysed

**Figure 6:** Schematic of uptake assays to assess the transport of substrates (blue) on non-polarised cell monolayers expressing/ overexpressing uptake transporters (e.g. OCT2, green). In the presence of an inhibitor uptake of the substrate is reduced resulting in less substrate in the supernatant after washing, lysing and centrifugation

#### 2.2.4. Conclusion

A substantial amount of time and a vast array of techniques are implemented in the pre-clinical phases of drug development to minimize CD failure during clinical trials. However, fluorescent substrates are mainly utilised in the earlier waves of testing in high throughput assays, whilst radioligands are widely used throughout the preclinical drug testing process. As such, there is currently no complete panel of fluorescence assays for the assessment of renal specific transporter functionality that can be utilised for profiling and problem solving assays. This chapter aims to address this need by developing assays to assess the functionality of transporters using fluorescent substrates, in the development of a panel of fluorescence assays for the characterisation of renal specific transporter capabilities.

**Table 3:** Selected probe substrates and inhibitors for renal drug transporters

Transporter	Fluorescent probe substrates	Probe substrates	Inhibitors	References
<b>P-gp</b>	Calcein-AM, Rhodamine 123, Hoechst 33342, Daunorubicin	Digoxin, Quindine, Vinblastine, Loperamide	Elacridar (GF120918), Quinidine, Verapamil, Ketoconazole, Cyclospine A	[55][56][57][58][59][60][25] [61][62][63][64][65][66][67][68][69][70][71][72]
<b>OCT2</b>	ASP <sup>+</sup> , NBD-TMA	MPP, Amantadine, Cimetidine, Memantine, Metformin	Ipratropium, Imipramine, TEA	[55][73][74][75][76][77][78][79][80][81][82][83]
<b>OAT1</b>	5-carboxyfluorescein, 6-carboxyfluorescein	Acyclovir, Adefovir, Methotrexate, Zidovudine, PAH	Probenecid, Cefradroxil, Cefamandole, Cefazolin	[55][84][85][86][87][88][89][90][91][92]
<b>OAT3</b>	5-carboxyfluorescein, 6-carboxyfluorescein	Cimitidine, Methotrexate, Zidovudine, Estrone sulphate	Probenecid, Cefadroxil, Cefamandole, Cefazolin, Eosin-Y	[55][84][85][92][93][94][95][96][97][98]
<b>BCRP</b>	Daunorubicin, Hoechst 33342, Doxorubicin, Mitoxantrone	Topotecan, Rosuvastatin, Methotrexate	Elacridar (GF120918), Ritonavir, Saquinavir, Fumitremorgin C	[55][99][100][101][102][103][104][105][106][107][108][109][110]
<b>MATE1</b>	DAPI, ASP <sup>+</sup> , NBD-TMA	MPP, TEMA, Meformin, TEA, Cisplatin, Cephalexin, Cephradine	Cimitidine, Imipramine, Ritanovir, Levofloxacin, Ciproflaxin, Mitoxantrone, Topetecan, Mitoxantrone, PYR	[111][112][113][114][115][50][116][117][118]

Table 3 continued:

Transporter	Fluorescent probe substrates	Probe substrates	Inhibitors	References
MATE2-K	DAPI, ASP <sup>+</sup> , NBD-TMA	MPP, Metformin, TEA, Cisplatin, Oxaliplatin	Cimetidine, Imipramine, Ritanovir, Levofloxacin, Ciprofloxacin, Ondansetron, PYR, Mitoxantrone, Nifekalant	[111][112][113][114][115] [50][116][117][118]

**Abbreviations:** ASP<sup>+</sup>; 4-(4-(dimethylamino)styryl)-*N*-methylpyridinium, NBD-TMA; *N,N,N*-trimethyl-2-[methyl(7-nitrobenzo[*c*][1,2,5]oxadiazol-4-yl)amino]ethanaminium, MPP; 1-methyl-4-phenylpyridinium, TEA; tetraethylammonium, DAPI; 4',6-Diamidino-2-phenylindole, PAH; *p*-Aminohippuric acid, TEMA; triethylmethylammonium, PYR; Pyridostigmine bromide

## 2.3. Materials and methods

### 2.3.1. Chemicals, reagents, consumables and equipment

A list of equipment used is provided in Appendices 1. Water used for the preparation of aqueous solutions was filtered using the MilliQ ultrafiltration unit (Millipore, UK). Sterilisation of solutions and suitable materials was performed either by autoclaving at 121 °C for 15 min using a Systec VX-95 autoclave (Systec, Germany), or by filtering through a 0.22 µm filter (Millipore, UK).

### 2.3.2. Cell lines

MDCKII (Manin-Darby Canine Kidney wild type; CRL-2936) cells for 12-well transwell experiments were purchased from the ATCC at Passage (P.) 80.

MDCK-MDR1, MDCK-BCRP and HEK-OCT2 cell lines for 96-well plate experiments were all produced in house at AstraZeneca and were used between P.3-5 post transfection.

### 2.3.3. Cryopreservation and cell resuscitation

MDCKII cells were cryopreserved at a density of  $1 \times 10^6$  cells/ml in a freezing medium of 90% FBS (fetal bovine serum; Fisher Scientific, UK) and 10% (v/v) DMSO (dimethyl sulfoxide; Sigma Aldrich, UK).

All cell lines were resuscitated by removal from liquid nitrogen storage and rapidly thawed in a 37°C water bath. Vials were half submerged and gently agitated until a sliver of ice remained. The vial was then transferred to the biosafety cabinet (BSC) and cell suspension removed and quenched in 9ml of pre-warmed DMEM in a 15ml centrifuge tube. The vial was rinsed with medium and the cell suspension and the tube centrifuged at 1200 rpm for 5 minutes. After centrifugation, the supernatant was removed and the cell pellet resuspended in 5ml of medium before seeding into a T-flask.

### 2.3.4. Medium formulation

DMEM (500mL) with phenol red, 4500 mg/L D-glucose, 110 mg/L sodium pyruvate supplemented with 2mM L-glutamine, and DMEM (500mL) with L-glutamine, 4500 mg/L D-glucose, 25mM 4-(2-Hydroxyethyl)piperazine-1-ethanesulfonic acid (HEPES) without

sodium pyruvate and phenol red (Fisher Scientific, UK) supplemented with 50mL fetal bovine serum (FBS) (Sigma Aldrich, UK) were used in the culture and initial transport assays of the MDCKII cells respectively. The medium was stored at 2 – 8 °C and used within one month of preparation.

DMEM (500mL) with phenol red, D-glucose and GlutaMAX supplemented with 500mg gentamicin (Life technologies, UK) and 50mL FBS were used in culture of the MDCK-MDR1 and MDCK-BCRP cell lines and in the initial stages of culture of HEK-OCT2 cells. Later culture of HEK-OCT2 cells was performed with the basal medium mentioned above supplemented with 10mM sodium butyrate (Alfa Aesar, USA) to enhance transporter expression.

### 2.3.5. Monolayer Culture

#### 2.3.5.1. T-flask culture

MDCKII cells were cultured for 4-6 with medium changes every 2 days until cells reached >80% confluency. On the day of passage, medium was aspirated and cells were washed with phosphate buffered saline without  $\text{Ca}^{2+}$  and  $\text{Mg}^{2+}$  (PBS; Lonza, UK). After the aspiration of PBS, pre-warmed 0.25% trypsin- EDTA (Life Technologies, UK) was added to the flask and incubated at 37°C for 8-15 MDCKII minutes for enzymatic digestion of the cell adherence proteins to the tissue culture plastic. After incubation the trypsin digestion was quenched with approximately double the amount of pre-warmed culture medium and the cell suspension was centrifuged for 5 minutes at 1200rpm. The supernatant was removed after centrifugation and the cell pellet was resuspended in the appropriate volume of culture medium. Cells were counted using a haemocytometer and the NC-100 (refer to Section 2.3.6.2.) for the calculation of desired seeding densities, with the flask seeding density at  $1 \times 10^6$  cells/mL.

#### 2.3.5.2. Transwell culture

Transwell types and seeding densities were established experimentally and details can be found in Appendices- Figure 51, but final methods for transwell culture of MDCKII and MDCK-MDR1 cells are as follows and summarized in Table 4.

For MDCKII cells cultured on Corning 12-well polyester transwell inserts (0.4µm pore size, 1.12cm<sup>2</sup> surface area; Sigma Aldrich, UK) transwell plates were incubated with culture medium for 1 hour at 37°C to equilibrate before seeding. Culture medium was then aspirated and fresh medium was added to the wells. Cell suspension from tissue culture flask passages was added to the inserts at  $1.3 \times 10^5$  cells/cm<sup>2</sup>. The plates were then incubated at 37°C and cultured for 5 days with medium changes on the 3<sup>rd</sup> and 4<sup>th</sup> day.

MDCKII and MDCK-MDR1 cells were cultured on Millipore 96-well polyester transwell inserts (0.4µm pore size, 1.11cm<sup>2</sup> surface area; Merc-Millipore, UK). Transwell plates were incubated with culture medium for 1 hour at 37°C to equilibrate before seeding. Culture medium was then aspirated and fresh medium was added to the wells. Cell suspension was then added to the inserts at  $2.7 \times 10^5$  cells/cm<sup>2</sup>. The plates were then incubated at 37°C and cultured for 3-4 days with no medium changes.

#### **2.3.5.3. Plate culture**

MDCK-MDR1 and MDCK-BCRP cells were cultured on Costar black clear bottom 96 well plates (0.32 cm<sup>2</sup> surface area, Sigma Aldrich, UK) and HEK-OCT2 cells were cultured on Costar clear 96 well plates (0.32cm<sup>2</sup> surface area, Sigma Aldrich, UK). Seeding densities in 96-well plates of the respective cell lines are summarized in Table 4. No medium changes were performed for the MDCK-MDR1 or MDCK-BCRP cells which were cultured for 3-4 days and 2-3 days respectively. HEK-OCT2 cells were cultured for 2-3 days in normal medium before replacing with medium containing 10mM sodium butyrate (Alfa Aesar, USA) and culturing for a further 24 hours to enhance transporter expression.

**Table 4:** Culture conditions for the various cell types used on different plates

Cell line	Plate type	Seeding density (cells/cm <sup>2</sup> )	Culture period	Medium changes
MDCKII	12-well Transwell plate	1.3 x 10 <sup>5</sup>	5 days	On days 3 and 4
MDCKII	96-well multiwell insert plate	3.6 x 10 <sup>5</sup>		
MDCK- MDR1	96-well multiwell insert plate	3.6 x 10 <sup>5</sup>	3-4 days	N/A
MDCK- MDR1	96-well plate	1.2 x 10 <sup>5</sup>	3-4 days	N/A
MDCK- BCRP	96-well plate	1.3 x 10 <sup>5</sup>	2-3 days	N/A
HEK-OCT2	96-well plate	6.3 x 10 <sup>5</sup>	2-3 days	24 hours before assay (with 10mM sodium butyrate supplemented medium)

### 2.3.6. Cell counting

#### 2.3.6.1. Trypan blue exclusion (manual cell counts)

Initial flask and transwell experiment cell counts were carried out using the Trypan blue exclusion method. From samples taken after trypsinisation of cells, an equal amount (usually 50µl) of Trypan blue (Life Technologies, UK) was added. The sample was then pipetted onto a haemocytometer with a cover slip and counted under a light microscope. Live cells with intact membranes are impermeable to Trypan Blue, whereas dead cells or those exhibiting membrane damage would allow Trypan blue absorption, and therefore be counted as non-viable. Viable cell numbers (per mL) were then ascertained from the haemocytometer and multiplied by sample volume to calculate the number of cells per sample. Cell counting calculations using a haemocytometer can be found in Appendices 2.1.

#### 2.3.6.2. Propidium iodide exclusion (semi-automated cell counts)

Semi-automated cell counts *via* propidium iodide (PI) exclusion were carried out on the NucleoCounter NC-100 automatic mammalian cell counter using two NucleoCassettes (Chemometec, Denmark) per sample. Viable cell counts (cells/mL) were performed by subtracting the non-viable cell count from the total cell count. Non-viable cell counts were performed by aspirating sample into the cassette and reading on the counter. Dead or damaged cells with compromised cell and nuclear membranes would allow the absorption of PI into the cell. Upon DNA binding within the nucleus the dye fluorescence is enhanced, therefore indicating these cells to be non-viable. Total cell counts were performed by the addition of 50µl NucleoCounter lysis buffer A and NucleoCounter stabilizing buffer B to 50µl of sample. After mixing the sample was aspirated into a second cassette and read. This step would allow all cells to be permeabilised therefore producing a total cell count. The total cell count would then be multiplied by 3 before subtraction of the non-viable count to take into account dilution factor.

### 2.3.7. Monolayer integrity assessment

The Lucifer yellow permeation assay was used to assess monolayer integrity by using threshold values to distinguish leaky and intact monolayers. Lucifer yellow (LY; Sigma

Aldrich, UK) was diluted in deionized water to make a stock solution of 1mM. This solution was stored out of light. After the bidirectional transport assay or on the day of integrity assessment the inserts were washed with pre-warmed Hanks balanced salt solution (HBSS; Sigma Aldrich, UK) containing 25mmol/L HEPES (Sigma Aldrich, UK), 0.1% (w/v) Bovine serum albumin (BSA; Sigma Aldrich, UK) at pH 7.4. 100 $\mu$ M LY was then incubated in the insert and fresh HBSS was placed in the well. The plate was then incubated for 30 mins on the shaking platform at 75rpm at 37°C with 100 $\mu$ l samples taken from the well before and after incubation and read on the fluorescence plate reader (FluoStar Omega) at Ex: 355nm and Em: 590nm. Monolayers with an LY amount permeation of 1% or below were deemed to be acceptable.

Transepithelial electrical resistance (TEER) measurements were taken using the REMS autosampler (World precision instruments, US) for MDCKII and MDCK-MDR1 cultured on 96-well multiwell insert plates. TEERs above 500 $\Omega$ /cm<sup>2</sup> indicated acceptable monolayer integrity of the cells. The LY and TEER thresholds were used to quality control the monolayer integrity assays used at AstraZeneca for cell lines cultured on porous inserts.

### 2.3.8. Bidirectional Transport Assay- P-gp Assessment

The bidirectional transport assay was used to determine the functional activity of P-gp in MDCKII (see Figure 5) by calculating the apparent permeabilities in both directions through the cell monolayer and generating the efflux ratio. Rhodamine 123 (Rho123; Sigma Aldrich, UK) was used as the fluorescent substrate for P-gp in the transport assay. Two solutions were generated for use in the assay, the donor solution containing Rho123 in transport buffer, and the receiver solution containing Dimethyl sulfoxide (DMSO) and transport buffer. Rho123 stock solutions were made at 100x their final concentration in DMSO to keep the DMSO amounts at 1% (v/v) and from these, final concentrations of Rho123 were achieved by a 1:100 dilution of 100x solution in transport buffer with receiver solution containing DMSO at 100x in transport buffer. Rho123 dilutions in DMSO for varying concentrations can be found in Table 5.

Concentrations of Rho123 ranging from 0.1 $\mu$ M to 200 $\mu$ M were determined initially from concentrations used in literature [119][120] and then from experimental procedure (see Section 2.4.1.). On the day of the experiment culture medium was removed and the

wells were washed with pre-warmed HBSS. The donor and receiver solutions were added according to the concentration and direction of the assay: analysis of the transport of Rho123 from the apical to basolateral (A-B) side of the membrane would utilize donor solution in the insert and receiver solution in the well, while looking at the basolateral to apical transport would use donor solution in the well and receiver solution in the insert (B-A). Twelve well transwell plates (MDCKII) were then incubated on the shaking platform at 75rpm at 37°C for 120mins away from light, whilst 96-well multiwell insert plates (MDCKII, MDCK-MDR1) were statically incubated. Samples (100µl) were taken from the receiver compartment at 30 minute intervals. After sampling, receiver compartments were replaced with 100µl of fresh receiver solution and samples were read on the fluorescence plate reader at 485nm excitation and 520nm emission. The apparent permeabilities were then calculated using these fluorescence measurements (see Appendices 2.4. and 2.5. for equations). Finally, the efflux ratios from monolayers exhibiting acceptable LY permeation percentage and TEER values in MDCKII and MDCK-MDR1 cells were then compared.

**Table 5:** Rho123 dilutions in DMSO to get 100x solutions for the production of varying concentrations of Rho123 with DMSO at 1% (v/v)

<b>Final Rho123 Concentration</b>	<b>100x concentration</b>	<b>Stock solution</b>
1µM	100µM	1mM
5µM	500µM	5mM
10µM	1mM	2mM
20µM	2mM	4mM
50µM	5mM	10mM
100µM	10mM	20mM
200µM	20mM	20mM

### 2.3.9. Fluorescence assays to assess transporter functionality

Functional assays were performed after cell culture (see Section 2.3.5.3.). The  $IC_{50}$  concentrations for each of the inhibitors used for the transporters: P-gp (Section 2.3.9.1), OCT2 (Section 2.3.9.2) and BCRP (Section 2.3.9.3) and concentrations used are summarised in Table 6. For all cell line fluorescence assays the transport buffer used was HBSS containing HEPES (Sigma Aldrich, UK) and balanced to pH 7.4.

#### 2.3.9.1. Fluorescence assay to assess P-gp functionality

Calcein-Acetoxyethyl (Calcein-AM) (Invitrogen; Life technologies, UK) was used as the probe substrate for P-gp on non-polarised monolayers of cells. Fluorescence is primarily achieved by energy independent esterases inside the cell cleaving the non-fluorescent Calcein-AM to produce fluorescent Calcein. By looking at cells incubated with Calcein-AM alone compared to cells with Calcein-AM and a P-gp specific inhibitor, P-gp efflux functionality in the cells can be assessed. As P-gp is an efflux transporter, intracellular fluorescence would increase in the presence of a P-gp inhibitor due to the accumulation of Calcein (which is not a P-gp substrate) inside the cell.

As in the bidirectional transport assay, DMSO concentration was diluted to 1% (v/v) in working solutions. Calcein-AM was made up to a stock solution of 0.5mM in DMSO before being diluted in transport buffer at 200x to a final concentration of 2.5 $\mu$ M (determined by protocols at AstraZeneca). Verapamil, Quinidine and the more potent P-gp inhibitor Ketoconazole concentrations were made up as stock solutions of 20mM and diluted down to 100 $\mu$ M in transport buffer containing Calcein-AM. The inhibitors were used at in excess of their inhibitory potencies ( $IC_{50}$ ) (see Table 6). This ensured the maximum (100%) inhibition of the transporter by the respective inhibitor. 96 well MDCK-MDR1 plates were washed twice in pre-warmed transport buffer after medium removal and incubated with the respective solutions in the fluorescence plate reader (PolarStar Omega). Monolayers were examined before and after the assay under the microscope to ensure cells had not detached throughout the assay. MDCK-MDR1 plates were read at Ex: 485nm and Em: 540-10nm, gain 1200 for 71 cycles at 37°C. Calcein-AM was then tested on a cell line overexpressing the transporter BCRP to test for substrate cross specificity with BCRP versus P-gp.

### ***2.3.9.2. Fluorescence assay to assess OCT2 functionality***

ASP<sup>+</sup> was used as a probe substrate for OCT in the presence and absence of the OCT2 inhibitors Ipratropium and Imipramine (Sigma Aldrich, UK). A concentration range for ASP<sup>+</sup> generated through a literature search of ASP<sup>+</sup> concentrations utilised in various cell types and methods, resulted in concentrations ranging from 1-25  $\mu\text{M}$  [121][78]. From this 1 $\mu\text{M}$ , 5 $\mu\text{M}$ , 10 $\mu\text{M}$  and 20 $\mu\text{M}$  ASP<sup>+</sup> was investigated in HEK-OCT2 cells in the presence and absence of the OCT2 inhibitors Ipratropium and Imipramine. Stock solutions of the inhibitors were made up at 20mM and diluted at 200x to 100 $\mu\text{M}$  in buffer containing ASP<sup>+</sup>. Pre-incubation solutions containing inhibitors at 100 $\mu\text{M}$  in transport buffer were also made up by adding DMSO in the place of the ASP<sup>+</sup> stock (Table 7).

For the HEK-OCT2 runs cells were washed twice with pre-warmed transport buffer after medium removal and incubated with the pre-incubation solutions for 15 minutes at 37°C. The pre-incubation solutions were then removed and the incubation solutions containing ASP<sup>+</sup> were applied and incubated for 20 minutes at 37°C. After incubation the solutions were removed and the plates were checked under the microscope to ensure cells were still attached before washing with ice cold transport buffer 3 times. To lyse the cells acetonitrile was applied for 30 minutes at -20°C before centrifuging the plate at 3000rpm for 15 minutes at 4°C. The supernatant was then sampled into a black bottom plate and read on the plate reader (PolarStar Omega) at Ex: 485, Em: 590, gain 1200.

### ***2.3.9.3. Fluorescence assay to assess BCRP functionality***

The fluorophore chosen as a BCRP substrate was Hoechst 33342 (H33342) [101], which is routinely used as a counterstain as it fluoresces when bound to DNA. H33342 was used in the presence and absence of the BCRP inhibitors Novobiocin and Ko143 (Sigma Aldrich, UK) to assess BCRP functionality on non-polarised monolayers of MDCK-BCRP. The concentrations of Hoechst 33342 described in the literature ranged from 1 $\mu\text{M}$  to 8 $\mu\text{M}$  [122][101]. Therefore concentrations of 1 $\mu\text{M}$ , 5 $\mu\text{M}$ , 10 $\mu\text{M}$  and 20 $\mu\text{M}$  were applied to the cells. H33342 was made up to stock solutions in DMSO at 200x before being diluted in transport buffer (Table 7). Novobiocin was diluted from a stock solution of 6mM to a final concentration of 30 $\mu\text{M}$  and Ko143 was diluted from a stock solution of

10mM to a final concentration of 50 $\mu$ M in transport buffer containing H33342. MDCK-BCRP plates were washed twice in pre-warmed transport buffer after medium removal and incubated with the respective solutions in the fluorescence plate reader (PolarStar Omega). Monolayers were examined before and after the assay under the microscope to ensure cells hadn't detached throughout the assay. MDCK-BCRP plates were read at Ex: 355nm and Em: 460-10nm, gain 1200 for 71 cycles at 37°C. H33342 was then tested on a cell line overexpressing the transporter P-gp to test for substrate cross specificity with P-gp versus BCRP.

**Table 6:** Inhibitor concentrations used and their IC<sub>50</sub> profiles for the transporter functionality assays

Transporter	Inhibitor	Concentration used ( $\mu$ M)	IC <sub>50</sub> ( $\mu$ M)	Reference
P-gp	Quinidine	100	14.9	[56]
P-gp	Verapamil	100	10.7	[24]
P-gp	Ketoconazole	100	3.07	[56]
BCRP	Novobiocin	30	0.40	[123]
BCRP	Ko143	50	0.01	[110]
OCT2	Imipramine	100	6.00	[124]
OCT2	Ipratropium	100	15.00	[124]

**Table 7:** Dilutions of ASP<sup>+</sup> and H33342 in DMSO for 200x stock solutions to produce the range of working solutions for ASP<sup>+</sup> and H33342

Probe	Final probe Concentration	200x concentration of probe	Stock solution of probe
ASP <sup>+</sup> , H33342	1 $\mu$ M	200 $\mu$ M	200 $\mu$ M
ASP <sup>+</sup> , H33342	5 $\mu$ M	1mM	1mM
ASP <sup>+</sup> , H33342	10 $\mu$ M	2mM	2mM
ASP <sup>+</sup> , H33342	20 $\mu$ M	4mM	4mM

## 2.4. Results

### 2.4.1. Rhodamine 123 assay development in MDCKII and MDCK-MDR1 cells

#### 2.4. 1.1. Rhodamine 123 concentration assessment in MDCKII cells

Before looking at the functional activity of P-gp in MDCK-MDR1 cells overexpressing P-gp, functional activity of P-gp in wild-type MDCKII cells was measured using the bidirectional transport assay with the fluorescent substrate Rho123. P-gp functionality was initially assessed on the wild type MDCKII cells as an endogenous baseline for canine P-gp activity within the transfected MDCK-MDR1 cells. Culture conditions for MDCKII cells on transwells were initially established in terms of days in culture versus seeding density as assessed by the LY monolayer integrity assay (Appendices- Figure 51).

To ascertain the optimal concentration of Rho123 for the bidirectional transport assay, pilot experiments were conducted to establish a concentration range in the absence of any inhibitors. Initially, 7 concentrations of Rho123 were tested alongside a no substrate cell control in the A-B and B-A directions: 1 $\mu$ M, 5 $\mu$ M, 10 $\mu$ M, 20 $\mu$ M, 50 $\mu$ M, 100 $\mu$ M, 200 $\mu$ M. The concentration of DMSO was controlled in the working solutions (transport buffer spiked with the stock solutions in DMSO) at 1% (v/v) due to the potential cytotoxic effects exerted at high concentrations (above 10%) [125]. LY permeability was assessed before and after the Rho123 assay in order to determine the monolayers were acceptable to run the assay, and monolayer integrity was not compromised during the assay. The experiment was repeated twice and is presented in the separate runs to demonstrate monolayer integrity effects on the permeability and active transport of Rho123.

All wells in run 1 showed acceptable permeation percentages before the assay at below 1% (Figure 7a). However there is evidence of damage to the cell monolayers by an increase in LY permeation after the assay (Figure 7b). The increase in the leakiness of the monolayer is predominantly seen in the B-A direction at the higher concentrations (>50  $\mu$ M) of Rho123 in the assay, with the percentage permeation of LY exceeding the threshold limit at 200 $\mu$ M post assay. This indicates higher concentrations of Rho123 above 20 $\mu$ M can compromise monolayer integrity, which may be a consequence of

some form of toxicity, which is concurrent with findings elsewhere [59]. In contrast to this, wells at 20 $\mu$ M, 50 $\mu$ M in both directions, and at 200 $\mu$ M in the B-A direction exhibited a higher percentage LY permeation than the acceptable limit before the assay in run 2 (Figure 8a). Post assay there was a similar increase in LY permeation in all wells to run 1, predominantly in the wells incubated at 50 $\mu$ M, 100 $\mu$ M and 200 $\mu$ M in the B-A direction. This may be due to the accumulation of Rho123 in the cells exerting a toxic effect (as P-gp is located on the apical membrane and would be subject to B-A transport), whereas Rho123 permeability through the apical membrane is more likely to be passive.

Consequently Rho123 transport varied through the concentrations, exhibiting lower permeation in the B-A direction than the A-B direction at 5 $\mu$ M, 20 $\mu$ M and 50 $\mu$ M (Figure 8c). ERs above 2 were exhibited at 1 $\mu$ M and 200 $\mu$ M, however due to high LY permeation post assay, this is not indicative of active transport.

Rho123 permeability was found to be higher in the B-A direction than in the A-B as shown in Figure 8c for run 1 at all concentrations. This follows the expected transport of the substrate as P-gp is located on the apical membrane of polarised cell monolayers [126]. The resulting ERs indicate active transport of Rho123 through the monolayer as they are all above 2, with the highest ERs obtained at 20 $\mu$ M and 200 $\mu$ M. However, due to the increased permeability of the monolayer from high concentrations of Rho123, 20 $\mu$ M would be the ideal concentration from run 1.

The data collected from both runs confirms that tight monolayers of cells with LY permeation below the quality control criteria set can be used to determine the active transport of Rho123 by P-gp. In transfected cells lines overexpressing P-gp there would be an increase in the active transport of Rho123 compared to the wild type. However, the assay is not robust in the 12-well plates and consequently Rho123 transport is not consistent between runs. This is most likely attributed to biological variability regarding membrane integrity, caused by either differences in seeding density or biological variability between cell aliquots in the bank. Monolayer integrity presents a problem for any assay looking at permeability, however, scaled down experiments in 96-well transwells have been successfully implemented at AstraZeneca for these types of assays.

They are also easier and less time consuming to handle, thereby reducing any operator error that may occur. The next step would therefore be looking at the Rho123 permeability in wild type and cell lines overexpressing P-gp in a scaled down (96-well plate) system.

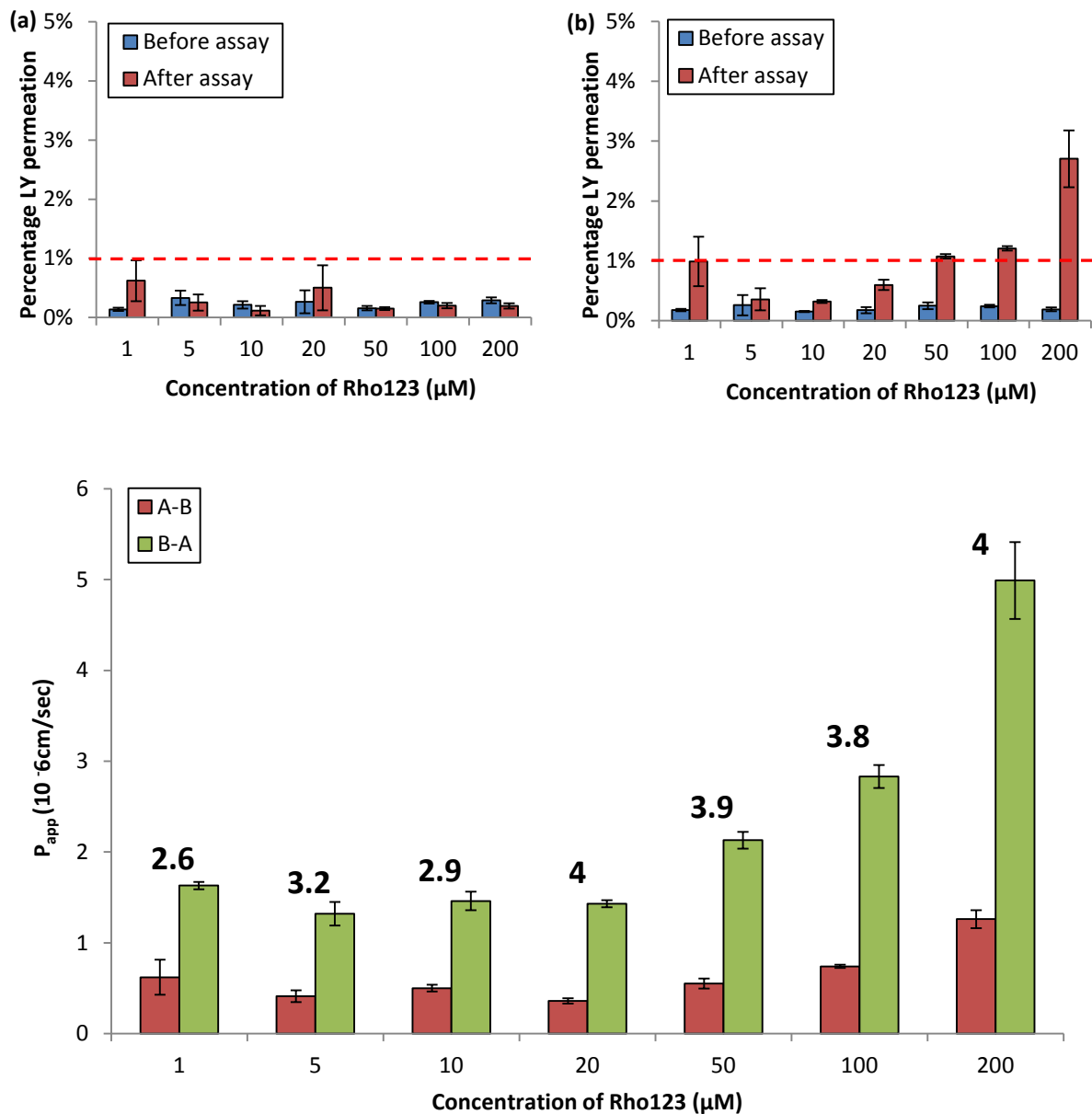


**Figure 7:** LY permeation values for wells used in the (a) A-B and (b) B-A directions at the 1 $\mu\text{M}$ -200 $\mu\text{M}$  Rho123 concentration range before and after the bidirectional transport with (c) the  $P_{app}$  of Rho123 at the 1 $\mu\text{M}$ -200 $\mu\text{M}$  concentration range in the A-B and B-A directions with the ERs assay in Run 1 (Mean value  $\pm$  SEM, n=3). The dashed red line indicates the threshold for acceptable LY permeation used

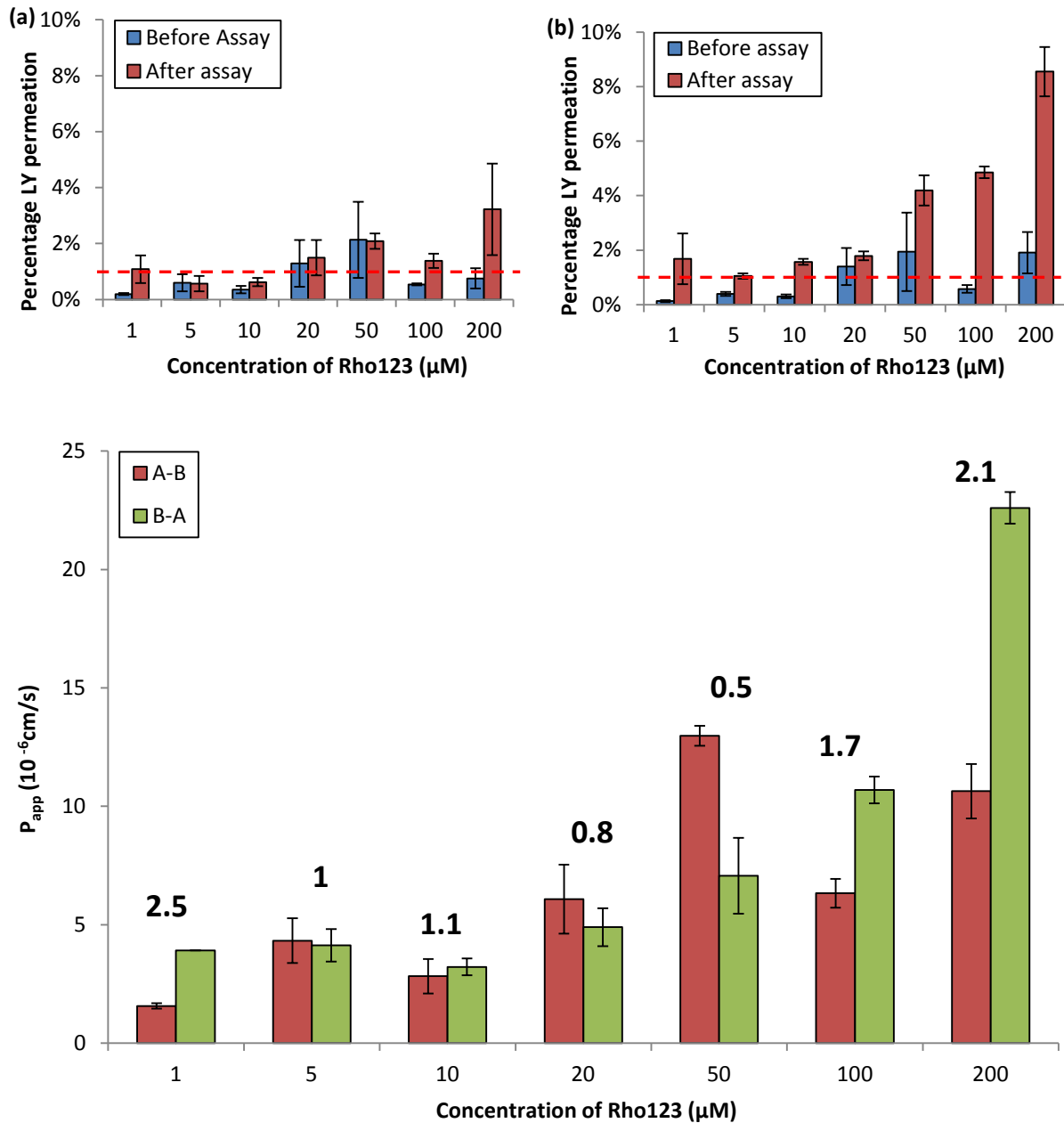


**Figure 8:** LY permeation values for wells used in the (a) A-B and (b) B-A directions at the 1μM-200μM Rho123 concentration range before and after the bidirectional transport assay with (c) The P<sub>app</sub> of Rho123 at the 1μM-200μM concentration range in the A-B and B-A directions with the ERs in Run 2 (Mean value ± SEM, n=3). The P<sub>app</sub> data determined for Rho123 is not considered to be acceptable based on failure of the LY acceptance criteria of <1% permeation (dashed red line)

### 2.4.1.2. Rhodamine 123 transport in MDCK-MDR1 and MDCKII cells

The repeat of the Rho123 concentration experiment described in Section 2.4.1.1. was scaled down from 12-well to 96-well multiwell insert plates to assess the robustness of the assay, and to incorporate MDCK-MDR1 cells. MDCK-MDR1 cells are transfected MDCKII cells which overexpress human P-gp/MDR1, and were also cultured to validate the assay. The concentration range of Rho123 was modified to exclude 200 $\mu$ M which had displayed compromised monolayer integrity previously (Figures 7 and 8). The new range consisting of: 1 $\mu$ M, 2 $\mu$ M, 5 $\mu$ M, 10 $\mu$ M, 20 $\mu$ M, 50 $\mu$ M, 100 $\mu$ M Rho123 was applied as before in Section 2.4.1.1. MDCKII and MDCKI-MDR1 cells were cultured for 3-4 days. Monolayer integrity was assessed before the assay by noting the TEERs, with results of above 500 $\Omega$ /cm<sup>2</sup> indicating suitable monolayer formation. This streamlined the protocols applied at AstraZeneca with the monolayer integrity methods applied in these assays. LY permeation was then tested after the assay to check whether the monolayers maintained integrity throughout the assay.

All MDCKII and MDCK-MDR1 wells displayed TEERs of >500 $\Omega$ /cm<sup>2</sup> before the assay (Appendices- Figure 52). A manual approach of measuring the TEER in transwells (which was trialled in the 12-well plate experiments) suffered from large measurement error introduced by physical movement of the operator. Therefore throughout the 96-well plate experiments automated TEER readers were employed. Although more accurate than manual techniques automated readers have been found to be sensitive to temperature between the beginning and the end of the plate. However, they are still widely used as a measure of monolayer integrity elsewhere [127][128]. The LY assay was therefore employed as the primary marker of monolayer integrity in the 12-well plates, and was applied post assay in the 96-well plates.

Both cell lines exhibited increased transport of Rho123 in the B-A direction compared to the A-B as seen in Section 2.4.1.1. However, with the exception of 1 $\mu$ M the ERs were all lower in both cell lines than were attained in 12 wells (Figure 9) at similar concentrations. Furthermore, ERs at 2 $\mu$ M, 5 $\mu$ M, 10 $\mu$ M, 20 $\mu$ M and 50 $\mu$ M were lower in the MDCK-MDR1 cells than in the MDCKII wild type. This is unexpected as P-gp is overexpressed in the

MDCK-MDR1 line and should exhibit greater transport of Rho123 in the B-A direction resulting in an increased ER.

Active transport (indicated by ERs over 2) of Rho123 was only increased through the MDCK-MDR1 monolayer at 1 $\mu$ M and 100 $\mu$ M of Rho123 compared to the MDCKII cells. The highest ER was also found at concentration 1 $\mu$ M in the MDCKII line, contradicting the findings in the 12-well experiments showing 20 $\mu$ M Rho123 to be actively transported in the wild type (Section 2.4.1.1.).

However, when looking at the LY percentage permeation after the assay, it is clear that the transport shown was due to monolayer damage as all wells in both lines apart from 1 $\mu$ M in the MDCK-MDR1 cells, which showed LY permeation above the 1% threshold. Although this is contradictory to the 12-well plate experiment, the higher amounts of LY permeation in the B-A wells compared to the A-B wells is observed in both plate formats. This gives a further indication to the potential toxicity of Rho123 from either uptake from basolateral or efflux from apical transporters. However differences in monolayer integrity assessment and the accuracy of the TEER reader (due to variation throughout the plate) need to be taken into account when considering the degree of difference between the 12-well and 96-well plates at the same concentrations. From the data collated from the scaled down (96-well plate) experiment, the assay was repeated at a lower concentration range in the same format to determine whether monolayer integrity could be preserved.

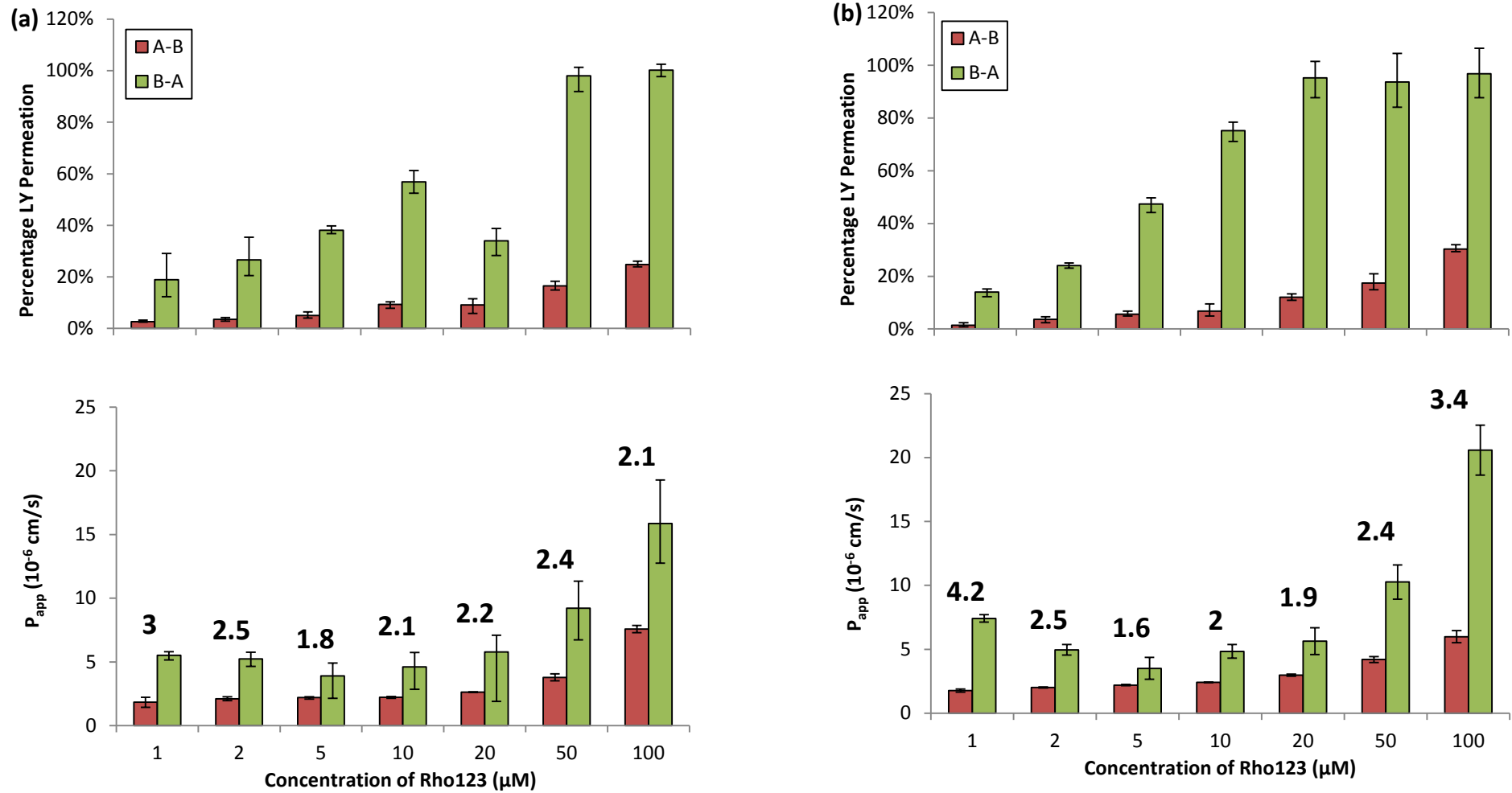


**Figure 9:** The LY permeation percentages after assay (top) and  $P_{app}$  of Rho123 (bottom) at the 1μM-100μM concentration range in the A-B and B-A directions with the ERs in (a) MDCKII and (b) MDCK-MDR1 cells (Mean value ± SEM, n=3)

The concentration range was reduced from the previous assay run to include: 10nM, 20nM, 50nM, 100nM, 500nM, 1000nM, 2000nM concentrations of Rho123 (Figure 10). As before, TEERs were taken before the assay, and LY permeation was applied after the assay. The TEERs for the wells were all of acceptable readings with little variation between the wells, although the readings were lower than in the previous run (Appendices- Figure 53).

Both cell lines exhibited improved monolayer integrity in both directions after the assay, with LY permeation below the 1% threshold limit in 10nM-100nM and 500nM in the MDCK-MDR1 wells, and 10nM-100nM in the MDCKII wells in the A-B direction. The LY permeation is higher in the B-A direction as observed previously, and exceeds the threshold at concentrations 50nM, 100nM, 500nM, 1000nM and 2000nM in both lines and 20nM in MDCKII.

Due to the increased leakiness of the monolayers (LY percentages above the 1% threshold),  $P_{app}$  and ERs at 50nM-2000nM in both cell lines must be disregarded. The ERs at the remaining concentrations in the MDCK-MDR1 cells conform to the expectation of increased transport of Rho123 compared to the MDCKII cells as P-gp is overexpressed in this cell line. This was not observed previously, and is shown at all concentrations except 100nM. However, while the ERs are increased in MDCK-MDR1 cells, they are all below 2 indicating the flux of Rho123 across the monolayers is not due to active transport. The lack of statistical significance between the B-A and A-B  $P_{app}$ s at these concentrations also confirms no active transport is occurring across the MDCK-MDR1 cell monolayers. Therefore, whilst monolayer integrity was preserved after the assay at the lower concentrations in the scaled down experiment active transport cannot be observed, demonstrating the unsuitability of Rho123 for bidirectional transport studies in the scaled down format. To demonstrate the activity of P-gp on this cell line and to assess the functionality of the transporter with a fluorescence probe, Calcein-AM (a known P-gp substrate) was employed in the MDCK-MDR1 cells (Section 2.4.2.1). This assay was first applied in non-polarised monolayers before being applied in primary cells (Section 3.4.2.1.).

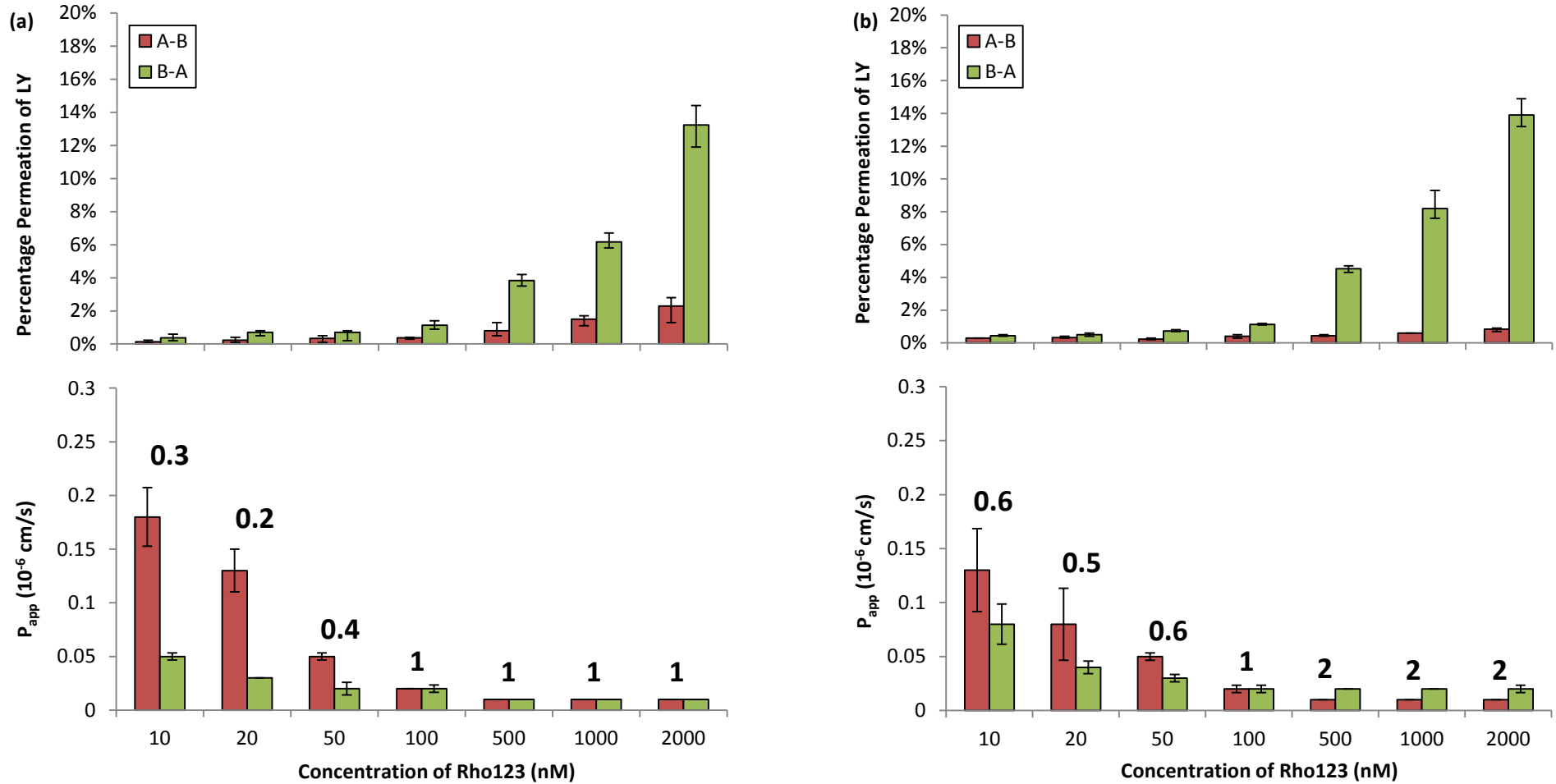


**Figure 10:** The LY permeation percentages after assay (top) and  $P_{app}$  of Rho123 (bottom) at the 10nM-2000nM concentration range in the A-B and B-A directions with the ERs in (a) MDCKII and (b) MDCK-MDR1 cells (Mean value  $\pm$  SEM, n=3)

## 2.4.2. P-gp functionality assessment in MDCK-MDR1 cells using Calcein-AM

### 2.4.2.1. Calcein-AM efflux in MDCK-MDR1 cells in the presence of P-gp inhibitors

Due to difficulties in developing the bidirectional transport assay using Rho123, it was decided to develop an assay utilising the widely used substrate Calcein-AM on non-polarised monolayers of cells (see Appendices- Figure 54 for full cycle graphs).

In cells incubated with Calcein-AM alone there is 3.31 fold increase in fluorescence in run 1, indicating a time dependent increase in the generation of Calcein from Calcein-AM (Figure 11). As expected the intracellular fluorescence due to the Calcein was increased in the presence of P-gp inhibitors. Comparing the inhibited samples to this non-inhibited baseline, inhibitor potency can be indicated alongside the P-gp functionality on the cells. 100 $\mu$ M Quinidine is the less potent inhibitor as shown by a 3.96 fold increase in fluorescence to the baseline after 71 minutes. In the presence of 100 $\mu$ M Verapamil this fold change is increased to 4.42 with statistical analysis *via* one-way ANOVA showing a significant increase in the presence of Verapamil compared to Quinidine inhibited samples ( $p \leq 0.05$ ). The most potent of the 3 P-gp inhibitors was Ketoconazole (100 $\mu$ M) which produced a 9.72 fold increase in fluorescence compared to the baseline in run 2. This increase was statistically significant to both the non-inhibited and inhibited cells. However the fluorescence increase between Verapamil and Quinidine inhibited samples was not significant as shown by ANOVA in run 2.

This assay demonstrated some variability in the 2 runs because the fluorescence in the second plate run was approximately 3 fold higher than the corresponding samples in the first plate. This indicates that variation due to operator error and possible dilution of the solutions is more likely rather than biological variability. Both assays also produced signal to noise ratios (SNRs) of  $>3$  (IUPAC guidelines for analytical techniques), demonstrating fluorescence increases in the presence of inhibitors with a reduced chance of being obscured by methodological noise. Therefore these patterns in fluorescence are a clear indication that the P-gp expressed on the MDCK-MDR1 cells is functional and Calcein-AM is a suitable substrate to be used in this type of assay.

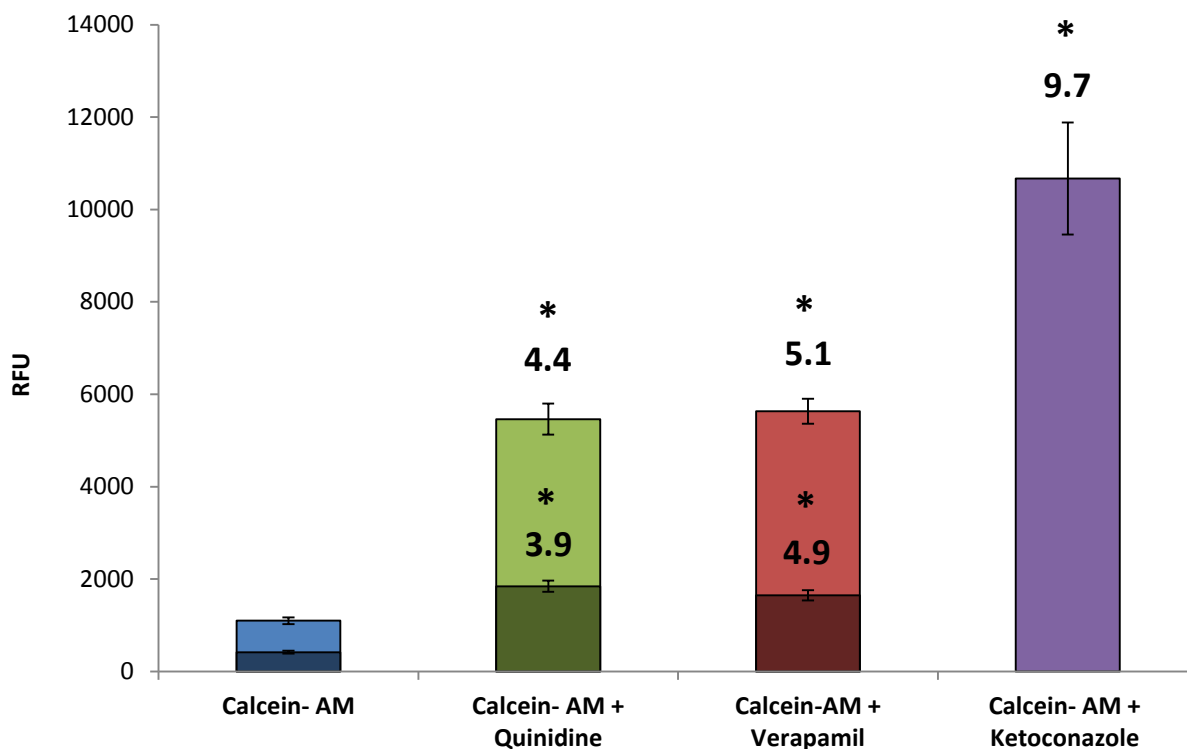


**Figure 11:** Calcein-AM (2.5 $\mu$ M) fluorescence in MDCK-MDR1 cells in the presence and absence of the P-gp inhibitors Verapamil (100 $\mu$ M), Quinidine (100 $\mu$ M) and Ketoconazole (100 $\mu$ M) after 71 cycles (approximately 71 minutes). The darker bars represent fluorescence from run 1 using Verapamil and Quinidine only. Data labels above the bars display fold changes in fluorescence from inhibited cells compared to the uninhibited data set. (Mean value  $\pm$  SD, n=9 for each run). \* significant decrease from the uninhibited sample,  $p \leq 0.05$  (ANOVA with Tukey *post hoc* analysis)

#### ***2.4.2.2. Native fluorescence of P-gp inhibitors in the presence and absence of Calcein-AM***

When applying the Calcein-AM assay to the MDCK-MDR1 cells, one repeat experiment resulted in abnormal RFUs being achieved. Briefly, there was no fluorescence exhibited by the non-inhibited or inhibited cells over the assay time period apart from quinidine inhibited cells, which exhibited an increase in fluorescence from the first cycle but did not change over the time period (Appendices- Figure 55). As factors had been kept consistent through the repeats yielding the expected results (see Section 2.4.2.1.), degradation of the Calcein-AM was suspected. Therefore the fluorescence of inhibitors in the presence and absence of Calcein-AM was investigated in the absence of cells to ascertain whether any fluorescence from inhibitors had contributed to the effects seen in Figure 11. The P-gp inhibitors Verapamil and Ketoconazole alongside the BCRP inhibitors Novobiocin and Ko143 were incubated with Calcein-AM, with fluorescence measured on the plate reader over 71 cycles. The concentrations of the inhibitors were those used in the respective assays and DMSO concentrations were kept at 1% (v/v).

When compared to Calcein-AM only, the fluorescence of Verapamil, Novobiocin and Ko143 were all similar (within 22RFU), with Ketoconazole producing the highest increase in fluorescence with a 100RFU. All inhibitor containing wells were statistically significantly different to the Calcein-AM only well when ANOVA was run ( $p \leq 0.05$ ). However these differences would not have any biological significance as they are small relative to cell based assay fluorescence (Figure 12). It can therefore be concluded that although inhibitors produce a small increase in fluorescence in the presence of Calcein-AM, they can be used in the P-gp functionality assay as they do not cross-react to give artificial fluorescence increases that may confound experimental results.

#### ***2.4.2.3. Assessing Calcein-AM as a P-gp specific substrate***

Calcein-AM was applied to cells overexpressing the transporter BCRP to assess the specificity of Calcein-AM to P-gp (Figure 13). This was required as the eventual goal for this assay was to determine the functionality of P-gp on human PTCs expressing a range of efflux transporters. The assay was repeated using the same concentrations of Calcein-AM (2.5 $\mu$ M), and the inhibitors: Ketoconazole to inhibit P-gp (100 $\mu$ M) and Novobiocin to

inhibit BCRP (100 $\mu$ M) with readings taken at cycle 1 and 71. Although there is a slight increase in fluorescence between Calcein-AM in the presence and absence of Ketoconazole at cycle 1, this fluorescence does not increase in the presence of the inhibitor (Figure 12). Furthermore, in the presence of Novobiocin, there is virtually no change through the cycles and the fluorescence actually decreases in the presence of the inhibitor from 391 RFU at cycle 1 to 385 at cycle 71. The initial values between Calcein-AM and Calcein-AM with Novobiocin are also very similar at 371 RFU and 395 RFU respectively. This indicates that Calcein-AM is not a substrate of BCRP, and can be used as a selective P-gp substrate in systems expressing multiple transporter types to assess the functionality of P-gp.

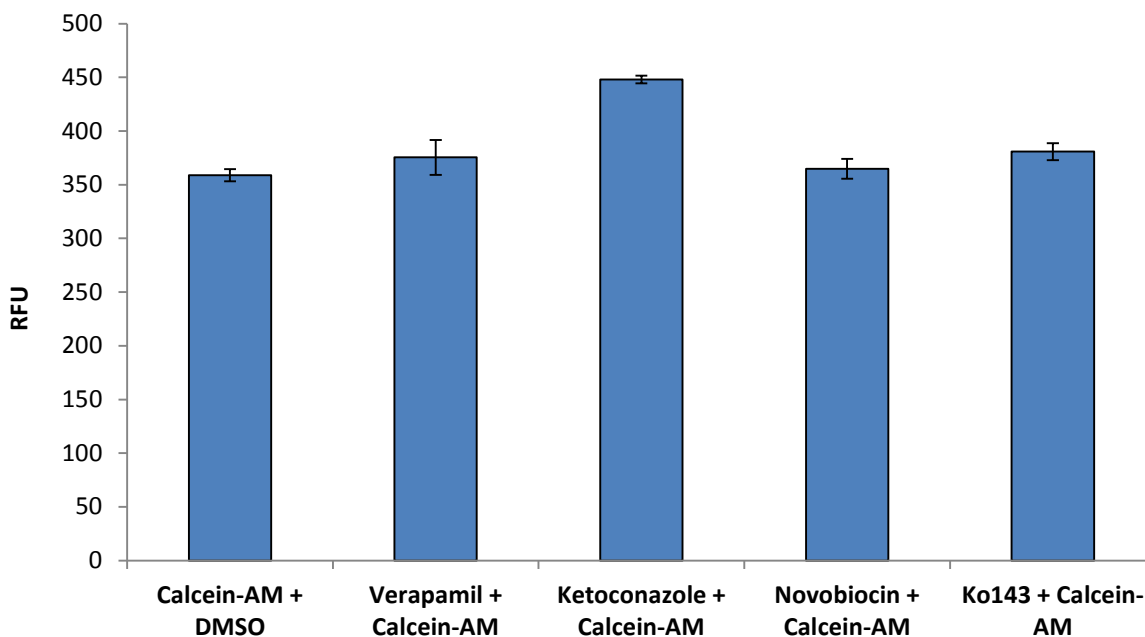


**Figure 12:** The fluorescence of Calcein-AM alongside P-gp inhibitors Verapamil (100 $\mu$ M) and Ketoconazole (100 $\mu$ M) and BCRP inhibitors Novobiocin (30 $\mu$ M) and Ko143 (50 $\mu$ M) in the presence of Calcein-AM at Ex: 485 Em: 520 (Mean value  $\pm$  SD, n=6)  $p \leq 0.05$  (ANOVA with Tukey *post hoc* analysis)

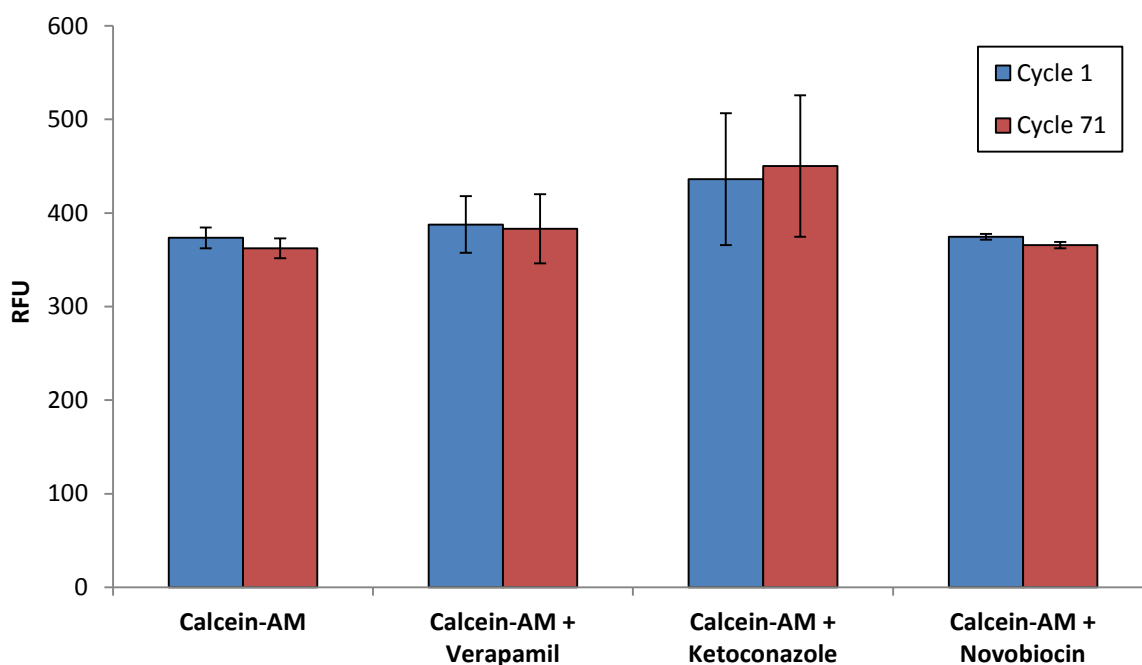


**Figure 13:** Calcein-AM (2.5 $\mu$ M) fluorescence in MDCK-BCRP cells in the presence and absence of the P-gp inhibitors Ketoconazole (100 $\mu$ M) and Verapamil (100 $\mu$ M) and the BCRP inhibitor Novobiocin (30 $\mu$ M) (Mean value  $\pm$  SD, n=6)

### 2.4.3. OCT2 functionality in HEK-OCT2 cells using ASP<sup>+</sup>

#### 2.4.3.1. ASP<sup>+</sup> uptake in HEK-OCT2 cells in the presence and absence of OCT2 inhibitors

As OCT2 is an uptake transporter located on the basolateral membrane on polarised monolayers of cells, the methodology applied to the P-gp assays (Section 2.3.9.2.) to observe substrate efflux were unsuitable to observe uptake transporter functionality. ASP<sup>+</sup> is a fluorescent compound transported by OCT2 into the cell [129] so an uptake assay was developed on non-polarised cell monolayers to observe ASP<sup>+</sup> transport. Due to the nature of the transporter, in the presence of OCT2 inhibitors the uptake of ASP<sup>+</sup> would be restricted and intracellular fluorescence would decrease.

The amount of ASP<sup>+</sup> recovered from lysed cells displays a concentration dependent increase, which was significantly inhibited by both OCT2 inhibitors (Figure 14). The ASP<sup>+</sup> recovery was variable at each concentration in the non-inhibited cells as shown by the error bars representing the SD. However, in the presence of Ipratropium and Imipramine there is a significant 10% and 68% fold respective decrease in fluorescence from the non-inhibited cells at 20µM ASP<sup>+</sup>. The potency of the 2 inhibitors is similar, as at each incubation concentration the decrease in fluorescence from the no inhibitor control is approximately the same. However, in Imipramine inhibited cell samples there is a higher fold decrease in fluorescence at each concentration compared to the non-inhibited cell samples, and is therefore slightly more potent in the HEK-OCT2 cell line. The percentage of ASP<sup>+</sup> recovered from Imipramine inhibited cells is lower by 2%, 15%, 10% and 9% at 1µM, 5µM, 10µM and 20µM respectively than in Ipratropium inhibited cells. However, a significant decrease ( $p \leq 0.05$ ) in fluorescence is only observed in the presence of Imipramine at 10µM of ASP<sup>+</sup> as well as with both inhibitors at 20µM ASP<sup>+</sup>, as calculated through ANOVA testing with Tukey *post hoc* analysis.

As there is a detectable difference in fluorescence in the presence of OCT2 inhibitors (SNRs of  $\geq 3$  in the presence of inhibitors), the concentration of ASP<sup>+</sup> to be used for human cell experiments is 20µM. This conclusion is also confirmed by the fact that there is a significant decrease in fluorescence by both inhibitors at 20µM, whereas this is not exhibited at any other concentration of ASP<sup>+</sup>. Although an increase in the concentration of ASP<sup>+</sup> would most likely yield a higher inhibition i.e. a lower fluorescence value in the

presence of inhibitors, the increase in variability over increasing concentrations of ASP<sup>+</sup> in the non-inhibited cells dictates that the concentration should be kept as low as possible.

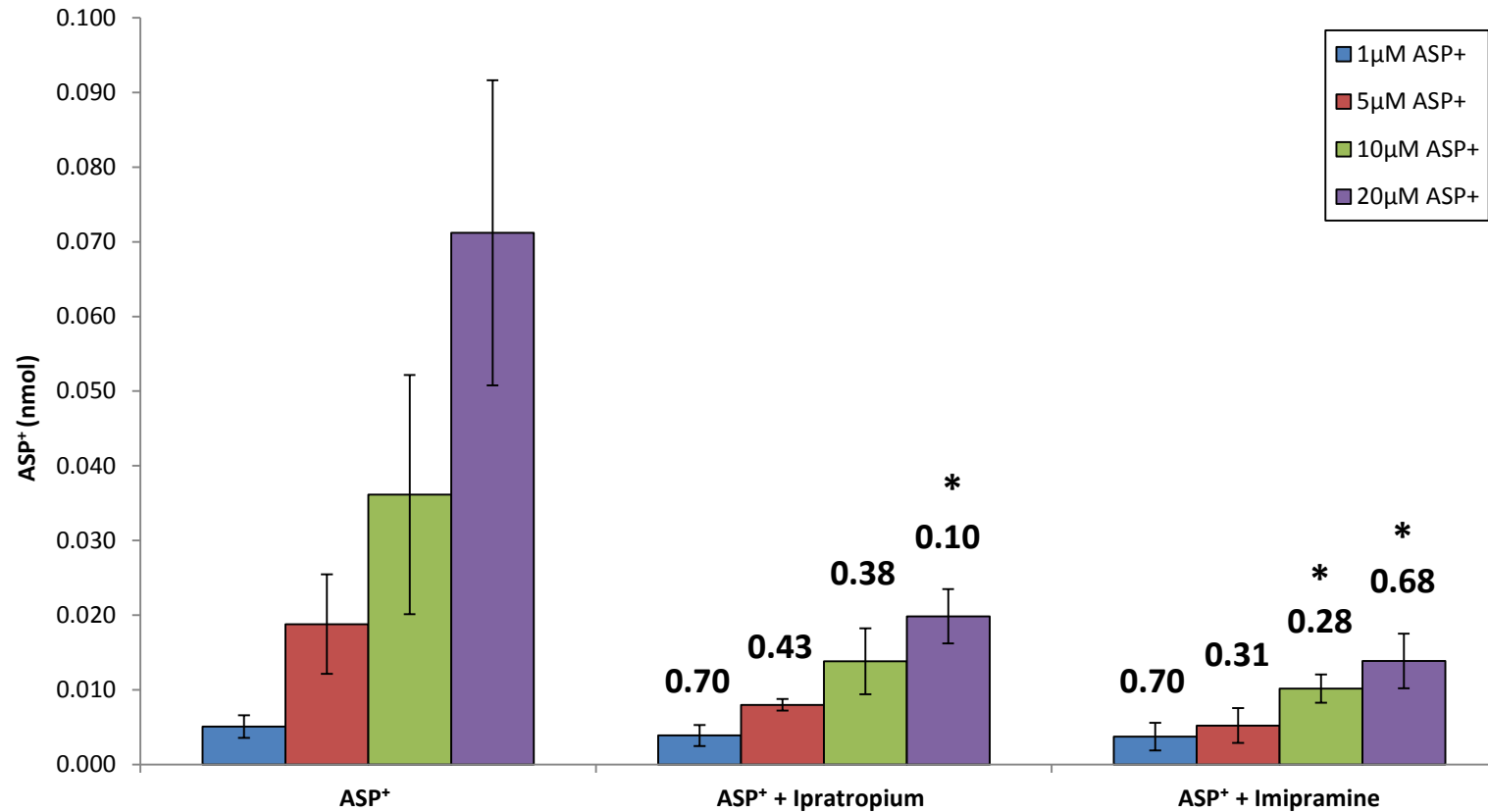


**Figure 14:** The ASP<sup>+</sup> uptake in HEK-OCT2 cells in the presence and absence of the OCT2 inhibitors Ipratropium (100μM) and Imipramine (100μM). Data labels above the bars display fold changes in amount of ASP<sup>+</sup> uptake in inhibited cells compared to the uninhibited cell uptake. (Mean value ± SD, n=6). \* significant decrease from the uninhibited sample at the respective concentration  $p \leq 0.05$  (ANOVA with Tukey *post hoc* analysis)

### 2.4.5. BCRP functionality in MDCK-BCRP cells using Hoechst 33342

#### 2.4.5.1. Hoechst 33342 concentration assessment for efflux assay

BCRP is an efflux transporter belonging to the same family of ABC transporters as P-gp. It is also located on the apical membrane of PTCs, so the same type of assay design used to test the functionality of P-gp on an overexpressed cell line could be employed on non-polarised cell monolayers. At 1 $\mu$ M the fluorescence in the non-inhibited sample at the final cycle (see Appendices- Figures 56 and 57 for full cycle graphs) is relatively low compared to the higher concentrations, but produces a significant 3.54 fold increase in fluorescence in the presence of Ko143 according to ANOVA with Tukey *post hoc* analysis ( $p \leq 0.05$ ). When the concentration of Hoechst 33342 is increased 5 $\mu$ M, 10 $\mu$ M and 20 $\mu$ M show significantly similar fluorescence values for non-inhibited and inhibited samples (Figure 15). Throughout the concentration range Novobiocin (30 $\mu$ M) exerts slight but insignificant inhibition on BCRP shown by the small increase in fluorescence from the uninhibited cells, with SNRs >3 for all samples. Although Novobiocin was used at a low concentration compared to inhibitors in other assays, previous work has found 30 $\mu$ M Novobiocin to be a potent inhibitor of BCRP (see Table 6). However, the data above suggests that higher concentrations would potentially be required to produce significant inhibition when incubated with Hoechst 33342.

Ko143 (50 $\mu$ M) is shown to be a potent inhibitor at all concentrations of Hoechst 33342 by the higher fluorescence values compared to Novobiocin and non-inhibited samples at each concentration, but demonstrates the largest inhibition with the lowest amount of error at 20 $\mu$ M. When run again at 20 $\mu$ M (Figure 16) there is inhibition by both Novobiocin and Ko143 on the MDCK-BCRP system. This is exhibited by a significant increase in fluorescence from the non-inhibited sample of 1.17 and 3.39 fold for Novobiocin and Ko143 respectively, confirming that 20 $\mu$ M is an appropriate concentration for further experiments.

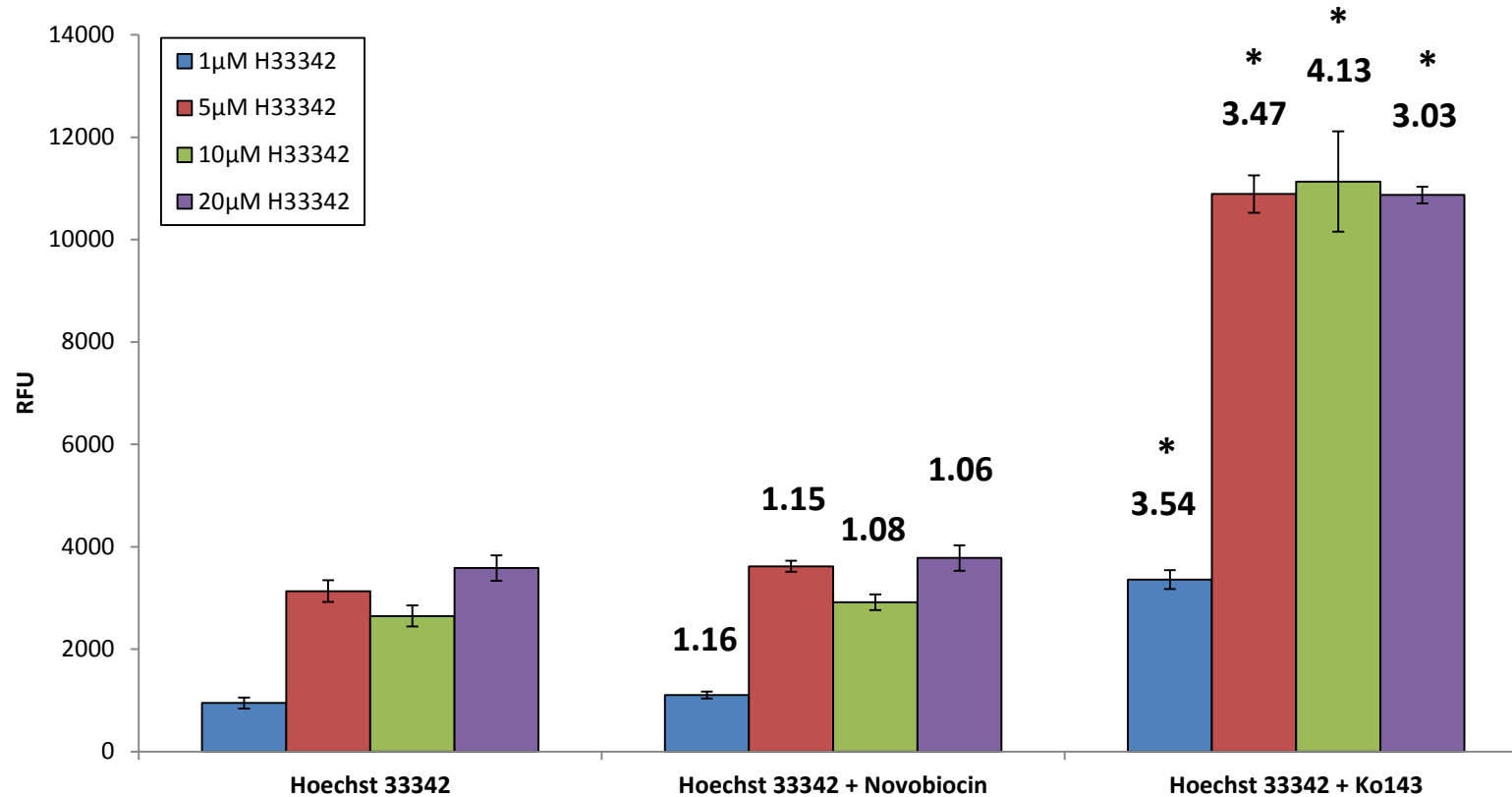


**Figure 15:** Fluorescence of Hoechst 33342 at a range of concentrations in MDCK-BCRP cells in the presence and absence of the BCRP inhibitors Novobiocin (30 μM) and Ko143 (50 μM) after 71 cycles (approximately 71 minutes) Data labels above the bars display fold changes in fluorescence from inhibited cells compared to the uninhibited data set. (Mean value  $\pm$  SD, n=8). \* significant decrease from the uninhibited sample at the respective concentration,  $p \leq 0.05$  (ANOVA with Tukey *post hoc* analysis)

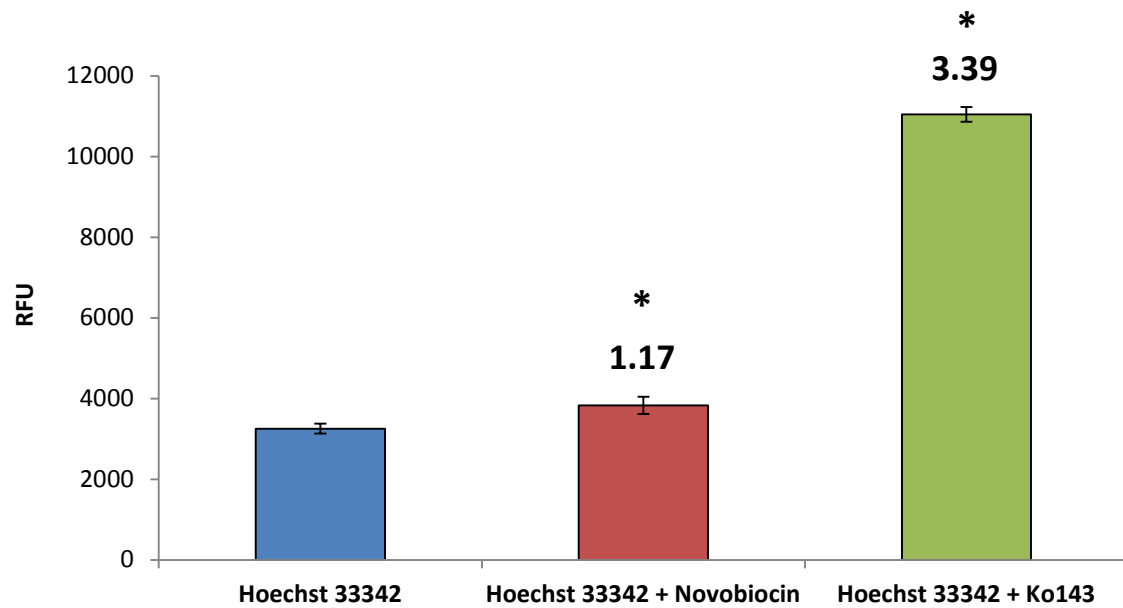


**Figure 16:** Fluorescence of 20µM Hoechst 33342 in MDCK-BCRP cells in the presence and absence of the BCRP inhibitors Novobiocin (30µM) and Ko143 (50µM) after 71 cycles (approximately 71 minutes) Data labels above the bars display fold changes in fluorescence from inhibited cells compared to the uninhibited data set. (Mean value  $\pm$  SD, n=18). \* significant decrease from the uninhibited sample,  $p \leq 0.05$  (ANOVA with Tukey *post hoc* analysis)

#### **2.4.5.2. Native fluorescence of BCRP inhibitors in the presence and absence of Hoechst 33342**

The fluorescence of P-gp and BCRP inhibitors used were ascertained in the presence of Hoechst 33342 to investigate any native (non-cellular) fluorescence of inhibitors or whether fluorescent complexes are formed between the substrate and inhibitors. The fluorescence of BCRP inhibitors Novobiocin and Ko143 alongside the P-gp inhibitors Verapamil and Ketoconazole were measured on the plate reader in the presence of Hoechst 33342 (Figure 17). The concentrations of the inhibitors were those used in the respective assays and DMSO concentrations were kept at 1% (v/v).

The fluorescence of Verapamil, Ketoconazole and Novobiocin in the presence of Hoechst 33342 is significantly lower compared to Hoechst 33342 alone ( $p \leq 0.05$ ). In the presence of Ko143 there is an increase in fluorescence of 554RFU compared to Hoechst 33342 alone. However as with Calcein-AM + inhibitor samples, this difference in fluorescence does not have any biological significance when compared to fluorescence increases in cell based assays. Therefore it can be concluded that BCRP inhibitors can be used without compromising the functionality of the assay.

#### **2.4.5.3. Assessing Hoechst 33342 as a BCRP specific substrate**

As with the Calcein-AM, it was important to assess the cross specificity of Hoechst 33342 in a system expressing transporters with similar specificities as the eventual aim of this assay was to test BCRP functionality in human PTCs. Hoechst 33342 (20 $\mu$ M) was tested in the MDCK-MDR1 cell line against P-gp inhibitors Verapamil and Quinidine at 100 $\mu$ M (Figure 18). When initially looking at the fluorescence at the beginning and end of the assay, it appears that Hoechst 33342 is a P-gp substrate as there appears to be an increase in fluorescence through the cycles. However, when looking at the increase in fluorescence throughout the assay in the presence and absence of inhibitors, the fluorescence increases are similar, indicating little effect of the inhibitor on fluorescence. There is in fact a significant decrease in fluorescence between the Quinidine inhibited sample compared to the non-inhibited, although the increase between the Verapamil inhibited sample and the non-inhibited is significant ( $p \leq 0.05$ ). This suggests that Hoechst 33342 might be an overlapping substrate for P-gp, although the lack of

inhibition by Quinidine and evidence on the similar potency of Quinidine and Verapamil (Figure 11) contradicts this. Therefore Hoechst 33342 can be utilised in a multi-transporter system to assess the functionality of BCRP in the presence of BCRP specific inhibitors, although the cross specificity of Hoechst 33342 should be taken into account.

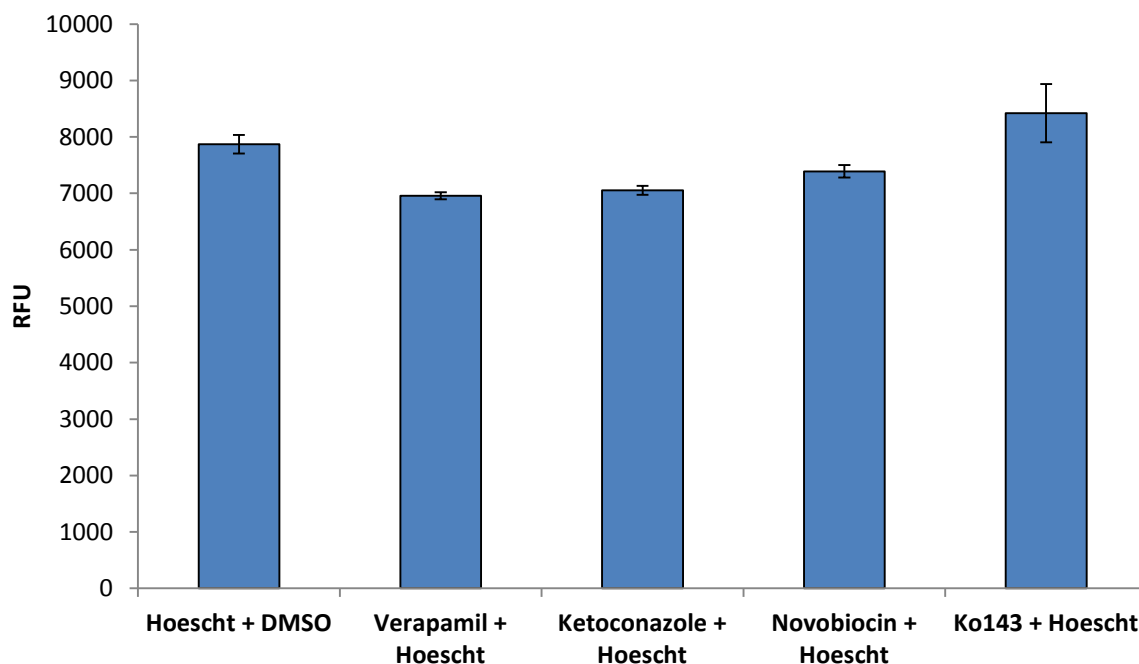


**Figure 17:** The fluorescence of Hoechst 33342 alongside P-gp inhibitors Verapamil (100 $\mu$ M) and Ketoconazole (100 $\mu$ M) and BCRP inhibitors Novobiocin (30 $\mu$ M) and Ko143 (50 $\mu$ M) in the presence of Hoechst 33342 at Ex: 355 Em: 460 (Mean value  $\pm$  SD, n=6)  $p \leq 0.05$  (ANOVA with Tukey *post hoc* analysis)

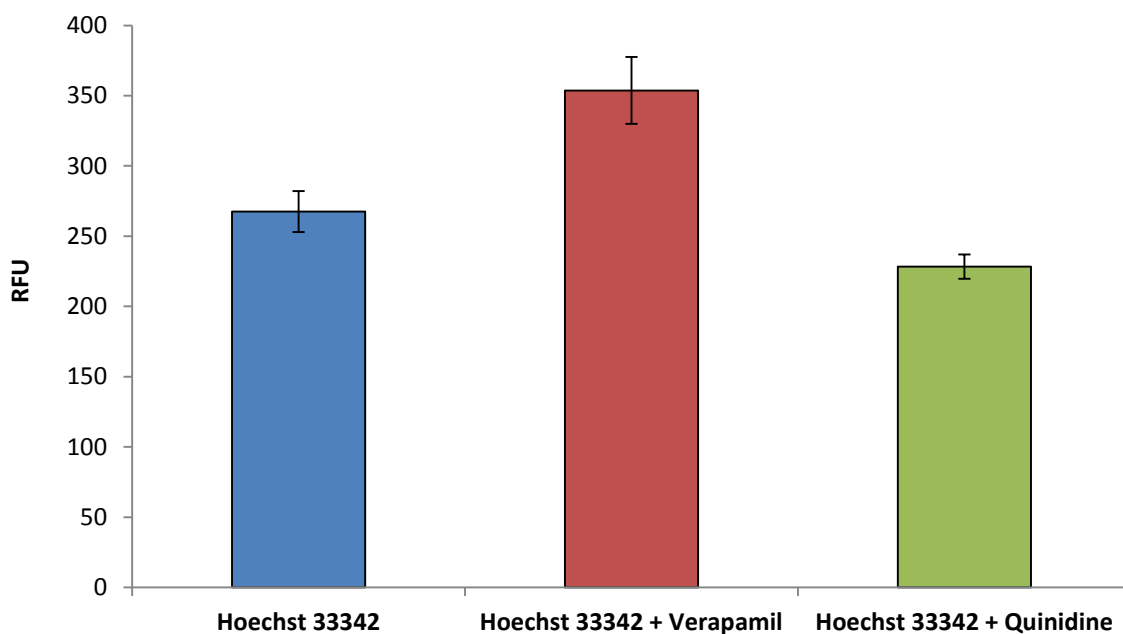


**Figure 18:** Hoechst 33342 (20 $\mu$ M) fluorescence increase in MDCK-MDR1 cells in the presence and absence of the P-gp inhibitors Verapamil (100 $\mu$ M) and Quinidine (100 $\mu$ M) through 71 cycles (approximately 71 minutes) (Mean value  $\pm$  SD, n=6)  $p \leq 0.05$  (ANOVA with Tukey *post hoc* analysis)

## 2.5. Chapter discussion and conclusion

### 2.5.1. Discussion

The focus of this chapter addresses the need for low cost, safe and efficient assays to assess transporter capabilities, and the generation of a panel of assays for the assessment of renal specific transporters, to be utilised through the stages of testing during drug development. As such, bidirectional transport assays were the preferred assays as cells cultured in polarised monolayers more accurately reflect the barrier functions and transport capabilities of the cells *in vitro*. Rho123 was identified as a substrate for the efflux transport P-gp, and had been implemented successfully as a fluorescent substrate previously [119]. However, during the assays using polarised monolayers of MDCKII cells, Rho123 demonstrated varying results in larger scale systems. Active transport was observed in cell monolayers that were intact after the assay throughout the concentration range, but these results could not be reproduced without the permeability of the monolayers increasing above the threshold value. The problems with cell monolayer permeability were also exhibited in smaller scale systems in MDCKII and MDCK-MDR1 cells at the same concentration range. The increase in permeability after the assay suggests that Rho123 may exert a potentially toxic effect on cells above a certain concentration, which has also been suggested by [59].

Another fluorescent substrate for P-gp was identified in the form of Calcein-AM, which fluoresces when cleaved by acetoxymethyl ester hydrolysis by intracellular enzymes to Calcein, which is not a substrate [130]. The nature of the probe required cells to be cultured as non-polarised monolayers. Consequently the results from these assays were an indirect indication for transport functionality in the presence and absence of P-gp specific inhibitors. The same limitations were applied for BCRP assessment, where Hoechst 33342 was used as a substrate and exhibited fluorescence after binding to DNA within the cells. Although these assays did not employ the optimal method of cell culture for quantifiable results, they did indicate the degree of transporter functionality, which could be used comparatively.

ASP<sup>+</sup> was an inherently fluorescent substrate for OCT2, and could have been utilised in a bidirectional transport assay to assess OCT2 uptake. However, due to the assay format

of the other two transporters, non-polarised monolayers of cells overexpressing OCT2 were used in the generation of the panel of assays for transporter functionality on renal cells.

### 2.5.2. Conclusion

Fluorescence assays have been utilised within the pharmaceutical industry for high throughput assays, but less so in the later stages of pre-clinical drug testing. This has been identified as a major gap in the knowledge (refer to Section 2.2.3.4.). As such, one of the aims of this thesis was to generate a panel of assays for the assessment of renal specific drug transporters i.e. P-gp, BCRP, OCT2, OAT1 and OAT3 and MATE1 using fluorescent substrates, which does not currently exist. This chapter has described the generation assays to assess the functionality of both efflux and uptake transporters using fluorescent substrates in the presence and absence of transporter specific inhibitors. The assays have also been assessed for the potential cross-specificity that could occur when applied in multi-transporter systems. The unsuitability of certain fluorescent substrates that have been used previously for the assessment of transporters has also been identified and corroborated by reports in literature. The fluorescence assays developed for these transporters will be applied in primary cell systems to assess transporter functionality over time in *in vitro* culture, as discussed in Chapter 3.

# **Chapter 3**

## **Characterisation of human proximal tubule cells**

### 3.1. Introduction

Cell lines are useful to develop assays, with cell lines overexpressing the desired transporter(s) offering a transporter specific model e.g. MDCK-MDR1 cells, and other epithelial cell lines offering a model with many transporters expressed e.g. Caco-2 cells. They also offer the ease of reduced culture times compared to primary cells, and are relatively inexpensive. However, they cannot translate the native processes found *in vivo* for specific tissues *in vitro* which primary cells offer.

Primary cells are notoriously difficult to culture *in vitro*, and while they may be able to display qualities such as attachment and doubling over many passages, they often exhibit a rapid, time-dependent, general loss of function [20]. However, when looking at model cell systems, they are the gold standard as they offer the native expression of transporter, enzymes and metabolic pathways found *in vivo*. When looking at model cell systems of the kidney, proximal tubule cells (PTCs) offer a variety of renal specific functions including reabsorption, metabolic and transport functions, the secretion of uremic toxins and xenobiotics, producing 1,25- dihydroxy vitamin D3 and performing immunomodulatory functions [131]. PTCs also possess a range of transporters: organic anion and organic cation transporters predominantly for basolateral drug uptake with ABC transporters present on the apical surface for luminal excretion. Many of the transporters are polyspecific i.e. accept compounds of different sizes and molecular structures, and have overlapping substrate specificities [132] (Table 2). For this reason, substrate and inhibitor specificity is an important factor in the assessment of transporter functionality.

In this chapter, the characterisation of human PTCs (RPTECs) will be described in terms of transporter expression, visualisation and functionality over a series of Population doublings. The growth of RPTECs on porous surfaces with various coatings will then be described, looking at the monolayer integrity and TEERs for each condition.

## 3.2. Review of the literature

### 3.2.1. Renal physiology

#### 3.2.1.1. Kidney anatomy

The kidneys are a pair of bean-shaped organs located along the posterior wall of the abdominal cavity. They are primarily responsible for the excretion of waste products such as urea and ammonia from the body through the urine. However, they also provide a variety of significant secondary functions through homeostatic, endocrine, immune and metabolic processes. The kidney consists of 3 main sections; the renal cortex (outer section), the medulla (middle section) and the renal pelvis. Nephrons, the functional units of the kidney are located in the cortex (cortical) and between the cortex and the medulla (juxtamedullary). They have a unique architecture and are each associated with their own blood system (Figure 19). Each kidney has approximately 1 million nephrons and can process up to 170L of blood per day. After the blood has been processed the waste is then transferred to the renal pelvis and into the urinary bladder for excretion. The nephrons can be split into 5 distinct sections according to their function; the Bowman's capsule, Proximal tubule, Loop of Henle, Distal tubule and Collecting duct. The Bowman's capsule (also known as the renal corpuscle) is an expansion at the closed end of the nephron and encases a bundle of capillaries known as the glomerulus. It is the site of ultrafiltration, where the blood entering the glomerulus through a wide afferent arteriole and leaving through a narrow efferent arteriole creates a build-up of pressure which forces small molecules from the blood into the capsule (ultrafiltrate). Large components such as proteins and cells remain in the blood and are supplemented with nutrients and metabolites further on in the nephron. The capsule membrane then extends to the proximal tubule, which is the main site of reabsorption and metabolism within the kidney and is discussed in length in Section 3.2.1.3. The isotonic ultrafiltrate then progresses into the loop of henle which in juxtamedullary nephrons extends into the medulla from the cortex. This is the site of water and ion (sodium;  $\text{Na}^+$ , chloride;  $\text{Cl}^-$ , potassium;  $\text{K}^+$ , calcium;  $\text{Ca}^{2+}$ , magnesium;  $\text{Mg}^{2+}$ ) reabsorption, with the descending limb impermeable to ions and slightly permeable to urea but permeable to water. The thin ascending limb is the reverse and is freely permeable to ions but impermeable to water.

The transport of both molecules is passive due to the osmotic gradient created in the loop and the interstitium, and only in the thick ascending limb is salt actively transported from the filtrate. On exit from the Loop of Henle the remaining filtrate is returned to its isotonic state. The distal tubule extends the reabsorption of  $\text{Na}^+$  and  $\text{Cl}^-$  whilst regulating the pH of the filtrate by secreting  $\text{H}^+$  and bicarbonate ions. It is also the primary site of hormone based calcium regulation in the kidneys in response to parathyroid hormone (PTH) and water reabsorption in response to anti-diuretic hormone (ADH). If ADH is not present the distal tubule is relatively impermeable to water. Once the filtrate has passed through the nephron it is transferred into the collecting duct and through to the renal pelvis. The collecting duct system is the final site of electrolyte regulation and is also influenced by the action of ADH. The filtrate leaves the kidney as urine through the renal pelvis and into the urinary bladder to be excreted.

#### **3.2.1.2. The renal interstitium**

The renal interstitium is comprised of the cellular elements and extracellular substances in the extravascular spaces of the renal parenchyma [133]. There are two contiguous cellular networks within the interstitium made up of fibroblasts and dendritic cells. Fibroblasts constitute the 'skeleton' of the kidney and are attached to the basement membranes of vessels and tubules by focal adhesions [134]. They play a major role in extracellular matrix (ECM) homeostasis by producing many of the ECM constituents (fibronectin, collagen I, III and V) alongside ECM-degrading proteases such as the matrix metalloproteinases [135]. Dysregulation of these (residential) fibroblasts however from injury and/or activation cause the appearance of myofibroblasts within the interstitium. These fibroblasts, characterised by the presence of alpha smooth muscle actin ( $\alpha\text{SMA}$ ) are the main cellular mediators of interstitial fibrosis, the main pathology of chronic kidney disease [136]. The generation of myofibroblasts is not well understood although possible sources include the activation of resident fibroblasts, the proliferation of fibroblasts expressing  $\alpha\text{SMA}$  or the conversion of epithelial or endothelial cells to cells with a mesenchymal phenotype. Dendritic cells belong to the mononuclear phagocyte system and continually probe the surrounding environment responding to insults that arise from the parenchyma. They form an organ spanning network which is narrowly intertwined with the fibroblastic

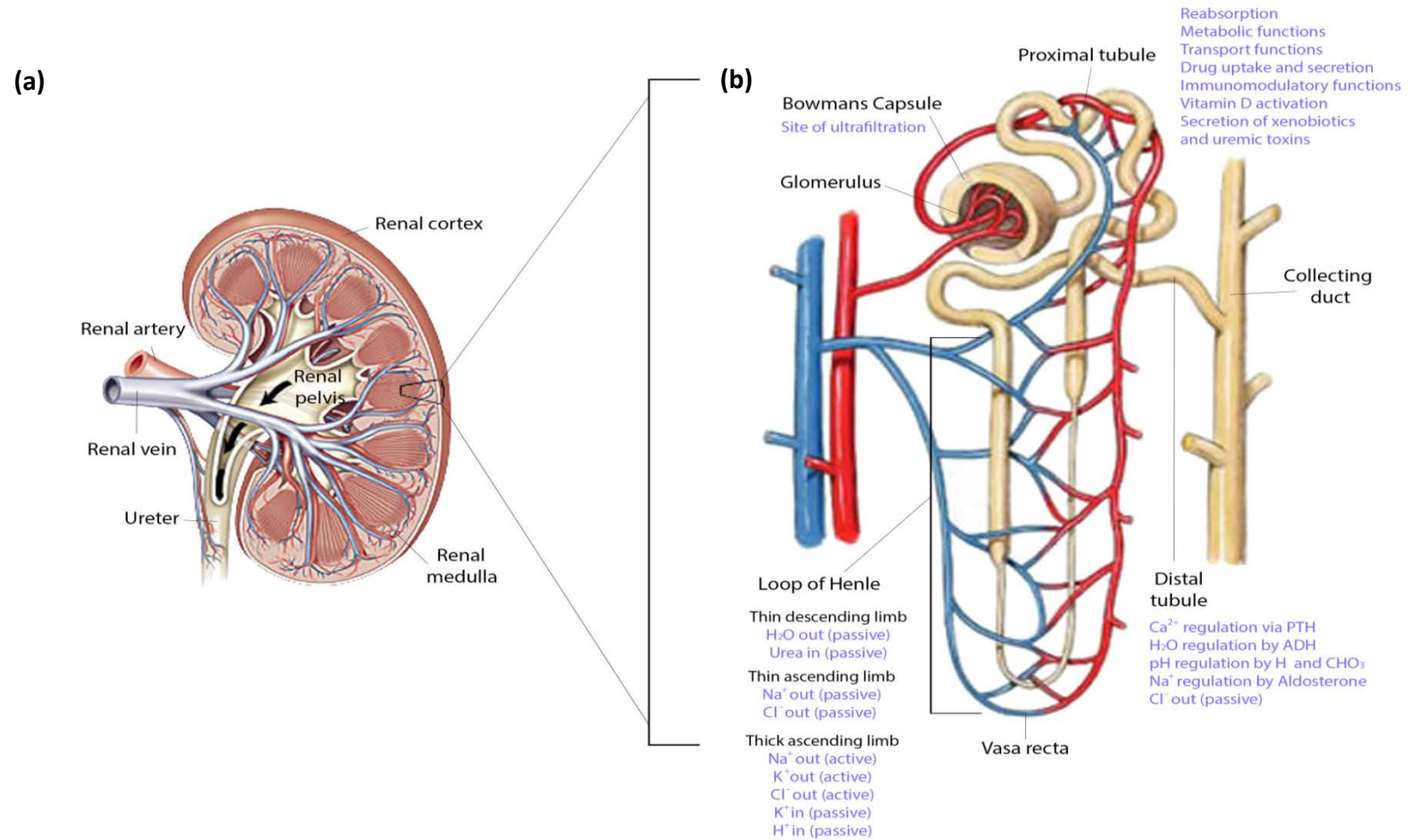


**Figure 19:** Structure of the kidney showing (a) the 3 main sections and (b) the structure of the nephron and the function of the Bowman's capsule, proximal tubule, loop of Henle, distal tubule and collecting duct. Adapted from [137][138]

skeleton. When activated from their immature phenotype they express increased levels of MHC II and co-stimulatory proteins with a high capacity for uptake of antigens [135].

Alongside the cellular network there is a vast array of ECM proteins making up the basement membranes for all parenchymal structures. The functions of the ECM in the cortex are distinctly different depending on its molecular components: in the glomeruli (glomerular basement membrane, Bowman's capsule, mesangial ECM), in the tubulointerstitium (tubular basement membrane, peritubular capillary basement membrane, interstitial ECM) and in larger vessels (within and around the vessels). The glomerular basement membrane (GBM) contains four main macromolecules: laminin, collagen IV, nidogen and heparin sulphate proteoglycans, and is thicker compared to other basement membranes. Its main function is to act as a selective filtration barrier between the vascular system and urinary space depending on charge and size. In contrast the mesangial ECM provides more of a structural support for the glomerular capillary convolute, connecting with the extra-glomerular mesangium and assisting in cell-matrix signalling in a bidirectional manner. Its composition is primarily fibronectin, collagen IV, collagen V, laminin A, B1 and B2, chondroitin sulphate and heparin sulphate proteoglycans, allowing for larger molecules to pass to the mesangium [136]. Tubular basement membranes (TBM) support the epithelial cells of the rest of the nephron and are critical to cell orientation and function, and if disrupted can lead to cell death and tissue destruction. Its function is also similar to the GBM in providing a selective barrier to macromolecules between the tubule and interstitium. The TBM is comprised mainly of collagen IV (approximately 50%) [139] laminin  $\alpha1\beta1\gamma1$  and  $\alpha5\beta1\gamma1$ , entactin/ nidogen, perlecan and bamacan and displays heterogeneity throughout the nephron [140].

The interstitial connective tissue supports the TBM and is composed of collagen I, II, V, VI, VII and XV, sulphated and non-sulphated glycosaminoglycans, glycoproteins and polysaccharides. In the medulla the interstitial ECM is more prominent, increasing from the outer to inner medulla/papilla [136]. ECM proteins in the kidney are listed in Table 8.

**Table 8:** ECM proteins present throughout the kidney\*

<b>Protein</b>	<b>Location</b>	<b>Reference</b>
<b>Collagen I</b>	I-ECM	[136][141]
<b>Collagen III</b>	I-ECM	[136] [141]
<b>Collagen IV</b>	GBM, TBM, M-ECM	[140] [141]
<b>Collagen V</b>	I-ECM, M-ECM	[136] [141]
<b>Collagen XV</b>	I-ECM	[136] [141]
<b>Fibronectin</b>	M-ECM	[136] [141]
<b>Laminin (<math>\alpha</math>, <math>\beta</math>, <math>\gamma</math>)</b>	Glomerulus, Nephron, M-ECM	[140] [141]
<b>Entactin</b>	TBM	[140]
<b>Nidogen</b>	TBM	[140] [141]
<b>Osteonectin</b>	Nephron	[141]
<b>Tenascin</b>	Stroma	[141]
<b>Aggrin</b>	GBM	[140]
<b>Perlecan</b>	TBM	[140]
<b>Bamacan</b>	TBM	[140]
<b>Dystroglycan- <math>\alpha</math>1</b>	Nephron	[141]
<b>Chondroitin sulphate</b>	M-ECM	[136]
<b>Heparan sulphate proteoglycans</b>	M-ECM	[136]

\*This is not an exhaustive list

**Abbreviations:** I-ECM; Interstitial extracellular matrix, GBM; Glomerular basement membrane, TBM; Tubular basement membrane, M-ECM; Mesangial extracellular matrix

### 3.2.1.3. Proximal tubule architecture and function

The proximal tubule (PT) is the extension of the Bowman's capsule primarily involved in the reabsorption of approximately 60-65% of the glomerular filtrate, amongst performing other secondary functions. The filtration, reabsorption and excretion rates of some substances within the kidney can be found in Table 9 [142]. The proximal tubule consists of two main sections; the proximal convoluted tubule (*pars convoluta*) and the proximal straight tubule (*pars recta*), which can in turn be further identified by 3 morphologically distinct segments. The S1 segment constitutes approximately two thirds of the *pars convoluta* and begins at the Bowman's capsule. It has a tall brush border on the apical surface of the cell (exposed to the lumen) with the basolateral membrane forming extensive lateral invaginations. Elongated mitochondria are found in the lateral processes which protrude from the apical surface and interlock with similar processes from other cells and provide energy for the nearby  $\text{Na}^+ - \text{K}^+$  ATPase pumps [155]. Sodium, water, glucose and bicarbonate reabsorption is approximately three fold greater in the S1 segment compared to the S2, and tenfold greater than in the S3 segment [142]. The ultrastructure of the S2 segment, which consists of the remainder of the *pars convoluta* and the initial portion of the *pars recta* is similar to the S1 segment. However the brush border is shorter and contains less prominent basolateral invaginations. The S3 segment is the remainder of the *pars recta*, and whilst possessing an intermediate brush border, lateral cell processes and invaginations are essentially absent. Complex extracellular compartments are formed between the interlocking lateral and basal processes between adjacent cells (Figure 20). The separation of this space by the plasma membrane and specialised tight junction (TJ) proteins (e.g. *Zona occludens 1* (ZO-1), Claudin-2) allows a continuous band to be formed around the luminal surface of each cell. This creates a selectively permeable barrier for molecules dependent on their size, charge and the type of proteins present. Claudin-2, is the dominant form of the claudin proteins in the proximal tubule and is inherently leakier than other forms such as claudin 4 or 8 (present in the collecting ducts). This results in a low transepithelial resistance (TER) and leakier membrane in terms of the paracellular permeability of molecules less than 4Å in size with a preference of cations over anions [156]. ZO-1 is also present on the PTCs and is indispensable in the formation of tight junctions in epithelial cells. The

**Table 9:** The filtration, reabsorption and excretion rates of nutrients and electrolytes in the kidney, the percentage of filtrate reabsorbed in the proximal tubule and their transport mechanisms

Substance	Filtered (meq/24h)	Reabsorbed (meq/24h)	Excreted (meq/24h)	Reabsorbed in the PT (%)	Transport in the PT (uptake from lumen, efflux to interstitium)	Reference
<b>Glucose (g/day)</b>	180	180	0	100	Na <sup>+</sup> -glucose symport- SGLT 1 and 2 (passive uptake) GLUT1 and 2 transporters (passive efflux)	[142][143]
<b>Sodium (meq/day)</b>	25,560	25,410	150	70	Na <sup>+</sup> -K <sup>+</sup> ATPase pump (active efflux) Na <sup>+</sup> dependent HCO <sub>3</sub> <sup>-</sup> -Cl <sup>-</sup> exchanger (active efflux) Na <sup>+</sup> ion channels (passive uptake) Na <sup>+</sup> -H <sup>+</sup> antiport (active uptake) Na <sup>+</sup> -glucose symport- SGLT 1 and 2 (active uptake) Co-transport with phosphate, amino acids and bicarbonate (active uptake)	[142][144] [145]
<b>Chloride (meq/day)</b>	19,440	19,260	180	60	NaCl-H <sup>+</sup> antiport (passive uptake) Cl <sup>-</sup> paracellular diffusion (passive uptake) Cl <sup>-</sup> -OH <sup>-</sup> exchanger (active uptake) Cl <sup>-</sup> -formate exchanger (active uptake) Cl <sup>-</sup> -oxalate exchanger (active uptake) Cl <sup>-</sup> ion channel (passive efflux) K <sup>+</sup> -Cl <sup>-</sup> co-transporter (active efflux) Na <sup>+</sup> dependent HCO <sub>3</sub> <sup>-</sup> -Cl <sup>-</sup> exchanger (active efflux)	[142][144] [146][145]

Table 9 continued:

Substance	Filtered (meq/24h)	Reabsorbed (meq/24h)	Excreted (meq/24h)	Reabsorbed in the PT (%)	Transport in the PT (uptake from lumen, efflux to interstitium)	Reference
<b>Potassium (meq/day)</b>	10	9.1	1.5	60-70	K <sup>+</sup> paracellular diffusion (passive uptake) Na <sup>+</sup> -K <sup>+</sup> ATPase pump (active efflux) K <sup>+</sup> -Cl <sup>-</sup> co-transporter (active efflux)	[147][148] [149]
<b>Phosphate (g/day)</b>	6	5.51	0.49	60-70	Na <sup>+</sup> dependent HPO <sub>4</sub> (active uptake) HPO <sub>4</sub> diffusion (passive efflux)	[150]
<b>Calcium (mg/day)</b>	10,000	9,700	300	60	Ca <sup>2+</sup> paracellular diffusion (passive uptake) Ca <sup>2+</sup> ion channels (passive uptake) Na <sup>+</sup> -Ca <sup>2+</sup> exchanger (active efflux)	[151][144]
<b>Bicarbonate (meq/day)</b>	4,320	4,318	2	85-90	Extracellular dehydration and Intracellular generation of HCO <sub>3</sub> <sup>-</sup> (passive uptake) NaHCO <sub>3</sub> co-transporter (active efflux)	[142][148] [152]
<b>Water (L/day)</b>	169	167.5	1.5	60-80	H <sub>2</sub> O paracellular diffusion (passive uptake) Aquaporin 1 and 7 H <sub>2</sub> O uptake (active uptake)	[142][153] [154]

protein is located on the cytoplasmic side of the TJ strands and is involved in the sequential steps of assembly of adherent and tight junctions as well as the physical segregation of the membrane [157]. The remainder of the intercellular compartment between the TJs and basement membrane contain other types of cell-cell junctions; adhering junctions (*zonula adherens*), desmosomes (*macula adherens*) and gap junctions. The *adherens* junctions lie directly below the TJs and are responsible for holding the cells together through membrane glycoproteins (predominantly E-cadherin). Desmosomes also use cadherin proteins (desmoglein, desmocollin) to connect cells however they are connected to intracellular circular plaques to provide strong intercellular connections. Gap junctions allow small continuous channels to be formed between cells, allowing the movement of inorganic ions and other small water soluble molecules (smaller than 1000kDa) [158].

With the intercellular movement of molecules restricted the major routes of nutrient and ion reabsorption occur by a variety of transporters and mechanisms through the cells. PTCs are also the major site of drug uptake, metabolism and excretion within the kidney, where most unbound polar drugs and metabolites are excreted in the urine after processing in the liver. Some of the transporters involved in drug uptake and secretion which are pharmacologically relevant in terms of drug-drug interactions are investigated in Chapter 2 and shown in Figure 20. Drug metabolism occurs in both the *pars convoluta* and *pars recta* cells through phase I (oxidation, reduction or hydrolysis) and II (conjugation) metabolism. Due to the increased amounts of smooth endoplasmic reticulum in the *pars recta* compared to other sites, S3 PTCs are also the main site of injury within the nephron from xenobiotic metabolite activation [159].

The proximal tubule is also involved in secondary functions such as: immunomodulatory functions where the production of IL-6 in the kidney stimulates the production of IL-10 in the liver influencing the outcome in endotoxin shock and gram-negative sepsis [160] and facilitating the activation of vitamin D from 25 hydroxyvitamin D to 1,25(OH)<sub>2</sub>D [161].

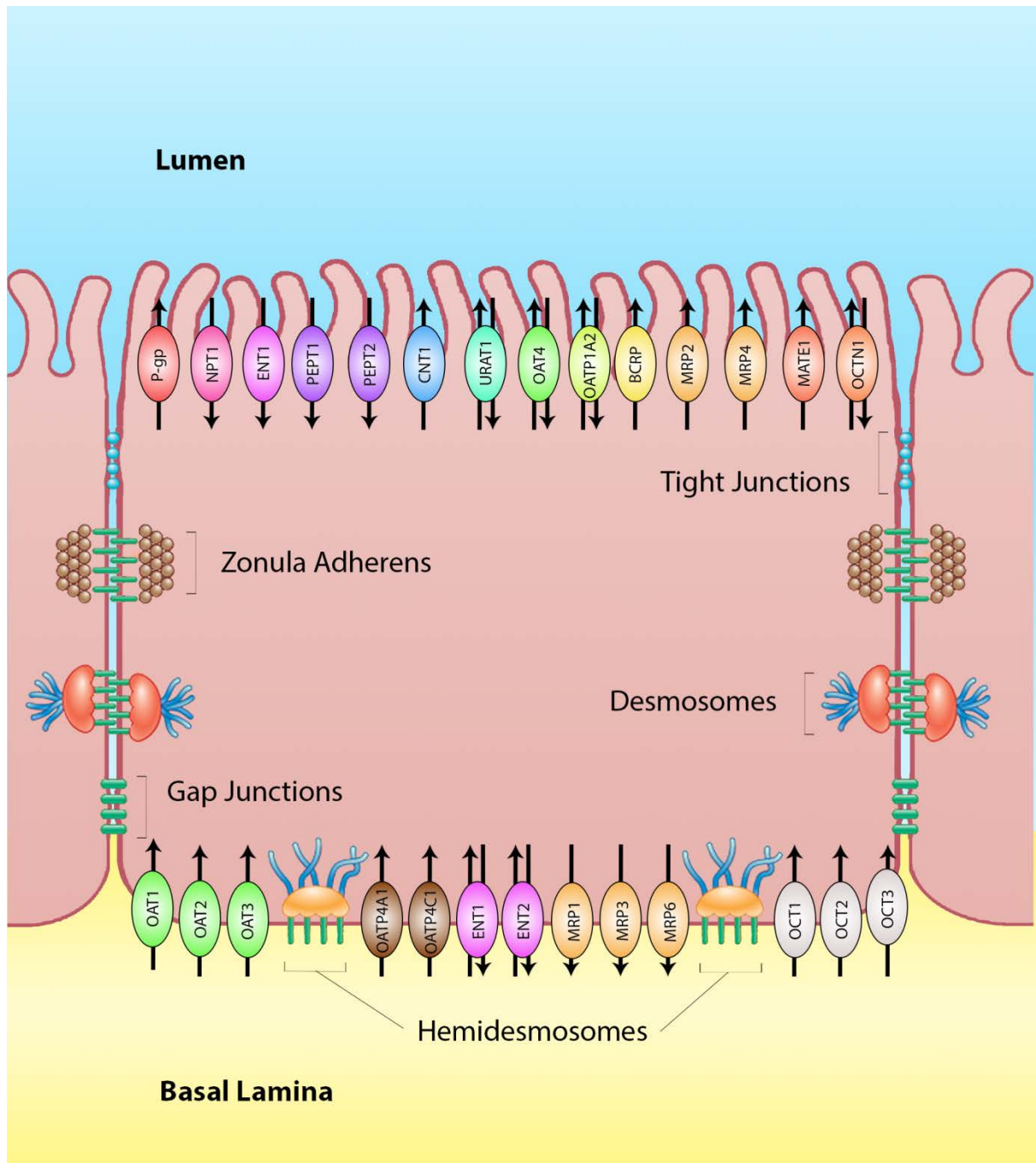


**Figure 20:** Structure of the PTC and the arrangements of proteins comprising the intercellular compartment. The diffusion of paracellular molecules are able to penetrate the proteins separating the cells through to the basal lamina and are dependent on size and charge. The location of drug transporters is also shown on the apical (lumen facing) or basolateral (basal lamina facing) membranes with the direction of molecule transport indicated by the arrows. Adapted from [162][163]

### 3.2.2. Cell sources for 2D models of the kidney

PTCs are the optimal cell type for renal models in drug development due to the wide variety of functions performed by the proximal tubule *in vivo* including being the primary site of drug metabolism in the kidney. However, choosing the appropriate source for *in vitro* models is imperative when building robust models for the IVIVE of CDs. Primary human PTCs (hPTCs) are best suited when modelling the PT *in vitro* due to documented heterogeneity between species in the presence, localisation, kinetics or regulation of some transport systems. These include the Na<sup>+</sup> -H<sup>+</sup> (NHE) transporter regulation and apical tissue distribution, basolateral Na<sup>+</sup>, K<sup>+</sup> -ATPase, organic anion and cation transport and paracellular pathways [164]. Moreover the down regulation of drug transporter expression (BCRP, OCT2, OAT3) between rat and human PTCs [165] and the differences in metalloproteinase inhibitor cytotoxicity between the rat, monkey and human [166] give evidence to the fact that human models are needed within the screening process in drug development for robust IVIVE to be made. hPTCs have been characterised in terms of high throughput screening as a predictive model (~76%-85% predictability) for tubular toxicity at early pre-clinical stage testing [167] and as a polarised primary cell culture model to look at xenobiotic transporter function [168]. They have also been shown to maintain measurable phase I (11 CYP enzymes and 3 glutathione S-transferases) and phase II (3 UDP-glucuronosyltransferases and 3 sulfotransferases) drug metabolising enzyme expression in *in vitro* culture [169]. Morphology, cellular energetics and redox status have also been validated in primary hPTC culture. However, it is well documented that the culture of epithelial cells *in vitro* can lead to the loss of differentiated properties, and in the case of PTCs: the loss of a brush-border plasma membrane, decreased expression and/or functionality of plasma membrane transporters, decreased expression of drug metabolising enzymes and a decreased mitochondrial function leading to the glycolytic pathway as the primary source of energy metabolism can occur [166]. There is also an issue of inter-donor variability which has been demonstrated by looking at the difference in marker gene expression in response to nephrotoxins from different hPTC donors [167]. This is problematic in terms of the reproducibility of results as the numbers of cells needed for drug screening assays far outweigh the availability of hPTCs. Two million PTCs are

typically isolated from one gram of cortical tissue [170], however for polarised monolayer assays approximately 3 million cells per 96-well plate are required. Furthermore issues of sterility are associated with primary cultures, and small degrees of contamination from other epithelial cell populations and interstitial fibroblasts can occur depending on isolation protocol used [166].

Using transformed cell lines addresses the issue of cell number and donor variability as these cells can be cultured *in vitro* for prolonged periods of time (cell immortalisation). Mammalian cells are generally easier to immortalise than human cells, and lines originating from the kidney such as the MDCK line from canine and LLC-PK from porcine sources have been used to model the PT epithelia. MDCK cells have been extensively studied and retain many of the differentiated properties associated with the kidney tubular epithelium including apical microvilli, junctional complexes and lateral membrane infoldings and are able to transport sodium and water in an apical to basolateral direction [171]. This makes them an excellent source of cells to use as a standardised *in vitro* model for drug transport and interaction studies when manipulated to overexpress human transporters (Section 2.4.2). However, due to the extensive manipulation and inter-species variation they cannot be used as a model for the proximal tubule. The HEK293 cell line originates from an uncharacterised kidney cell in the human embryo transformed with sheared adenovirus 5 DNA. However, due to the manipulation process, the cells do not provide a relevant model, but are widely used in the transfection of drug transporters in screening and as an expression tool for recombinant proteins [172]. Human cell lines such as the HK-2, HKC and more recently the RPTEC/TERT1 have been developed from the manipulation of adult hPTCs utilising a variety of methods. HK-2 cells use the E6/E7 genes from the human papilloma virus 16 (HPV16) to immortalise kidney tubular cells. These cells have survived for over one year in culture whilst retaining functional characteristics of primary PTC cultures such as typical BBM-associated enzymes and Na<sup>+</sup> dependent glucose uptake [173]. However, dome formation, a hallmark of transporting epithelium that retains vectorial active transport, and the formation of functional TJs have not been identified in this cell line [174]. The HKC line is immortalised using a hybrid adeno-12-SV40 virus and when compared to the HK-2 cell line shows similar differentiated features *in vitro*. However

they also share the same caveat that they have the inability to form polarised monolayers capable of vectorial transport [175]. RPTEC/TERT1 cell immortalisation targets the overexpression of human telomerase (hTERT) with [176] or without [177] the SV40 Tag gene to stabilise telomeres and extend the cell life span. These cells have demonstrated growth for up to two years in culture and largely maintain the original differentiation status and functionality. The retention of high levels of brush border enzymes, significant Na<sup>+</sup> dependent glucose uptake and phosphate uptake and the presence of microvilli have all been demonstrated by the cells throughout culture. Furthermore the formation of domes and the presence of TJs and desmosomes indicate the ability of vectorial transport as is present *in situ*, making them a valuable tool in the development of PTC models for many applications including drug screening.

Utilising stem cells as a pluripotent and self-renewable source of cells could provide an abundant source of PTCs and other renal cells. Human embryonic stem cells have recently been differentiated into proximal tubule-like cells when cultured on Matrigel in renal epithelial cell medium and exposure to BMP2 and 7. Polarised monolayers of cells have been formed which expressed TJs and apical microvilli alongside the genetic expression of drug transporters present on hPTCs which were retained in both 2D and 3D culture. However, the degree of de-differentiation is comparable to hPTCs in *in vitro* culture, although the issues of cell sourcing and inter-donor variability are addressed [178]. Induced pluripotent stem (iPS) cells also offer an abundant ethically sound source of cells which have been developed to derive cells of the renal lineage which give rise to apically ciliated tubular structures that co-express various PT markers [179]. However, the differentiation of pluripotent stem cells down renal cell lineages is still in the early stages and requires further characterisation before application in pharmaceutical and clinical research. Therefore, primary cells remain as one of the most reliable options for both applications in research as *in vitro* models and clinical uses.

### 3.2.3. Conclusion

The proximal tubule is the main site of reabsorption, secretion and drug metabolism within the kidney. The anatomy of the PT, whilst fairly complex, relies on the compartmentalisation of the ultrafiltrate from the vascular network by the epithelial cells, non-parenchymal cells and ECM proteins to fulfill its function. To make an efficient barrier, TJ proteins must be present to restrict the intercellular movement of molecules and allow processing and vectorial transport of substances through the epithelial cell monolayer. A variety of cell sources exist to model the PT functions, although they fail to balance the ability of long term *in vitro* culture with the retention of specific functions found *in vivo*. Therefore, as one of the most reliable options is using primary cells as an *in vitro* model of the PT, focus on the method of culture to allow *in vivo* characteristics to be retained over culture *in vitro* must be applied. This chapter aims to address this aspect by investigating drug transporter genetic and surface expression and functionality on primary cells over time in *in vitro* culture, which has not been addressed in the literature to date. The proliferation of PTCs on protein coated porous membranes is also addressed to ascertain the formation of tight monolayers, thereby allowing the compartmentalisation that is found *in vivo*.

### 3.3. Materials and methods

#### 3.3.1. Cell Lines

RPTEC (Human Renal Proximal Tubule Epithelial Cells; CC-2553) were purchased from Lonza (Belgium) at passage 3 and were cryopreserved at passages 5 and 7. Cells are guaranteed by the manufacturer for 15 population doublings (Pds), and transwell coating experiments used cells at a final passage of 7 (9 population doublings). Population doublings were calculated using Equation 2 (Appendices 2.2.).

#### 3.3.2. Cryopreservation and Cell Resuscitation

RPTECs were cryopreserved at a density of  $1.5 \times 10^6$  cells/ml in a freezing medium of 80% supplemented REGM basal medium (Lonza, Belgium), 10% (v/v) FBS (Fisher Scientific) and 10% (v/v) DMSO (Sigma Aldrich, UK).

Cells were resuscitated by removal from liquid nitrogen storage and rapidly thawed in a 37 °C water bath. Vials were half submerged and gently agitated until a sliver of ice remained. The vial was then transferred to the BSC and the cell suspension seeded into a T-flask containing pre-warmed supplemented REGM as per the manufacturer's instructions (Lonza, Belgium).

#### 3.3.3. Medium Formulation

REBM basal media was supplemented with 0.1% hEGF, 0.1% hydrocortisone 0.1% epinephrine, 0.1% (v/v) insulin, 0.1% (v/v) triiodothyronine, 0.1% (v/v) transferrin, 0.1% (v/v) Gentamicin and 0.5% (v/v) FBS. The complete growth medium was stored at 2 – 8 °C and used within one month of preparation.

#### 3.3.4. Monolayer Culture

##### 3.3.4.1. T-flask culture

RPTECs were cultured for 6-8 days with medium changes every 2 days until cells reached >80% confluency. On the day of passage, medium was aspirated and cells were washed with PBS. After the aspiration of PBS, pre-warmed 0.25% trypsin- EDTA was added to the flask and incubated at 37°C for 2 minutes for enzymatic digestion of the

cell adherence proteins to the tissue culture plastic. After incubation the trypsin digestion was quenched with approximately double the amount of pre-warmed culture medium and the cell suspension was centrifuged for 5 minutes at 220g. The supernatant was removed after centrifugation and the cell pellet was resuspended in the appropriate volume of culture medium. Cells were counted using the NC-3000 nucleocounter (see Section 3.3.5.) for calculation of desired seeding densities. RPTECs were grown for 1 passage before seeding into other vessels for experimentation.

#### **3.3.4.2. Transwell culture**

Transwell types and seeding densities were established experimentally but final methods for transwell culture of RPTECs are as follows and summarized in Table 10. RPTECs were cultured on Corning 12-well polycarbonate transwell inserts (0.4  $\mu\text{m}$  pore size, 1.12 $\text{cm}^2$  surface area; Sigma Aldrich, UK). Before seeding, transwell plates were incubated with culture medium for 1 hour at 37°C to equilibrate. Culture medium was then aspirated and fresh medium was added to the wells. Cell suspension from tissue culture flask passages was added to the inserts at  $4.5 \times 10^5$  cells/ $\text{cm}^2$ . The plates were then incubated statically for 1 day at 37°C before transferring to a shaking incubator at 90rpm at 37°C for the remainder of the culture period. Cells were cultured for 8-16 days with medium changes every 2 days.

#### **3.3.4.3. Plate culture**

Due to loss of cells during the assay duration in 96-well clear bottomed black plates (BD, UK), wells were coated in matrigel overnight at a concentration of 0.125  $\mu\text{g}/\mu\text{L}$  (see Section 3.3.7.1. for full method) for P-gp and BCRP assays. For the OCT2 assay 48-well plates were coated at the same concentration. RPTECs were seeded at 4 Pd 0, 5, 7 and 9 at  $1.6 \times 10^4$  cells/ $\text{cm}^2$  in 96-well 48-well plates and cultured for 4 days with medium changes at 2 days. Plates at Pd=0 were seeded directly from frozen whereas plates at later doublings were cultured in uncoated T-75 and T-175 flasks before seeding. The Pds were calculated according to the RPTEC growth curve generated (Appendices- Figure 58).

**Table 10:** Culture conditions for the various cell types used on different plates

Cell line	Plate type	Seeding density (cells/cm <sup>2</sup> )	Culture period	Medium changes
RPTEC	Transwell (12-well)	4.5 x 10 <sup>5</sup>	16 days	Every 2 days
RPTEC	48 and 96-well plates (coated)	1.6 x 10 <sup>4</sup>	4 days	Every 2 days

### 3.3.5. Cell counting- Aquadin orange and propidium iodide exclusion (automated cell counts)

Automated cell counts via aquadin orange (AO) permeation and PI exclusion were carried out on the NucleoCounter NC-3000 automatic mammalian cell counter using one viability and cell count cassette.

Total cells, viable cells, Non-viable cells (cells/mL) and viability (%) were calculated by the machine alongside estimated cell diameter ( $\mu\text{m}$ ) from 200 $\mu\text{l}$  samples of cell suspension.

### 3.3.6. Fluorescence assays to assess transporter functionality

Functional assays were performed after cell culture (see Section 3.3.4.3.). The IC<sub>50</sub> concentrations for each of the inhibitors used for the transporters: P-gp (Section 3.3.6.2.), BCRP (Section 3.3.6.3.) and OCT2 (Section 3.3.6.4.) and concentrations used are summarised in Table 6 (Chapter 2).

#### 3.3.6.1. Transport buffers for functional assays

The transport buffer used was modified Krebs buffer based on [168] (see Table 11) balanced to pH 7.4.

#### 3.3.6.3. Fluorescence assay to assess BCRP functionality

H33342 was made up to a stock solution of 4mM before being diluted at 200x in transport buffer to 20 $\mu\text{M}$ . Novobiocin was diluted from a stock solution of 6mM to a final concentration of 30 $\mu\text{M}$  and Ko143 was diluted from a stock solution of 10mM to a

final concentration of 50 $\mu$ M in transport buffer containing H33342. RPTEC plates were washed twice in pre-warmed transport buffer after medium removal and incubated with the respective solutions in the fluorescence plate reader (FluoStar Omega). RPTEC plates were read at Ex: 355nm and Em: 460nm, gain 1000.

**Table 11:** Modified Krebs buffer component concentrations

Additive	mmol/L	g/L
NaCl (Sodium Chloride)	140	8.18
KCl (Potassium Chloride)	5.4	0.4
MgSO <sub>4</sub> (Magnesium Sulphate)	1.2	0.14
K <sub>2</sub> HPO <sub>4</sub> (Potassium Hydrogen Phosphate)	0.3	0.041
Na <sub>2</sub> HPO <sub>4</sub> (Sodium Hydrogen Phosphate)	0.3	0.036
CaCl <sub>2</sub> (Calcium Chloride)	2	0.22
Glucose	5	0.90
HEPES	10	2.38

#### 3.3.6.4. Fluorescence assay to assess OCT2 functionality

ASP<sup>+</sup> was made up to a stock solution of 4mM before being diluted at 200x in transport buffer to 20 $\mu$ M. Stock solutions of the Imipramine and Ipratropium were made up at 20mM and diluted at 200x to 100 $\mu$ M in buffer containing ASP<sup>+</sup>. Pre-incubation solutions containing inhibitors at 100 $\mu$ M in transport buffer were also made up (see Table 7). RPTECs were washed once with pre-warmed transport buffer after medium removal and incubated with the pre-incubation solutions for 20 minutes at 37°C. After incubation the solutions were removed the incubation solutions containing ASP<sup>+</sup> were applied and incubated for 50 minutes at 37°C. After incubation the cells were washed with ambient temperature transport buffer twice. To lyse the cells lysis buffer containing 1% TritonX-100 (v/v) was applied for 1 hour at room temperature on a shaking platform at 100rpm. After pipette mixing the plate was centrifuged at 3000rpm for 15 minutes and the

supernatant sampled. The samples were read on the plate reader (FluoStar Omega) at Ex:485, Em:590, gain 1200.

### **3.3.7. Transwell Coatings and monolayer integrity analysis**

Corning 12-well polycarbonate transwell inserts were used for the coating experiments using RPTECs. During coating periods, inserts were removed from the well plates and transferred to Nunc 6-well plates. Unless otherwise stated, during coating periods plates were kept in the BSC in covered plates. Corning transwell-Col (bovine collagen I and III coated wells) 12-well inserts were transferred into plates containing coated transwells. Wells were pre-incubated with medium to equilibrate and RPTECs (Pd=9) were seeded at  $4 \times 10^5$  cells/ insert. Cells were cultured for 16 days on a shaking incubator at 90rpm with LY assays (as described in Section 2.3.7.) performed every 2 days from day 2. TEER measurements were taken before LY assays on each day and medium changes were performed after the assays.

#### **3.3.7.1. Matrigel Single Coating**

All pipette tips and stripettes were frozen, and medium, plates and centrifuge tubes were refrigerated before use and placed in cold beads in the BSC. Matrigel (BD Bioscience, UK) was thawed in the fridge and diluted in cold DMEM (Life Technologies, UK) to make a  $0.125\mu\text{g}/\mu\text{L}$  solution. A volume of  $150\mu\text{L}$  was placed in the inserts and refrigerated overnight. Before seeding with cells, the plates were removed to room temperature for 1 hour and residual medium was aspirated.

#### **3.3.7.2. Gelatin Single Coating**

A 0.2% gelatin in PBS solution was generated from 2% (v/v) gelatin (Sigma Aldrich, UK). A volume of  $250\mu\text{L}$  was placed in the inserts and left overnight. Before seeding residual solution was aspirated and the inserts were rinsed with PBS.

#### **3.3.7.3. DOPA + Collagen IV Double Coating**

Tris buffer (10mM Trizma base at pH 8.5; Sigma Aldrich, UK) was used to dilute 3,4-Dihydroxy-L-phenylalanine (DOPA; Sigma Aldrich, UK) to a 0.2% solution. A volume of  $150\mu\text{L}$  was placed in the inserts and left overnight.

Human collagen IV (Sigma Aldrich, UK) was submerged in cold beads and slow thawed at 4°C for 3 hours before suspending in HBSS to generate a 150µg/ml solution. DOPA wells were washed with PBS 3 times, and 200µL of collagen added to the wells. The plates were left for 2 hours at room temperature, and before seeding residual solution was aspirated and the inserts were washed with PBS and kept in the fridge.

### 3.3.8. Immunostaining procedure and analysis

Immunostaining was used to visually detect drug transporters using antibodies on the surface of RPTECs. The transporters and corresponding primary and secondary antibodies and antibody dilutions used can be found in Table 12. A range of dilutions were first carried out in optical bottom black plates (Nunc) to determine the appropriate dilution for each antibody. RPTECs were cultured on clear bottom 96-well black plates coated with 0.125µg/µL Matrigel for 4 days with medium changes every 2 days until the cells were confluent. On day 4 medium was aspirated and cells were washed with PBS before fixing in 4% paraformaldehyde (PFA; BD Bioscience, UK) for 20 minutes at room temperature. After aspiration of fixative and washing with PBS, wells were incubated with blocking buffer (1 x PBS, 5% normal goat serum, 0.3% triton-X100; Sigma Aldrich, UK) for 1 hour at room temperature away from light. After aspiration of the blocking buffer, the primary antibody solutions diluted in 1% BSA were added to the wells and incubated at 4°C overnight away from light. Primary antibodies were then removed and wells were washed thoroughly (5 times) with PBS before the addition of fluorophore conjugated secondary antibodies and phalloidin to the wells (see Table 12). Antibodies were incubated for 1-2 hours at room temperature away from light and washed thoroughly with PBS after antibody removal. The cells were then counterstained with 300nM DAPI (Life Technologies, UK) solution for 5 minutes at room temperature away from light before mounting with Prolong gold anti-fade mounting solution. Images were taken on the Nikon Eclipse Ti fluorescence microscope and analysed on the Nikon software NIS-elements. Individual cells were isolated in the image and the mean intensity in the FITC channel (AlexaFluor 488 bound to primary antibodies) was calculated. Exposures and LUTs were kept consistent through doublings for each transporter. The gain was kept consistent at 1.00x for all images. See Table 13 for analysis settings.

### 3.3.9. RT-PCR and preparation

#### 3.3.9.1. RNA extraction for RT-PCR

RNA was extracted from cells cultured in T-25 flasks for 4 days with medium changes every 2 days. Extraction methods were carried out using the RNeasy Plus mini kit (Qiagen, UK) according to manufacturer's protocols. The RNA concentration was then determined using the NanoDrop 2000c (Thermo Scientific, UK) before samples were frozen.

#### 3.3.9.2. RNA integrity assessment

The integrity of the RNA was checked using the Agilent RNA 6000 Pico kit and Agilent 2100 Bioanalyser (Agilent Technologies, UK). The gel and dye was prepared according to the manufacturers protocol and loaded onto the gel alongside the supplied RNA ladder. RNA was diluted down to 5ng/ $\mu$ l in RNase free water for analysis and 1 $\mu$ l was applied to the chip (11 samples per chip).

#### 3.3.9.3. RT-PCR

All reagents and consumables were sourced from Life technologies for RT-PCR. The primers for the 4 genes of interest plus the reference gene primer can be found in Table 14. The Taqman gene expression assays and express One-step superscript Universal reagents were used alongside stock RNA diluted to 50ng/ $\mu$ l. MicroAmp 96-well plates and films were used and the reactions were run in the StepOne plus RT-PCR system (Applied Technologies, UK). The standard cycling program was used according to the manufacturer's protocol for the Express one-step SuperScript kit.

**Table 12:** List of primary antibodies to selected transporters and fluorescent secondary antibodies and fluorophores used in RPTEC immunostaining

<b>Antibody/ Fluorophore</b>	<b>Host</b>	<b>Antibody type</b>	<b>Supplier</b>	<b>Dilution</b>
Anti- P-gp	Mouse	Primary	Abcam	1:10
Anti- OCT2	Rabbit	Primary	Sigma Aldrich	1:20
Anti- BCRP	Mouse	Primary	Abcam	1:20
Anti- MRP2	Mouse	Primary	Abcam	1:10
Anti- MATE1	Rabbit	Primary	Abcam	1:50
Anti- OAT3	Rabbit	Primary	Abcam	1:100
AlexaFluor 488 anti-mouse	Goat	Secondary	Life Technologies	1:1000
AlexaFluor 488 anti-rabbit	Goat	Secondary	Life Technologies	1:1000
AlexaFluor 594 Phalloidin	-	Secondary- Conjugated	Life Technologies	1:40

**Table 13:** Analysis settings for transporter fluorescence quantification (FITC channel)

<b>Transporter</b>	<b>Number of cells analysed</b>				<b>Exposure (s)</b>	<b>LUTs</b>	
	<b>Pd=0</b>	<b>Pd=5</b>	<b>Pd=10</b>	<b>Pd=15</b>			
<b>P-gp</b>	816	533	434	488	5	L: 200	R: 2400
<b>OCT2</b>	770	546	450	436	10	L: 300	R: 2600
<b>BCRP</b>	885	552	415	472	10	L: 300	R: 1300
<b>OAT3</b>	833	581	431	480	7	L: 400	R: 1600
<b>MRP2</b>	998	528	402	511	27	L: 1000	R: 2400
<b>MATE1</b>	730	547	442	383	5	L: 200	R: 3000

**Table 14:** The name of the primers and identification designated by Life technologies

<b>Transporter</b>	<b>Gene</b>	<b>Assay identification</b>
<b>P-gp</b>	ABCB1	Hs00184500_m1
<b>BCRP</b>	ABCG2	Hs01010790_m1
<b>OCT2</b>	SLC22A2	Hs01010723_m1
<b>MATE1</b>	SLC47A1	Hs00217320_m1
<b>OAT3</b>	SLC22A8	Hs00188599_m1
-	GAPDH	Hs02758991_g1

## 3.4. Results

### 3.4.1. Transporter expression on hPTCs

#### 3.4.1.1. Transporter gene expression on hPTCs through passages

RNA integrity was shown to be acceptable for all 3 biological repeats at each doubling (Appendices- Figure 59). Pds 5, 7 and 9 were used to investigate transporter expression and function to allow the expansion of cells up to a certain doubling whilst retaining similar transporter characteristic to the initial population. There was a lot of variability in BCRP and MATE1 expression between the biological repeats over the population doublings, as is seen in Figure 21. This is particularly evident at Pd=5 and 9 for BCRP and Pd=5 for MATE1. Due to this variability a significant difference was not observed in expression of these genes over the doublings compared to Pd=0. However the mean expression appears to increase over time for BCRP and decrease over time for MATE1 compared to the initial population (Pd=0). P-gp expression was significantly decreased at Pd=5 and 7 compared to Pd=0 with a 34% and 39% decrease respectively. However, there was no difference at Pd=9 from the initial doubling, which could indicate the up regulation of the ABCB1 gene after a certain period of time in culture. OCT2 expression decreases over time, although only at Pd=7 and 9 were the fold changes significant with a 54% and 61% decrease respectively. The decrease in gene expression concurs with the idea that over time specific cell functions including transporter expression is lost *in vitro* [20].

The OAT3 assay was also applied to the RNA at the various Pds alongside the other primers for the transporters mentioned above. However a  $C_T$  value was not able to be determined at any of the Pds. Troubleshooting to investigate the cause of the assay failure included; running the OAT3 assay alone to eliminate possible fluorescent noise from the other transporter wells, increasing the number of cycles from 40 to 45, and increasing the RNA concentration from 50ng/ $\mu$ l to 70ng/ $\mu$ l. After consultation with the manufacturer no flaws in the assay methodology could be found so a new batch of primer was applied for OAT3 detection to the increased RNA concentration. However, a  $C_T$  value still could not be ascertained. It was therefore decided to not pursue the OAT3 gene expression detection *via* PCR when considering the time and cost limitations. OAT3

expression was detected on the RPTECs at all doublings *via* immunostaining (Section 3.4.1.2.), so it can therefore be concluded that the primer used is not suitable for assessing OAT3 gene expression using the one-step RT-PCR method outlined in Section 3.3.9.3.

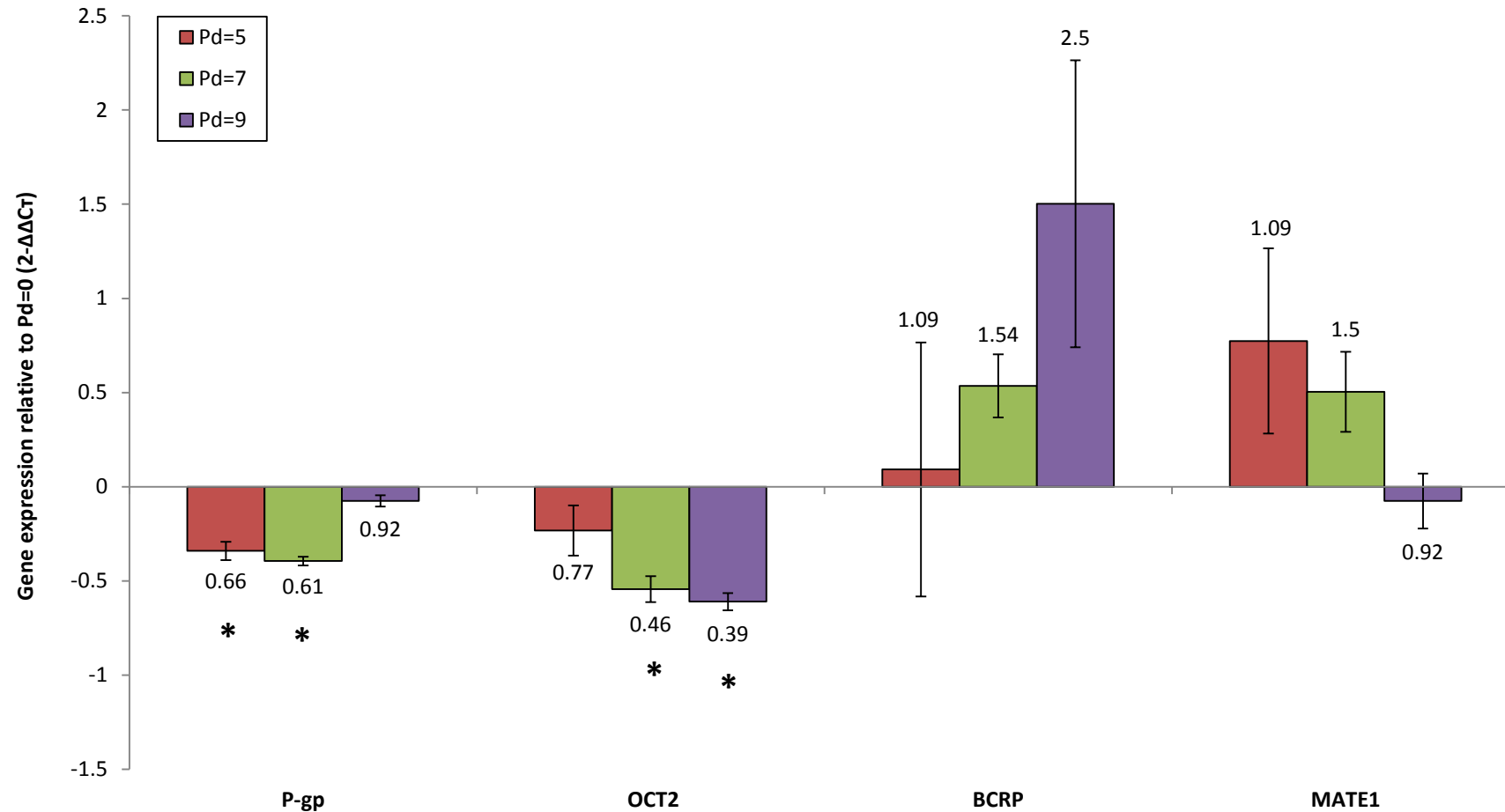


**Figure 21:** The comparative gene expression of P-gp, OCT2, BCRP and MATE1 on RPTECs over 9 population doublings compared to Pd=0. Data labels display the fold change from Pd=0 (set at 0 for each transporter). (Mean value  $\pm$  SEM, n=3). \* significant decrease in expression from the respective genes at Pd=0,  $p \leq 0.05$  (ANOVA with Tukey *post hoc* analysis)

### 3.4.1.2. *Transporter visualisation in hPTCs through doublings*

Morphological differences were observed throughout the population doublings of the RPTECs. At Pd=0 dome formation, considered as a feature of transporting epithelia in culture, was exhibited and was also seen across some wells at Pd=5: OCT2 (Figure 26b), MATE1 (Figure 23b) and BCRP (Figure 22b) but to a lesser extent. This phenomenon is characterised by the swirl formation of cells which are slightly raised above the cell monolayer (Figures 22-27a). The cells also exhibited cobblestone morphology at the earlier doublings consistent with PTCs from the proximal convoluted tubule. However, at the later doublings (Pd=7 and 9) the cells are more elongated (Figures 22-27c and d) and resemble cells from the *Pars Recta* [180]. This change in morphology is most likely due to the extended period of culture *in vitro* and concurs with the idea that transporter expression on cell monolayers decreases over time.

From the intensity analysis a decrease from Pd=0 is indicated for BCRP expression (Figure 22) although the mean intensity appears similar across all doublings. This decrease in expression however is visible in the images (Figures 22a-d) and is particularly noticeable at the later doublings (Pd=7 and 9) compared to Pd=0. For MATE1 the decrease in expression between Pd=0 and Pd=5 is extremely noticeable and is concurrent with the statistical analysis indicating a slight increase in expression at Pd=7, and a significant decrease ( $p \leq 0.05$ ) in expression overall compared to Pd=0 (Figure 23). A significant decrease in expression of MRP2 can also be visualised through the doublings compared to Pd=0 (Figure 24). The background noise from the antibody staining (green) was quite high in the original images, however the antibody applied does not cross react with other MRPs in the kidney and is more likely non-specific binding of the antibody (green spots). Contradictory to most transporters OAT3 expression appears to increase over time, peaking at Pd=5 (Figure 25b). This can be visualised at Pd=5 and 9 with more cells stained for the transporter compared to Pd=0 (Figure 25a), but less so at Pd=7 (Figure 25c). Non-specific binding of the antibody is again observed in these images. The decrease in intensity can be seen between Pd=0 and 5 for OCT2, indicating a decrease in transporter expression (Figure 26e). However OCT2 expression appears to be similar at Pd=7 and 9, concurring with the PCR results that there is a significant decrease in gene expression from Pd=0, but contradicting the

intensity analysis. This may be due to the non-compliance of the intensity measurements to the ANOVA assumptions regarding the homogeneity of variance. Although the data was transformed to better satisfy the assumption (by using the log of each value) the results of the ANOVA are not as robust as if all the criteria were met. Consequently the results of the ANOVA on intensity can only be used as an indication rather than a cut off. For most transporters the images and intensity measurements correlate with the output of the ANOVA. This can be seen for P-gp expression also, where the intensity decreases from Pd=0 overall, but increases at Pd=7 from the other doublings (Figure 27). However this expression pattern contradicts the results of the PCR where expression at Pd=9 is increased from Pds 5 and 7. This may indicate that the protein translation in cells at Pd=9 might be inefficient compared to the earlier doublings, causing a decrease in the surface expression of P-gp.

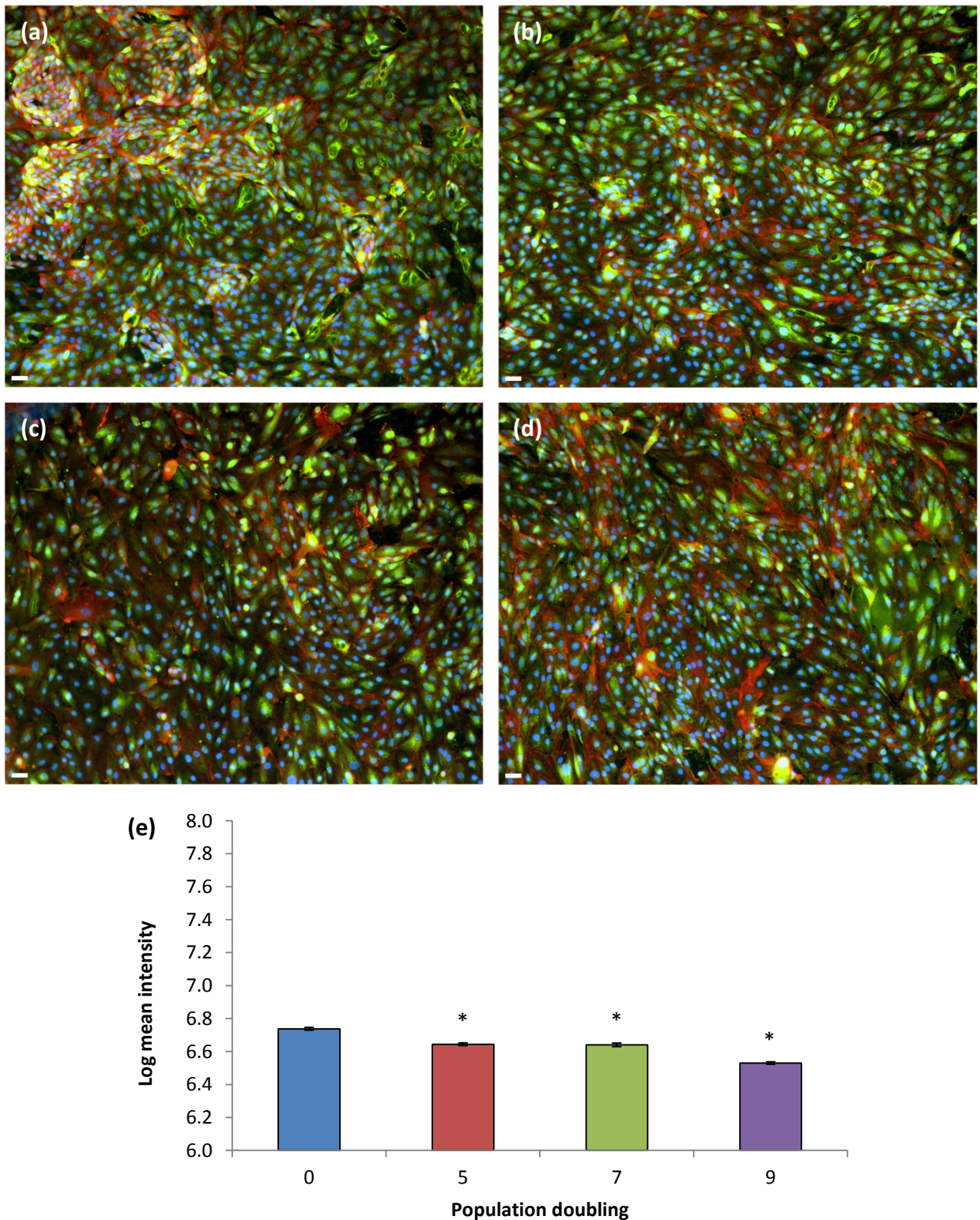


**Figure 22:** RPTECs stained for BCRP (green) at (a) Pd=0 (b) Pd=5 (c) Pd=7 and (d) Pd=9 with cytoskeletal (red) and nuclei staining with DAPI (blue) at 10x magnification. Mean intensity across doublings is shown in (e) (Log mean value  $\pm$  SEM). \* indicates a significant difference in intensity from Pd=0,  $p \leq 0.05$  (ANOVA with Tukey *post hoc* analysis). Scale bars = 10 $\mu$ m

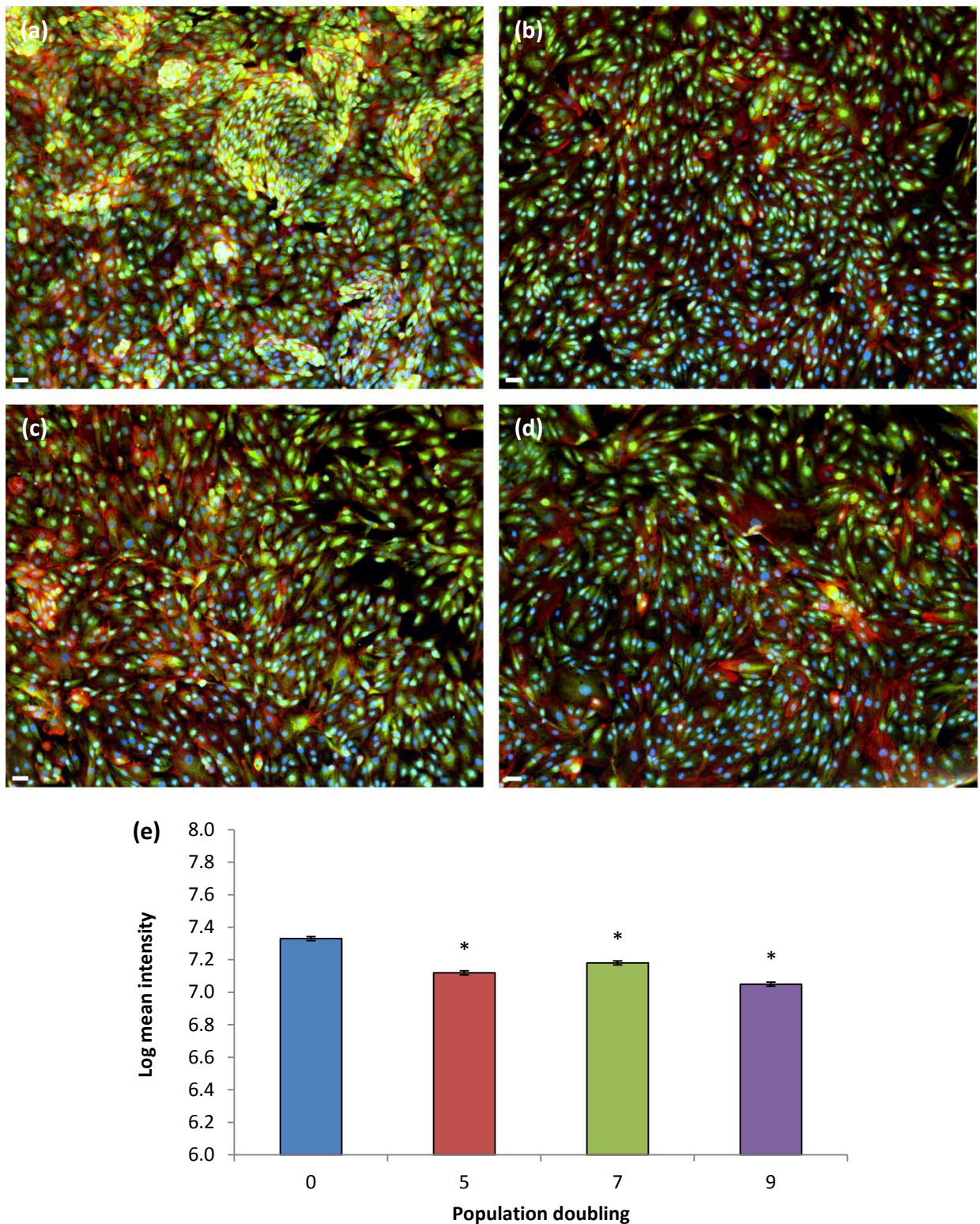


**Figure 23:** RPTECs stained for MATE1 (green) at (a) Pd=0 (b) Pd=5 (c) Pd=7 and (d) Pd=9 with cytoskeletal (red) and nuclei staining with DAPI (blue) at 10x magnification. Mean intensity across doublings is shown in (e) (Log mean value  $\pm$  SEM). \* indicates a significant difference in intensity from Pd=0,  $p \leq 0.05$  (ANOVA with Tukey *post hoc* analysis). Scale bars = 10 $\mu$ m

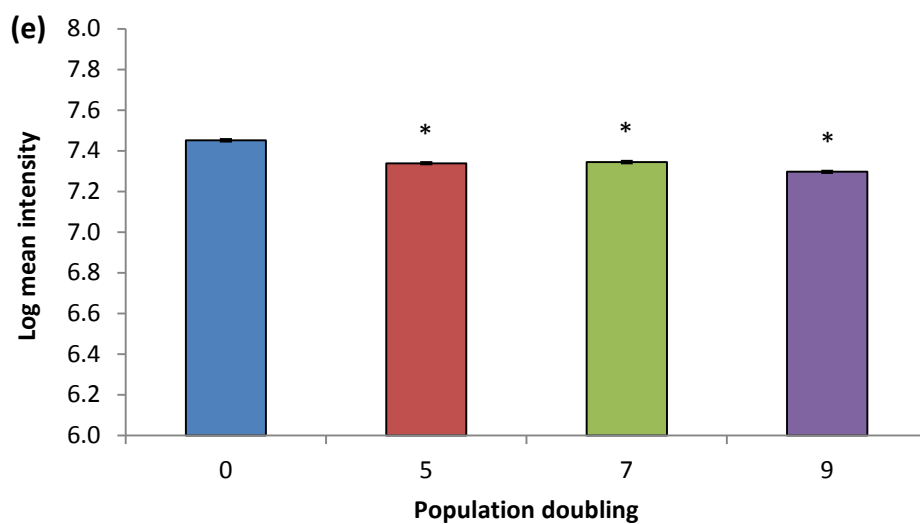
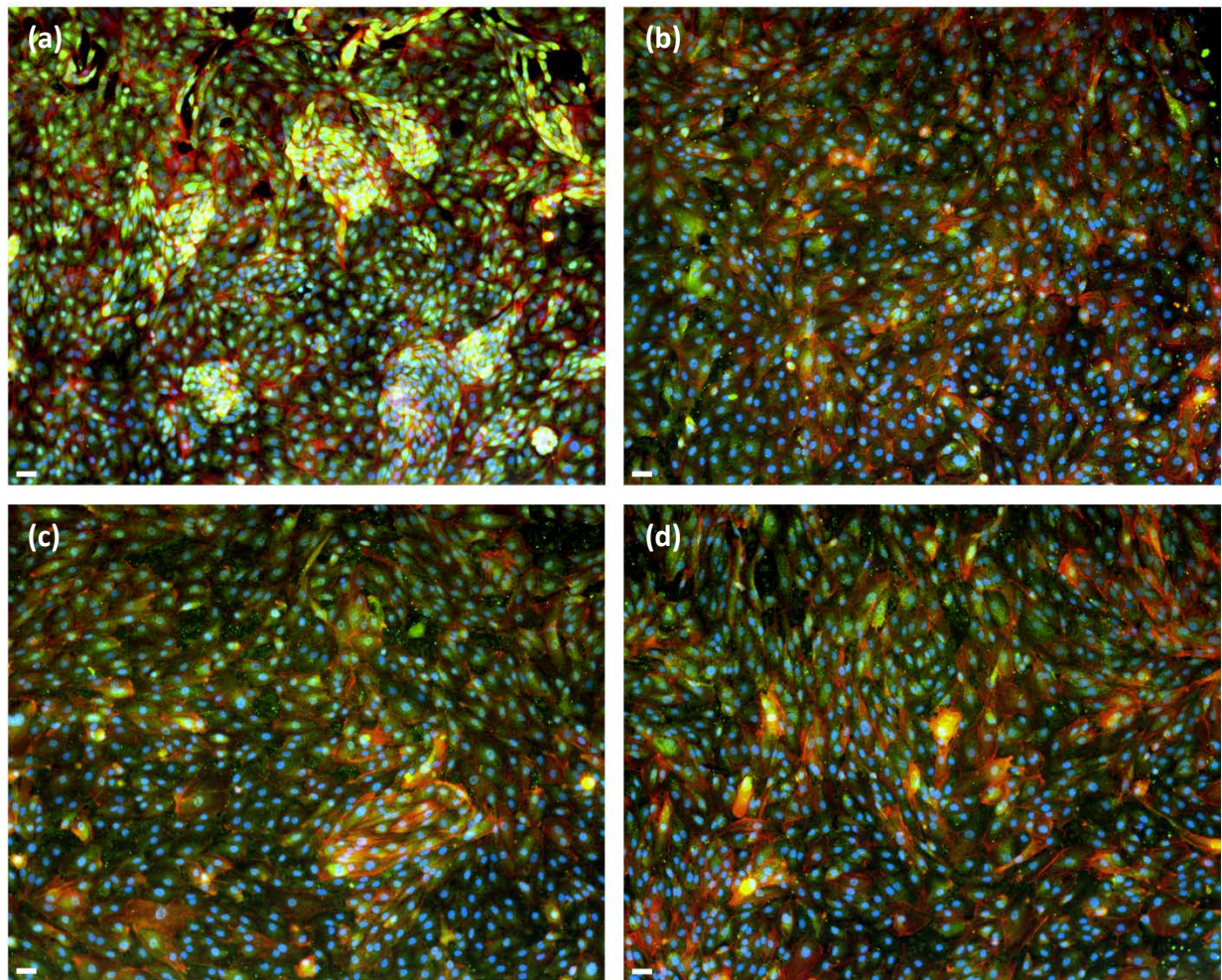


**Figure 24:** RPTeCs stained for MRP2 (green) at (a) Pd=0 (b) Pd=5 (c) Pd=7 and (d) Pd=9 with cytoskeletal (red) and nuclei staining with DAPI (blue) at 10x magnification. Mean intensity across doublings is shown in (e) (Log mean value  $\pm$  SEM). \* indicates a significant difference in intensity from Pd=0,  $p \leq 0.05$  (ANOVA with Tukey *post hoc* analysis). Scale bars = 10 $\mu$ m

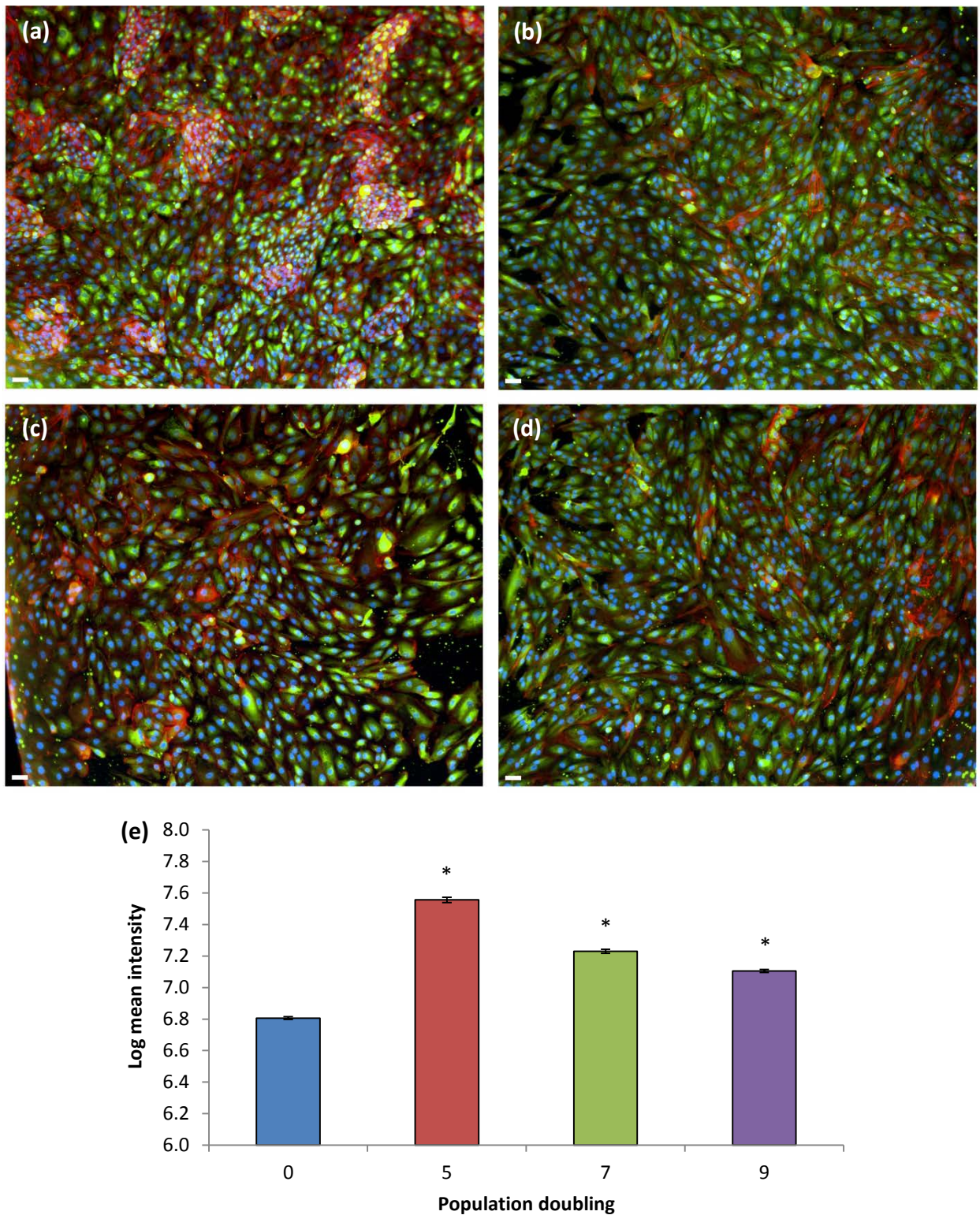


**Figure 25:** RPTECs stained for OAT3 (green) at (a) Pd=0 (b) Pd=5 (c) Pd=7 and (d) Pd=9 with cytoskeletal (red) and nuclei staining with DAPI (blue) at 10x magnification. Mean intensity across doublings is shown in (e) (Log mean value  $\pm$  SEM). \* indicates a significant difference in intensity from Pd=0,  $p \leq 0.05$  (ANOVA with Tukey *post hoc* analysis). Scale bars = 10 $\mu$ M

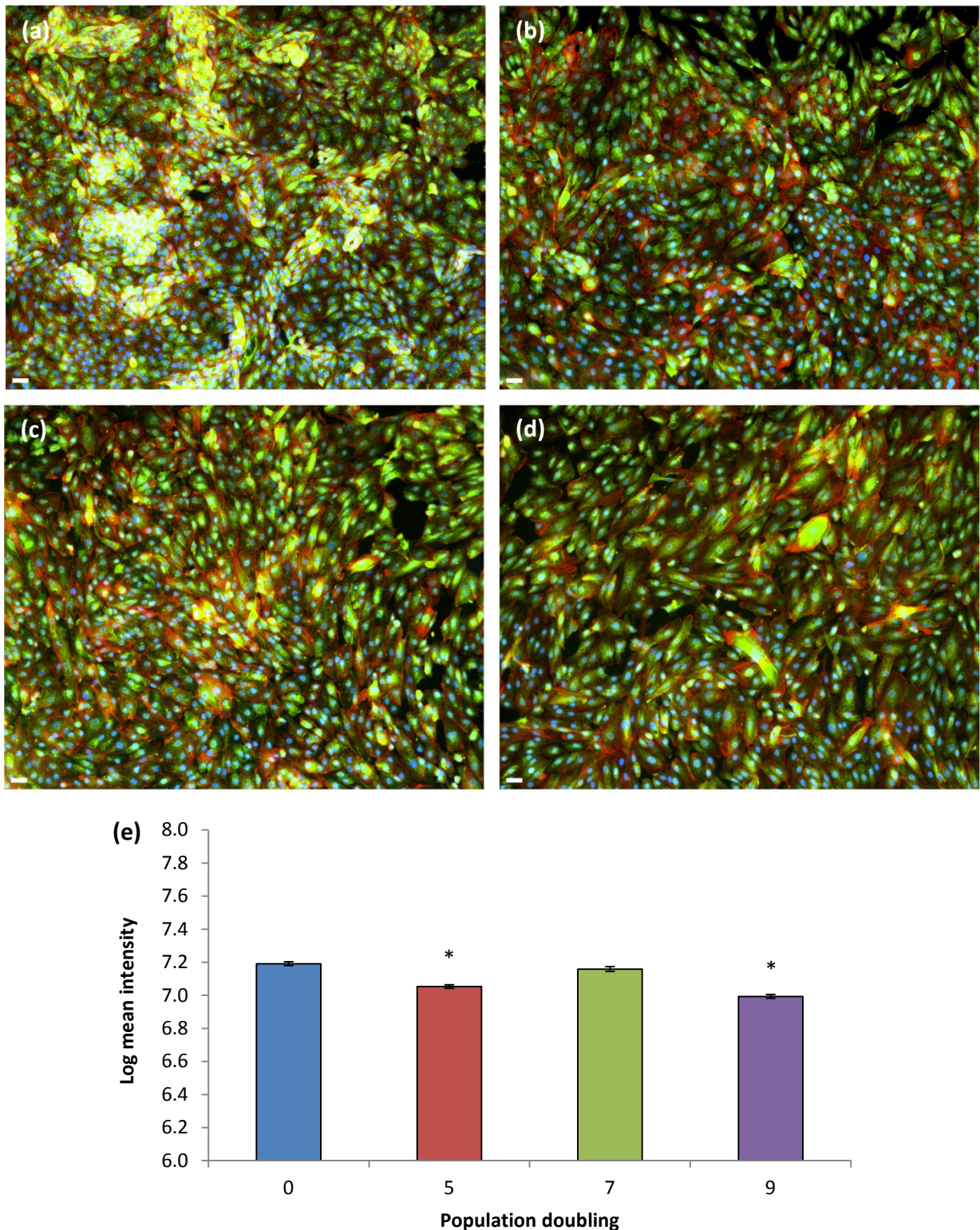


**Figure 26:** RPTECs stained for OCT2 (green) at (a) Pd=0 (b) Pd=5 (c) Pd=7 and (d) Pd=9 with cytoskeletal (red) and nuclei staining with DAPI (blue) at 10x magnification. Mean intensity across doublings is shown in (e) (Log mean value  $\pm$  SEM). \* indicates a significant difference in intensity from Pd=0,  $p \leq 0.05$  (ANOVA with Tukey *post hoc* analysis). Scale bars = 10 $\mu$ m

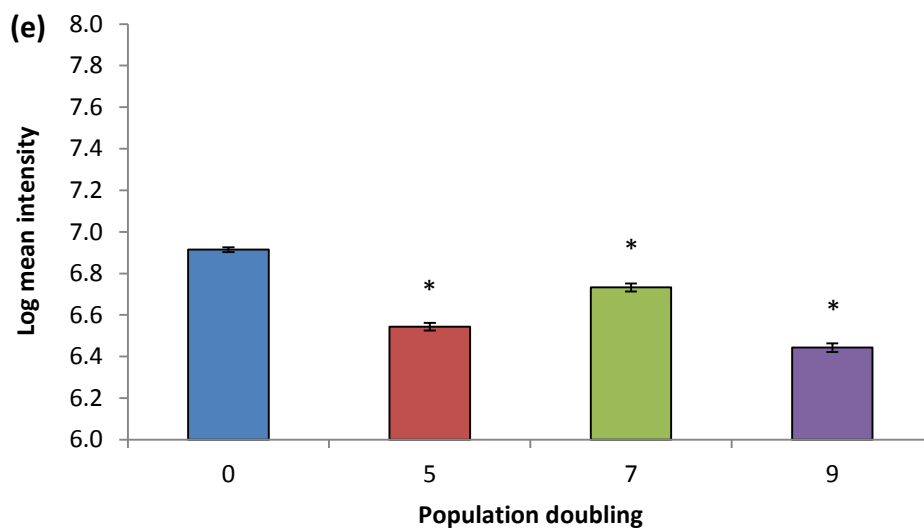
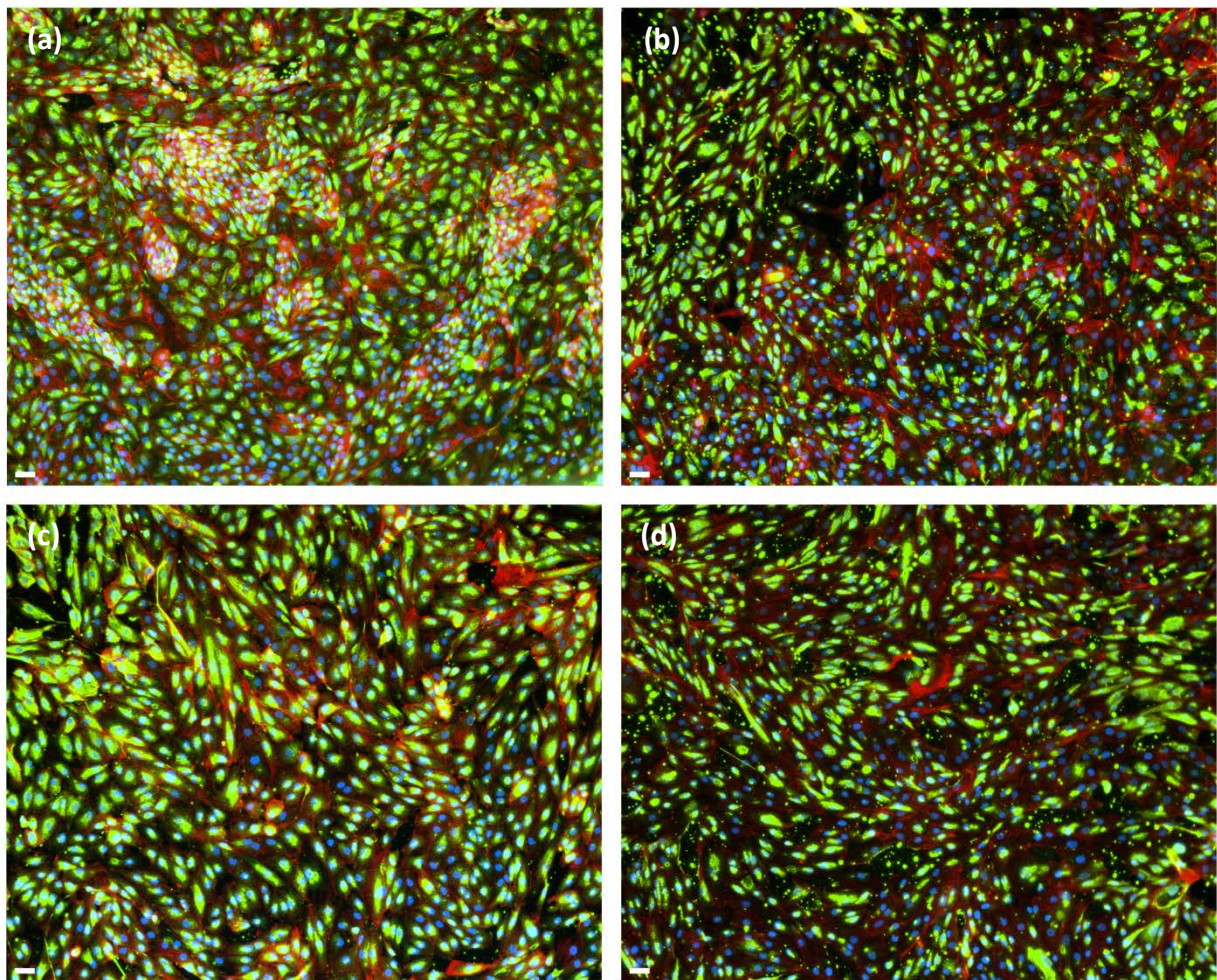


**Figure 27:** RPTECs stained for P-gp (green) at (a) Pd=0 (b) Pd=5 (c) Pd=7 and (d) Pd=9 with cytoskeletal (red) and nuclei staining with DAPI (blue) at 10x magnification. Mean intensity across doublings is shown in (e) (Log mean value  $\pm$  SEM). \* indicates a significant difference in intensity from Pd=0,  $p \leq 0.05$  (ANOVA with Tukey *post hoc* analysis). Scale bars = 10 $\mu$ m

### 3.4.2. Transporter functionality in hPTC

#### 3.4.2.1. P-gp functionality through population doublings

Wells throughout the doublings range showed similar patterns of fluorescence in the presence and absence of Verapamil and Ketoconazole compared to those found in the MDCK-MDR1 cells over 71 cycles (Appendices- Figure 60). However the fold change in fluorescence of the inhibited samples is lower in the RPTECs over all doublings than in the cell line equivalent (Figure 11). This fluorescence decrease indicates a lower amount of functional P-gp present on the primary cells than the modified cell line (Figure 28).

At Pds 0 and 5 the difference in the fold change increase in fluorescence between the uninhibited cells and the inhibited samples at each doubling decreases by approx 15%, as is expected in primary cells due to reported the loss of functionality over time in other primary cell types. However, although there is a significant increase in fluorescence ( $p \leq 0.05$ ) for Ketoconazole inhibited cells at Pd=5 compared to uninhibited cells, there is a high degree of variability which results in a SNR of 3. This indicates that the fluorescence at this doubling although significant may be obscured by methodological noise. The variability in this sample can be accounted for by the difference in fluorescence between the 2 plates that were run, and is not seen through any of the other samples at that Pd. Therefore the amount of error may be explained by: a loss of functional P-gp in the cells, a loss of cells from that plate or the dilution of the solutions from incomplete removal of washing buffer in those wells. As the cells were seeded from the same batch and cultured in identical culture conditions between plates the most likely cause of this variation is the dilution of the Ketoconazole solutions in samples at that end of the plate.

At Pd=7 the fold change in fluorescence decreases further in the Verapamil inhibited samples from the previous Pds, whereas Ketoconazole inhibited cells exhibit an increase from Pds 0 and 5. Although the SNRs for these samples are  $>3$  indicating a reduced chance of interference of fluorescence by methodological noise, Verapamil inhibited cells do not demonstrate a significant difference in fluorescence from the uninhibited cells. Furthermore, at Pd=9 the highest fold change in fluorescence from uninhibited cells overall is exhibited by Ketoconazole inhibited cells at 6.96. The fold change in Verapamil inhibited cells is also the highest out of all Verapamil inhibited cells, and both

samples exhibit a significant increase according to ANOVA with Tukey *post hoc* analysis. It can therefore be concluded that whilst functional on cells through all Pds, P-gp increases through the Pds with the most functional transporters present at Pd=9. This may be indicative of upregulation of P-gp at Pd=9, which would concur with an insignificant decrease in P-gp gene expression between Pd=0 and Pd=9 but a significant decrease at Pd=5 and 7 from Pd=0 (Figure 21). However, this is not corroborated by the immunostaining images (Figure 27), which show a decrease in fluorescence intensity from Pd=0 with the lowest mean intensity at Pd=9.

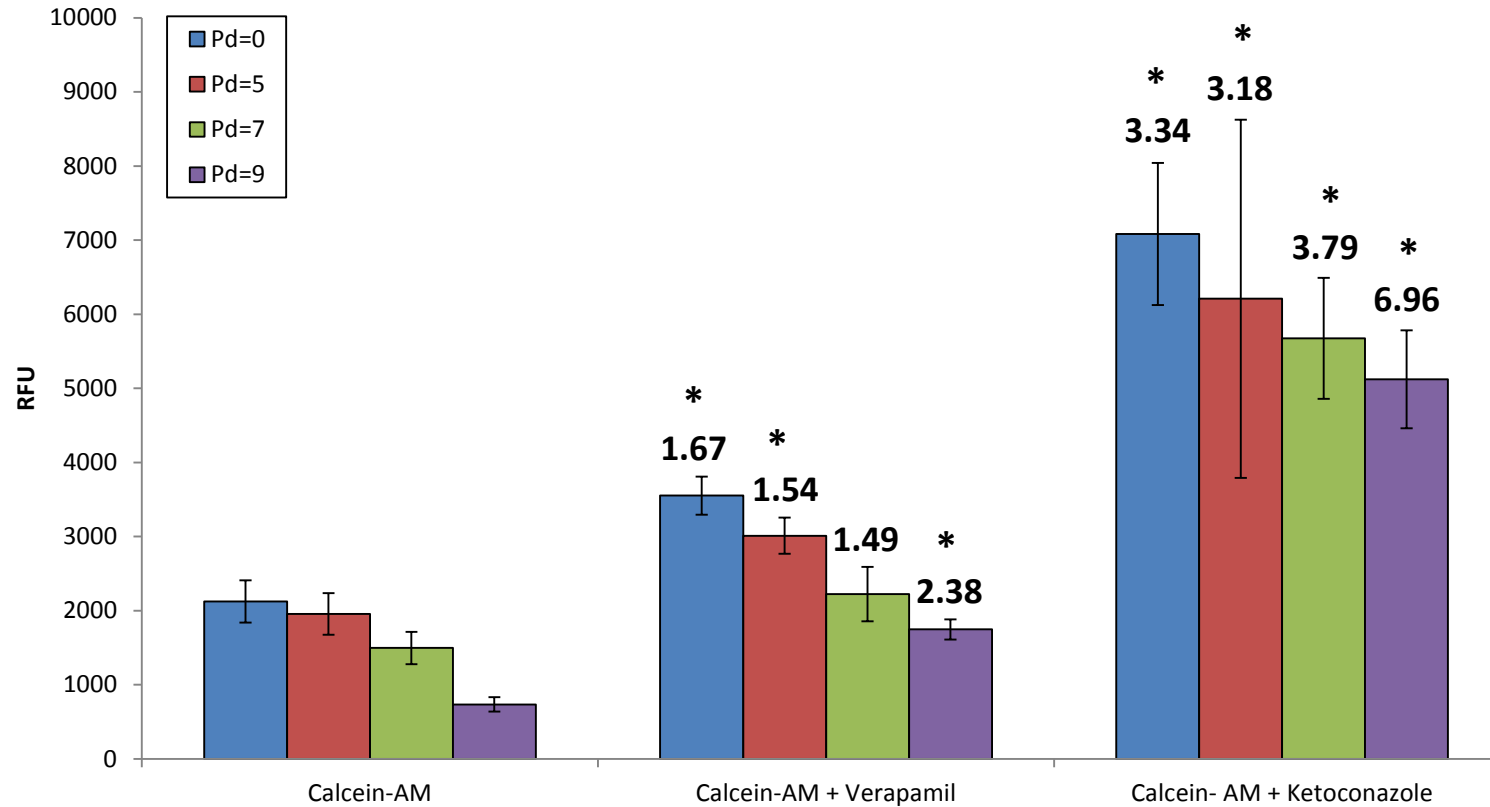


**Figure 28:** Calcein-AM (2.5 μM) fluorescence in RPTECs at Pd 0, 5, 7 and 9 in the presence and absence of the P-gp inhibitors Verapamil (100 μM) and Ketoconazole (100 μM) after 71 cycles (approximately 71 minutes) Data labels above the bars display fold changes in fluorescence from inhibited cells compared to the uninhibited data set. (Mean value ± SD, n=36). \* indicates a significant increase in fluorescence from the respective samples at Pd=0, p ≤ 0.05 (ANOVA with Tukey *post hoc* analysis)

### 3.4.2.2. OCT2 functionality through population doublings

The OCT2 assay was originally performed on cells cultured in 96-well plates as were the other assays. However, due to the nature of the assay there was a substantial loss of cells from numerous wash steps and buffer removal through the assay. Consequently the results of these assays demonstrated a large amount of error. The assay was then transferred to a 48-well format where a reduced amount of cell loss was observed through the assay.

Basal uptake of ASP<sup>+</sup> decreases significantly through the Pds (Figure 29) until Pd=9, where there is no significant difference from Pd=0 ( $p \leq 0.05$ ). This decrease is independent from noise signal as SNRs are above 4 at all Pds for basal ASP<sup>+</sup> fluorescence. When looking at the fold change decrease between the inhibited and non-inhibited samples (Figure 29), the amount of ASP<sup>+</sup> uptake appears to follow the same pattern as Calcein-AM fluorescence. At Pds 0 and 5 the amount of ASP<sup>+</sup> uptake decreases, only to increase at Pd=7 with Imipramine exerting the more potent inhibition. However statistical significance is only exhibited between the uptake in the Imipramine inhibited samples versus the non-inhibited samples at Pds 0, 5 and 9. Furthermore the SNRs for the Imipramine inhibited samples are mostly below 4 indicating fluorescence is interfered with by noise. Only Imipramine inhibited cells at Pd=0 show a significant 0.67 fold decrease in ASP<sup>+</sup> from uninhibited cells which is independent from noise signals. From the data collected in this assay functional OCT2 appears to be only present on cells at the earliest doubling (Pd=0) and diminishes through the later doublings. However, due to the loss of cells through the assay at all doublings alongside interference from noise (Pd=5 Imipramine inhibited cells) and insignificant fluorescence results, OCT2 functionality cannot be confirmed at the later doublings.

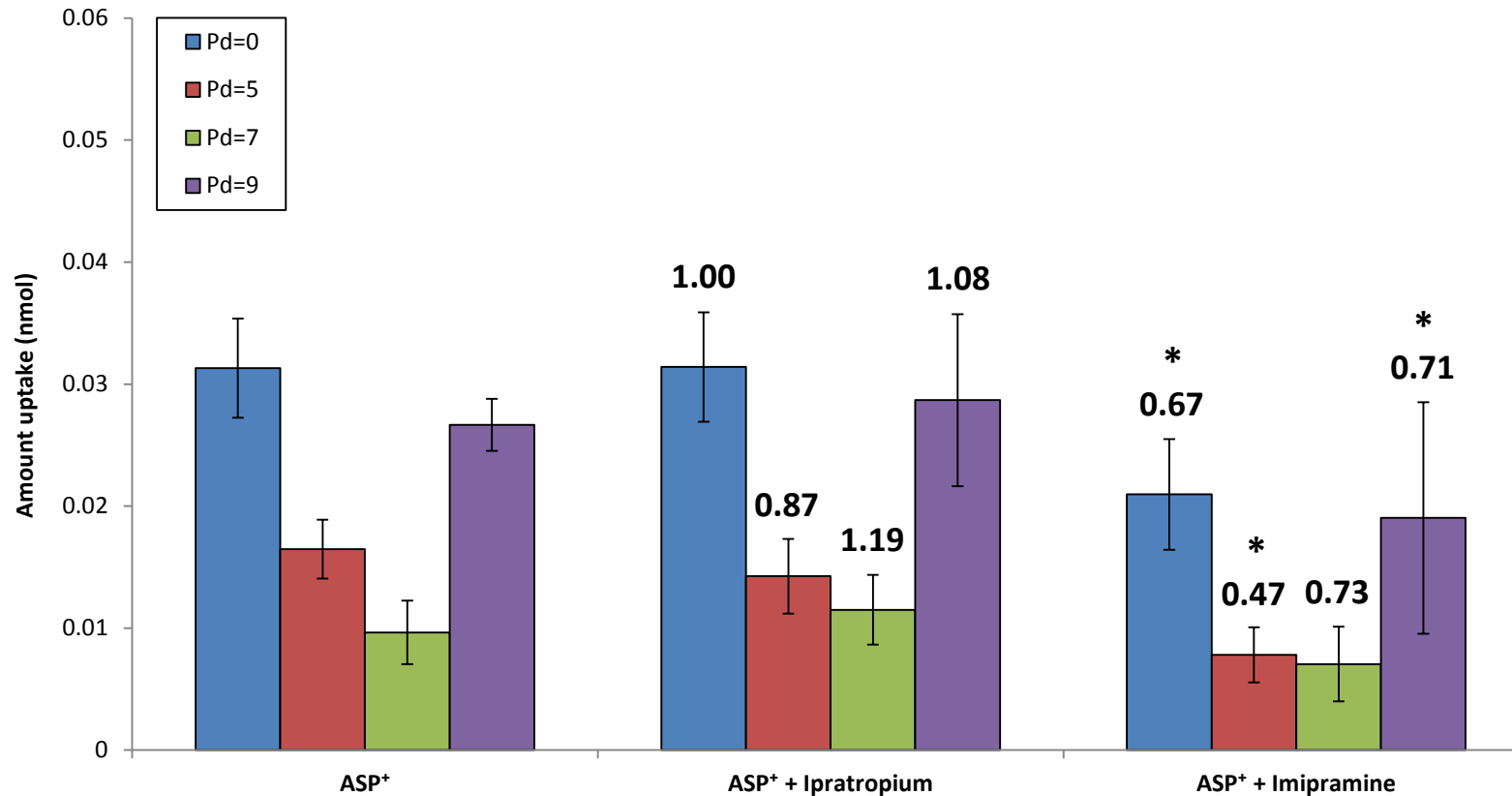


**Figure 29:** ASP<sup>+</sup> (20 $\mu$ M) uptake in RPTCEs at Pd 0, 5, 7 and 9 in the presence and absence of the OCT2 inhibitors Ipratropium (100 $\mu$ M) and Imipramine (100 $\mu$ M). Data labels above the bars display fold changes in fluorescence from inhibited cells compared to the uninhibited data set. (Mean value  $\pm$  SD, n=12). \* indicates a significant decrease in fluorescence from the respective samples at Pd=0,  $p \leq 0.05$  (ANOVA with Tukey *post hoc* analysis)

### 3.4.2.3. BCRP functionality through population doublings

Similar to the assay results in the MDCK-BCRP cells (see Appendices- Figure 61 for full cycle graphs), RPTECs at Pd=0 show a significant increase ( $p \leq 0.05$ ) in fluorescence between the basal and Ko143 inhibited samples (Figure 30) indicating that Ko143 is the more potent inhibitor. However, no significant increase in fluorescence is exhibited in the presence of Novobiocin at Pd=0 or any other Pds, although all fluorescence measurements were independent of background noise.

The fold changes in fluorescence from the uninhibited and Ko143 inhibited samples seem to agree with those found in the P-gp assay up until Pd=9. A significant decrease in fold change from the uninhibited sample is exerted at Pd=5 from Pd=0 before increasing at Pd=7 in the Ko143 inhibited cells. However, there is no significant increase in fluorescence at Pd=9 in the Ko143 inhibited cells from the uninhibited cells. As with the Ketoconazole inhibited cells in the P-gp assay (Figure 28) there is a high degree of variability displayed at Pds 0 and 7 in the Ko143 inhibited cells, which is not seen by the Novobiocin inhibited or uninhibited cells of the same Pd. This can again be attributed to operator error, specifically dilution of the incubation solutions with wash buffer in the Ko143 inhibited wells leading to a difference in starting fluorescence between the 2 plates.

Despite this variability it appears that like P-gp, there is more functional BCRP on cells at Pd=7 demonstrated by the increase in fluorescence in the presence of Ko143 compared to the earlier Pds. This differs from both gene expression data which did not demonstrate a change in expression from the initial population (Figure 21) (although error between the repeats was high), and surface expression, where all doublings decreased in the intensity of BCRP from Pd=0. These differences in expression and functionality may be due to post translational inefficiencies at later doublings as described for P-gp.

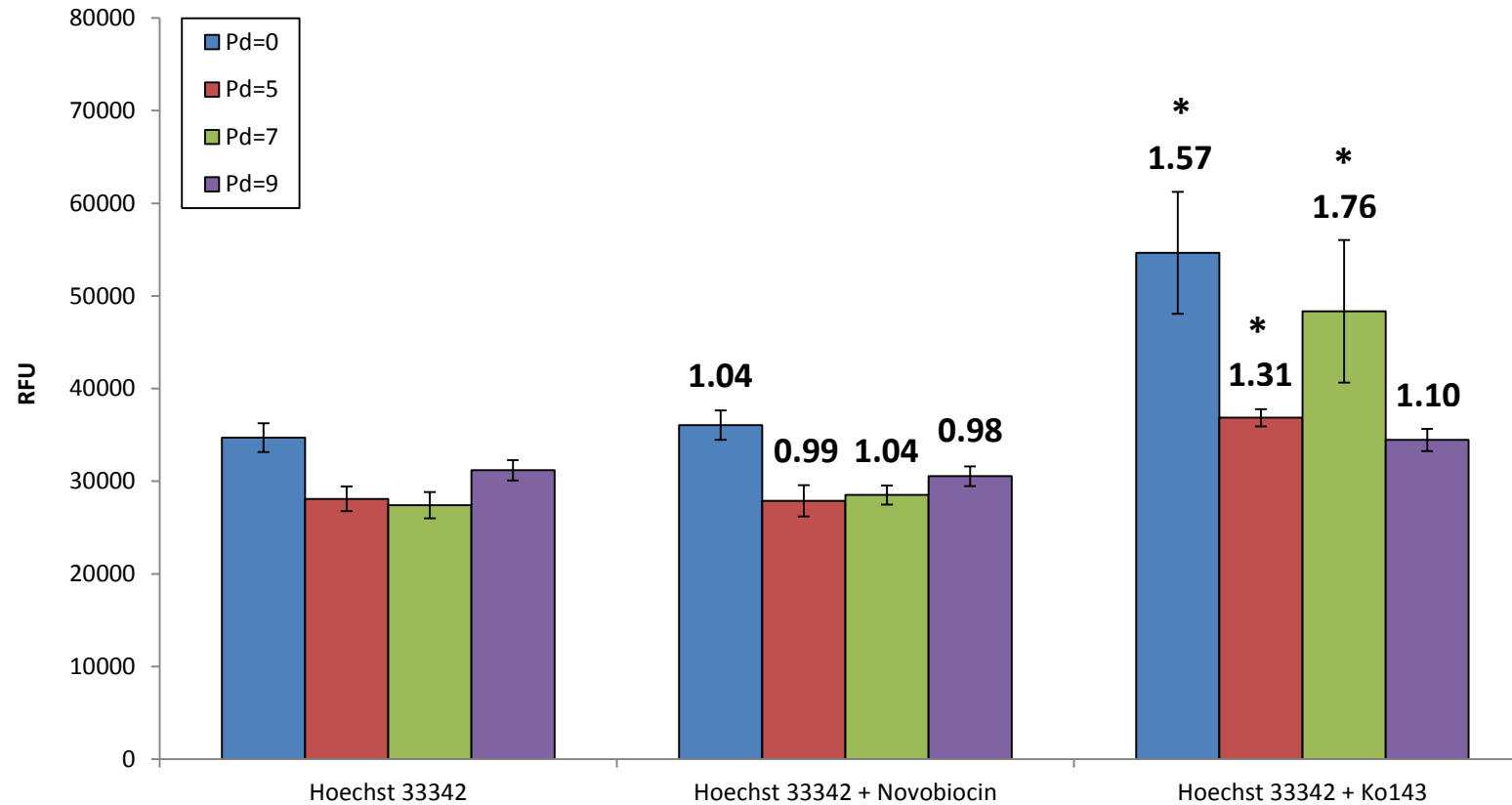


**Figure 30:** Hoechst 33342 (20 $\mu$ M) fluorescence in RPTECs at Pd 0, 5, 7 and 9 in the presence and absence of the BCRP inhibitors Novobiocin (30 $\mu$ M) and Ko143 (50 $\mu$ M) after 71 cycles (approximately 71 minutes) Data labels above the bars display fold changes in fluorescence from inhibited cells compared to the uninhibited data set. (Mean value  $\pm$  SD, n=36). \* indicates a significant increase in fluorescence from the respective samples at Pd=0,  $p \leq 0.05$  (ANOVA with Tukey *post hoc* analysis)

### 3.4.3. hPTC growth on porous surfaces

RPTECs were seeded at a high density on transwells compared to MDCKII cells as per the supplier's instructions and previous attempts at RPTEC culture on inserts. From preliminary experiments, culturing cells whilst continuously shaking appeared to yield better results in terms of monolayer integrity compared to static culture (Appendices-Figure 62). This generated the investigation into membrane coatings for improved RPTEC monolayer formation on the transwells and subsequent applicability to the fibres in the hollow fibre bioreactor. Coatings were selected either for their commercial availability (Bovine collagen coated PTFE transwell inserts), regular usage for cell attachment (Gelatin and Matrigel) or reference in literature (DOPA + Collagen IV) (Figure 30) [181].

All conditions failed to produce RPTEC monolayers at or below the 1% permeation threshold of LY over the 16 days (Figure 31). It is thought that primary cells are inherently leaky [182], however raised thresholds of 2-3% were still not achieved by the cell monolayers at any condition. TEER measurements inversely correlated the percentage LY permeation for each of the samples, however, their use in assessing monolayer integrity alone was not done due to high variability between readings for each well. This variability arose from the manual method used as opposed to the automated method utilised in Section 2.4.1.2.

There is no significant ( $p \leq 0.05$ ) difference in LY permeation between the control (uncoated) and coated wells from days 2-6, although the lowest mean amount of LY permeation is observed at day 4. However, for Matrigel the mean LY permeation significantly decreases from day 8 onwards compared to the uncoated control. Although bovine collagen demonstrates the lowest amount of LY permeation at day 6, it is only from day 12 onwards that the permeation differs from the control. Gelatin exhibits the lowest amount of LY permeation at day 8 which is significantly different from the control, however, it is double the amount of the threshold value. DOPA + Collagen IV does not demonstrate any significant decrease in LY permeation from the control at any day, with the lowest amount of LY permeation at triple the threshold value and a fairly consistent LY permeation amount throughout the culture period.

To check the effects of the coatings on the porosity of the transwell inserts, wells coated without cells were also run alongside their seeded counterparts as porosity controls. The mean of the controls throughout the culture period was then taken for each condition (Figure 32) and an ANOVA test was run on the samples. The Matrigel coated wells demonstrate a lower permeability of LY throughout the culture period compared to the control, which is also confirmed by the ANOVA with a statistically significant decrease in the LY permeation. This indicates that the concentration of Matrigel applied blocks the pores and therefore does not accurately indicate monolayer formation *via* the LY assay.

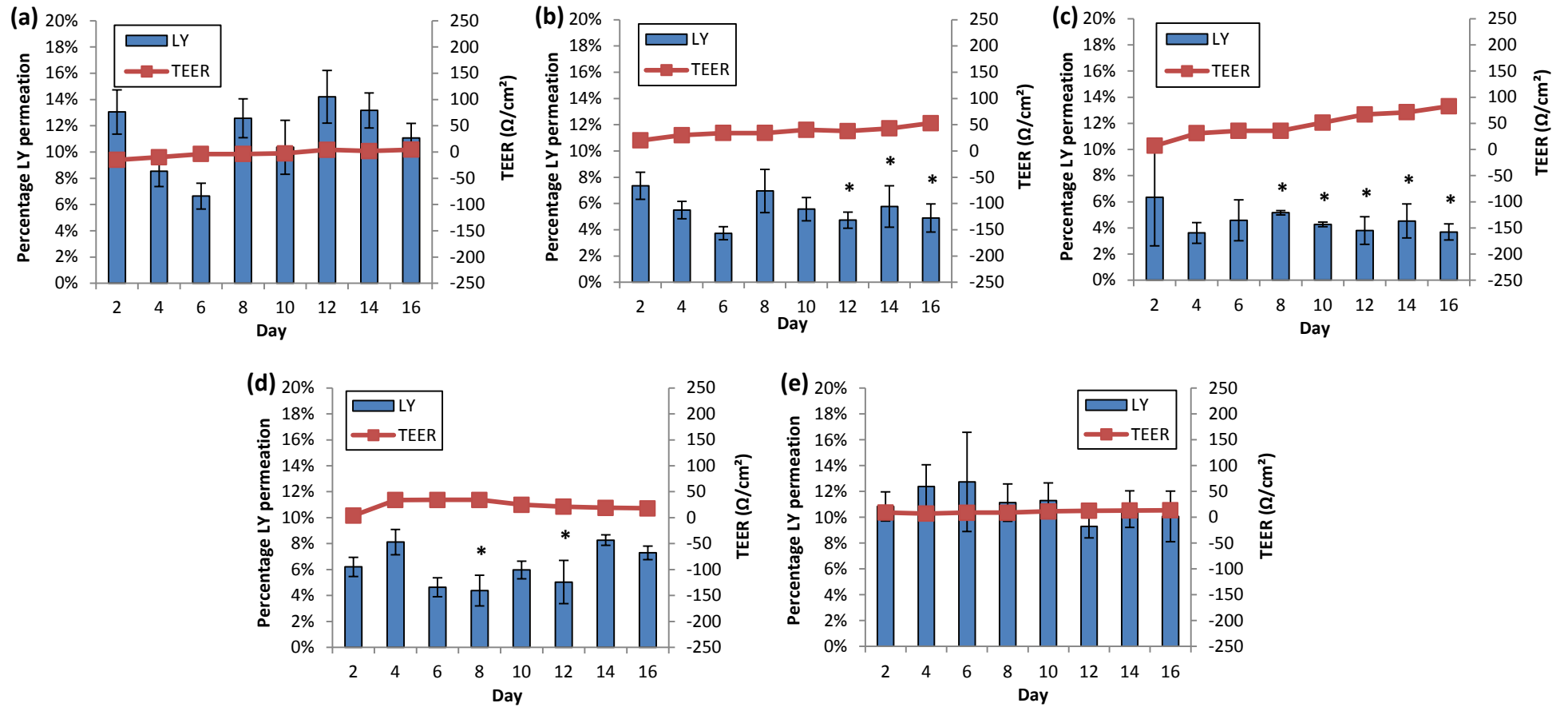


**Figure 31:** Percentage LY permeation and TEER readings of RPTECs cultured on (a) Uncoated transwells or inserts coated with (b) Bovine collagen (c) Matrigel (d) Gelatin (e) DOPA + Collagen IV. RPTECs were cultured for 16 days with measurements every 2 days (Mean value ± SEM, n=3). \* indicates a significant difference in LY permeation from the uncoated control (a), p ≤ 0.05 (ANOVA with Tukey post hoc analysis)

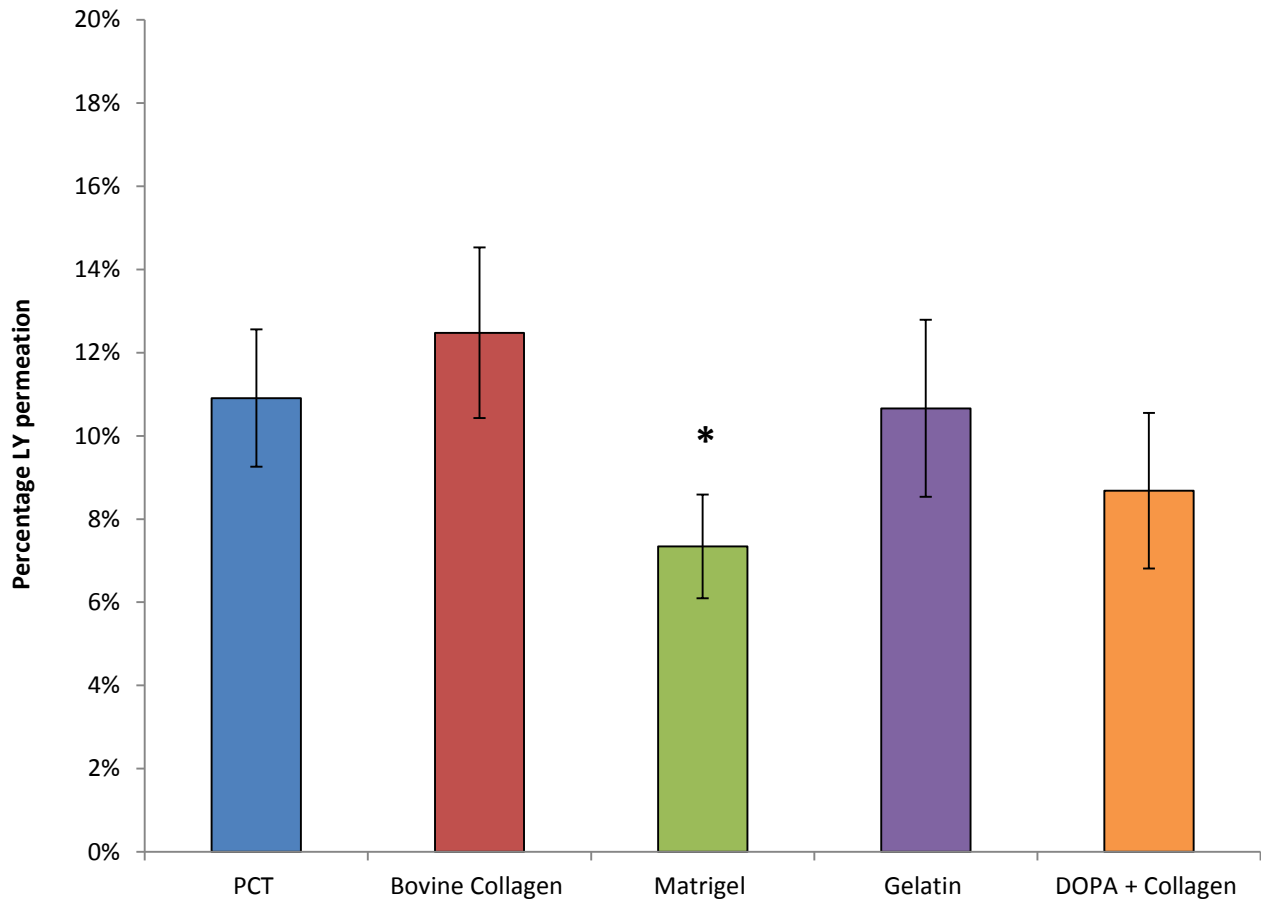


**Figure 32:** Percentage LY permeation of control PCT transwells at Uncoated (PCT) and coated with Bovine collagen, Matrigel, Gelatin, DOPA + Collagen IV. Percentage permeation was averaged over the 16 days (Mean value  $\pm$  SEM,  $n=3$ ). \* indicates a significant difference in LY permeation from the uncoated control,  $p \leq 0.05$  (ANOVA with Tukey *post hoc* analysis)

### 3.5. Chapter discussion and conclusion

#### 3.5.1. Discussion

The focus of this chapter is on the characterisation of the transporter capabilities on primary cells over periods of *in vitro* culture dependent on population doublings. Extensive research has been applied to hepatocyte culture leading to the view that primary cells lose their specific functional capacity in *in vitro* culture [20]. In the case of PTCs, the loss of a brush border plasma membrane, decreased expression and/or functionality of plasma membrane transporters, decreased expression of drug metabolising enzymes and a decreased mitochondrial function leading to the glycolytic pathway as the primary source of energy metabolism is thought to occur [166]. As such, this is an important aspect to be considered in the generation of a BAK device incorporating this cell source, primarily as a measure of the degree of functionality of cells within the device. It is also crucial to consider the costs of cell culture and quantity versus functionality to reflect the end point of the device (for pharmaceutical research).

A few options were available as a source of primary PTCs including freshly isolated cells or commercially sourced primary cells. Although freshly isolated cells would be comparatively cheaper, the harvest protocols and validation of PTC retrieval would introduce time and variability into the process compared to commercially sourced cells.

From the panel of 6 drug transporters identified as pharmacologically relevant, genetic and surface expression and functionality of P-gp and OCT2 generally decreases, corroborating the widely held belief that drug transporters lose expression of culture *in vitro*. The genetic expression of BCRP and MATE1 contradicts this belief, although the functionality (for BCRP) and surface expression data complies. This belief is also contradicted by the surface expression of OAT3 where the mean intensity is significantly higher than the starting population in all for the later doublings. Although P-gp expression generally decreases over time as said before, there is an increase in genetic expression and functionality at the latest doubling, adding to the hypothesis that not all drug transporter capabilities are lost over time in *in vitro* culture. Upregulation of drug transporters could occur for renal proximal tubule epithelial cells over time in *in vitro* static culture, although this has not been investigated in literature.

The second aspect of this chapter was to assess the extent of monolayer formation on porous inserts with different protein coatings in order to mimic the compartmentalisation aspect of the physiological environment of the PT. The results indicate that cells perform the best on Matrigel coated inserts. However, the hypothesis is that this decrease in LY permeation could be due to pore blocking by the gel instead of the cell monolayer formation. LY permeation could also be impeded by binding to Matrigel, as it is a complex ECM with a variety of components as opposed to the simpler coatings such as gelatin. However, no such interactions between Matrigel or general proteins and LY have been reported in literature.

### 3.5.2. Conclusion

A variety of cell sources are available to use as an *in vitro* model of the PT. However, due to the lack of retention of renal specific functions and transporter capabilities by cell lines, primary renal PTCs have been identified as the appropriate cell source. For device development, variability within the process needs to be minimal. For this reason commercially sourced PTCs from the same donor have been utilised over freshly isolated cells. To address the gap in the knowledge regarding the expression of drug transporters on PTCs over time in *in vitro* culture, the characterisation techniques mentioned above have been implemented with varying degrees of success. The fluorescence efflux assays developed previously (Chapter 2) have been successfully implemented in the primary cell cultures, although the uptake assay was not suitable due to cell loss throughout. Genetic expression *via* PCR has also been successful in comparing the expression in P-gp and OCT2 over time compared to the initial doubling, whereas for BCRP and MATE1, the variability between biological repeats was too large. Surface transporter expression has also been successful, showing a general decrease in the panel of transporters over time in culture. PTC culture has not been successful on porous membrane inserts, even after coating with various proteins. For BAK device generation a suitable porous culture substrate is required. Therefore polymer blend development to generate a suitable renal cell culture substrate will be described in Chapter 4.

# **Chapter 4**

**Tailoring polymer blends for hollow fibre  
production**

## 4.1. Introduction

It is widely regarded that different cell types require different material surface properties for optimal proliferation, viability and functionality. In the case of primary human renal cells, surface properties such as hydrophilicity and negative charge are thought to be preferable. It has been reported that some positively charged surfaces achieved by coatings (e.g. poly-D-lysine) may enable renal cells to attach more easily, however, they might not encourage cell proliferation and/or sustain growth [181]. The adhesiveness of a surface can be influenced by the amount of functional groups such as carboxyl and hydroxyl groups present [183], which is paramount when looking at protein adsorption and subsequent cell adhesion on porous surfaces. However, in the case of porous surfaces, the roughness determined by the existence of the pores may reduce the available surface area, as well as inhibiting the contact with the existing functional groups [184]. This consequently results in loose cell attachment.

A hollow fibre bioreactor for cell culture typically depends on fibre porosity to allow nutrient and gas exchange to the cells. Considering this, fibres must be suited to the cell type as well as being sufficiently porous to allow the permeation of nutrients and metabolites. It is therefore important to consider membrane tailoring i.e. using polymers with additives or using treatments during production, as opposed to membrane coating for the hollow fibre production. Whilst coating commercially sourced fibres could be more consistent, there is a possibility of lowering the degree of porosity as a result of pore blockage due to coatings (see Section 3.4.3.), although this deduction needs further confirmation. Therefore producing hollow fibres with tailored properties is the preferable option, and will be adopted in this thesis.

This chapter describes the production of four types of polysulfone (PSF) based membranes using several different types of molecules as additives: polyvinylpyrrolidone (PVP), malonic acid (MA) and glutaric acid (GA). Characterisation of the generated flat sheet membranes was performed with the aim of investigating the physical properties of each blend and to assess cell performance with regards to cell adhesion on different chemistries. This knowledge was used for the production of hollow fibres to be used

in the bioreactor. The hollow fibre production and characterisation together with device assembly and cell cultivation will be described in Chapter 5.

## 4.2. Review of literature

### 4.2.1. Biomaterial surface features desirable for cell growth

Biomaterials are used in a wide range of applications including medical implants and devices, scaffolds for cellular models and tools for cell culture and expansion. Accordingly there are a variety of requirements that a biomaterial must possess depending on their application with the major one being biocompatibility. However biocompatibility is a complex phenomenon and is difficult to define due to the fact that the applications of the materials are specific to the parts of the body or cell type in question. For medical devices and implants, materials should not initiate immunological or inflammatory reactions, generate toxic or carcinogenic products or produce unwanted deterioration of the material and tissue to be classed as biocompatible. For cell scaffolds and cell culture equipment, biocompatible materials are also required to take into account the properties of the cell type(s) that are being cultured when considering the composition and configuration of surfaces and biomolecules [185].

Cells do not interact directly with the man-made surface when cultured on biomaterials; instead there is a rapid chain of events initiated when the material is exposed to the biological fluid or medium containing serum. This results in a layer of extracellular biomolecules adsorbed to the surface (Figure 33a). Therefore the biological adhesiveness of the surface to proteins is a major factor in the biocompatibility of the selected material. Initial contact with water produces a mono or bi-layer of water molecules on the surface. The molecule arrangement is dependent on the material properties. Hydrophilic (wetable) surfaces have the ability to interact with water molecules in two ways depending on their reactivity. Highly reactive surfaces form a hydroxylated (OH- terminated) surface from the dissociation of water molecules, whilst less reactive surfaces interact with intact water molecules *via* hydrogen bonding. In contrast, hydrophobic (non-wetable) surfaces have a weak tendency for binding water. The subsequent binding of hydrated ions form a water shell, to which small proteins from the fluid, serum or coating begin to adsorb to [186]. Alongside wettability, other physiochemical properties that are thought to influence protein adsorption to a surface include: the characteristics of the protein, the surface free energy, chemical nature,

thickness, density and roughness of the material, as well as the mobility of the existing functional groups on the surface. On hydrophilic surfaces, protein adsorption occurs through polar and ionic interactions between the hydrophilic amino acid side chains and the water layered surface, leading to a weak and reversible adsorption of the intact protein. However protein adsorption on hydrophobic surfaces is often irreversible due to the dehydration of the interface providing the entropic driving force for binding. This leads to a conformational structural change of the proteins with partial or total unfolding thus exposing the hydrophobic core to the hydrophobic patches of the surface. The degree of conformational change of the protein balances the strength of the protein- surface interactions, resulting in the distribution of the polar charged residues towards the aqueous boundary [185]. The electrostatic interactions between the charged residues of the protein and the surface play a lesser, but equally important role in protein adsorption. As proteins generally bear a net negative charge, anionic surfaces generally adsorb less protein than cationic surfaces [187]. Secondary layers of proteins bind reversibly to the protein adsorbed on the surface due to the low affinity of the molecules. This process occurs within the first few seconds of contact between the surface and the protein contained in the medium and promotes and facilitates cell adhesion, growth and proliferation.

Cell adhesion relies on the affinity of the anchorage proteins on the cell membranes (primarily integrins) to the proteins adsorbed on the surface. From the initial association if protein affinity is high, the cells will start to spread across and interact with the surface forming points of adhesion (i.e. focal points) and thus initiating the biochemical cues for growth and proliferation. However if the affinity to the surface proteins is low the cells will stay loosely attached and display a rounded morphology, which in most cases eventually leads to apoptosis (Figure 33b). Generally, hydrophilic surfaces promote cell adhesion due to the adsorption of proteins in their native conformation. In contrast hydrophobic surfaces counteract cell adhesion due to the conformational change of adsorbed proteins causing a lack of specific recognition sequences required for extracellular protein interaction [186].

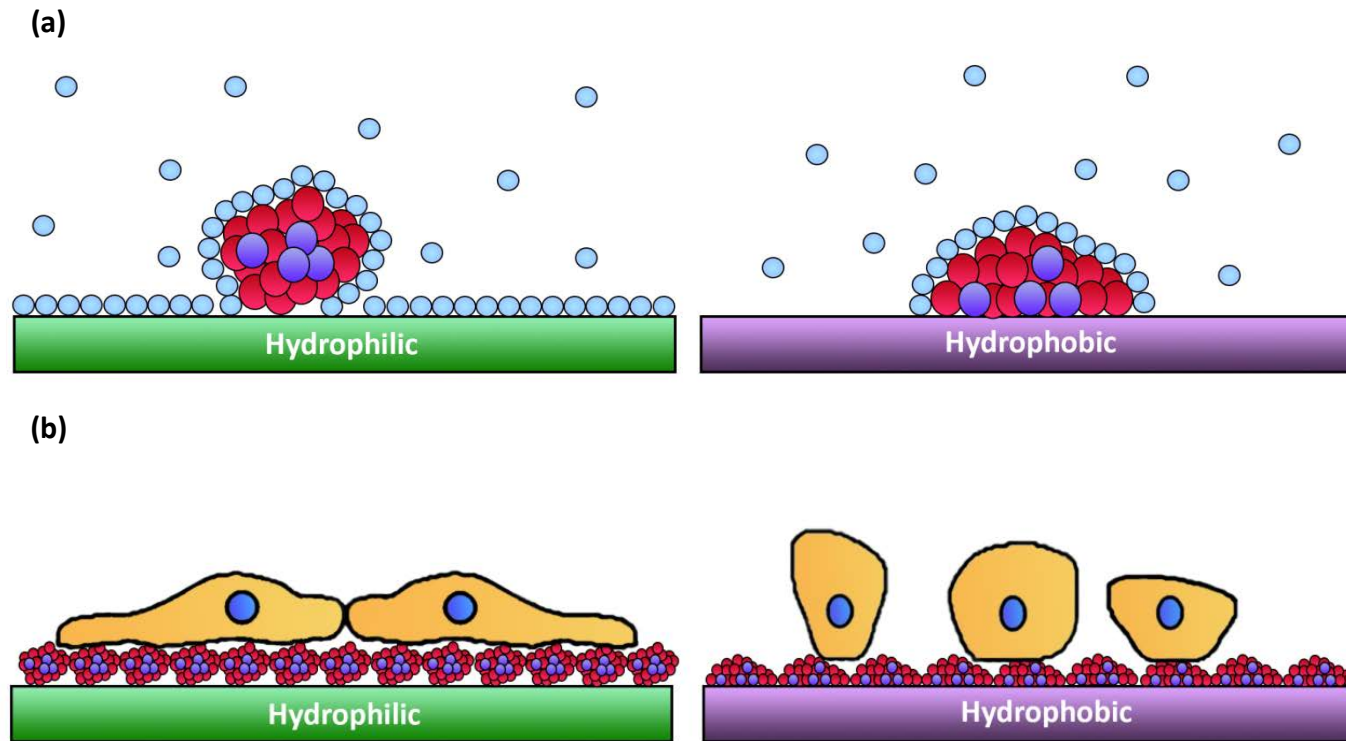


**Figure 33:** Mechanisms of (a) protein adsorption and (b) cell attachment on hydrophilic and hydrophobic surfaces. Proteins on hydrophilic surfaces retain their native conformation and adsorb to the surface, whereas proteins interacting with hydrophobic surfaces partially or fully denature to protect their hydrophobic cores. As a result cell adhesion and proliferation could be affected with cells exhibiting a rounded loosely attached morphology on hydrophobic materials. Light blue dots represent water molecules, red dots represent hydrophilic portions of the proteins with the hydrophobic cores indicated by the purple dots. Modified from [185] and [186]

#### 4.2.2. Materials used for renal replacement devices and potential therapies

Early BAK devices consisted of renal cells seeded into a haemodialyser with the intention of developing a clinical tool to surpass conventional dialysis treatments. Haemodialyser cartridges contain hollow fibres made from a range of porous semi-permeable membranes with properties supporting the low, medium and high flux of small molecules (e.g. electrolytes, low molecular protein breakdown products from blood). The movement of these molecules occurs mainly through diffusion along the concentration gradient from the blood to the dialysis fluid, but is also subject to convection, adsorption to the membrane and as a consequence of fluid flux across the membrane. Haemodialysis cartridges are not best suited for the cultivation of renal cells within the lumen of these fibres due to the presence of a smooth skin layer designed to prevent the adhesion of erythrocytes and proteins from the blood on the inside, and a larger porous surface on the outside [12]. They have, however, provided a valuable starting point for bioreactor design and material choice for renal cell cultivation.

##### 4.2.2.1. Cellulosic and synthetic membranes

Regenerated cellulose membranes are formed from the dissolution of cellulose (chains of  $\beta$  linked D-glucose subunits) pulp, and have a wide variety of applications including wound healing, encapsulation and as hollow fibre membrane material in the early iterations of haemodialysis cartridges [188]. Modifications to the hydroxyl groups on the cellulose subunits (cellobiose unit) have produced a variety of membranes with increased biocompatibility (reduction in complement activation), whilst retaining the hydrophilic and microporous properties [189]. However, when looking at the applicability of RC membranes for BAK or kidney *in vitro* models, poor renal cell growth has been observed, with primary hPTCs unable to form differentiated epithelia on these membranes [181].

Synthetic membranes utilised in haemodialysis cartridges can be divided into four groups depending on the techniques used for hydrophilisation: hydrophilic by nature, hydrophilic by process, hydrophilic by blending and hydrophilic by treatment. PSF, polyacrylonitrile (PAN) and polyamide are hydrophobic by nature and require treatment to render them hydrophilic to increase biocompatibility and allow the filtration of blood

toxins, whereas ethylvinylalcohol co-polymers (EVALs) are naturally hydrophilic [189]. Out of these four groups, PSF based membranes have been the most commonly utilised in the development of BAK devices, although EVALs have been extensively used for BAK generation by Saito et al [190].

PSFs are amorphous (non-crystalline) thermoplastic polymers characterised by the presence of the para-linked diphenylsulfone group as part of the aromatic backbone repeating units. There are three commercially relevant types of PSFs which exhibit slight changes in some of the polymer properties: PSF, polyethersulfone (PES) and polyphenylsulfone (PPSF). Generally PSF membranes exhibit excellent thermal stability, a high glass-transition temperature, minimal shrinkage during fabrication, high strength, stiffness and resistance to many forms of radiation. The hydrophilicity of PES is higher than PSF due to the substitution of the hydrophobic isopropylidene unit with the hydrophilic sulfone group [191]. Differentiated hPTC epithelium has, however, been observed on both PES and PSF membranes, although the formation was relatively slow [181]. PSFs also have the ability to be blended with various molecules in order to modify their surface characteristics. A prime example is the addition of PVP to increase the hydrophilicity of the PSF or PES membranes. This has been historically utilised in water separation and more recently BAK applications. Untreated PES/PVP and PSF/PVP however, have not been able to produce differentiated PTC epithelia in some experiments [181][192]. Other moieties blended with PSF or PES bases include Fullcure (an acrylic based monomer) [181] and the phospholipid polymer PMBU [193] which reported improved renal epithelium formation and increased cytocompatibility when compared to the unblended membranes respectively.

Other membranes which have been employed (primarily in 2D culture platforms) include polycarbonate (PCT) and polyester (PET) membranes, most commonly in the form of commercially available Transwell® inserts. When applied to hPTCs there were contradictory reports in the literature regarding the achievement of polarised cell monolayers [194][168], although the results from the RPTEC growth on porous membranes in Section 3.4.3. concurred with others [194]. Monomeric units of the various materials used for renal cell culture platforms are shown in Figure 34 and a summary of membrane properties is provided in Table 15.

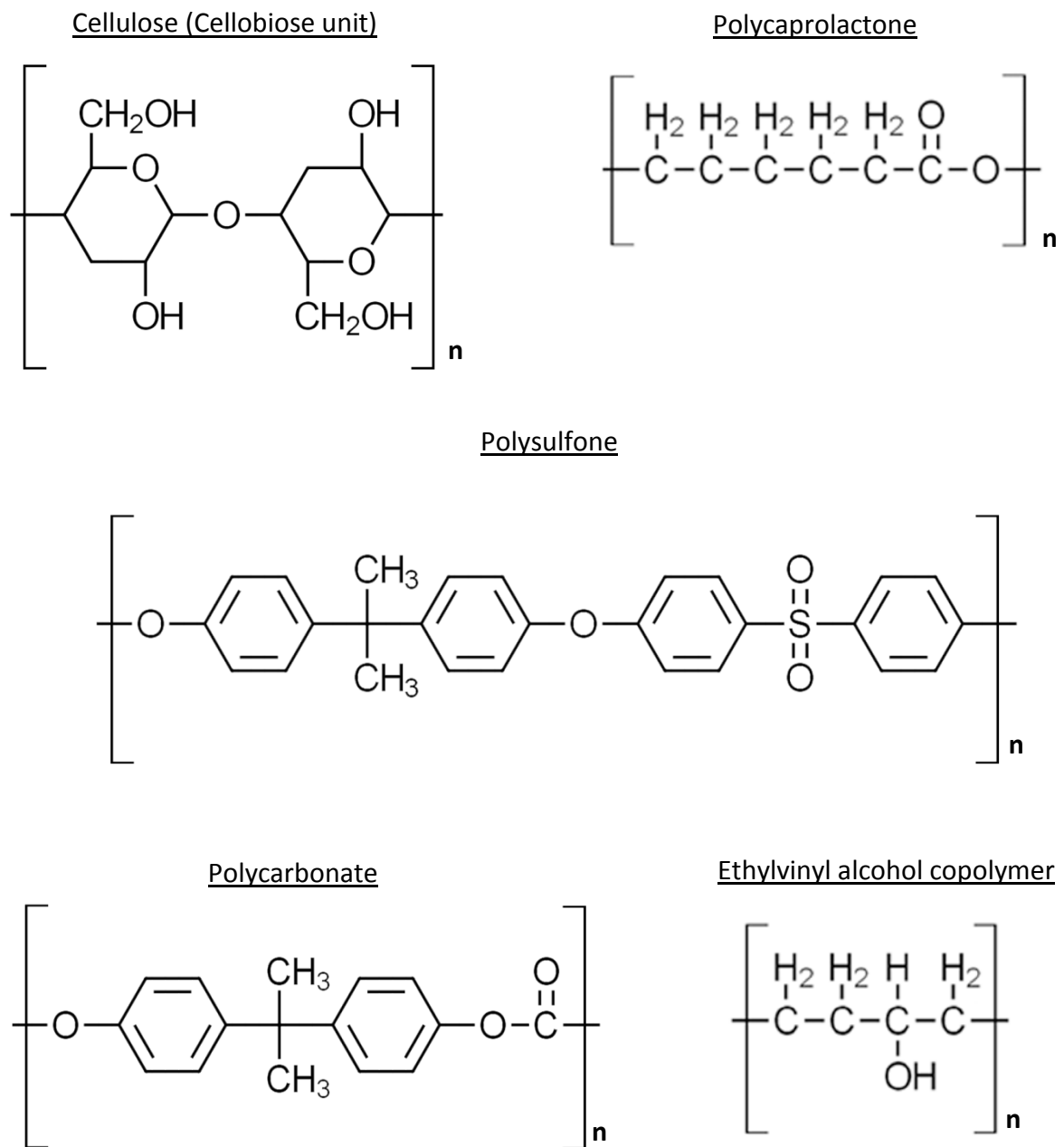


**Figure 34:** Structures of polymer units commonly used for haemodialysis, BAK devices and renal cell growth applications

**Table 15:** Properties of membranes commonly used for haemodialysis, BAK devices and renal cell growth applications

Polymer	Sub-types	Properties	Applications	Use in PTC cultivation	References
<b>Regenerated cellulose (RC)</b>	Hemophan <sup>TM</sup> - Etherification with DEAE, SMC <sup>TM</sup> - Substitution of benzyl with hydroxyl group, PEG modified cellulose, Cellulose acetate	Very hydrophilic (CA ~12°), Functional hydroxyl groups on the surface, Negative surface charge (-9.5mV)	Haemofiltration cartridges, Reverse osmosis membranes, Wound care, Encapsulation, Cell scaffolds	Investigation into PTC growth	[188][181] [195][196] [197][198]
<b>Polysulfone (PSF)</b>	PES PES bound with PVP PSF bound with PVP PSF bound with FC PSF bound with PMBU	Hydrophobic (CA ~70°), Functional sulfone groups on the surface, Negative surface charge (-2mV)	Haemofiltration, Ultrafiltration membranes, Medical instruments, Gas separation, Industrial filtration	Membranes coated with Poly-L-lysine, Gelatin, Pronectin, Collagen and deposited ECM Haemofiltration / hollow fibres coated with: Pronectin L, DOPA+Collagen IV	[181][190] [191][192] [131][195]
<b>Ethylvinyl alcohol co-polymer (EVAL)</b>		Hydrophobic (CA ~65°), Functional hydroxyl groups on the surface, Negative surface charge	Haemofiltration, Cell scaffolds, Hydrogels, Active food packaging	Haemofiltration fibres coated with attachin for PTC cultivation	[190][199] [200][201] [202]
<b>Polycarbonate (PCT)</b>		Hydrophobic (CA ~63°), Functional carbonate groups on the surface, Negative surface charge (~-25mV)	Cell culture platforms, Electronics, Packaging	2D renal model using PCT transwell inserts, Renal tubule-on-a-chip microfluidic device coated with Matrigel	[168][203] [204]

Table 15 continued

Polymer	Sub-types	Properties	Applications	Use in PTC cultivation	References
<b>Polycaprolactone (PCL)</b>	UPy-U PCL and PLGA composite	Hydrophobic (CA ~82°), Functional carboxyl group on the surface, Negative surface charge (-36mV)	Drug delivery, Sutures, Wound dressing, Fixation devices, Cell scaffolds	Electrospun membranes for PTC cultivation, Biomaterials development for <i>in vivo</i> applications	[194][205] [206][207] [208]

**Abbreviations:** DEAE; dimethylaminoethyl, CA; Contact angle, mV; Millivolts, FC; Fullcure, UPy-U; ureido-pyrimidinone- urea, PLGA; poly(lactic-co-glycolic acid)

#### 4.2.2.2. Surface modifications for renal cell attachment and proliferation

To aid the cell attachment and proliferation of renal cells on the membrane types described, various methods of surface treatment have been employed. These methods either increase the presence of functional groups on the surface and increase hydrophilicity, or increase the amount of protein adsorption on the surface of the membranes preferable for hPTC cultivation. Here, several methods of interest for the current application such as: oxygen plasma treatment, oxidising agent treatments and protein coatings are described.

Oxygen plasma treatment is utilised in many disciplines for cleaning surfaces and depositing functional groups or activating the surface. This occurs when oxygen plasma consisting of neutral atoms, atomic ions, electrons, molecular ions and molecules in both excited and ground states, interacts with the surface. Compared to untreated surfaces/membranes, the deposition or activation of functional groups (e.g. carboxylic groups) facilitates protein adsorption on the surface, thus aiding renal cell attachment [181].

Oxidising agents can also be used to introduce functional groups such as carboxyl and hydroxyl groups on the surface rendering it more hydrophilic. Combinations of acids (e.g. nitric, phosphoric, sulphuric acid) with hydrogen peroxide can alter the surface chemistry of a polymer *via* various reactions, the most common being hydrolysis [209]. When applying to PES/PVP membranes, hydrogen peroxide was shown to reduce water contact angles by approximately 20° when compared to the untreated sample (62.5°) [181].

Another type of surface modification widely used in the cultivation of specific cell types is the coating of the culture surface with a specific protein. Most often, these are either proteins which induce a general change in the surface characteristics of ECM proteins specific for cultivation of the cell type in question. For example poly-L-lysine (PLL) bears a net positive charge and has been shown to aid cell attachment [210]. As outlined in Table 8 there are many proteins which make up the basement membrane for the proximal tubule with collagen IV being the most abundant. As a result, when cultured on Tissue culture plastic (TCP) coated with either collagen IV, laminin or complex ECM

coatings (i.e. a mixture of 4 basement membrane proteins) hPTCs exhibited excellent monolayer and tight junction formation [131]. However when applying ECM coatings to polymer surfaces for use in BAK generation, collagen IV was not shown to generate confluent monolayers of hPTCs with tight junction formation on PSF+PVP membranes. Treating the surface with DOPA before applying the collagen IV coating appeared to generate differentiated hPTC epithelium after one week [181][192]. Alternative ways of generating more complex ECM coatings that simulate the physiological stimuli experienced by cells *in vivo* are to apply a combination of proteins (complex ECM coatings) or use the ECM proteins deposited by other cells (e.g. HK-2 cells [131], Matrigel). However, these methods of protein coating are costly, and are less reproducible when complex ECM deposition from cell lines is used in terms of batch variation and heterogeneity of protein deposition. Furthermore, issues such as pore blocking (as indicated in Section 3.4.3.) are detrimental when the transport of substrates through cells are being assessed.

#### 4.2.2.3. ECM scaffolds for organ regeneration

Recent developments in bioengineering and regenerative medicine have identified the use of decellularised scaffolds as a method for organ regeneration. These preserve the native architecture and ECM structure whilst removing the cellular components. The most widely utilised method for decellularisation is flushing the structure with ionic detergent to remove cells from the basement membranes. Although this is effective at completely removing cells, there has been evidence of some ECM disruption. Alternative methods include the use of other chemical agents such as solvents and alcohols, biological agents such as enzymes or chelating agents and physical methods involving temperature, force or pressure [211]. Reseeding of simple structures such as vessels and bladders has demonstrated good short and mid-term results when implanted into patients [212]. Successful decellularisation of the more complex kidney structure has also been achieved [213], and decellularised ECM scaffolds seeded with proximal tubule cells have been developed to generate functional *in vitro* proximal tubule models [214]. However these models are yet to be optimised and validated for use in clinical and pharmaceutical applications. Taking this into consideration for the generation of *in vitro*

renal models, membrane tailoring by optimising formulations or surface treatments are the preferred options.

#### 4.2.3. Methods of membrane production

The fundamental methods for asymmetric polymeric membrane production have been developed over the years to generate membranes with tuneable features for separation processes. These methods are still utilised for many of the membranes commonly used (see Table 15) for renal cell growth and bioartificial kidney devices.

The dry-wet phase inversion method also known as non-solvent induced phase separation (NIPS) was originally developed for seawater desalination using cellulose acetate [215]. The polymer and additives are most often dissolved in a strong highly volatile solvent to produce a dope solution which can then either be cast onto a flat surface to produce asymmetric membrane sheets, or processed through a spinneret to produce hollow fibres. Two desolvation steps then take place to form the porous polymer membrane: solvent evaporation immediately after casting and solvent-non-solvent exchange when the casted film is immersed in the non-solvent (coagulation/gelation) bath. A smooth skin layer is formed on the top of the flat membranes due to the fast solvent evaporation, followed by the diffusion of solvent out of the film in exchange for the non-solvent, which is usually water. Thus the creation of solid films from liquid dispersions can be generated by solvent/non-solvent exchange. By altering the amount of polymer in the dope solution, the properties of the membrane (e.g. the porosity of the skin layer) can be modified. Polymer membranes produced by this method possess a broad pore size distribution range which limits selectivity for size-based separations, but is adequate for nutrient and gas permeability for cell cultivation [195][216]. To address this issue, other phase separation methods have been developed to generate membranes with more isotropic cross-section morphologies. These methods include thermally induced phase separation (TIPS), evaporation induced phase separation (EIPS) and vapour induced phase separation (VIPS) which are typically used in the production of commercially available microfiltration membranes [216].

Electrospinning has gained interest as a method for producing membranes over the past 5-10 years due to its ease of use, adaptability and the ability to engineer fibres on the

nanometer scale in terms of porosity and surface topography. This method uses a high voltage source to apply a charge of a certain polarity into the polymer solution, which is then accelerated towards a collector of opposite polarity or ground plate. As the solution travels through the atmosphere the solvent evaporates, depositing the solid polymer onto the collector. Electrospinning can be used to make sheets or fibres from biodegradable, non-biodegradable and natural materials with typical diameters ranging from nanometers to micrometers. This method has been utilised in tissue engineering [217][218][219] and drug delivery [220][221] applications especially due to the size of the fibres produced [222], but has also been applied in separations research [223][224].

#### 4.2.4. Conclusion

There are many factors that affect the biocompatibility of a biomaterial including: wettability, surface chemistry, surface free energy, surface roughness and the mobility of functional groups on the surface. These characteristics ultimately affect the degree of protein adsorption on the surface, subsequently affecting cell adhesion and proliferation. There has been a wide range of materials used to generate renal cell culture substrates for both BAK devices and *in vitro* model development. These have employed both material and surface modification and protein coating. The most common of these polymers is PSF as it is versatile, robust and can be blended with additives to generate membranes with modified surfaces. However, as of yet there is no polymer porous membrane material that is standard for the cultivation of renal cells. This chapter aims to address this need by comparing standard polymer blends with experimental blends in order to develop an optimal renal cell culture substrate for the cultivation of PTCs within the BAK device.

### 4.3. Materials and methods

#### 4.3.1. Formulation

Four polysulfone based dope solutions were created to generate porous polymer membranes. Weight percentage of polymers and solvent in each solution can be found in Table 16. PSF pellets were dissolved in 1-methyl-2- pyrrolidinone (NMP) by continuous stirring using a magnetic stirrer for 24 hours to ensure PSF was thoroughly dissolved. PVP, MA or GA in powder form (Sigma Aldrich, UK) were then added and continuously stirred for a further 24 hours.

**Table 16:** Amounts of solvent and polymer used in the generation of PSF based dope solutions

Dope solution	PSF (%)	PVP (%)	MA (%)	GA (%)	NMP (%)
PSF	25	-	-	-	75
PSF + PVP	20	5	-	-	75
PSF + MA	20	-	3	-	77
PSF + GA	20	-	-	3	77

#### 4.3.2. Membrane generation

Flat sheet membranes were generated by casting the dope solutions described in Section 4.3.1. onto glass slides using a spin coater (Delta 20BM; BLE, Germany) and immersing in water, thus allowing phase inversion of the solvent to generate the solid membrane. 1mL of the dope solution was applied to a glass slide (4cm x 4cm) and spun at 500rpm for 30 seconds. Coated slides were then removed from the spin coater and immersed in deionized water. After natural peeling, the glass slides were removed and water was changed twice a day for 48 hours as part of membrane washing in order to remove any traces of unreacted reagents.

### 4.3.3. Wettability

Wettability of the membranes was measured by the static sessile drop method using an OCA 20 goniometer (DataPhysics, Germany). 2 $\mu$ L water drops were dispersed onto the membrane and captured after approximately 5 seconds to allow the drop profile to settle. The mean advancing contact angles of the drop were then calculated using the SCA20 software. The reported contact angles are an average of 6 different drops (12 contact angles) per membrane.

### 4.3.4. Surface chemistry

Flat sheet membrane samples were analysed using the K-Alpha<sup>TM</sup> X-ray photon spectrometer system (Thermo Scientific, UK). A survey scan was performed to determine the chemical and atomic signatures. The binding energies were then cross referenced to functional groups and bond types present using the Handbook of X-ray Photoelectron Spectroscopy [225]. Two points were measured on each membrane at a take off angle of 90° and analysed using the Thermo Scientific Avantage data system.

### 4.3.5. Surface topography

Membrane topography was analysed using the Veeco Explorer atomic force microscope (AFM) (Veeco Instruments, USA). Membranes were cut to fit the sample platform and analysed on the tops and bottoms of each polymer blend. Three points on each of the samples were analysed at both 20 $\mu$ m x 20 $\mu$ m and 5 $\mu$ m x 5 $\mu$ m sample areas and the maximum peak height ( $R_{max}$ ), average roughness ( $R_a$ ) and root square mean roughness ( $R_{rms}$ ) were calculated by the software.

### 4.3.6. Membrane and fibre imaging

Membranes were imaged using the Field Emission Gun Scanning Electron Microscope (FEGSEM) (Carl Zeiss, Germany) after sputtering with gold (Emitech SC7640 Sputter Coater; Quorum Technologies, UK). The coating was applied for 90 seconds in a vacuum (10<sup>-2</sup>mbar) with a current of 20 $\mu$ A at 20kV to produce a coating thickness of approximately 10nm. Images were acquired at 1, 5, 10 and 15 thousand times magnification using the SE2 lens.

#### 4.3.7. Membrane sterilization

Membranes were cut into discs with a surface area of 1.8cm<sup>2</sup> and placed in 24-well plates. Each membrane was tested twice with the following sterilization methods:

##### 4.3.7.1. Immersion in IMS

1mL of 70% IMS was placed in each well and kept at RT in a covered plate in the BSC for 30 minutes. The IMS was then removed and the membranes were left to dry at room temperature in a covered plate.

##### 4.3.7.2. Incubation with antibiotic/antimycotic solution

1mL of antibiotic/antimycotic solution containing 10,000 units/mL penicillin G, 10mg/mL streptomycin and 25µg/mL amphotericin B (Sigma Aldrich, UK) was placed into each well and kept at 4°C for 6 hours in a covered plate. The solution was then removed, the wells were washed 3 times for 3 minutes with sterile PBS and then left to dry at room temperature in a covered plate.

##### 4.3.7.3. Autoclaving and sterility testing

Discs were placed in autoclavable boxes before inserting into plates. Discs were then autoclaved for 15 minutes at 121°C before placing into plates in the BSC.

After sterilization, one plate was incubated with nutrient broth (Sigma Aldrich, UK) prepared to manufacturer's instructions (13g to 1L deionized water) for 48 hours at 37°C. After incubation 1mL of the broth was removed and the optical density (OD) was read at 600nm against a sterile broth blank and a positive control of *E.coli* K-12 (NCIMB, UK) incubated for 48 hours at 37°C.

500µL of the broth was also removed and spread onto nutrient agar spread plates (prepared to manufacturer's instructions- 40g agar, 13g nutrient broth, 1L water; Sigma Aldrich, UK) using aseptic technique. The positive control was diluted 10 and 100 fold before plating. The plates were then incubated at 37°C overnight and colonies were manually counted.

The second plate of membranes was then imaged using the FEGSEM to ascertain any damage to the membranes during the various sterilization processes.

#### 4.3.8. Cell viability assay- Presto blue

The Presto Blue assay incorporates resazurin, an oxidation-reduction (REDOX) indicator to detect cell metabolic activity. When applied, resazurin, a virtually non-fluorescent, non-toxic molecule permeates into the cells and is reduced to produce the fluorescent resorufin. Viable cells continuously reduce resazurin, allowing the quantitative measure of cytotoxicity and cell viability.

Before seeding, 24-well plates containing autoclaved membrane discs attached to the bottom of the plates by a thin layer of agar (Sigma Aldrich, UK) were incubated with medium for 1 hour at 37°C alongside untreated TCP. Medium was then aspirated and RPTECs were seeded at a density of  $2 \times 10^5$  cells per well. Plates were incubated for 4 hours at 37°C to allow cell attachment to the membrane prior to the viability assay. 100µL of the spent medium was then aspirated from each well before the addition of the Presto Blue reagent (Invitrogen; Life technologies, UK). Plates were then statically incubated for 40 minutes at 37°C in the dark (wrapped in aluminium foil) before sampling. 100µL samples were taken from 3 points in each well, and each membrane was tested in triplicate. The samples were then run against a positive control, negative control and blank on a 96-well optical bottom black plates (Nunc). The positive control was represented by 100% reduced 10% (v/v) Presto Blue in growth medium achieved by autoclaving. The negative control was represented by 0% reduced 10% (v/v) Presto Blue in growth medium while the blank was represented by fresh growth medium. Fluorescence intensity was measured on the microplate plate reader at Ex: 544nm, Em: 590nm, gain 1067.

To assess cell recovery, the reagent was removed and the seeded membranes were washed three times with PBS. The cells were then trypsinised off the membrane surface and counted on a NucleoCounter NC-100. A calibration curve equating the fluorescence from the reduction of Presto Blue to cell number was also generated to predict cell numbers (Appendices- Figure 63).

## 4.4. Results

### 4.4.1. Predicted chemistries and structures of polymer blends

Four polymer chemistries were employed in the study presented in this chapter. The exact compositions of the polymer blends are presented in Table 16 (see Section 4.3.1.). The formulations without additive and with PVP as an additive were identified as being suitable from the literature research [226][227]. The formulation using MA and GA as additives were chosen based on the predicted properties required for renal cell attachment and proliferation.

The predicted binding of pure PSF membranes after casting leaves the hydroxyl groups on the sulphur available for binding to the cells via electrostatic interactions (Figure 35a). The addition of PVP is thought to increase the biocompatibility of a surface [228] by making it more hydrophilic than pure PSF. When dissolved in NMP the PVP binds to the oxygen on the sulphone, where the formal charges of the sulphur (positive) on the PSF molecule and oxygen on the PVP molecule (negative) are sustained (Figure 35b). During coagulation in water the negative charge of the oxygen on the PVP molecule attracts hydrogen from a water molecule. The remaining hydroxyl group is attracted to the positive charge on the sulphur in the PSF molecule to nullify the charge, thus precipitating to form the porous membrane. PVP is therefore strongly bound to the PSF molecule, and is thought to be able to withstand fluidic forces as the membrane blend has been used in microfiltration applications and heat treatment of 300°C [229][230]. Increasing the presence of functional groups is also applied to surfaces through methods like oxygen plasma treating and surface coating (as tested in Section 3.4.3) to aid cell attachment. Carboxyl and hydroxyl groups present on the surface have also been shown to aid cell attachment [231] so on this basis two carboxylic acids MA (Figure 35c) and GA were added to increase hydroxyl groups on the surface with different length carbon chains. The mechanism of binding of the acids to the PSF backbone is similar to PSF+PVP. In NMP the oxygen on the sulphone molecule interacts with the carbon of the acid, causing a formal negative charge on the acid oxygen and a formal positive charge on the sulphur in the PSF. When cast into water the formal negative and positive charges attract a hydrogen and hydroxyl group from the water molecule respectively thus causing the precipitation of the polymer. This increases the net surface charge due to an

increase in functional (hydroxyl and carboxyl) groups present on the surface. As there are two oxygen species on the sulphone for acid binding on the PSF molecule, twice the amount of acid to PSF was used in the dope solutions.

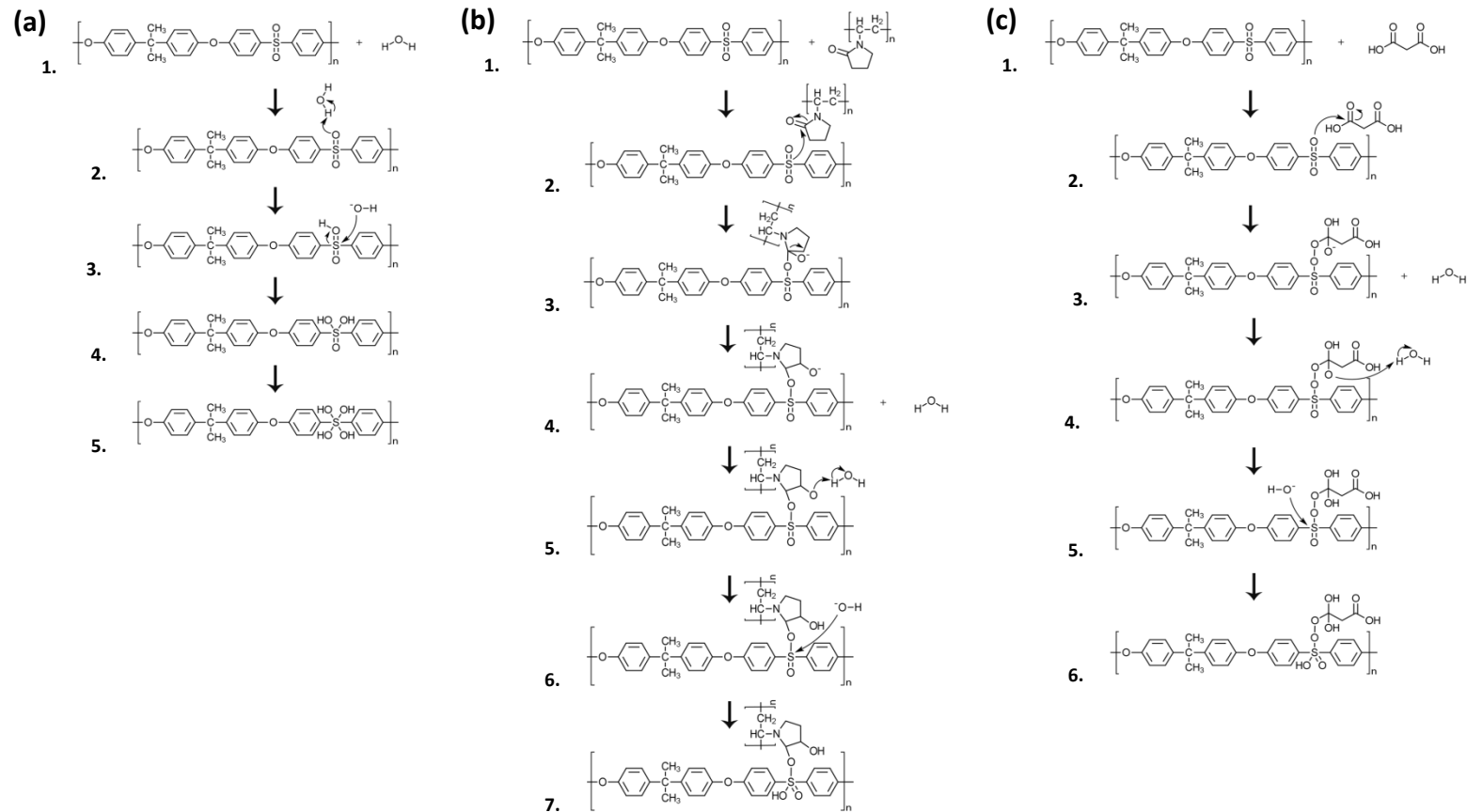


**Figure 35:** The predicted reaction mechanisms of (a) PSF, (b) PSF+PVP and (c) PSF+ (malonic) acid. PVP and MA additive reactions in NMP are described from (b) 1-4 and (c) 1-3 respectively, after which the precipitation mechanisms in water for PSF (a), PSF+PVP (b) 4-7 and PSF+MA (c) 3-6 are detailed

#### 4.4.2. Membrane wettability

Membrane hydrophilicity was assessed by measuring the water contact angles (WCA) of water on the top and the bottom of the four generated polymer membranes of different chemistries. According to the literature the expected WCA of PSF is 70° [53]. This value was measured on the bottom of the PSF membranes. However, on the top of the PSF membranes the WCA recorded was lower, being  $63.1^{\circ} \pm 1.6^{\circ}$  (Figure 36e). The membranes formulated with additives exhibited similar WCA values both on the top and bottom, with the PSF+PVP formulation possessing the lowest value on the top of the membrane ( $60.2^{\circ} \pm 1.5^{\circ}$ ). This is a common phase separation phenomena due to instantaneous demixing at the interface resulting in a skin layer being formed on the top of the PSF based membranes [232]. The similarity in surface topography therefore leads to a similarity in WCA (see Section 4.4.4). Subsequently when ANOVA tests were run on the WCAs for the top sides of all blends, there was no significant difference ( $p \leq 0.05$ ) between the formulation containing MA as additive and the pure PSF. However there was a significant increase in WCA between pure PSF and PSF+GA indicating an increase in hydrophobicity. On the other hand PSF+PVP showed a significantly lower WCA than all other polymer blends indicating an increase in hydrophilicity which is concurrent with findings in literature [228]. The WCAs on the bottom were not taken into account in the statistical analysis as the method of fibre spinning would mimic the reactions at the top of the membranes (NIPS).

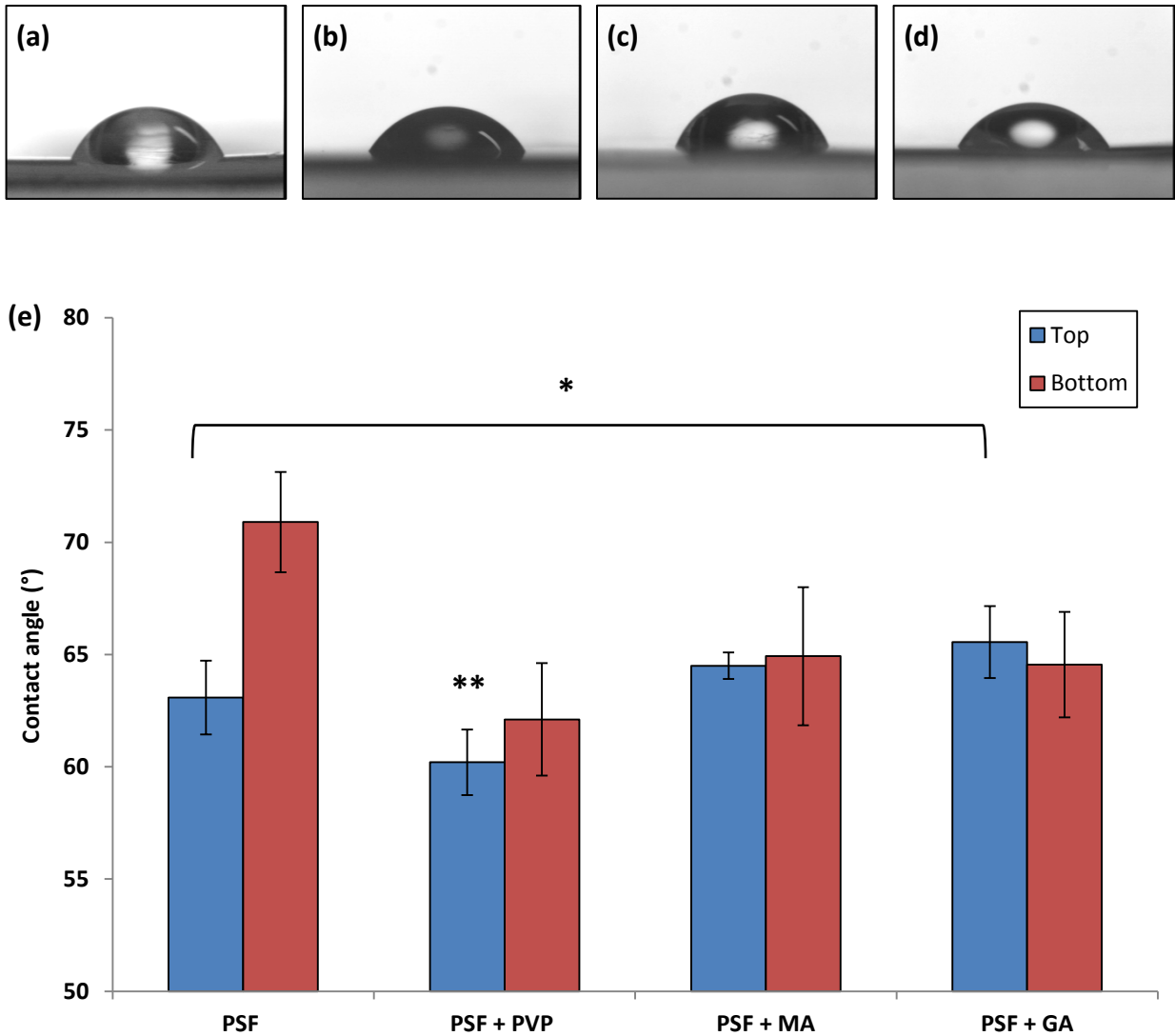


**Figure 36:** Photographs of water droplets on the top side of (a) PSF, (b) PSF+PVP, (c) PSF+MA and (d) PSF+GA membranes. (e) Water contact angles on the top and bottom sides of the flat sheet membranes (Mean  $\pm$  SD, n=6). \* indicates statistically significant difference to the highlighted samples, \*\* indicates statistically significant difference to all top samples,  $p \leq 0.05$  (ANOVA with Tukey *post hoc* analysis)

#### 4.4.3. Surface chemistry analysis

Although the ratio of MA and GA associated with PSF could not be discerned from the XPS data, PSF+PVP membranes were able to be analysed compared to PSF membranes by XPS (Figure 37). In all samples there was nitrogen contamination present in the form of nitrates and ammonia. This could have originated from the membrane formation process or be down to NMP residue on the membrane surface. The PSF membranes produce atomic breakdowns on XPS similar to the expected atomic breakdown, the only difference being the nitrogen based contaminations. In the PSF+PVP membranes the amount of nitrogen from the PVP is shown by the increase in the peak indicating C+N and C+S from the PSF peak (3.58%). Comparing this difference to the percentage of S present gives a ratio of 1.2:1, indicating each PSF molecule is bound to approximately one PVP molecule. When comparing the PSF+MA to the PSF membrane, the amounts of C and O present are relatively similar compared to pure PSF. This indicates that there is little MA associated with the surface. In contrast, the amount of C is slightly higher than PSF in the PSF+GA membranes indicating the presence of GA. However, the Oxygen content is lower than all of the other blends indicating that there is little GA bound to the surface. This XPS data concurs with the membrane wettability results that the PSF+PVP membranes are more hydrophilic due to the association of PVP at the surface with the hydrophobic portion of the PSF molecule. The content of MA or GA bound to the surface is also in agreement with the WCA measurements that show little or null MA or GA association with the PSF.

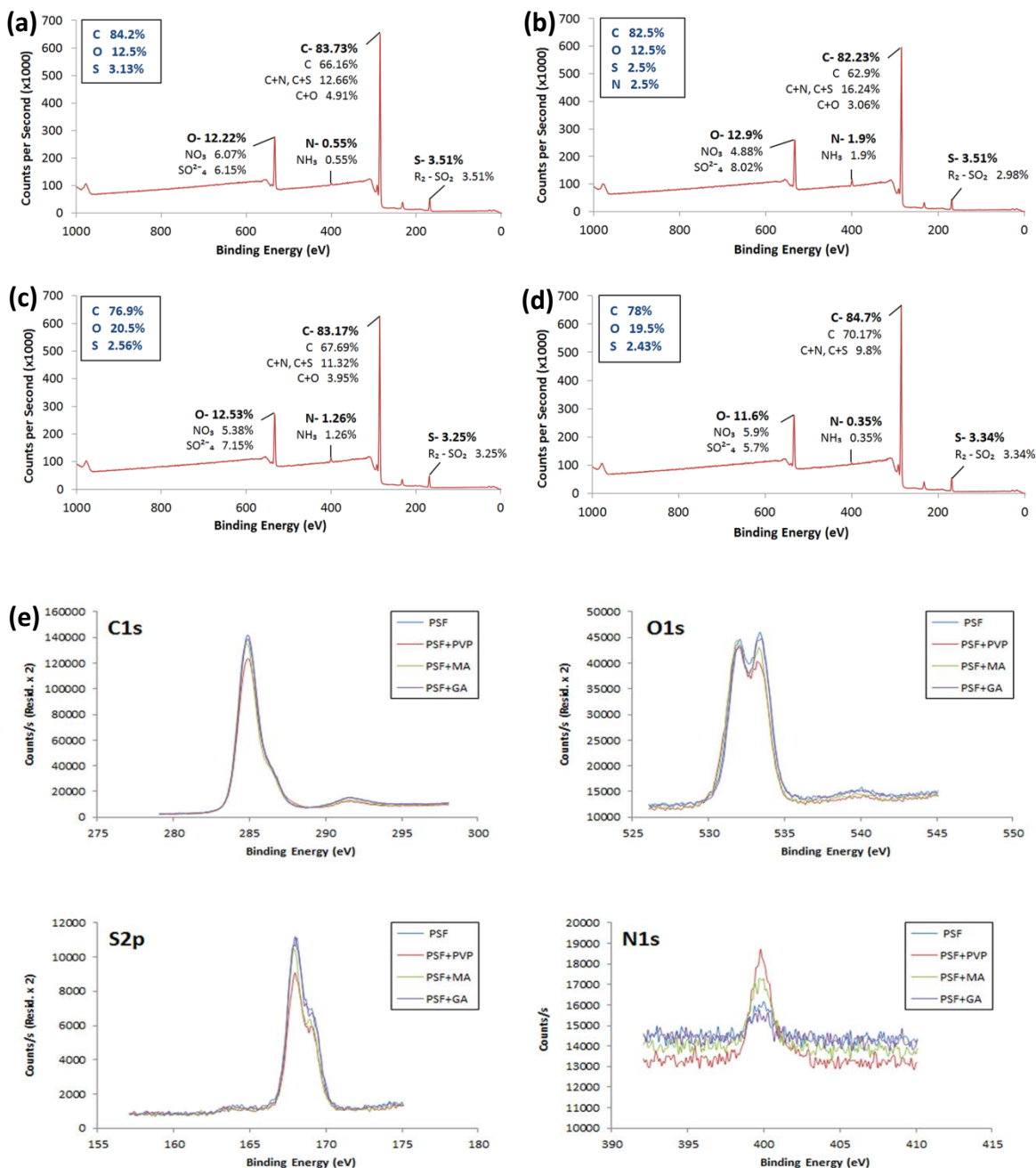


**Figure 37:** XPS spectra of (a) PSF, (b) PSF+PVP, (c) PSF+MA and (d) PSF+GA membranes showing the expected atomic % breakdown (blue) and the atomic % breakdown recorded by XPS analysis. The percentage of bond types cumulating in the elemental percentage is shown and an overlay of the spectral regions for each element is shown in (e). C=Carbon, O=Oxygen, N=Nitrogen, S=Sulphur, NO<sub>3</sub>=Nitrate, SO<sub>4</sub><sup>2-</sup>=Sulphate, NH<sub>3</sub>=Ammonia, R<sub>2</sub>-SO<sub>2</sub>=Sulphone

#### 4.4.4. Membrane topography

A marked difference in the topography of the water facing 'top (T)' of the membranes and the glass facing 'bottom (B)' of the membranes was seen (refer to Figure 38). This surface difference was expected due to the fast exchange of solvent during the membrane production and water resulting in a 'smooth' layer on the top surface. Contrary to the top, the bottoms of the membranes demonstrated a slower exchange of solvent and water as a result of the contact between the polymer and the glass slide resulting in a rougher surface. This was confirmed by the roughness values measured and presented in Table 17. PSF displayed the roughest surface of all the membranes on the top and bottom sides given by the  $R_a$  and  $R_{rms}$  values, although the  $R_{max}$  was the highest for the bottom side of the PSF+PVP membrane. Basic correlations between water repellency and surface roughness were originally described by Wenzel and Cassie and Baxter. In the Wenzel state the liquid conforms to the surface roughness which increases its interfacial contact area and increases the hydrophilic/hydrophobic character of the surface. In contrast the Cassie-Baxter bridging state reduces the contact area of the liquid, with gas bubbles filling the hollows and the liquid sitting on top of the roughness. This is also known as the 'Fakir effect'[233][234]. Reports in literature have also linked the surface roughness with the WCA values, with a rougher surface exhibiting a low WCA [229]. Although this does not fully support the mean WCA and the roughness values measured, the membranes displayed similar roughness on the top and bottom sides. No significant difference (ANOVA,  $p \leq 0.05$ ) was recorded between the different polymer blends.

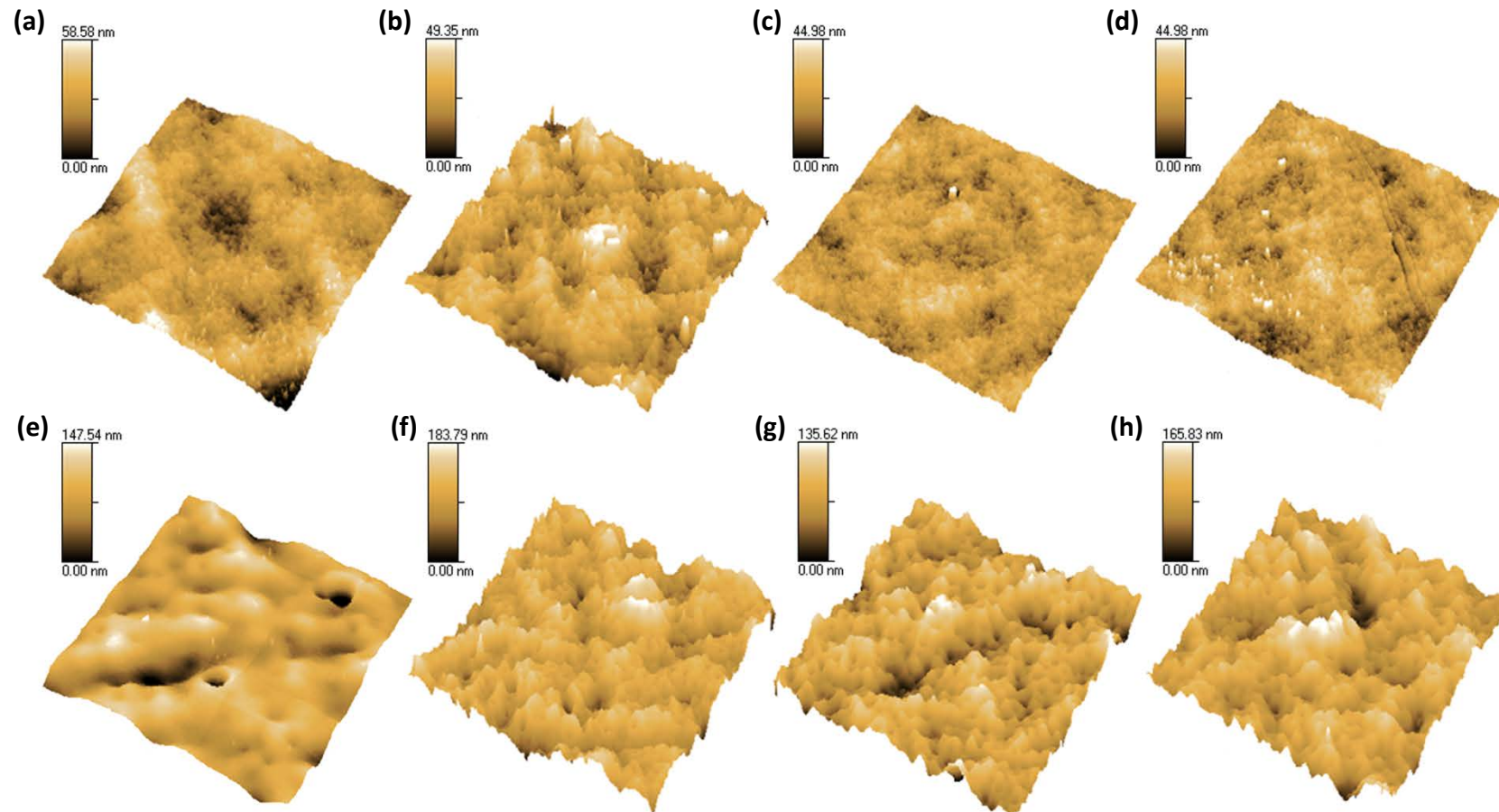


**Figure 38:** Representative AFM images of the tops (top row) and bottoms (bottom row) of PSF (a)(e), PSF+PVP (b)(f), PSF+MA (c)(g) and PSF+GA (d)(h) membranes. Each image displays a 20 μm x 20 μm sample area

**Table 17:** Parameters of the polymer surfaces (Mean value  $\pm$  SEM, n=3)

Polymer	Side	$R_{\max}$ (nm)	$R_{\text{rms}}$ (nm)	$R_a$ (nm)
PSF	Top	95.96 $\pm$ 27.3	14.30 $\pm$ 4.8	11.03 $\pm$ 4
	Bottom	163.88 $\pm$ 8.4	48.73 $\pm$ 10.6	35.73 $\pm$ 7.9
PSF+PVP	Top	50.13 $\pm$ 3.5	11.57 $\pm$ 3.1	7.70 $\pm$ 1.4
	Bottom	188.32 $\pm$ 7	27.87 $\pm$ 1.6	21.20 $\pm$ 1.2
PSF+MA	Top	46.05 $\pm$ 4.8	7.83 $\pm$ 1.3	5.57 $\pm$ 0.7
	Bottom	131.42 $\pm$ 5.2	21.30 $\pm$ 0.7	16.53 $\pm$ 0.9
PSF+GA	Top	65.35 $\pm$ 13.1	10.33 $\pm$ 2	7.63 $\pm$ 1.5
	Bottom	134.78 $\pm$ 42.3	26.20 $\pm$ 9.3	20.60 $\pm$ 7.6

#### 4.4.5. Membrane structure

As seen in the AFM images acquired (see Figure 38), all of the polymer blends produced a similar structure of the top (water exposed) sides of the membranes. There were no pores observed at the magnification used, however some pores were visible on the bottom and were most likely as a result of the slower exchange of solvent and water taking place during membrane production. These pores were not evenly distributed on the bottom surface of the flat sheets, and were more numerous on the PSF+PVP membranes (Figure 39). This finding could be attributed to the viscosity of the dope solutions when casting. Thus the PSF+PVP dope solution was noticeably less viscous than the other polymer blends enabling it to cover the slide quicker during the spin coating and minimising the exposure time to the atmospheric humidity. The cross sections of the membranes show the characteristic 'finger like' macrovoids with porous walls generated by the slowest exchange of solvent and water occurring in the middle of the membranes. There are contradicting reports that PVP may cause the suppression or enlargement of macrovoids [235][236], but there was no difference observed between these membrane blends. Although clean cut cross sections could not be generated due to sample preparation, the structural integrity of the membranes could be identified and assessed.

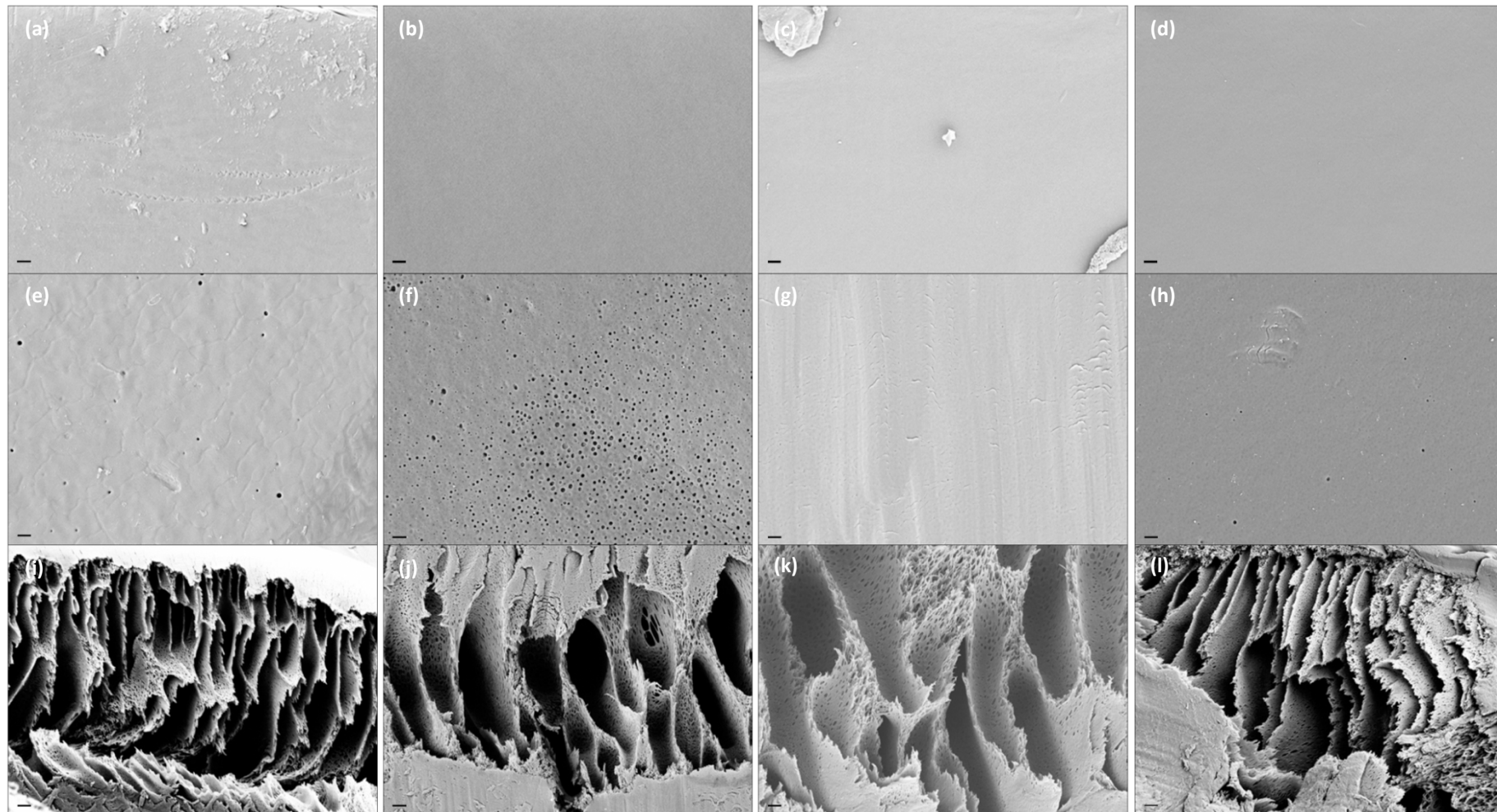


**Figure 39:** SEM images of PSF (a), (e), (i), PSF+PVP (b), (f), (j), PSF+MA (c), (g), (k) and PSF+GA (d), (h), (l) top sides (a-d), bottom sides (e-h) and cross sections (i-l) at 5K magnification. Scale bars = 2 $\mu$ m

#### 4.4.7. Membrane preparation and cell viability

##### 4.4.7.1. Membrane sterilisation

All methods of sterilisation employed were proven effective for all the membrane blends as any microbial growth was prevented. The OD of the incubated nutrient broth for each sample was found negative against the positive *E.coli* control. Furthermore, colony counts from each membrane sample except for PSF sterilised with antibiotics and PSF+GA sterilised by autoclaving were zero, indicating no microbial growth (see Appendices- Figures 64 and 65). However, for the two samples that did show some signs of microbial growth based on the colony counts (2 colonies per mL), the OD measurements were contradictory indicating no microbial contamination. The contaminations were therefore recorded as operator error within the aseptic technique employed.

Membrane discs were then sterilised using the methods described in Section 4.3.7. and imaged *via* SEM to assess if any visible structural changes occurred compared to the unsterilized samples (Figure 40). No obvious structural change was observed, with all samples showing similar structures to the unsterilized membranes on both the top and the bottom sides (Figure 38), as well as the cross sections (Appendices- Figure 66). However, despite no evident structural changes, the membranes sterilised with the antibiotic/ antimycotics displayed a yellow staining from the solution that was not removed during the washing step. The presence of stains on the membrane suggests a degree of absorption within the internal structure, which would possibly require a more vigorous and thorough washing to be performed. The length of time required for sterilisation was also the longest and as a result, this sterilisation method was not employed further. The sterilisation method based on immersion in IMS required the shortest sterilisation time; however, it also required extensive washing to remove the IMS from the membrane. Within literature membrane sterilisation using the 3 techniques used here have been assessed, with autoclaving reported to have achieved high biocompatibility on PSF+PVP membranes [237][226]. Autoclaving provided the easiest and quickest method overall with no visible membrane structural change and

high efficiency. Therefore, autoclaving has been selected as the main method employed for membrane sterilisation.

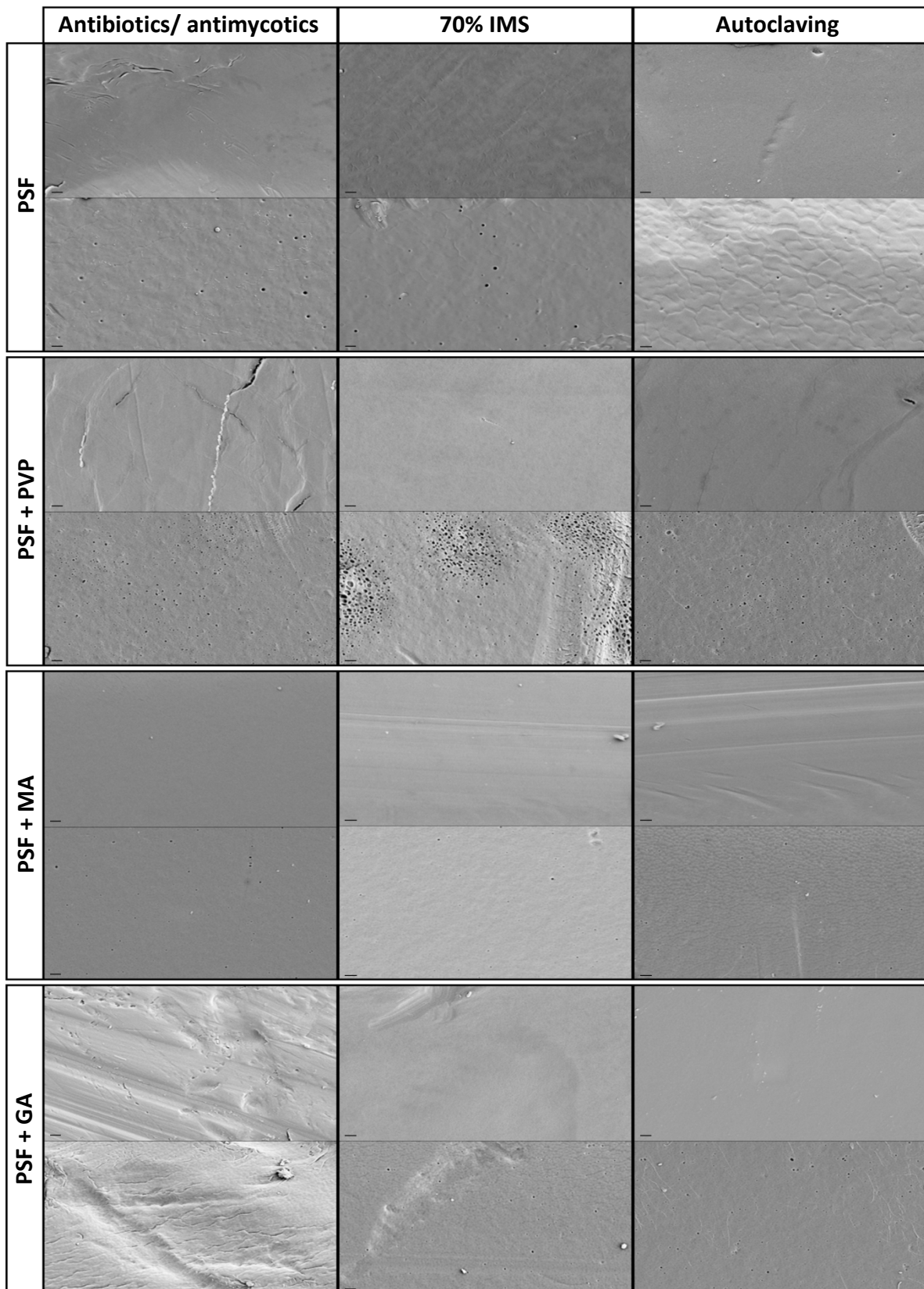


**Figure 40:** SEM images of the tops (top row) and bottoms (bottom row) of PSF, PSF+PVP, PSF+MA and PSF+GA membranes after sterilisation. Images at 5K magnification. Scale bars = 2 $\mu$ m

#### 4.4.7.2. Cell attachment and viability on membranes

Presto blue reduction was measured to assess cell viability after 4 hours post seeding and was corrected against a fully reduced sample. Cells on the membranes exhibited between 8%-10% reduction of Presto Blue compared to the positive control (fully reduced Presto Blue), with similar amounts of Presto Blue reduction observed on the top and bottom of all the membrane blends. TCP was used as a control for cell attachment and displayed a significantly higher percentage of Presto Blue reduction than all the membranes with the exception of the top side of PSF+PVP (Figure 41a). This finding indicates that the top surface of the PSF+PVP membrane is a favourable surface for renal cell culture.

Contrary to the Presto Blue percentage reduction, the cell recovery (Figure 41b) from the top surface of the PSF+PVP membranes was one of the lowest values cell, indicating a lower degree of initial cell attachment. However, when compared to the TCP, all membrane formulations had a poorer performance. Due to the opaque nature of the membranes cell detachment could not be confirmed by visually by light microscopy. Taking into consideration that the same cell harvesting protocol (e.g. trypsin incubation time) was applied for all culture substrates, there is the possibility that the harvesting protocol presented different efficiencies on different culture substrates. As a result, the low cell recovery from the PSF+PVP membranes could be attributed to the harvesting protocol employed. In order to improve the harvesting efficiency, the cells cultured on the different substrates were incubated in trypsin for additional time and then mixed thoroughly before sampling. However even after the improvement, complete cell harvesting from TCP was still not achieved which may also account for the lower numbers of cells recovered from the membranes. Taking into account both percentage reduction of Presto Blue and the cell recovery, the PSF+PVP membrane was assumed to be the best performing formulation for RPTEC culture.

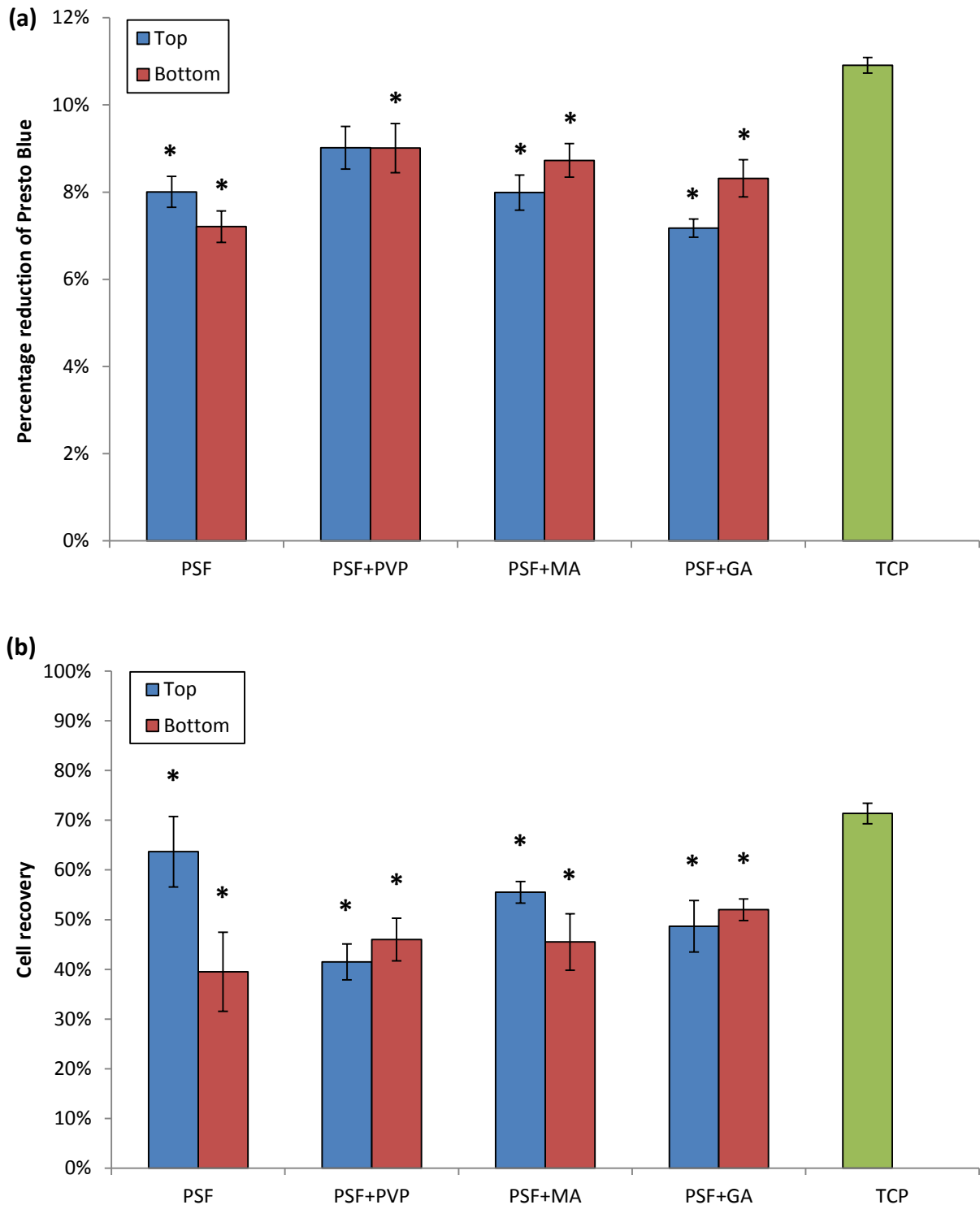


**Figure 41:** Cell performance on the top and bottom of the flat sheet membranes shown by (a) Presto blue percentage reduction and (b) cell recovery from initial seeding numbers. (Mean value  $\pm$  SEM,  $n=3$ ) \* indicates significant difference to TCP,  $p \leq 0.05$  (ANOVA with Tukey *post hoc* analysis)

## 4.5. Chapter discussion and conclusion

### 4.5.1. Discussion

This chapter focuses on the generation and characterisation of PSF based membranes as an improved cell culture substrate for renal PTCs. Although the group of sulfone based membranes is not a good renal cell culture substrate without protein coatings according to some reports in literature [181], its robustness, ease of handling and modification make it an attractive polymer backbone to employ. Alongside PSF and PSF+PVP, which have been used as renal cell culture substrates previously; carboxylic acid additives have also been applied in this work in an attempt to beneficially modify the surface of the PSF backbone. These additives should have theoretically introduced hydroxyl and carboxyl groups on the surface, however, these were not detected through the characterisation techniques. This may be due to a lower amount of acid being present in the system than is required for random binding to PSF and the presence of carboxylic acids on the surface. Nitrogen contaminations were also detected on the surface of the membranes, which were most likely introduced from the air during production. Methods of dope solution generation in literature use a vacuum to degas the solutions, which may be beneficial in further membrane development [238]. Consequently, renal cell attachment and metabolism was not beneficially affected on either membrane with the carboxylic acid additive. PSF+PVP did improve surface characteristics as expected, which resulted in improved renal cell attachment and metabolic activity comparative to standard TCP. Although graphically this similarity is not evident, ANOVA on the results indicates no significant difference between the top surface of PSF+PVP and TCP. Through the method of membrane casting and production the effects of smooth surfaces versus porous surfaces was also investigated. This is important to ascertain as literature has reported smooth, haemocompatible skin layers of fibres like those found in haemodialyser cartridges may be unsuitable for cell cultivation [192]. However, the results presented in this chapter indicate that smooth skin layers are not disadvantageous to PTC metabolic activity, and, in the case of PSF+PVP, are actually beneficial.

#### 4.5.2. Conclusion

There are many biomaterials that have been generated for the culture of renal cells. Whilst some of these use natural polymers such as cellulose, most applications employ synthetic membranes due to their robustness and surface modification or treatment potential. Sulfone based polymers have been utilised previously and were implemented in this work as the backbone for polymer blends from the predominantly positive reports in literature. Physical properties of the membranes have been characterised due to their effect on cell attachment and proliferation. Although the test polymer blends incorporating carboxylic acids did not appear to beneficially modify the membrane surface, the addition of PVP increased the hydrophilicity of and was detected on the surface. Furthermore renal cell attachment and metabolic activity on the top of PSF+PVP membranes is comparative to TCP. The membranes were also easy to sterilize through a variety of methods, which did not appear to alter their intra-membranal structure. This has in part satisfied the aim of generating an improved porous renal cell culture substrate. The production of hollow fibres from this membrane blend, subsequent characterisation device assembly and cell cultivation will be discussed in Chapter 5.

# Chapter 5

**Assembly and assessment of the bioartificial  
kidney device**

## 5.1. Chapter introduction

Various applications in the tissue engineering field have utilised bioreactors, such as the culture of cells on biodegradable scaffolds for implantation into the body, the development of 3D *in vitro* models for diseased states and pharmaceutical research and for extracorporeal support for patients waiting for organ transplants [239]. These types of bioreactors have advantages such as the controllable and adaptable environment for cell cultivation, increased nutrient and oxygen transfer to cells compared to 2D platforms and an increased similarity to the physiological architecture. For this reason, existing bioartificial kidney devices have mainly utilised hollow fibre bioreactors, initially in the form of haemofiltration cartridges seeded with renal cells for both renal replacement therapies and as *in vitro* models [190][178].

Hollow fibre bioreactors have been utilised in many applications including wastewater treatment [240], fermentation [241] and enzyme reactors [242] alongside tissue engineering applications. As such, hollow fibre bioreactors have been extensively developed and optimised for the selected application. In terms of tissue engineering, numerous mathematical models have been developed in order to understand how parameters such as nutrient and gas transfer, fluid flow and transmembrane flux are affected under different operating conditions. As a result, the conditions most suitable for promoting cell proliferation whilst maintaining cell function could be predicted.

This chapter focuses on the assembly and sterilisation of the developed device, alongside the assessment of transmembrane flux through the fibre and physical characterisation of the fibres. RPTec performance was then assessed on the fibres under static conditions, and after exposure to flow within the developed bioreactor.

## 5.2. Review of literature

### 5.2.1. Bioreactors in tissue engineering

Bioreactors have been frequently utilised in many diverse areas including fermentation, water treatment and animal cell culture for the production of proteins, vaccines [239] and more recently, in cell expansion for cell therapies [243]. Bioreactors can generally be defined as devices in which closely monitored and tightly controlled environmental and operating conditions such as: pH, temperature, pressure, nutrient supply and waste removal allow for the cultivation of cells and/or the development of biochemical processes [239]. For tissue engineering applications, various bioreactors have been employed to aid the culture of cells in environments mimicking physiological conditions more closely. A summary of the types of bioreactors detailed below can be found in Table 18.

#### 5.2.1.1. Stir tank bioreactors

Continuous stir tank bioreactors have historically been used in bioprocessing; typically for the large scale fermentation of microorganisms *e.g.* yeast. Smaller scale vessels such as spinner flasks have been utilised in cell culture on 3D porous scaffolds for the generation of cartilage and bone constructs. For example, Vunjak-Novakovic *et al* (1996) suspended scaffolds with needles inside the spinner flask vessel and performed cell inoculation in a dynamic manner. A magnetic stirrer was placed at the bottom of the vessel and used for nutrient and oxygen mixing and reduction of the concentration of boundary layer at the construct surface [244][239]. As a result of mixing, an eddy was formed by the fluid flowing over the superficial scaffold pores, aiding the transport of fluid to the centre of the scaffold. However, despite the improvement in fluid transport, mass transfer in spinner flasks was not sufficient to deliver nutrients and gas homogeneously to the cells [245]. Typically eddies are associated with the transition and turbulent flow and consist of clumps of fluid particles which have a swirling motion superimposed on the mean linear motion of the fluid particles [246]. Cartilage constructs have been cultured to a diameter of 5mm in spinner flasks, although this is not sufficient to be used clinically, which requires a construct of 1-5mm thick with a 5cm diameter. However, the ability to adjust nutrient concentration over time and the

exposure to shear stress are advantageous to chondrocyte proliferation. This is through the countering of ECM deposition to allow construct permeability and through the improved cell morphology and cartilage properties [247]. Bone constructs are also often cultured in spinner flasks due to the increased expression of alkaline phosphatase (ALP), osteocalcin (OC) and calcium deposition in this culture method [248]. Spinner flasks and stir tank bioreactors have also been employed in cell expansion, especially in the emerging field of regenerative medicine. In these vessels, adherent cells such as mesenchymal stem cells (MSCs) have been expanded with the use of microcarriers at small and large scales under serum and serum free conditions. Regardless of the conditions employed, MSCs were able to retain multipotency indicated by the maintenance of their characteristic immunophenotype and expansion down to the osteogenic, chondrogenic and adipogenic lineages after 14 days in culture [243][249].

#### ***5.2.1.2. Rotating wall bioreactor***

For cells sensitive to shear, rotating wall bioreactors (RWBs) could be a valid option. This type of bioreactor has been utilised for a variety of cell types, including chondrocytes [250], cardiac [251] and tumour cells [252][253]. The RWB consists of two concentric cylinders, within which the pre-seeded scaffold submerged in medium is contained. The outer wall of the vessel is capable of rotation, thus producing an upward hydrodynamic drag force that balances out the downward gravitational force. This micro gravitational environment allows the scaffold to be suspended, providing a more homogenous cell distribution compared to the static culture. As the tissue construct grows within the bioreactor, the wall speed needs to be increased to balance out the gravitational force and allow the continued suspension of the scaffold. Chondrocyte culture in RWBs has been relatively successful, exhibiting a 95% construct seeding efficiency within the first 24 hours of culture and extensive proliferation and ECM deposition after 28 days [254]. Cardiac constructs consisting of spontaneously and synchronously contracting elongated cells have also been cultured from neonatal rat and embryonic chick cells after 14 days [251]. However, when comparing RWBs with static and spinner flask culture for rat marrow stromal cells [255] and hMSCs [256], a lower expression of osteoblastic markers (OC, ALP) was exhibited. This is thought to be due to the low shear stresses on the cells or the collision of scaffolds in the bioreactor [248].

### 5.2.1.3. Compression and strain bioreactors

For the formation of tissues that typically experience physiological stresses *in vivo*, bioreactors capable of exposing constructs to mechanical stimuli are required. The exposure to different mechanical stimuli could enhance cell functionality *in vitro*. Compression bioreactors are typically used to engineer cartilage and bone constructs, and are capable of applying both static and dynamic loading. Dynamic loading has provided better results in terms of cartilage formation over other stimuli and static loading, and is more representative of physiological stimuli [245]. When applied to bone marrow MSCs the application of cyclic loading has resulted in predifferentiation down the osteogenic lineage, indicated by the genetic expression of osteogenic markers [257]. Mass transfer was also improved as fluid flow through the scaffold was increased from the compressive motion applied.

Strain bioreactors typically have similar designs to compression bioreactors; consisting of a motor, a system providing linear motion and a controlling mechanism. The difference lies in the way the force is transferred to the construct, either directly or using a rubber membrane to anchor the scaffold and deforming the membrane [245]. Tensile strain bioreactors are commonly utilised for the engineering of tendon [258], ligament [259] and cartilage. However, scaffold constraint in bioreactors directly attached to the construct was shown to impede the differentiation of chondrocytes from MSCs.

### 5.2.1.4. Perfusion bioreactors

Perfusion bioreactors have been used to engineer various tissue and constructs including bone [260], keratinocytes [261], hepatocytes [262], cardiomyocytes [263] and chondrocytes [264]. Perfusion bioreactors generally consist of a pump connected to a scaffold chamber by tubing, and sometimes contain a medium reservoir. Medium is perfused through the stationary scaffold, thus reducing the mass transfer limitations at both the construct periphery and within the scaffold pores. As a result, homogenous cell distribution can be achieved [265]. When compared to static culture, fluid flow as in spinner flasks or RWBs, a higher cell density was achieved in a perfusion bioreactor after 14 days [266]. Shear forces from fluid flow through the bioreactor provided mechanical

stimuli to the cells, which was shown to enhance the osteoblastic phenotype expression [260]. However, the effects of direct perfusion in 3D cultures was highly dependent on medium flow rate and the stage of cell maturation within the constructs, as demonstrated in chondrocyte cultures [267]. Therefore, perfusion bioreactors must be designed to balance the mass transfer of nutrients and waste removal, as well as to retain newly laid ECM by the cells for optimal performance [239].

#### 5.2.1.5. Hollow fibre bioreactors

Hollow fibre bioreactors (HFBs) consist of a fibre (a cylindrical lumen surrounded by a porous wall or membrane) or fibre bundles, contained in an external housing. Cells are most often contained in the extracellular compartment with medium flow through the lumen to transport nutrients and gas through the membrane via diffusive and convective transport. In this way, cells are immunoisolated and protected from shear stress, whilst mass transfer is improved within the device compared to static culture. However, different HFB designs have been previously employed dependent on the application.

HFBs have been widely used in the early development of bioartificial liver devices (BALs) which have progressed through to clinical trials. Devices such as the Extracorporeal liver assist device (ELAD, Amphioxus technologies) [268] and Bioartificial liver support system (BLSS, Excorp medical) [269] have utilised human cell line and porcine cells respectively, cultured in the extracapillary space (ECS) of the bioreactor. Other devices such as the HepatAssist (Circe biomedical) [268] utilised porcine aggregates attached to microcarriers within the fibre lumen. This set-up has allowed direct interaction between the cells and the perfusate (Plasma), although it has removed the immunological barrier [269]. The results of these phase I and II trials were largely positive and the treatment was well tolerated by patients. However, improvements on the design have been further investigated. Multi-compartmental devices consisting of interwoven hollow fibres have been devised to mimic the physiological environment of the liver more closely. Counter current medium perfusion and gas supply is provided in the fibres with human hepatocytes cultured in the ECS. This bioreactor design has been used in both the clinical setting [270] and pharmacological applications as a scaled down *in vitro* model [271]. For the engineering of blood brain barrier (BBB) models HFBs have also been

utilised to co-culture brain endothelial and glial cells on the lumen and ECS sections respectively. Perfusion of medium through the lumen exposes the endothelial cells to shear stresses mimicking the conditions in the brain capillaries resulting in tight monolayers with improved barrier function, with cells able to remain in culture for 30 days [272][273]. The modelling of HFBs for bone tissue engineering [274] and culturing skin cells [275] has also been investigated. However, alongside BALs HFBs have been the primary bioreactor type for the development of BAK devices.

**Table 18:** Properties of bioreactors used in tissue engineering. Images modified from [239]

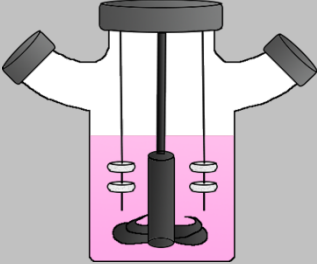
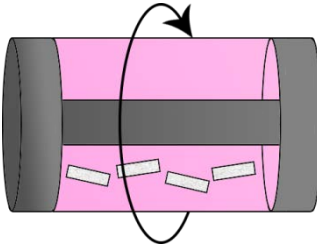
Bioreactor	Advantages	Disadvantages	Applications	References
<p><b>Stir tank bioreactor/ Spinner flask</b></p> 	<p>Enhanced fluid transport Reduction in the concentration boundary at the construct surface Controllable shear within the flask Easy to scale up</p>	<p>Poor mass transfer when applying to static scaffolds Non-homogenous distribution of cells in the scaffold Perception that high shear stress can have damaging effects of cells</p>	<p>Cell cultivation on scaffolds (Cartilage, Bone) Cell expansion (MSCs) Spheroid formation</p>	<p>[239][243] [245][247] [248][276]</p>
<p><b>Rotating wall bioreactor</b></p> 	<p>Enhanced fluid transport Produces a low shear microenvironment More homogenous distribution of cells than static culture</p>	<p>Common for scaffolds to collide with other scaffolds or the sides of the vessel Low, non-controllable shear microenvironment</p>	<p>Cell cultivation on scaffolds (Chondrocytes, Cardiomyocytes, Tumour cells, Bone, MSCs)</p>	<p>[239][248] [250][251] [252][253] [254][255] [256]</p>

Table 18 continued:

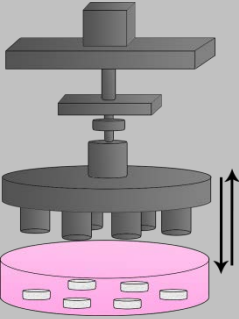
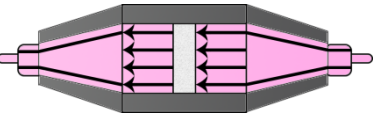
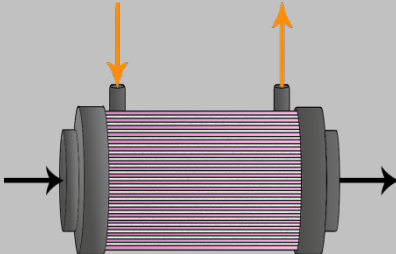
Bioreactor	Advantages	Disadvantages	Applications	References
<p data-bbox="232 448 510 533"><b>Compression/ Strain bioreactor</b></p> 	<p data-bbox="636 584 1048 655">Application of loading similar to physiological stimuli</p> <p data-bbox="658 671 1025 746">Fluid flow and mass transfer improved</p>	<p data-bbox="1162 584 1520 655">Direct attachment of the construct to the bioreactor impedes cell differentiation</p>	<p data-bbox="1632 584 1845 655">Cell cultivation on scaffolds</p> <p data-bbox="1632 671 1845 791">(Cartilage, Bone, MSCs, Chondrocytes)</p>	<p data-bbox="1890 584 2033 611">[245][257]</p> <p data-bbox="1890 627 2033 654">[258][259]</p> <p data-bbox="1924 670 2000 697">[277]</p>
<p data-bbox="232 919 510 946"><b>Perfusion bioreactors</b></p> 	<p data-bbox="624 967 1061 1038">Higher cell density achieved than in other bioreactors</p> <p data-bbox="640 1054 1046 1126">Mechanical stimulation (shear) from fluid flow</p> <p data-bbox="624 1142 1061 1262">Reduction in mass transfer limitations at construct periphery and within the scaffold</p>	<p data-bbox="1144 967 1543 1086">Perception that high shear stress can have damaging effects of cells</p> <p data-bbox="1144 1102 1543 1214">Fluid flow and shear may disrupt the microenvironment within the scaffold</p>	<p data-bbox="1632 967 1845 1038">Cell cultivation on scaffolds</p> <p data-bbox="1632 1054 1845 1262">(Bone, Keratniocytes, Hepatocytes, Cardiomyocytes, Chondrocytes)</p>	<p data-bbox="1890 967 2033 994">[239][260]</p> <p data-bbox="1890 1010 2033 1037">[261][262]</p> <p data-bbox="1890 1053 2033 1080">[263][264]</p> <p data-bbox="1890 1096 2033 1123">[266][267]</p>

Table 18 continued:

Bioreactor	Advantages	Disadvantages	Applications	References
<p data-bbox="215 448 528 475"><b>Hollow fibre bioreactor</b></p> 	<p data-bbox="663 448 965 523">Mechanical stimulation (shear) from fluid flow</p> <p data-bbox="707 539 920 566">Easy to scale up</p> <p data-bbox="629 582 999 657">Cells can be protected from shear</p> <p data-bbox="707 673 920 748">Potential for immunoisolation</p> <p data-bbox="629 764 999 839">Efficient surface area for cell attachment</p>	<p data-bbox="1088 448 1458 491">Non-uniform cell distribution</p> <p data-bbox="1088 496 1458 619">Fibre membrane can act as a physiological transport barrier</p> <p data-bbox="1088 635 1458 758">Large nutrient, metabolite, pH and pO<sub>2</sub> gradients can occur along the fibre</p> <p data-bbox="1088 774 1458 799">Difficult to monitor <i>in situ</i></p>	<p data-bbox="1536 448 1850 523">Cell expansion (skin cells)</p> <p data-bbox="1536 539 1850 662">Bioartificial liver devices (ELAD, BLSS, HepatAssist)</p> <p data-bbox="1536 678 1850 753">Bioartificial kidney devices (RAD)</p> <p data-bbox="1536 769 1850 844">Model systems (Blood brain barrier, kidney)</p> <p data-bbox="1536 860 1850 887">Bone tissue engineering</p>	<p data-bbox="1890 448 2040 491">[239][245]</p> <p data-bbox="1890 496 2040 539">[268][269]</p> <p data-bbox="1890 544 2040 587">[270][271]</p> <p data-bbox="1890 592 2040 635">[272][273]</p> <p data-bbox="1890 639 2040 683">[274][275]</p> <p data-bbox="1890 687 2040 730">[278]</p>

### 5.2.2. Existing bioartificial kidneys

One of the first BAKs to assemble both an ultrafiltration device and a unit containing semi-permeable hollow fibres seeded with renal PTCs was described by Aebischer *et al* in 1987. MDCK and LLC-PK1 cell lines were cultivated on an acrylic copolymer and polysulfone fibres until confluency (within three weeks on the acrylic copolymer), and showed distinct differentiated morphology depending on the chemical and physical properties of the polymers. This was thought to influence the ability of the cells to perform specialised tasks [9]. Further work by the same group investigated the effects of attachment substrates on cellulose nitrate membranes, the age of the cells on glucose transport and the transport of inulin, PAH and glucose through confluent membranes of MDCK and LLC-PK1. They showed that cells cultured on Matrigel were the best performing with regards to glucose transport. Active transport of the solutes was exhibited by the cell monolayer and the net glucose flux across the LLC-PK1 monolayer increased with the age of the cells [279]. The control of water flux within the BAK was also investigated by looking at the effect of transmembrane pressure (TMP) on cell morphology and the influence of cells on the hydraulic permeability ( $L_{(p)}$ ) in a flow chamber. Asymmetric fluid transport occurred on the seeded membranes in the basolateral to apical direction, with the  $L_{(p)}$  being reduced on cell seeded membranes 3-10 fold compared to the cell free membranes. The cell seeded membranes were also found to be strongly dependent on TMP, with a higher TMP resulting in a higher  $L_{(p)}$ . However, the magnitude of the applied TMP had no effect on the  $L_{(p)}$  on cell free membranes. The application of shear rates between 2.6 and 10.5  $\text{sec}^{-1}$  did not have an effect on  $L_{(p)}$  or cell attachment. Furthermore the application of TMP in the apical chamber had a positive effect on cell morphology, with the maintenance of their squamous morphology, whereas cells became more columnar with increased intercellular space in the reverse direction [10].

BAKs were then developed for clinical use as renal replacement devices to surpass conventional dialysis methods. Where haemodialysis simply filters the blood which is then replenished with an electrolyte balancing solution before administering back into the patient, BAKs were additionally thought to provide the excretory and metabolic functions of the kidney through renal PTCs. The renal assist device (RAD) coined by

Humes *et al* (2004) was the first BAK device to be tested in a Food and Drug administration (FDA) approved trial (Figure 1a). Similarly to the device designed by Aebischer *et al* (1987) the extracorporeal device consisted of a standard haemofiltration cartridge combined with a pronectin L coated hemofiltration cartridge inoculated with ( $10^8$ ) cells. In pre-clinical studies using several large animal models including various canine and porcine models [280][281][282][283], BAKs were shown to effectively replace the filtration, transport, metabolic and endocrinologic functions, and have measurable effects on circulating mediators of inflammation whilst improving cardiovascular performance associated with changes in cytokine profiles. From these positive outcomes the RAD was then tested under phase I/IIa clinical trials in patients suffering from acute kidney injury (AKI) and multiple organ failure (MOF). Although the cells within the RAD demonstrated differentiated metabolic and endocrinologic activity and the 28- day mortality rate was improved by 27%, the phase IIb trial was halted due to suboptimal clinical protocol design and fabrication and manufacturing hurdles [278]. Furthermore the clinical trial has drawn some criticism noting: the lack of documentation on the expected effect size, the incomplete treatment of patients assigned to continuous veno-venous haemofiltration and RAD treatment and the lack of statistical significance of the primary results with comparisons performed as an as-treated rather than an as-randomised intention-to-treat sample [284].

The promising results from the clinical trials prompted further investigation into various aspects of BAKs such as the hollow fibre membrane material (Table 15), the cell sources and the device design itself. These studies have been aimed both at developing the BAKs for clinical use but also for utilising them in research as potential renal models as a result of flow being thought to be a potent modulator of PTC phenotype [285]. Mammalian cell lines such as MDCK and LLC-PK1 have been previously employed in the development of BAKs for long term use. Although  $\text{Na}^+$  transport was demonstrated in MDCK cultures for two weeks [286] and LLC-PK1 cells actively transported water, sodium and glucose for 10 days, transport deteriorated after this period alongside cells forming multilayers within the device [287]. hPTCs have therefore been used as the primary source of cells in BAK development, although recent studies have investigated the potential of the differentiation of human embryonic stem cells into renal epithelial like cells (described in

Section 3.2.2.). BAK designs have also evolved for both research and clinical purposes. The emergence of microfluidic devices and the development of 'Kidney on a chip' devices are addressing the need for simple and reliable 3D *in vitro* models (Figure 1b). These devices utilise either hollow fibres [288] or membranes for cell culture assembled within a PDMS body, and have a significantly smaller footprint than the haemofiltration cartridges used previously. The application of medium exerting  $0.2 \text{ dyn/cm}^2$  (tubular shear stress is estimated in the range of  $0.2\text{-}20 \text{ dyn/cm}^2$ ) through the channel seeded with cells has shown improved results in cytoskeletal protein, tight junction protein, ion transporter and drug transporter (*e.g.* OCT2) expression compared to the static models. Furthermore exposure to nephrotoxic compounds has shown the ability of the microsystem to recapitulate the *in vivo* toxicity of the drugs [289][14]. However, the development of these devices is at an early stage and requires further optimisation. The functional characterisation of clinically relevant drug transporters should be investigated to establish an ideal *in vitro* model system.

A new generation of BAKs for clinical use has been developed, characterised by a more compact design and the ability to be cryogenically frozen and stored as described on Section 1.1.(Figure 1c). BRECS incorporates niobium coated porous carbon discs coated with collagen IV for cell culture, with the therapeutic dose set at  $10^8$  in a perfusion bioreactor. After cryopreservation a 10% loss in viable cells was reported for the device. Flow rates were optimised to provide adequate nutrient and oxygen delivery and cells were maintained in the BRECS for over 5 months, with a consistent metabolic profile throughout the *in vitro* culture and the presence of differentiated apical membrane enzymes. Pre-clinical testing in a porcine model with acute renal failure demonstrated therapeutic efficacy and prolonged survival time alongside improved cardiovascular performance. These initial results are promising and the reduced footprint of the device compared to the RAD is favourable in terms of handling, shipping and storage [15]. The major advantage of this system is the ability to cryogenically freeze and reconstitute the device allowing it to be used in time-critical situations in the clinic.

### 5.2.3. Engineering a hollow fibre bioreactor

The development of bioreactors require a multidisciplinary approach, therefore when designing the system many engineering concepts need to be understood to be able to accurately model and develop systems suitable for cellular applications. These are especially important in the development of HFBs as monitoring parameters such as concentration gradients, pH and  $pO_2$  cannot be measured directly due to the size and design of the device. Some important aspects to consider are described below.

#### 5.2.3.1. Fibre geometry and fluid dynamics

Many groups have utilised the Krogh cylinder approximation of HFBs when developing numerical models. This model views the fibres in an idealised hexagonal arrangement within the casing [242]. The cylinder consists of a lumen, membrane and extracapillary space, with one fibre being representative of the entire bundle (Figure 42). The flow through the membrane and ECS is mostly neglected in modelling axial flow HFBs when the pressure drop across the membrane or ECS is not significant. Flow through the lumen can therefore be described by Poiseuille's law [290]. In closed shell configurations of HFB systems *i.e.* when there is no net convective flow from the lumen to the ECS, the axial pressure drop causes the lumen pressure to be greater than the ECS in the first part of the device. At the end of the fibre the reverse is true, and the resulting pressure profile causes a recirculation flow (analogous to the Starling recirculation flow in capillary tissue systems), where fluid flux out of the lumen to the ECS is balanced by flux into the lumen at the end of the fibre [291]. However in models assuming significant permeation through the membrane, Navier-Stokes equation and/or Darcy's law have been used [291][292][293]. These laws apply to laminar (smooth) flow through the lumen, which is commonly seen in small scale bioreactors, but must be considered in the case of turbulent flow which can occur during cross flow microfiltration with porous membranes or when scaling up the device [294]. When cultivating cells, especially those sensitive to shear within the device, the shear stress exerted on the wall should be considered. Shear stress can be calculated using the Poiseuille- Hagen equation. A longer fibre equates to a greater pressure drop, resulting in the need for an increase in flow rate to provide a defined shear stress on the cells throughout the device. However, high

flow rates exert shear stresses which may be damaging to the cells or remove them from the surface [295].

### *5.2.3.2. Mass transfer*

When culturing cells in HFBs, it is important to assess substrate mass transfer within the device. Large concentration gradients along the fibre have been identified as one of the major flaws in HFB design, with simulations demonstrating that diffusion limitations may exist at the far end of the reactors [296]. Many groups have therefore modelled various substrate transport profiles within HFBs, the most common being oxygen which is considered as the rate limiting nutrient. Oxygen consumption also varies between different cell types, and as such models have been developed for bone tissue [292][297], hepatocytes [298][299][300][301][302][303][304], cardiomyocytes, pancreatic cells and chondrocytes [290]. Michaelis-Menten kinetics are commonly used to model oxygen uptake, capturing the dependence of uptake on the underlying concentration. However due to the non-linear nature of Michaelis-Menten kinetics numerical solutions alongside analytical solutions have been described in literature. A strategy to address this problem has developed operating parameters dependent on oxygen consumption by different cell types; with analytical approaches being used for high oxygen requirements within the device, and numerical solutions required for low oxygen requirements [290]. Modelling of other substrates required for cell growth such as glucose have also been developed and applied with oxygen uptake models [292]. Collectively, these models provide useful information on the design and optimisation of HFBs for different cell types. These models have not, as of yet been applied to renal cell culture within small scale devices as required within the pharmaceutical sector, although microfluidic devices are being developed. This therefore highlights an important optimisation step to be implemented in the development of BAKs for widespread use within the industrial setting.

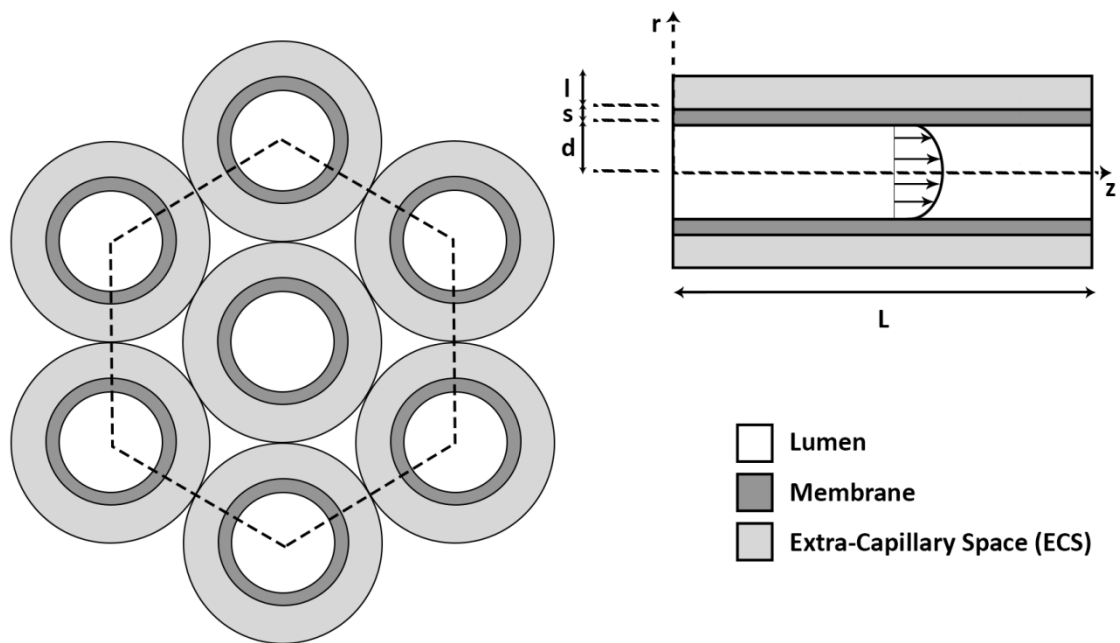


**Figure 42:** The idealised hexagonal arrangement of the fibre bundle comprised of seven Krogh cylinder units (left) and a cross section through one fibre including the fluid velocity profile in the lumen (right).  $L$ = fibre length,  $z$ = axial direction of flow,  $d$ = radius of the lumen,  $s$ = membrane thickness,  $l$ = depth of the ECS and  $r$ = radial diffusion. Modified from [290]

#### 5.2.4. Conclusion

A wide variety of bioreactors are utilised in tissue engineering applications as they can create environments for cell culture similar to the physiological environment. In terms of BAK device generation, hollow fibre bioreactors have been intensively studied in the past with various cell types, mostly for the generation of RRTs. Current iterations of these devices have incorporated perfusion bioreactors for the scale down of these systems for both clinical and research model end points. This chapter aims to add to the existing wealth of knowledge by incorporating the characterised hPTCs on the developed membrane for the cultivation of cells in the HFB. The metabolic activity of the cells throughout the culture period will be assessed with the aim of generating a complete monolayer of cells, which can be characterized using the assays previously utilised as a comparison between 2D and 3D dynamic culture. Although computational modeling will not be employed in this project, it is imperative to understand the concepts of mass transfer and fluid flow, and is valuable in the further development of this device.

### 5.3. Materials and methods

#### 5.3.1. Hollow fibre production

Based on polymer selection studies performed in Chapter 4, the PSF+PVP dope solution was further employed for hollow fibre production in a rig using a custom spinneret (University of Bath, UK) of approximately 700 $\mu\text{m}$  bore size (see Figure 43). Three separate batches were produced using different pressures and bore fluid water flow rates (see Table 19). Once the fibres were produced and, collected they were immersed in deionised water for 3 days with daily water changes in order to remove any impurities and traces of reagents.

**Table 19:** Process parameters and sizes of 3 batches of PSF+PVP hollow fibres

Batch	Pressure	Water flow rate	Mean Inner diameter	Mean Outer diameter
Batch 1	5 bar	8mL/min	656 $\mu\text{m}$	738 $\mu\text{m}$
Batch 2	4 bar	7mL/min	725 $\mu\text{m}$	805 $\mu\text{m}$
Batch 3	5 bar	10mL/min	860 $\mu\text{m}$	995 $\mu\text{m}$

#### 5.3.2. Fibre porosity measurements

The density of the dry fibres was measured using a pycnometer (multi-volume pycnometer 1305; Micromeritics, USA). The fibre sections were then immersed in deionised (DI) water for 2 days to allow complete soaking, followed by straining and lightly drying by gently tapping with filter paper. Then the hydrated fibres were weighed after absorption of DI water and then dried for a week until constant weight was achieved and weighed. The porosity of the fibres from each batch was then calculated using Equation 6 (refer to Appendices 2.6.) [305].

### 5.3.3. Surface topography

Fibre topography was analysed using the JPK Nanowizard 3 Bioscience AFM (JPK Instruments, UK). Fibres from each batch were cut and mounted on glass slides to expose the exterior and luminal sides. Three points on each of the samples were analysed over a 20µm x 20µm sample area and the peak to valley roughness ( $R_T$ ),  $R_a$  and  $R_{rms}$  were calculated.

### 5.3.4. Module assembly, sterilisation and disassembly

Glass casings were autoclaved before use alongside fibres (contained in autoclavable boxes) at 121°C for 15 minutes. After transferring to the BSC, the sterile fibres were placed in the modules and attached vertically to the plastic vial holders. Epoxy resin (Evo-Stik; Bostik Ltd, UK) was applied to the top end of the module and allowed to permeate approximately 1cm into the casing. The modules were then rotated 180° and set overnight. The next day the same method was applied to the other end of the module to seal both sides. The modules were left for 3 days overall to allow the resin to set, and then trimmed to remove excess fibre. The modules were attached to a syringe of sterile filtered DI water, and after flushing water through the lumen the module outlet was blocked. Water was pumped through the lumen at 500nl/min using a syringe pump (PHD Ultra; Harvard Apparatus, USA) overnight to allow water permeation into the pores of the fibre, as well as to remove any remaining impurities. The sample ports and ECS were left unblocked and clear. The module outlets were then unblocked and water was removed from the lumen. Assembled modules were then autoclaved at 121°C for 20 minutes to ensure complete sterility. After use, the modules were autoclaved again for 15 minutes at 121°C. The ends of the modules were then heated using a power Bunsen burner to melt and remove the resin. The modules were allowed to cool down to room temperature and then were soaked in acetone overnight followed by thorough cleaning to remove any residue.

### 5.3.5. Hydraulic permeability

Modules were assembled with a syringe of DI water at the inlet, two pressure gauges (DPI 705; GE Druck, UK) connected by three way valves and a clip on the outlet. A third

pressure gauge was connected to the top sample port by a T-connector (Fisher, UK) with a clip to block the ECS. Water was flushed through the lumen before blocking the outlet, and the ECS was left open. Both three way valves were opened and all the pressure gauges were set to zero. The pressure within the fibre was increased to approximately 15mbar and then allowed to reach a consistent TMP overnight with DI water pumped in at 500nl/min. On the day of the experiment the ECS was filled with DI water and blocked, the pressure in the fibre was released and all pressure gauges were set to zero. The flow rate of 500nl/min was resumed and applied for 4.5 hours, with water samples collected every 30 minutes. The water samples were weighed and applied into Equations 7 and 8 (see Appendices 2.7. and 2.8.) to calculate the volumetric water flux and hydraulic permeabilities of the fibres. Each module was repeated 3 times and a total of 3 modules were assessed.

#### 5.3.6. Module integrity assessment

Modules were assembled with peristaltic pumps feeding (Dose It; Integra Biosciences Group, USA) into two reservoirs and two pressure gauges (DPI 705; GE Druck, UK) connected by three way valves. With the three way valves closed to the pressure gauges water was flowed for 1 hour at 10mL/min through the modules to wet the fibres. The water was then removed from the lumen circuit and replaced with 100 $\mu$ M LY solution. The valves were opened and the inlet and outlet pressures were recorded. 300 $\mu$ l samples were taken from the reservoirs before closing the valves and leaving the modules to run at 10mL/min. After 24 hours the valves were opened and the inlet and outlet pressures were recorded alongside taking 300 $\mu$ l from the reservoirs. After flowing water through the lumen and at 10mL/min for 1 hour to remove the LY, the modules were autoclaved at 121 $^{\circ}$ C for 15 minutes. The pressure drop measurements and incubation with LY were then repeated.

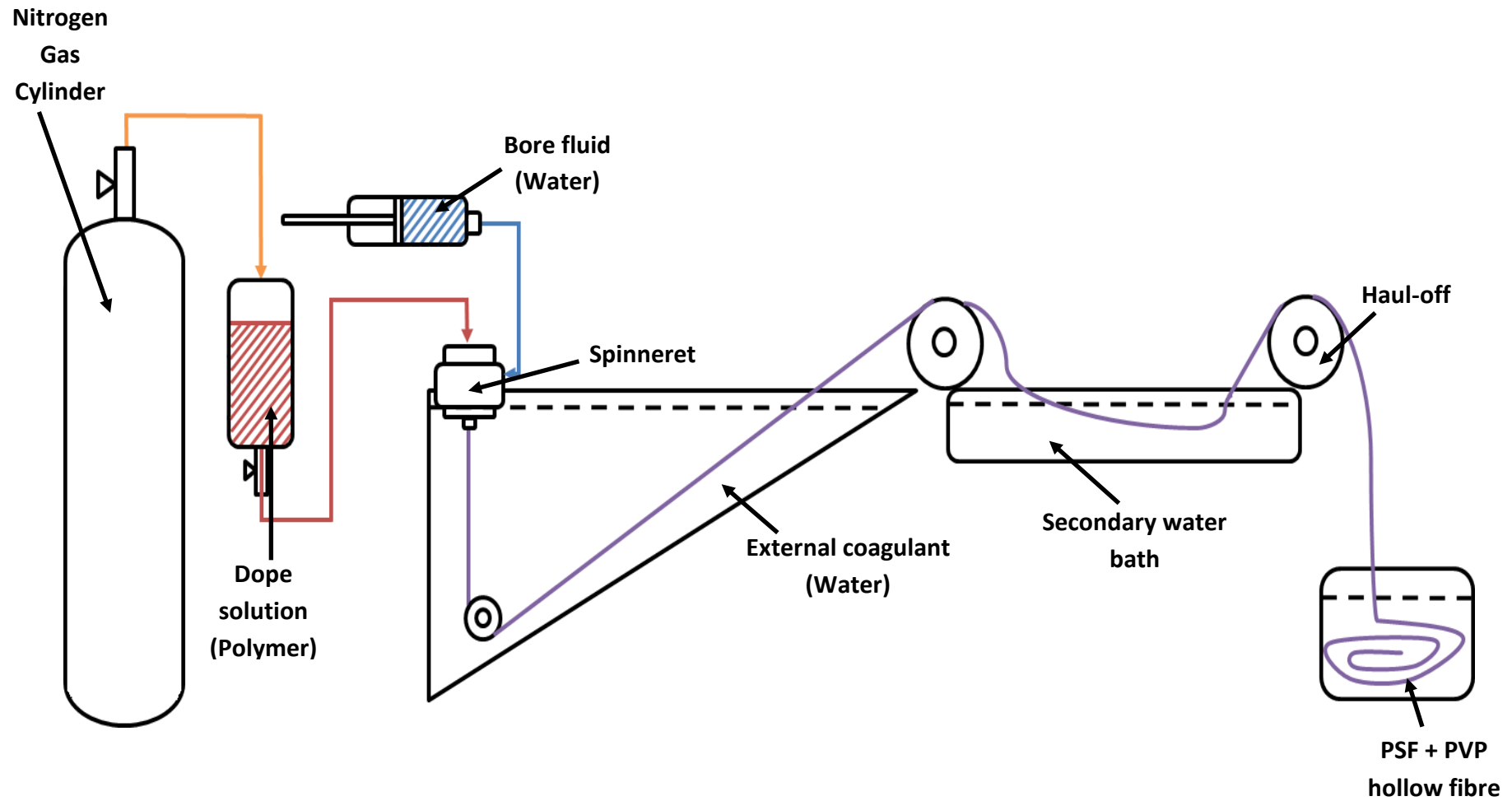


**Figure 43:** Schematic of the extrusion rig used to produce hollow fibres from PSF + PVP dope solution using water as the bore fluid and external coagulant

### 5.3.7. Fibre seeding- static culture

Fibres from each batch were immersed in DI water and autoclaved at 121°C for 15 minutes. After sterilisation, the fibres were cut into 1.5cm pieces with a sterile scalpel and placed in a Corning 24-well ultralow attachment plate (Sigma Aldrich, UK). Three fibre sections from each batch were used. 0.5mL FBS was added to the wells and incubated overnight to condition the fibres by allowing proteins to be adsorbed onto the surface and help facilitate cell adhesion to the fibres. Before cell inoculation, the fibres were washed with RPTEC medium, after which cells were seeded at  $2.3 \times 10^5$  cell/cm<sup>2</sup> and incubated for 2 hours at 37°C. The cell suspension was then removed and the fibres were turned over before dispensing the cell suspension back into the wells. Cells were cultured for 9 days with medium changes performed every 2 days.

### 5.3.8. Cell viability assay- Presto blue

For analysis of cells seeded on the fibres in static conditions, the Presto Blue reagent was added into the wells at a 1:10 dilution and incubated for 40 minutes at 37°C (as described in Section 4.3.8.). Three samples of 100µl were taken from each well and read on a microplate reader (FluoStar Omega; BMG Labtech, Germany) at Ex: 544nm, Em: 590nm and a gain of 1000 measured against a positive and negative control and a medium blank.

For the analysis of cells within the fibres under flow conditions the Presto Blue reagent was diluted in medium at a 1:10 dilution. 0.5mL of the solution was then aspirated into 2.5mL luer lock syringes (Terumo Medical Corporation, USA) and pumped through the fibre lumens at 50µl/min for 8 minutes. The bioreactors were incubated in static conditions for 40 minutes at 37°C in the dark before applying flow through the lumen at 50µl/min for 10 minutes to collect the sample. Three samples of 100µl were taken from each module and measured on the microplate reader at Ex: 544nm, Em: 590nm and a gain of 1000 against positive and negative controls and medium blanks.

### 5.3.9. Cell visualisation- Live/ dead staining

On day 9 of static cell culture on fibres, cells were stained using the live/dead staining kit (Life Technologies, UK). Ethidium bromide (dead stain) was added to PBS at a 1:500

dilution and mixed thoroughly by vortexing in the dark. Calcein-AM (live stain) was then added at a 1:2000 dilution and mixed thoroughly. Medium was aspirated from the wells and fibres were incubated in 0.5mL live/dead stain for 40 minutes at 37°C in the dark before imaging on the Nikon Eclipse Ti fluorescence microscope.

#### 5.3.10. Bioreactor seeding and cell cultivation

Sterilised modules were exposed to a UV cycle on the BSC (1 hour) on both sides before assembling with sterilised (autoclaved) platinum cured silicone tubing (Polymax, UK) and luer locks (Cole-Parmer, UK) as shown in Figure 44. All components were sterilised by autoclaving at 121°C for 20 minutes and exposing to a UV cycle after assembly. The fibre lumens were pre conditioned with FBS overnight at 37°C before rinsing with RPTEC medium. RPTECs at Pd=5 were seeded at  $4.38 \times 10^5$  cells/cm<sup>2</sup> and rotated 90° every hour for 4 hours to allow cell attachment to the fibre. The ECS was left clear and cells were incubated for 2 days under static conditions at 37°C. The ECS was then filled with RPTEC medium and the module was connected to 20mL syringes (Terumo Medical Corporation, USA). Initially an incubation chamber was assembled to house the modules during culture (Appendices- Figure 67), however, due to problems with CO<sub>2</sub> control the bioreactors were set up in an incubator at 37°C with 5% CO<sub>2</sub>. RPTEC medium was pumped through the lumen and ECS at 50µl/min for 6 hours, after which the bioreactors were transferred to the BSC to replace the medium from the bottle (Eppendorf, UK) back into a new syringe. Every 2 days the medium was removed from the reservoirs and replaced with fresh medium after the Presto Blue assay. Cells were cultured for 9 days (including the static incubation period). Tube lengths and fittings sizes are described in detail in Table 20.

#### 5.3.11. Spent medium analysis

To assess nutrient and metabolite concentrations of RPTECs within the device, 2mL of spent medium was aspirated daily and frozen until analysis. Samples (1mL) were run on the Cedex Bio HT Bioprocess analyser and glucose, lactate and ammonium concentrations were measured.

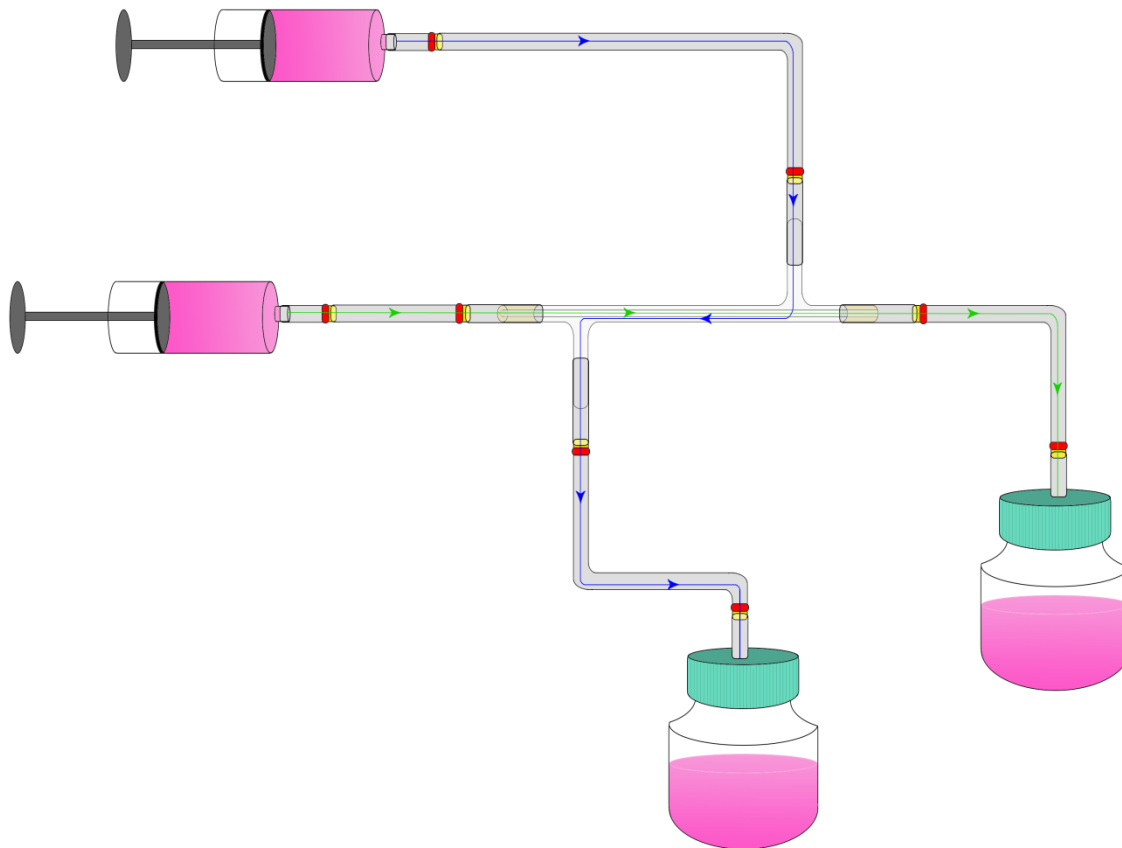


**Figure 44:** Schematic of the bioreactor layout incorporating medium flow through the ECS (blue) and lumen (green) (left) at a  $50\mu\text{l}/\text{min}$  flow rate in both flow paths. An image of the device setup in the incubator (right) shows the medium reservoirs in front of the modules with the pump for the ECS circuit on top and the pump for the lumen loop on the bottom left. Every 2 days medium was removed from the reservoirs and replaced with fresh medium in the syringe and reservoirs for each circuit.

**Table 20:** Components used in the assembly of the HFBs

Component	Description	Size/ Length	Manufacturer
<b>Silicone tubing</b>	Connection between the luer locks and module/syringe	2cm	Polymax, UK
	Connection from lumen port to medium reservoir	15cm	
	Connection from syringe to ECS port	40cm	
	Connection from ECS port to medium reservoir	20cm	
<b>Luer fittings</b>	Male luer lock to barb connector	1/16 inch ID	Cole-Parmer, UK
	Female luer lock to barb connector	1/16 inch ID	
	Luer lock caps	-	
<b>Syringes</b>	20 mL medium syringes	20mL	Terumo medical corporation, USA
	2.5mL luer lock syringes for cell seeding and Presto Blue assay	2.5mL	
<b>Medium reservoir bottles</b>	100mL glass bottles. Cap attached to autoclavable air filter and line into bottle	100mL	Eppendorf, UK

## 5.4. Results

### 5.4.1. Fibre structure after sterilisation

Fibres were sterilised by autoclaving and imaged on the outer side, lumen side and cross section. As damage occurred during preparation of the flat sheet membranes for imaging by slicing (Section 4.4.5.), fibres were pulled apart until breaking and attached to the carbon pad. The outer and lumen surfaces displayed a smooth surface with the absence of visible pores. This concurs with the images of the top side of the flat sheet membranes as water was used for the bore fluid and gelation bath during fibre production, allowing fast evaporation of solvent and producing a smooth surface. Batch 1 fibres show the most uniform fibre wall thickness of  $\sim 82\mu\text{m}$  (Figure 45c). However, the structure within the fibre wall was vastly different to the other batches. The structure is less organised with round macrovoids between the exterior and the lumen and small cubical voids closer to the edges of the fibre. This irregularity could be due to both different rates of solvent evaporation within the fibre and the non-uniform dispensation of the dope solution from the spinneret.

Batch 2 fibres displayed a mean wall thickness of  $80\mu\text{m}$ , however the thickness around the fibre drastically varied (Figure 45g). The mean thicknesses of the thinner and thicker sides were  $63\mu\text{m}$  and  $122\mu\text{m}$  respectively. A lower pressure and slower water flow rate was used in the fibre production, which may have resulted in the coagulated fibre in the gelation bath pulling the newly forming fibre, therefore distorting the shape of wall. The fibres did however show a similar structure within the wall to those observed in the flat sheet membranes *i.e.* finger like macrovoids with pores in the dividing structures. Batch 3 fibres also showed this characteristic structure, although the dividing sections of the macrovoids were thicker (Figure 45k). The mean thickness of the membrane was  $135\mu\text{m}$ , although there was some variation around the fibre wall and along the length of the fibre. Due to the increased water flow rate the lumen side would be smoother due to the faster rate of solvent evaporation compared to the other fibres. However, no differences in structure were observed on the lumen side between any of the fibres at 5K magnification.

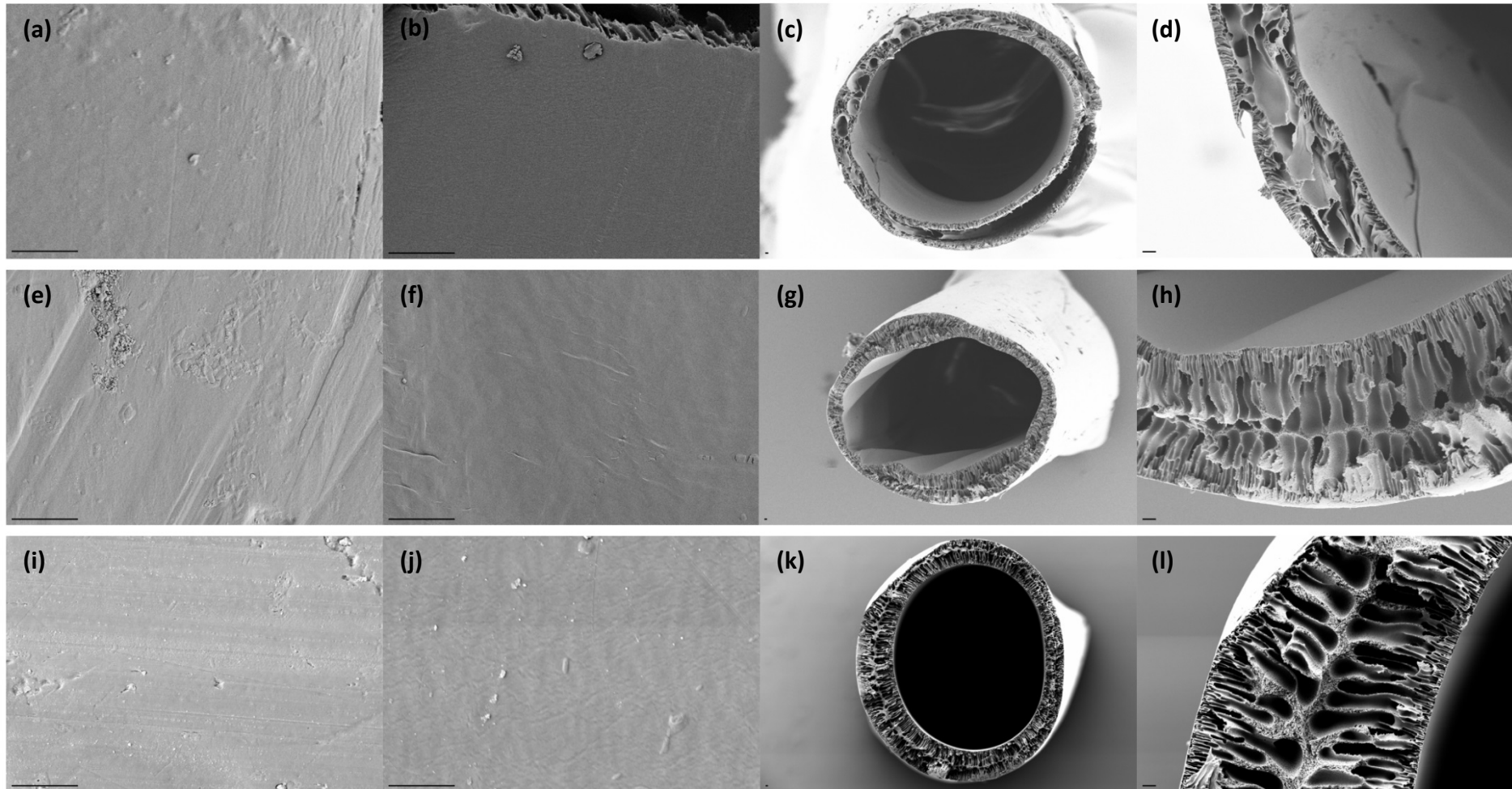


**Figure 45:** SEM images of the PSF+PVP hollow fibres: Batch 1 (top row), batch 2 (middle row) and batch 3 (bottom row) outer sides (a, e, i), lumen sides (b, f, j) and cross sections (c, d, g, h, k, l). Magnifications at 5K were used for outer and lumen side imaging, and 200 (c, g, k) and 1K (d, h, l) magnifications were used for the cross sections. Scale bars = 10 $\mu$ m

### 5.4.2. Physical characteristics of the fibres

As seen in the images (Figure 45c), batch 1 fibres displayed the lowest and relatively consistent thickness of all the fibre batches. Batch 2 fibres displayed a similar value (within the error range) to batch 1 fibres, although the variability was higher. As seen in Figure 45g this was due to the fibre containing different wall thicknesses around the circumference of the fibre which was observed throughout the batch. Due to the fragility and variation within the batches of fibre integrity, the hydraulic permeability could not be determined. Batch 3 fibres had the thickest wall, which allowed the hydraulic permeability to be measured. As the porosity of the batch 3 fibres was the lowest of all the batches, the water flux was also expected to be lower. When compared to initial results from batch 2 fibres (Appendices- Table 22) the water flux was similar in both batches. However the consequent hydraulic permeability was ~35% lower in batch 3 fibres than batch 2 fibres owing to a larger TMP within the larger fibres.

The surface roughness of the fibres was also investigated. Batch 2 fibres exhibited the best growth of RPTECs over 8 days (See Section 5.4.5.- Figure 49) and displayed the mid  $R_{rms}$  and lowest  $R_a$  values. Batch 3 fibres, which exhibited poor RPTEC performance, had the lowest and highest average  $R_a$  and  $R_{rms}$  values respectively. However batch 3 fibres also displayed the highest average exterior  $R_T$  values, indicating that peaks and troughs may have been present on the surface resulting in large variability in average roughness. The  $R_{rms}$  and  $R_a$  lumen values for batch 2 and 3 fibres were similar to the exterior batch 2 values, although the  $R_T$  values were lower in batch 3 fibres. All batches showed similar surface patterns on the lumen surface as opposed to the exterior surfaces where they varied significantly (Appendices- Figure 68). However, when comparing the values between batches via ANOVA with Tukey *post hoc* analysis, there was no significant difference ( $p \leq 0.05$ ) found between the lumen and exterior of all the batches, indicating that surface topography was not a major factor in cell performance on the exterior of the fibres. Surface roughness has been identified in affecting cell attachment and proliferation within the literature, with varying degrees of roughness beneficially affecting different cell types [306]. However, the effect of surface roughness has not been investigated in renal cells. The physical characteristics are presented in Table 21.

**Table 21:** Physical characteristics of the 3 batches of fibres (Mean value  $\pm$  SEM, n=3)

Fibre Batch	Mean Wall Thickness ( $\mu\text{m}$ )	Surface Roughness (nm)			Porosity (%)	$L_p$ ( $10^9 \text{ Pa m}^3/\text{m}^2\cdot\text{s}$ )
		$R_T$	$R_{\text{rms}}$	$R_a$		
<b>Batch 1</b>	82.13 $\pm$ 6.59	Exterior: 1540 $\pm$ 210	Exterior: 237.13 $\pm$ 13.4	Exterior: 188.43 $\pm$ 5.50	86.66 $\pm$ 0.63	-
		Lumen: 1720 $\pm$ 200	Lumen: 437.83 $\pm$ 52.17	Lumen: 375.17 $\pm$ 45.95		
<b>Batch 2</b>	92 $\pm$ 11.06	Exterior: 1870 $\pm$ 320	Exterior: 265.47 $\pm$ 26.13	Exterior: 214.67 $\pm$ 23.04	83.90 $\pm$ 1.42	-
		Lumen: 1470 $\pm$ 410	Lumen: 260.67 $\pm$ 95.52	Lumen: 205.33 $\pm$ 74.30		
<b>Batch 3</b>	135.38 $\pm$ 14.49	Exterior: 2150 $\pm$ 190	Exterior: 287.03 $\pm$ 25.28	Exterior: 141.65 $\pm$ 70.02	70.10 $\pm$ 1.23	154.84 $\pm$ 8.67
		Lumen: 1270 $\pm$ 180	Lumen: 282.83 $\pm$ 54.71	Lumen: 234.13 $\pm$ 49.62		

### 5.4.3. Module sterilisation

Modules were initially assembled on the benchtop from the fibres and casings, and were sterilised by autoclaving for 15 minutes at 121°C. However, after plating out medium incubated in the module ECS and lumen, floating impurities were visible under the microscope. As it was unclear whether this was a sign of microbial infection, alternate methods of assembly and sterilisation were investigated. Fibres and casings were autoclaved for 15 minutes at 121°C and then transferred to the BSC to be assembled. Modules were either sterilised by soaking the ECS and lumen in 70% IMS for 15 minutes and drying overnight, or pumping with water overnight and then autoclaved for 20 minutes at 121°C. The modules were then incubated with medium overnight before removing and plating in a 48-well plate. After 2 days of incubation, the autoclaved modules did not present with any microbial infection, whereas one of the modules soaked in IMS showed a clear bacterial infection in both the ECS and lumen samples (see Appendices- Figure 69). However, floating impurities could still be seen in all the samples, and although there was slight motility, it was still unclear whether this was due to Brownian motion or due to a microbial infection. Newly assembled modules were sterilised by autoclaving using the same methodology as in the previous experiment and incubated with medium overnight. The medium was then removed and incubated in a 48-well plate as before. The medium was also plated out onto nutrient agar plates using aseptic technique, and both plates were incubated for 7 days. After 7 days, no colonies could be observed on the sample plates from the ECS or lumen, although the floating impurities were still visible under the microscope (Figure 46). The positive control in the 48-well plates showed clear microbial contamination, and the agar plates (inoculated with *E.coli* K-12) showed a lawn of bacterial growth. The floating impurities were therefore thought to be debris from the resin, and the methodology for sterilisation by autoclaving was considered efficient and employed further.

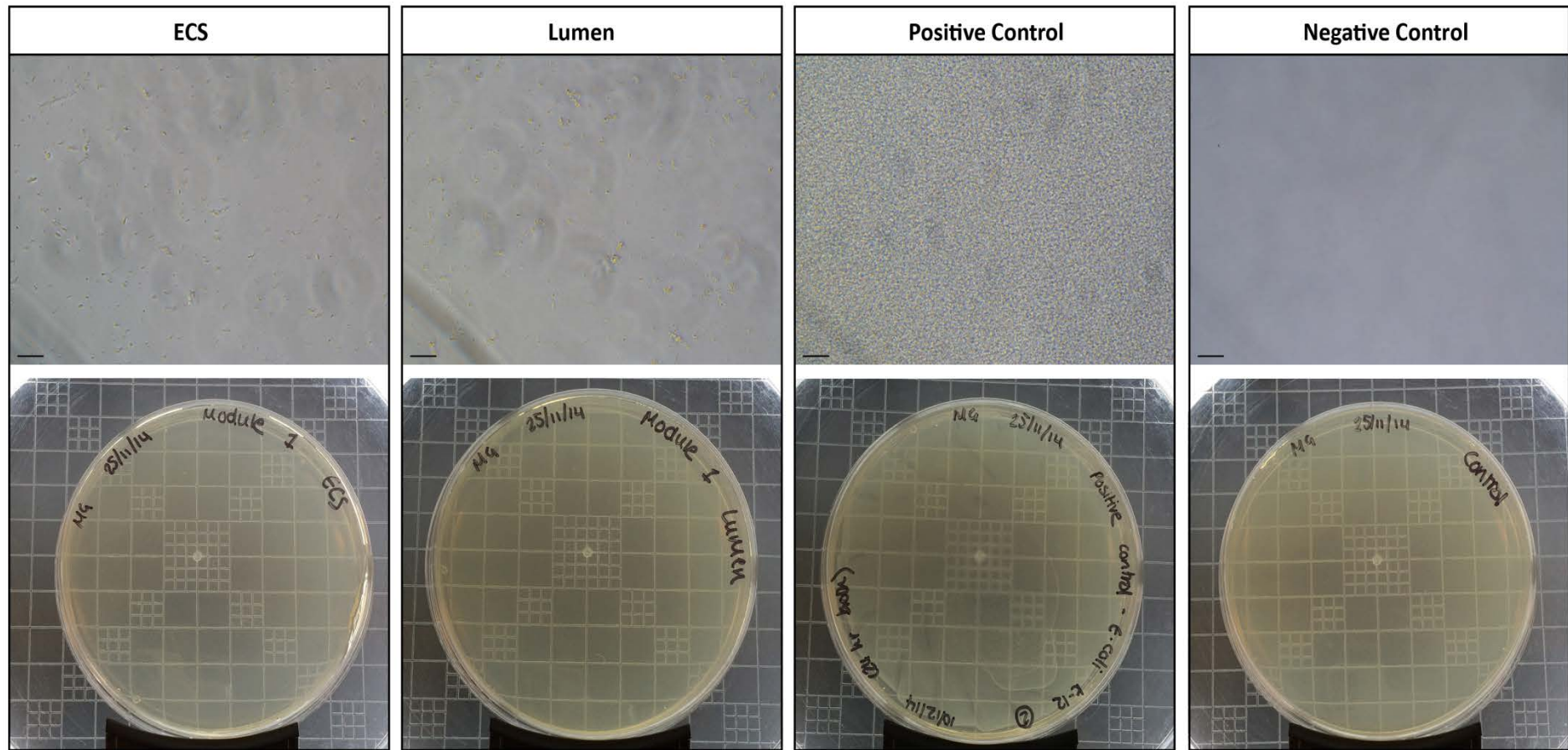


**Figure 46:** Medium samples from modules sterilised by water permeation and autoclaving. Samples were plated in TCP plates and viewed under the microscope at 40x magnification, and on nutrient agar plates and imaged after 7 days incubation. Smear marks can be seen on the positive control showing bacterial lawn, and cannot be seen in any of the other samples. Scale bars = 20µm

#### 5.4.4. Module integrity assessment

For the utilisation of the module as a bioreactor to model substrate transport, the integrity of the fibre itself alongside the epoxy resin seal was assessed (Figure 47). The pressure drop within the fibres did not vary significantly over the 2 hours indicating good fibre integrity before autoclaving. After autoclaving the modules an increase in the pressure drop was observed at both 0 and 24 hour time points, although the increase was not significantly different to the pressure drops seen before autoclaving at the respective time points. This increase could have been due to a change in either fibre surface causing an increase in the friction factor, or a decrease in the internal diameter of the fibre. However, despite the change in pressure drop, the integrity of the modules after sterilisation was maintained. This was further confirmed by the LY permeation percentages, which showed no significant difference in permeation before or after autoclaving.

Although it was possible to assess the module integrity for the intact modules using batch 2 fibres, the variation of the fibres throughout the batch was large with many modules failing. This was either due to fibre breakage or leaks within the fibre appearing after fluid flow, observed by a drop in pressure through the fibre.

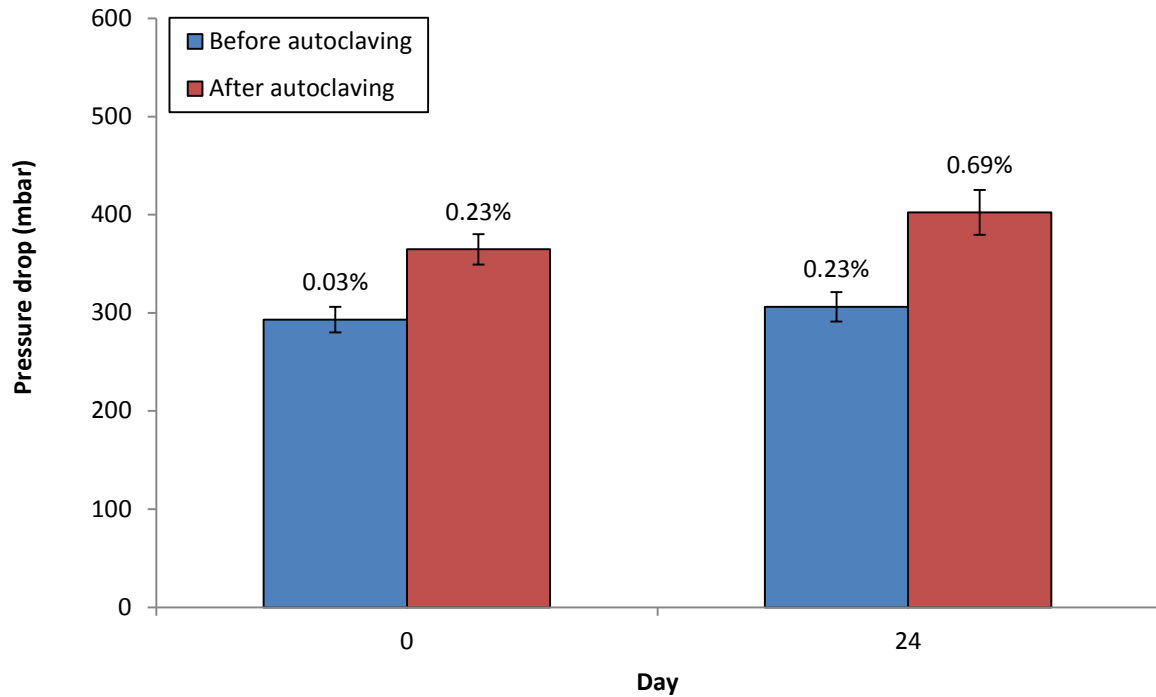


**Figure 47:** The pressure drop across modules incorporating batch 2 fibres at 0 and 24 hours after flow at 10mL/min. The LY permeation from within the fibre through to the ECS is shown as data labels. No significant difference between the pressure drop before and after autoclaving at the respective time points, and between LY permeation was demonstrated. (Mean value  $\pm$  SEM, n=3)

#### 5.4.5. Long term cell viability on fibres in static conditions

Based on results obtained from the short term attachment and viability studies on the polymer membranes (see Section 4.4.7.2.), RPTECs were cultivated in static conditions on each batch of PSF+PVP fibres produced to assess long term performance. The Presto Blue reagent was added directly to the wells at a 1:10 dilution according to manufacturer's protocols and previous protocols, and due to the secretion of factors by the RPTECs required for cell maintenance on the growth substrate. However, this methodology resulted in a large amount of fluorescence on day 2 due to the unattached, but still viable cells alongside the attached cells on the fibres in each well as shown in Figure 48. All batches showed a similar trend in growth and metabolic activity according to the fluorescence, which increased from day 4 to day 6, and declined at day 8. Both the fluorescence values and the equated cell numbers were significantly different on each fibre batch on each day with the exception of day 2 ( $p \leq 0.05$ ). This is again thought to be due to the number of metabolically active unattached cells present within the well. All fluorescence values were also significantly higher than the negative control, indicating the presence of metabolically active cells.

To investigate morphology of cells on the fibres, the cells were stained with a live/dead staining kit. Batch 1 fibres showed a good coverage of cells along the fibre with the least amount of dead cells. However, the cells were elongated and did not appear to form a connected monolayer (Figure 49a-b). Cells cultured on batch 3 fibres performed the poorest, with a vast amount of the fibre showing no cell attachment. The fibres also showed the highest number of dead cells out of the three batches (Figure 49e-f). This could be due to the degradation or dissociation of PVP within the dope solution over time, resulting in a poor cell culture surface after the production of hollow fibres. Cells seeded on the batch 2 fibres performed the best, with a confluent monolayer achieved at day 9. Cells also exhibited dome like formations (Figure 49c), indicative of polarised transporting epithelium.

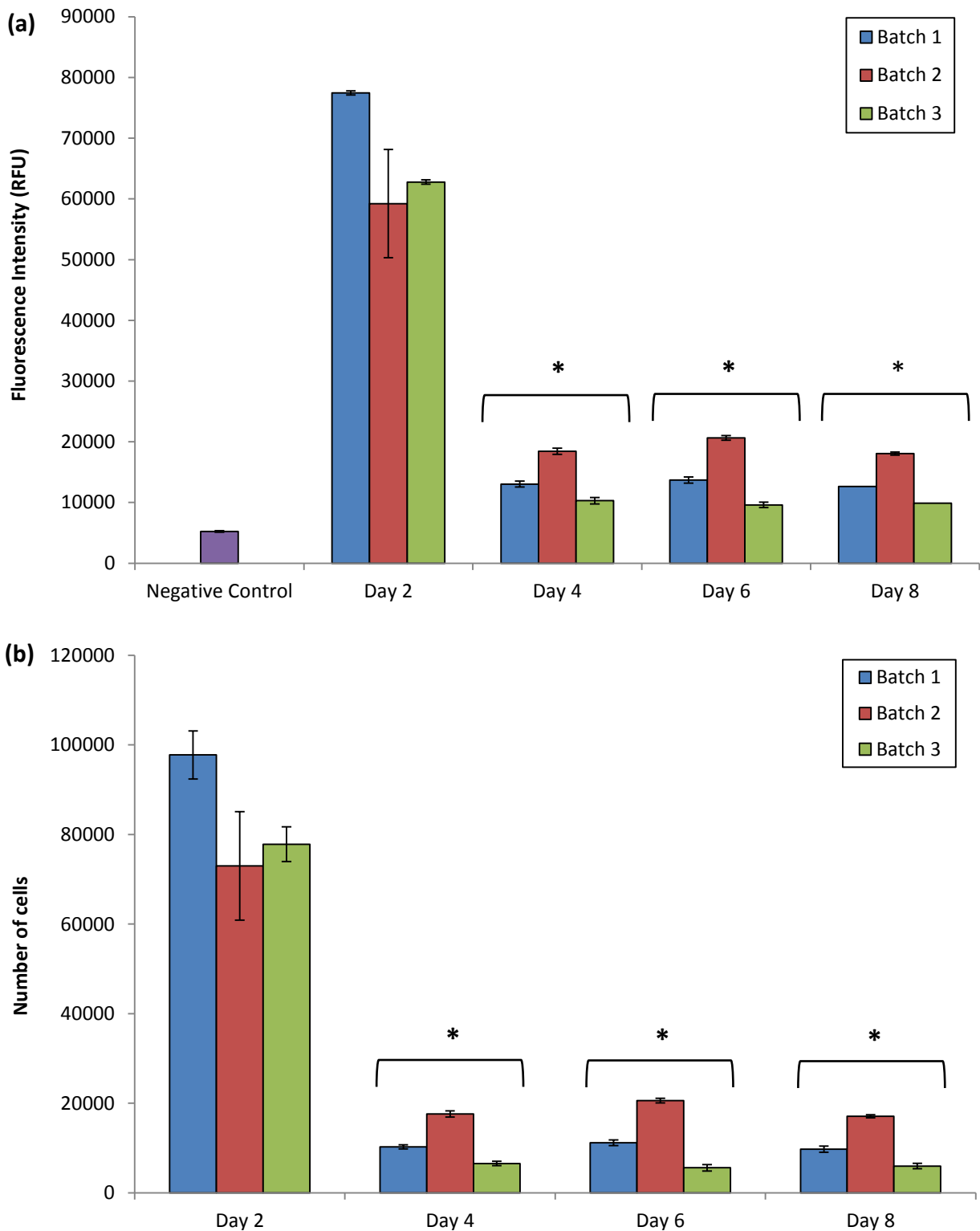


**Figure 48:** The Presto blue reduction by RPTECs on each fibre batch (a) and the cell number on each fibre batch (b) over 8 days in culture (Mean value  $\pm$ SEM, n=3). \* indicates a significant difference between all batches. All fibre batches on each day show a significant increase in RFU compared to the negative control,  $p \leq 0.05$  (ANOVA with Tukey *post hoc* analysis)

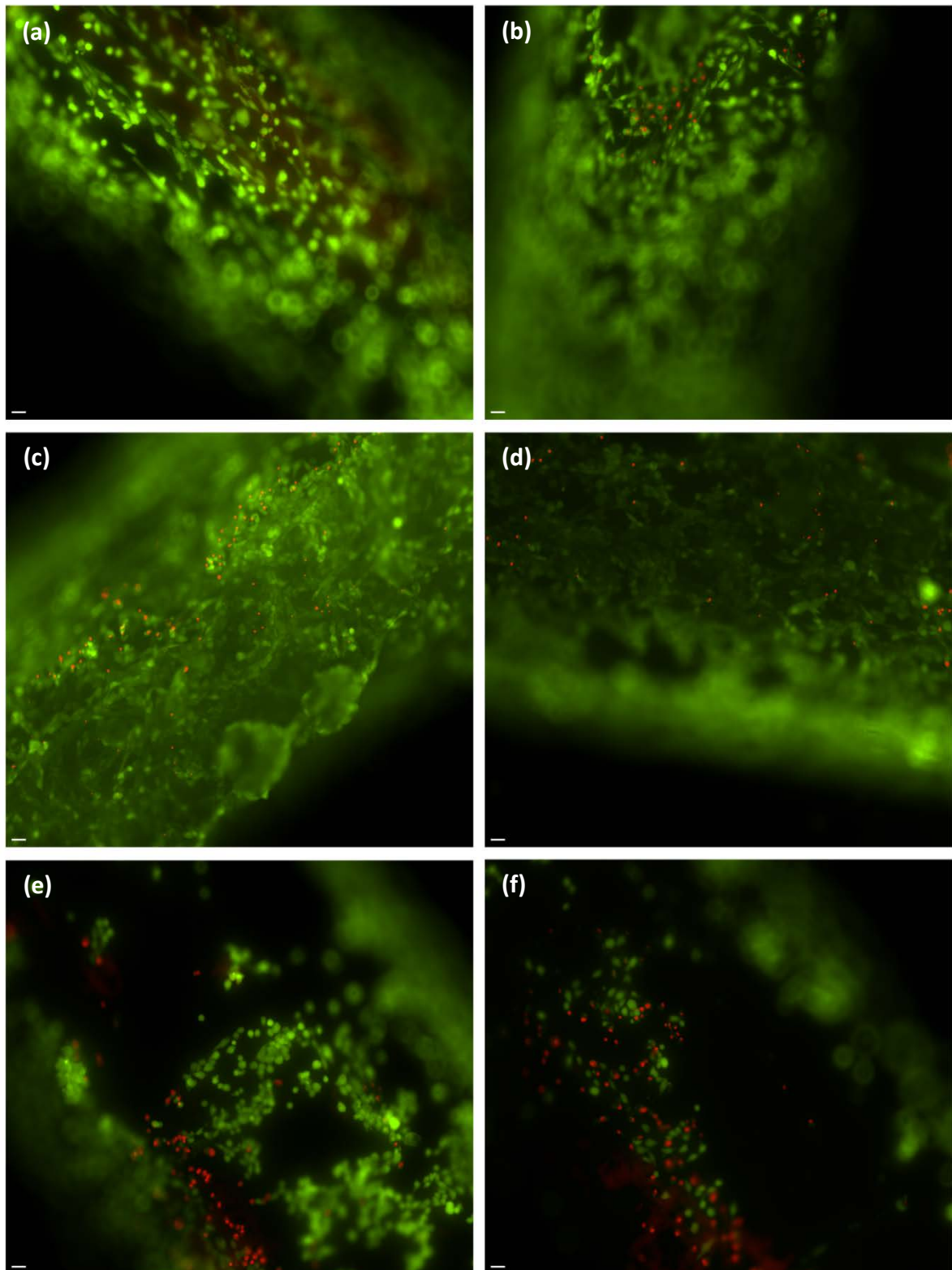


**Figure 49:** Visualisation of viable cells (green) and non-viable cells (red) on the exterior of batch 1 (a)(b), batch 2 (c)(d) and batch 3 (e)(f) after 9 days of RPTEC culture. Scale bar = 10 $\mu$ m

#### 5.4.6. Cell performance in the hollow fibre bioreactors

Throughout the culture period the modules maintained cell attachment and viability as demonstrated by the Presto Blue analysis (Figure 50). The highest number of cells was recorded at day 2 after the static culture period, but depleted over the remainder of the culture period under flow conditions. However, after the initial significant depletion, the cell number remained constant (no statistical significant decrease in cells between the remaining days). The predicted cell numbers over days 4-8 were within the range of  $5 \times 10^3$ -  $8 \times 10^3$ , a mere 0.5%- 0.8% of initial cell seeding. The low cell attachment and metabolic activity within the bioreactors was thought to be due to the leakage of the fibres as tears were detected along the fibre after initial seeding, leading to cell migration into the ECS. This prediction however was not confirmed by nutrient and metabolite analysis (Figure 50b-d). Glucose consumption and lactate production was shown to be higher within the lumen circuit indicating the presence of cells compared to the ECS. Characteristic peaks and troughs were seen every 2 days in lactate production in the lumen due to the complete medium exchange, whereas ECS lactate amounts were constant indicating little metabolite transfer through to the ECS. The glucose consumption and lactate production also corresponded with the cell numbers indicated from the Presto Blue analysis, depleting over the time in culture. The yield of lactate from glucose was  $\sim 0.4$  mol/mol, below the maximum value of lactate production from glucose ( $\sim 2$  mole) [307]. As it is assumed that the culture conditions did not limit the atmospheric oxygen, this indicated that cells were utilising glucose through the citric acid cycle via aerobic respiration. Ammonium production was similar within the lumen and ECS indicating a low rate of amniogenesis, which may have been due to the glutamine concentrations within the medium. However, glutamine concentrations within the samples could not be reliably determined.

Although cell numbers in the bioreactors were low and cell migration due to compromised fibre integrity was suspected but disproved, modules with intact fibres produced improved results. Presto Blue reduction was higher at all days in culture with a decrease from day 2 on days 4 and 6, but an increase back up to the fluorescence exhibited at day 2 on day 8 (Appendices- Figure 70). The nutrient and metabolite data showed a lower amount of glucose and higher amount of lactate within the lumen

circuit, indicating the presence of cells, although the trends did not correlate with the cell numbers indicated by the Presto Blue results as with the previous data. These results are promising, and may have resulted in higher cell numbers with a longer period of culture. However, they could not be reproduced due to the batch variation of the fibres within the batch.

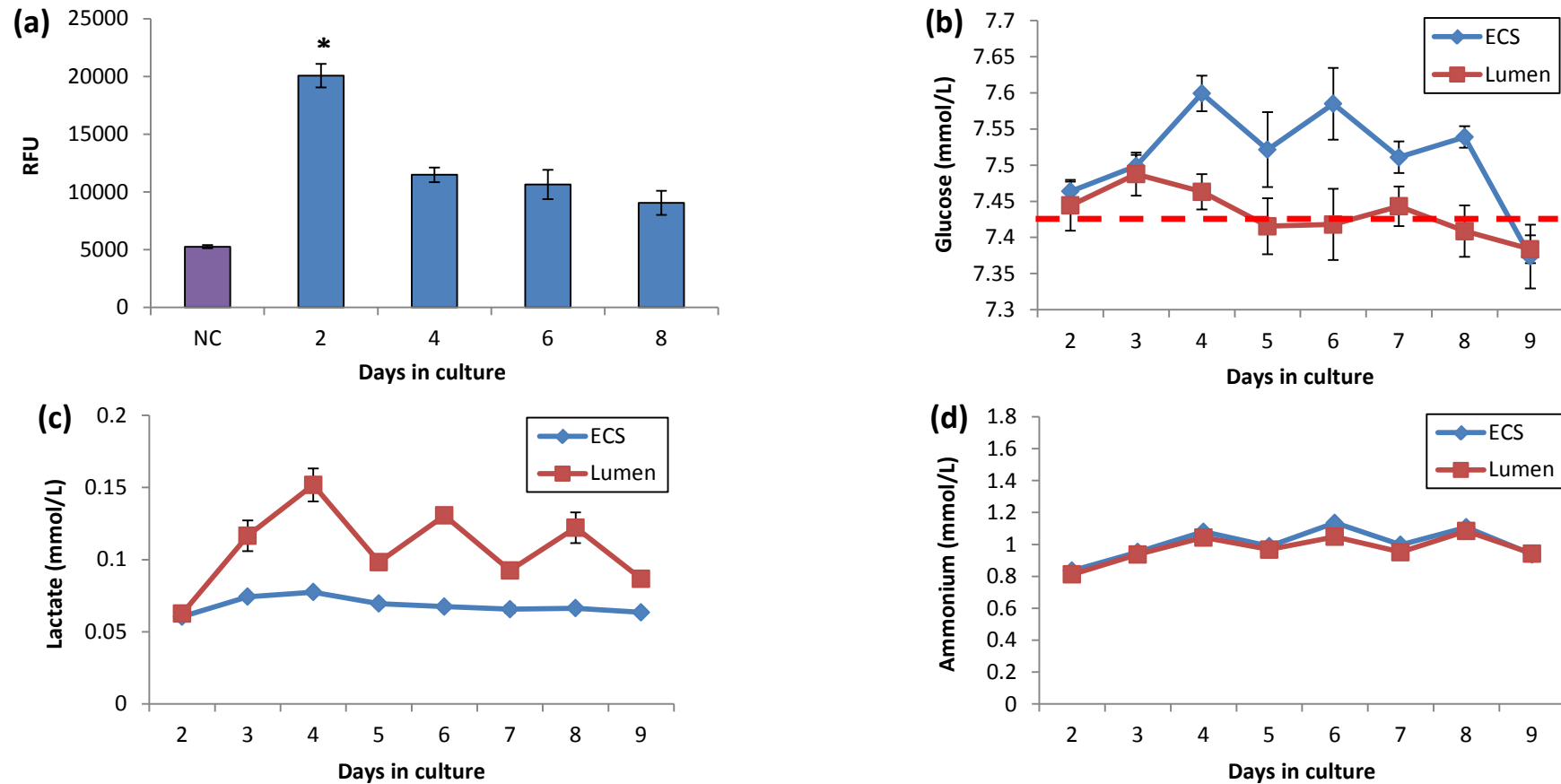


**Figure 50:** (a) The Presto blue reduction by RPTECs in single hollow fibre bioreactors under flow conditions (Mean value  $\pm$  SEM,  $n=3$ ). \* indicates statistically significant difference to rest of the days in culture. All samples on each day show a significant increase in RFU compared to the negative control (NC),  $p \leq 0.05$  (ANOVA with Tukey *post hoc* analysis), (b) the glucose, (c) lactate and (d) ammonium spent medium analysis over 7 days culture under flow conditions (9 days overall). The red dashed line indicates the starting concentration of glucose in the medium

## 5.5. Chapter discussion and conclusion

### 5.5.1. Discussion

This chapter focuses on the generation of a BAK device incorporating tailored PSF+PVP hollow fibres as a renal culture substrate for characterised hPTCs. The assessment of long term RPTEC growth on the exterior of the different batches of fibres generated interesting results. Although all 3 batches of fibre were produced from the same dope solution, they yielded distinctly different results in cell proliferation, morphology and metabolic activity, with the greatest difference between batch 2 and 3 fibres. This finding questions reports in literature stating that PSF+PVP is not a good culture substrate for renal cell culture [181]. Furthermore, the variation between batches of fibres produced from the same dope solution identifies the need for thorough characterisation of polymer membranes when using additives. Aspects such as the bore solution and gelation bath parameters, the purity of the dope solution and degradation of the additive should be thoroughly investigated to ensure consistency between results.

The use of epoxy resin as a sealant after the incorporation of the fibres into the glass casings has also identified some unexpected aspects that had not been reported previously. Small fragments were observed in culture that was not identified in previous assessments of sterilisation on flat sheet membranes. This calls into question the suitability of epoxy resin as a sealant, which has been used previously [238], and the long-term effects of these fragments on cells within the bioreactor.

After incorporation within the HFB, physical characterisation of the fibres is incomplete alongside non-reproducible cell growth and proliferation. This is due to the suspected effects of fibre tearing within the cases. The use of the spinneret method of hollow fibre production and the effects of sterilisation on the fibre integrity should therefore be investigated. The spinneret method produced fibres with varying wall thicknesses in each batch, and as such, physical characterisation of the fibres could not be completed. The sterilisation effects have also not been completely ascertained, and may produce structural changes as has been shown in literature for other scaffolds [237], which may be detrimental. As a result of a lack of fibre integrity, parameters such as  $L_{(p)}$  and TMP could not be ascertained and as such, the effects of these parameters on RPTECs within

the bioreactor could not be reported, as done by Aebischer *et al* [10]. Cell growth, proliferation and metabolic activity could not also be reproducibly reported leading to the incomplete assessment of the device as a whole. However, some of the findings from this chapter are essential in the further development BAK devices as a whole.

### 5.5.2. Conclusion

Bioreactors have been widely utilised throughout the tissue engineering field for the cultivation of a variety of cell types. For the generation of BAK devices, HFBs have been routinely used, as they are able to mimic the native architecture of the PT. The assembly of the device includes a number of design aspects, and as such, various parameters such as fibre generation and properties, choice of sealant and the method and effect of sterilisation have been identified as requiring further investigation from the findings in this chapter. Of notable importance is the difference in cell proliferation and metabolic activity between the fibre batches, drawing importance on the fact that although a key parameter was maintained (the same dope solution), there were vastly different results achieved. Cells however were not able to be reproducibly cultivated successfully within the device due to the time constraints of the project. There are many improvements, which can be made on the device as a whole in the generation of an optimised BAK device as an *in vitro* model for pharmaceutical research, which will be detailed in Chapter 6.

# Chapter 6

**Summary, Discussion, Conclusions and Further  
work**

## 6.1. Summary

The generation of reliable *in vitro* models is paramount in the current climate, where the demand for affordable, efficacious drugs is increasing with an expanding and aging population. The particular emphasis on pre-clinical model development arises from the time and monetary investments in bringing a new drug to market, with only 1 in 6 drugs that enter clinical development in phase I progressing through to FDA approval [308]. Current methods of pre-clinical testing utilising cellular models or proteins do not accurately represent *in vivo* conditions, thereby allowing the progression of unsuitable CDs through to the later stages of testing. With IVIVEs inaccurately reported, the lack of reliable and representable models is a major contributing factor to the failure rate of drug approval. The DDI potential of drugs is of particular concern in the case of renal diseases, as the kidney is the secondary site of drug metabolism and excretion within the body. Patients with impaired kidney function such as CKD are either subject to lifelong RRTs due to the shortage of organs available for transplantation, or subject to lifelong courses of immunosuppressants after transplantation. This reduction in patient quality of life alongside the cost of dialysis and drug therapies highlights the need for the generation of renal models indicative of the *in vivo* environment. With these factors in mind, the overall vision of this doctoral thesis was to develop a bioartificial kidney device utilising primary proximal tubule cells as an *in vitro* model to assess the DDI potentials of CDs. To achieve this four aims encompassing the pharmacological, biological, chemical and engineering aspects of the project were identified and addressed.

Due to its application the need for robust fluorescence assays for HTS were identified to characterise the functionality of the drug transporters of interest. The advantages offered using fluorophores over radioligands currently utilised in HTS assays include being more cost effective, safe and easier to handle. Polarised monolayers of cells were initially desired to characterise the functionality of P-gp, as the arrangement of cells with specialised barrier functions are more indicative of native epithelial cells. P-gp was chosen as the transporter of interest as it is an efflux transporter with a wide range of substrate specificities. Initial assay development focussed on the transport of Rho123 through monolayers of MDCKII (wild type) cells. Although the active transport of Rho123

was detected, the results could not be reproduced. This was due to high LY percentage permeation through the monolayers during the assay of the second run indicating monolayer damage. The cause for this damage across all concentrations was unknown in the second run, however, in both runs LY permeation increased after the assay. In run 1, this exceeded the 1% threshold in the B-A direction at the higher (50 $\mu$ M-200 $\mu$ M) concentrations tested, indicating the potential toxicity of Rho123. When scaled down to incorporate Rho123 transport through MDCK-MDR1 cells alongside MDCKII cells, active transport was detected at the lower (1 $\mu$ M and 2 $\mu$ M) concentrations. Although the LY permeation was above the threshold percentage, the assay was run again at a lower concentration range to decrease the likelihood of monolayer damage due to Rho123. Monolayer integrity was acceptable at the 10nm-100nm concentration range; however, no active transport was demonstrated through either cell line. It was therefore concluded that the Rho123 assay for the assessment of the functionality of P-gp on polarised monolayers of cells was unsuitable.

As a lack of intact polarised cell monolayers were achieved on transwell inserts alternative methods of transporter characterisation were investigated. These utilised non-polarised monolayers of cells grown on flat well plates. Calcein-AM was established as a probe substrate for the P-gp efflux assay as the molecule becomes a P-gp substrate after it has been cleaved into its fluorescent form inside the cell. In the presence of inhibitors the fluorescence increased indicating P-gp functionality on MDCK-MDR1 cells. The cross specificity of Calcein-AM for other efflux transporters was also investigated by applying the assay to MDCK-BCRP cells in the presence and absence of BCRP and P-gp inhibitors. The resulting lack in fluorescence from the uninhibited sample set confirmed that Calcein-AM could be applied as a selective P-gp substrate in multi-transporter systems to assess P-gp functionality.

For the assessment of the efflux transporter BCRP Hoechst 33342 was selected as the fluorescent probe in the same assay design used for P-gp characterisation. A range of concentrations were applied to MDCK-BCRP cells to ascertain the most suitable concentration. 20 $\mu$ M of Hoechst 33342 provided the highest fold increase in fluorescence from the uninhibited sample in the presence of Ko143 with the lowest amount of error. Hoechst 33342 was also found to be a specific substrate for BCRP in

cells overexpressing P-gp as there was no significant increase in fluorescence in the presence of P-gp inhibitors from the uninhibited sample. Ko143 was found to be a potent inhibitor of BCRP, whereas Novobiocin was less effective at the concentrations used. This could be due to Novobiocin exerting the inhibitory effect on a part of the transporter not responsible for Hoechst 33342 efflux. Regardless of the Novobiocin ineffectiveness, Hoechst 33342 was confirmed as a suitable probe substrate for BCRP in the presence of other efflux transporters.

OCT2 was selected as the uptake transporter of significance to be characterised on HEK-OCT2 cells. ASP<sup>+</sup> uptake was assessed at a range of concentrations in the presence and absence of the OCT2 inhibitors Imipramine and Ipratropium. Due to the nature of the transporter the assay design was altered and required lysing of the cells to measure the amount of ASP<sup>+</sup> taken up within the cells. This led to a high amount of variability in the uninhibited sample set, however, a significant decrease in fluorescence was detected in the presence of both Imipramine and Ipratropium at the 20 $\mu$ M concentration. As ASP<sup>+</sup> is a fluorescent molecule the uptake amount was able to be quantified which was an advantage over the efflux assay design. ASP<sup>+</sup> is also an OCT2 specific substrate and can therefore be applied in cells expressing multiple uptake transporters without the need of cross specificity analysis.

Once the assays had been developed to assess the functionality of specified transporters they were then applied in RPTECs alongside the genetic and surface transporter expression analysis. Due to the cost of the cells per vial the degree of transporter loss was characterised over a range of doublings. This was to enable cell banking whilst retaining transporter expression and functionality similar to the initial doubling. Cells seeded at Pd=5 demonstrated the functionality of BCRP and OCT2, the surface expression of P-gp, BCRP, OCT2, MRP2, OAT3 and MATE1 and the genetic expression of BCRP and OCT2 similar to Pd=0 over the other doublings tested. The functionality results and genetic expression data for P-gp showed an increase at the later doubling (Pd=9) from the initial decrease, indicating an upregulation in the transporter. This may be demonstrative of cell adaptation to the *in vitro* environment, although the surface expression appeared to decrease through the doublings. However, overall Pd=5 proved

to be the most suitable doubling to seed at whilst allowing the most cost effective method of generating sufficient cell numbers for incorporating into the bioreactor.

Due to the potentially porous nature of the generated fibres, RPTEC culture on porous surfaces with a range of coatings was investigated. Although utilised in literature for renal cell growth [168] PCT transwell inserts did not provide a suitable surface for RPTEC culture, with consistently high LY permeation throughout the culture period. The monolayer integrity was not improved when cultured on the various coated surfaces as LY permeation remained above the adjusted 2% threshold. Furthermore transwell inserts coated with Matrigel, which showed the best maintenance of the cell monolayer over the culture period, was found to block the membrane pores. This deemed the coating unsuitable as it may have impaired the transport of substrates through the membrane, impeding the use of the developed assays and further testing within the final device.

As surface coatings could not be applied to the membranes in the final device, the generation of membranes specific to renal cell growth was investigated. Properties favourable to renal cell growth include hydrophilic, negatively charged surfaces. Therefore, carboxylic acids were incorporated onto the PSF backbone alongside PVP which is widely used to increase the biocompatibility of surfaces. The generated flat sheet membranes using MA and GA as an additive did not show incorporation of the acids onto the surface and an increase in hydrophobicity from the pure PSF membranes. Although the surface roughness was similar for all membrane blends, the consequent RPTEC culture demonstrated a decrease in the metabolic activity of cells over a short term culture period on these membranes. The inclusion of PVP onto the PSF backbone increased the hydrophilicity of the surface and demonstrated renal cell attachment and metabolic activity similar to the TCP control. The membranes were also able to be effectively sterilised by autoclaving whilst retaining their structural integrity, proving valuable for both the cell culture application and the assembly process.

Hollow fibres were produced using the NIPS method utilised in the flat sheet membrane generation. 2 continuous batches were initially produced, altering the pressure and water flow rates to adjust the wall thicknesses. Due to the fragility of these fibres, a

third batch with thicker walls was later produced. Although the fibres were easier to handle they were less porous and permeable to water than the previous batches. Long term growth of RPTECs on the exterior of the fibres was also drastically impaired, concurrent with the long term viability of renal cells on membranes incorporating PVP in literature [181]. However the earlier batches of fibres demonstrated a vast improvement in cell growth and metabolic activity, with cells cultured on batch 2 fibres performing the best with cell morphology indicating polarised transporting epithelium formation. Upon further investigation this was not due to the surface topography of the fibres, which were similar across all batches on the interior and exterior sides, and therefore may be due to the degradation of the PVP in the dope solution over time.

Batch 2 fibres were then incorporated into single fibre glass casing to produce modules for cell seeding. Sterilisation by autoclaving was effective, although water was required to permeate the fibre to ensure the complete sterilisation of the fibre and casing. Although the fibres were fragile they demonstrated the ability to remain intact under high flow rates over 24 hours after sterilisation. However, variability in the fibre integrity throughout the batch was discovered and many modules failed due to unseen tears within the fibres. The compromised fibres consequently demonstrated poor cell performance over 7 days under flow conditions when seeded with RPTECs. Calculated cell numbers dropped to 0.5% of the initial seeding density, which was reflected in the metabolic activity and nutrient and metabolite analysis over the culture period. Subsequent analysis techniques such as imaging and PCR could not be undertaken due to the low cell numbers. However, in intact fibres the metabolic activity pattern indicated a rise in cell numbers after an initial drop after applying flow conditions. This is promising and may have led to an increase in cell numbers to form an acceptable monolayer over an extended culture period.

## 6.2. Discussion

The device generated from this project satisfied a number of criteria that are required in a reliable *in vitro* model for pharmaceutical research. The device incorporated primary renal cells, which had been characterised in terms of drug transporter expression and functionality. The methods of drug transporter functionality were developed as fluorescence assays to reduce the monetary, safety and disposal concerns currently encountered from the use of radioligands. The porous polymer membrane had been tailored as a renal culture substrate without the use of protein coatings and demonstrated the proliferation of cells and the formation of a tight monolayer of cells in static culture. For the application of flow, shear stresses similar to the physiological environment of the PT [19] were applied to encourage the formation of an improved functional monolayer of cells within the device. The device design was also generated to mimic the native architecture of the PT to a degree, allowing the formation of a tubule of cells with the lumen representing the ultrafiltrate, separated by the membrane support from the ECS representing the vascular supply.

Although the device demonstrated progression in various aspects such as assay development, drug transporter capabilities of primary cells over time in *in vitro* culture and polymer membrane development as a substrate for renal cell culture; the functionality of the device as a whole is yet to be improved compared to the models that currently exist. hPTC monolayer formation and cell functionality is yet to be demonstrated within the device, as reported in many other devices such as the RAD [11], Kidney on a chip [13] and BRECS [15]. The degree of similarity between the generated device and the existing models also varies significantly. The generated device and the RAD share a similar structure to the PT, generating a tubule of cells with a lumen and an ECS, whereas the Kidney on a chip device forms a flat monolayer of cells to separate the apical and basolateral compartments of the device. In this way the transport of substances through the monolayer can still be ascertained. However, there is no flow in the basolateral compartment. The BRECS varies the most in device design, owing to the clinical endpoint of the device. Although this allows the generation of a large cell population within the device, transport capabilities are not assessed, and the generation of small proteins and hormones is ascertained by the a selective filter. The footprint of

the devices is also an important aspect to consider when developing models for pharmaceutical research. The generated device has a relatively large footprint owing to the requirement of 2 pumps to provide flow to the lumen and ECS circuits, whereas the requirement of the Kidney on a chip device is reduced. The size of the Kidney on a chip device is also drastically reduced compared to the generated device, allowing multiple devices to be utilised. The generated device, whilst allowing multiple modules to be run at the same time, is more difficult to handle due to its increased size and setup. Another important design aspect that is addressed in the Kidney on a chip system is the use of transparent components in order to observe cells directly within the device. Due to the use of PSF+PVP membranes the resulting hollow fibres were opaque, and cells were monitored indirectly via metabolite analysis and Presto blue reduction. One of the final criteria which has not been addressed in this device is the complete characterisation of fluid flow through and across the before and after cell seeding. This was addressed in the HFB generated by Aebischer *et al* [9][10][279], detailing the effect of fluid flow through the fibre in terms of shear stress effects on cells, and through the membrane wall in terms of TMP effects on cells.

These criteria, once addressed will aid in the generation of an optimised *in vitro* model of the proximal tubule for use in pharmaceutical research. Other aspects to be addressed to achieve this aim are detailed in Section 6.4.

### 6.3. Conclusions

This doctoral thesis addresses the need for more reliable *in vitro* models within the pharmaceutical industry by developing a bioartificial kidney device incorporating primary human renal cells. The approach to this project identified four main elements, summarised in Section 1.2., which have been investigated as thoroughly as possible.

The first aim of the project was to develop a panel of fluorescence assays to replace the current assays using radioligands to assess renal drug transporter functionality. Although functionality assays using fluorescent substrates have been developed, there is currently no complete panel available. Assays assessing the functionality of 3 renal transporters: P-gp, BCRP and OCT2 were developed in cell lines overexpressing the transporter in question. The cross specificity of substrates between the 2 efflux transporters was also addressed to ensure the functionality for the individual transporter could be assessed in cell systems expressing multiple transporters. However, these assays were developed in non-polarised monolayers of cells, as intact cell monolayers could not be achieved through the bidirectional transport assay developed for the assessment of P-gp.

The second aim of the project was to determine the transporter capabilities of primary human renal proximal tubule cells over time in *in vitro* culture. As well as defining the transporter characteristics over time *in vitro*, which has not been reported in literature to date, the expansion of cells was also required in order to generate the numbers of cells required for the seeding of the device. The functionality assays developed previously were employed alongside genetic expression analysis and surface visualisation to determine the degree of transporter expression and function loss. Pd=5 demonstrated sufficient transporter functionality and expression compared to the starting doubling, although later doublings indicated the upregulation and increased function of P-gp. OCT2 functionality however could not be reliably determined due to the assay format resulting in the loss of cells.

The third aim of the project was develop a suitable substrate for renal cell culture. Membrane tailoring arose from the finding that porous commercial membranes did not generate acceptable monolayers of cells, even with the use of protein coatings. Therefore polymer blends based on a PSF backbone were produced and physically

characterised. Although reported as an unsuitable renal cell culture substrate, PSF+PVP demonstrated the best results, in terms of increased hydrophilicity, alteration of surface chemistry and short-term renal cell metabolic activity. The membranes were also shown to be sterilised effectively with no apparent structural changes. The success of the PSF+PVP blend allowed the progression into hollow fibre production and the achievement of the next project aim.

The fourth project aim was to incorporate hollow fibres into glass casings to generate single HFBs for the culture and assessment of RPTECs. Devices were generated and cells were successfully seeded within the device, however reproducible cell expansion did not occur and the resulting analysis of transporter expression and functionality could not be done. The investigation into long-term static culture on the exterior of the hollow fibres did present some interesting results, prompting the need for further research into the variation between fibre batches and the status of PVP in the dope solution over time.

#### 6.4. Further Work

This work has demonstrated proof of concept of the assembly of a bioartificial kidney device incorporating primary human renal cells with characterised transporter expression and functionality for use in DMPK research. However, to be a fully functional validated *in vitro* model a number of challenges must be addressed.

Developing functionality assays for the full panel of transporters desired for assessment (OAT3, MRP2 and MATE1) alongside improving the existing method for uptake (OCT2) transporter analysis would be required. Fluorophores and specific inhibitors for the remaining transporters would need to be identified and applied in cell lines overexpressing the transporters to assess both the viability of the compounds and the cross specificity of the substrates. The continued development of assays on polarised monolayers would also be advantageous to understand the transport of substrates through cell monolayers representative of the native renal epithelium. This would initially require the culture of intact cell line monolayers on transwell inserts for assay development, before the application of the transport assays on RPTEC monolayers. To achieve this RPTEC culture could be tested out on a variety of membranes over a long culture period to ascertain the optimal conditions for monolayer integrity. Fluorophores utilised in the assays detailed in this thesis may need to be changed in the alteration of the assay design to inherently fluorescent molecules. This would allow the detection of substrate in the transport buffer and allow standard curves to be generated.

Alongside assay development and transporter functionality, further characterisation of RPTECs seeded at Pd=5 compared to the initial doubling would be beneficial. The genetic expression of the full panel of transporters would indicate the changes in expression over time *in vitro*. Alternative cell sources could also be characterised to investigate whether a more cost effective source of cells with similar or improved transporter expression and functionality is available. The presence of tight junction complexes would also need to be ascertained by to ensure the cells are capable of forming polarised monolayers *in vitro*.

Further development of the membrane materials for RPTEC culture is required to characterise the dope solution, assessing the rate of degradation of the PVP and to

control the porosity and skin layer formation during production. The removal of the nitrogen contaminations found in this work by degassing the dope solution under a vacuum also may prove valuable in terms of physical properties and renal cell performance. Other blends incorporating acrylic based monomers or phospholipid polymers could be trialled as reports in literature indicate they are an improved substrate for renal cells [181][193]. The development of membranes with good optical properties will also be beneficial to observe cells on the membranes and eventually within the fibres. However, this will require the formulation of new polymer based blends as PSF based blends are opaque. The long term viability of cells on the membranes and the ability for cells to form confluent monolayers would also need to be assessed alongside the other physical characterisation techniques used in this thesis.

The method of fibre production is a key challenge to address as much of the resulting data collected was impaired due to a lack of fibre integrity. The production process would need to be fully characterised, including determining the pressures and water flow rates with the corresponding wall thicknesses, and ensuring a consistent feed of homogenised polymer into the gelation bath to improve the uniformity of the wall thickness. Introducing an air gap into fibre production before entering the gelation bath may also be beneficial to increase the porosity of the fibre exterior [309] thereby improving transport through the membrane. Transport of small molecules through the lumen layer would also need to be established, with the porosity of the skin layer altered accordingly by introducing a non-solvent/water mix as the bore fluid. This is a key aspect in the device design as water flux was found to be quite low in the fibres generated and is required for determining the transport of compounds through the cell-fibre layer.

Modelling is also an important tool to utilise in further development of the device. By applying mass transfer models described in literature [290][292] alongside the computational analysis of aspects such as fluid flow through the fibre, an optimised BAK device can be generated for renal cell proliferation.

To produce a model capable of reproducible results, the individual assembly of the device would need to be kept consistent. This would include the method used to seal

the fibres into the module, the position of the fibre within the module and the environment within the casing. Using adhesives which do not produce residues, as seen in this work would be beneficial as the effect of the fragments on the cells is unknown and could exert damaging effects over the culture period. Producing disposable modules would reduce the time spent on cleaning the casings and ensure all residues are removed from the module before each run. However, the module would need to be able to withstand autoclaving as other methods of sterilisation such as gamma irradiation are not as cost effective.

The device design would also need to be optimised to allow easy incorporation into current methods employed in DMPK testing. In this thesis, syringes pumps with maximum syringe volumes of 20mL were utilised to allow more than 2 modules to be run at the same time. Syringe pumps were utilised as they were the best option at the time of design to provide both a low flow rate and a smooth action of flow within the device. However, to apply the desired flow rate of 50 $\mu$ l/min, the syringe had to be replaced and refilled from the medium reservoir every 6 hours. This is not practical for use in industry; however, a number of options are available to counter this problem. The device could be scaled down to allow a smaller flow rate to be applied to exert the same shear stress on the cells within the fibres. However, this would require smaller modules and fibres to be produced, which would prove more difficult to assemble and adequately sterilise. A more effective scaled down design would resemble a kidney-on-a-chip type layout, of which there are currently many being developed. Another option is to incorporate a recirculatory pump within the device instead of a syringe pump to allow the constant exchange of medium throughout the culture period. Peristaltic pumps which provide the low flow rates required for this device are available, although the medium flow is pulsatile which is less comparable to the flow within the proximal tubule. However, the capacity for some peristaltic pumps range between 4 and 32 channels (205S/CA; Watson Marlowe. UK), allowing the multiple running of modules at the same time. This is therefore a more desirable option using the same module setup described within this thesis.

To make the bioreactor suitable for application in DMPK testing, the culture of cells into a polarised monolayer would have to be demonstrated and assessed. This would require

the development of permeability assays similar to the LY permeation assays utilised in the assay development section of this work. Other possible fluorescent molecules for permeation studies include FITC-inulin which does not permeate an intact cell monolayer and is widely used in literature [168][310][311]. Wider studies into the monolayer formation within the device also need to be applied to ascertain the optimal conditions for renal cell growth. These include the optimal flow rate to apply within the device by looking at cell removal from the lumen at different flow rates, the optimal culture period for cell culture to produce a confluent polarised cell monolayer, and the effect of co-current versus counter current flow of medium in the ECS compared to the lumen. As the device will be utilised for DMPK studies the monolayer does not need to be maintained for a prolonged period of time, however, alternative applications of this device could be for use in long term toxicity and clearance studies. For these applications it would be necessary to maintain polarised cell monolayers for weeks to allow long term testing.

Finally, cells will need to be characterised within the device utilising assays developed in this thesis alongside other assays described in this further work section. The device will require validation to ensure consistency and reproducibility of results before being incorporated into the industrial setting. The enhanced expression and functionality of transporters within the device will provide an *in vitro* model more indicative of the physiological conditions within the proximal tubule. This will enable IVIVE more predictive of the *in vivo* situation, therefore allowing time and money to be reduced in both the DMPK and wider development of NCEs in the future.

# Chapter 7

## References

- [1] “Deaths from Renal Diseases in England, 2001 to 2008,” NHS, Short report, Jun. 2010.
- [2] C. J. Pino and H. D. Humes, “Stem cell technology for the treatment of acute and chronic renal failure,” *Transl. Res. J. Lab. Clin. Med.*, vol. 156, no. 3, pp. 161–168, Sep. 2010.
- [3] H. D. Humes and M. S. Szczyпка, “Advances in cell therapy for renal failure,” *Transpl. Immunol.*, vol. 12, no. 3–4, pp. 219–227, Apr. 2004.
- [4] Keith DS, Nichols GA, Gullion CM, Brown J, and Smith DH, “Longitudinal follow-up and outcomes among a population with chronic kidney disease in a large managed care organization,” *Arch. Intern. Med.*, vol. 164, no. 6, pp. 659–663, Mar. 2004.
- [5] “Organ donation and transplantation Activity report 2013/14,” NHS Blood and Transplant, May 2014.
- [6] “Organ donation and transplantation statistics.” National Kidney Foundation, 09-Aug-2014.
- [7] J. F. et al D. Ansell, “UK Renal Registry Annual Report,” The Renal Association.
- [8] A. Baker and R. Green, “Renal replacement therapy in critical care,” *World federation of societies of anaesthesiologists*, 194, Aug. 2010.
- [9] P. Aebischer, T. K. Ip, G. Panol, and P. M. Galletti, “The bioartificial kidney: progress towards an ultrafiltration device with renal epithelial cells processing,” *Life Support Syst. J. Eur. Soc. Artif. Organs*, vol. 5, no. 2, pp. 159–168, Jun. 1987.
- [10] H. Uludag, G. Panol, and P. Aebischer, “Control of water flux in a bioartificial kidney,” *ASAIO Trans. Am. Soc. Artif. Intern. Organs*, vol. 35, no. 3, pp. 523–527, Sep. 1989.
- [11] H. D. Humes, W. F. Weitzel, R. H. Bartlett, F. C. Swaniker, E. P. Paganini, J. R. Luderer, and J. Sobota, “Initial clinical results of the bioartificial kidney containing human cells in ICU patients with acute renal failure,” *Kidney Int.*, vol. 66, no. 4, pp. 1578–1588, Oct. 2004.
- [12] Z. Y. Oo, R. Deng, M. Hu, M. Ni, K. Kandasamy, M. S. bin Ibrahim, J. Y. Ying, and D. Zink, “The performance of primary human renal cells in hollow fiber bioreactors for bioartificial kidneys,” *Biomaterials*, vol. 32, no. 34, pp. 8806–8815, Dec. 2011.

- [13] K.-J. Jang, A. P. Mehr, G. A. Hamilton, L. A. McPartlin, S. Chung, K.-Y. Suh, and D. E. Ingber, "Human kidney proximal tubule-on-a-chip for drug transport and nephrotoxicity assessment," *Integr. Biol. Quant. Biosci. Nano Macro*, vol. 5, no. 9, pp. 1119–1129, Sep. 2013.
- [14] K. Jin Jang and D. Ingber, "Human kidney proximal tubule-on-a-chip for drug transporter and nephrotoxicity assessment," presented at the 15th International Conference on Miniaturized Systems for Chemistry and Life Sciences, Seattle, Washington, 2011.
- [15] D. A. Buffington, C. J. Pino, L. Chen, A. J. Westover, G. Hageman, and H. D. Humes, "Bioartificial Renal Epithelial Cell System (BRECS): A Compact, Cryopreservable Extracorporeal Renal Replacement Device," *Cell Med.*, vol. 4, no. 1, pp. 33–43, Jan. 2012.
- [16] D. W. Light, "Drug R&D Costs Questioned," *Genet. Eng. Biotechnol. News*, vol. 31, no. 13, pp. 6–7, Jul. 2011.
- [17] F. . Scherer, "R&D Costs and Productivity in Biopharmaceuticals," F. Kennedy School of Government, Harvard University, 2011.
- [18] A. Astashkina, B. Mann, and D. W. Grainger, "A critical evaluation of in vitro cell culture models for high-throughput drug screening and toxicity," *Pharmacol. Ther.*, vol. 134, no. 1, pp. 82–106, Apr. 2012.
- [19] Y. Duan, N. Gotoh, Q. Yan, Z. Du, A. M. Weinstein, T. Wang, and S. Weinbaum, "Shear-Induced Reorganization of Renal Proximal Tubule Cell Actin Cytoskeleton and Apical Junctional Complexes," *Proc. Natl. Acad. Sci.*, vol. 105, no. 32, pp. 11418–11423, Aug. 2008.
- [20] R. Fahrig, M. Rupp, A. Steinkamp-Zucht, and A. Bader, "Use of Primary Rat and Human Hepatocyte Sandwich Cultures for Activation of Indirect Carcinogens: Monitoring of DNA Strand Breaks and Gene Mutations in Co-cultured Cells," *Toxicol. Vitro Int. J. Publ. Assoc. BIBRA*, vol. 12, no. 4, pp. 431–444, Aug. 1998.
- [21] P. Ballard, P. Brassil, K. H. Bui, H. Dolgos, C. Petersson, A. Tunek, and P. J. H. Webborn, "The right compound in the right assay at the right time: an integrated discovery DMPK strategy," *Drug Metab. Rev.*, vol. 44, no. 3, pp. 224–252, Aug. 2012.

- [22] M. Cereijido, E. S. Robbins, W. J. Dolan, C. A. Rotunno, and D. D. Sabatini, "Polarized monolayers formed by epithelial cells on a permeable and translucent support," *J. Cell Biol.*, vol. 77, no. 3, pp. 853–880, Jun. 1978.
- [23] M. R. Baghaban Eslami Nejad, M. Rezazadeh Valojerdi, and S. Kazemi Ashtiani, "A comparison of polarized and non-polarized human endometrial monolayer culture systems on murine embryo development," *J. Exp. Clin. Assist. Reprod.*, vol. 2, p. 7, Apr. 2005.
- [24] E. Crivellato, L. Candussio, A. M. Rosati, F. Bartoli-Klugmann, F. Mallardi, and G. Decorti, "The Fluorescent Probe Bodipy-FL-Verapamil Is a Substrate for Both P-glycoprotein and Multidrug Resistance-related Protein (MRP)-1," *J. Histochem. Cytochem.*, vol. 50, no. 5, pp. 731–734, May 2002.
- [25] R. V. Kondratov, P. G. Komarov, Y. Becker, A. Ewenson, and A. V. Gudkov, "Small molecules that dramatically alter multidrug resistance phenotype by modulating the substrate specificity of P-glycoprotein," *Proc. Natl. Acad. Sci. U. S. A.*, vol. 98, no. 24, pp. 14078–14083, Nov. 2001.
- [26] M. Ginai, R. Elsby, C. J. Hewitt, D. Surry, K. Fenner, and K. Coopman, "The use of bioreactors as in vitro models in pharmaceutical research," *Drug Discov. Today*, vol. 18, no. 19–20, pp. 922–935, Oct. 2013.
- [27] S. Ekins, J. Mestres, and B. Testa, "In silico pharmacology for drug discovery: methods for virtual ligand screening and profiling," *Br. J. Pharmacol.*, vol. 152, no. 1, pp. 9–20, Sep. 2007.
- [28] G. C. Terstappen and A. Reggiani, "In silico research in drug discovery," *Trends Pharmacol. Sci.*, vol. 22, no. 1, pp. 23–26, Jan. 2001.
- [29] "Biotechnology / Life Sciences in Baden-Württemberg Drug screening - higher throughput, quicker and more effective thanks to automation." [Online]. Available: <http://www.bio-pro.de/magazin/thema/00138/index.html?lang=en>. [Accessed: 17-Oct-2014].
- [30] J. Hughes, S. Rees, S. Kalindjian, and K. Philpott, "Principles of early drug discovery," *Br. J. Pharmacol.*, vol. 162, no. 6, pp. 1239–1249, Mar. 2011.
- [31] E. L. Lecluyse and E. Alexandre, "Isolation and culture of primary hepatocytes from resected human liver tissue," *Methods Mol. Biol. Clifton NJ*, vol. 640, pp. 57–82, 2010.

- [32] Y. Sambuy, I. De Angelis, G. Ranaldi, M. L. Scarino, A. Stammati, and F. Zucco, "The Caco-2 cell line as a model of the intestinal barrier: influence of cell and culture-related factors on Caco-2 cell functional characteristics," *Cell Biol. Toxicol.*, vol. 21, no. 1, pp. 1–26, Jan. 2005.
- [33] D. C. Evans, A. P. Watt, D. A. Nicoll-Griffith, and T. A. Baillie, "Drug-Protein Adducts: An Industry Perspective on Minimizing the Potential for Drug Bioactivation in Drug Discovery and Development," *Chem. Res. Toxicol.*, vol. 17, no. 1, pp. 3–16, Jan. 2004.
- [34] Z. Yan, N. Maher, R. Torres, G. W. Caldwell, and N. Huebert, "Rapid detection and characterization of minor reactive metabolites using stable-isotope trapping in combination with tandem mass spectrometry," *Rapid Commun. Mass Spectrom.*, vol. 19, no. 22, pp. 3322–3330, Nov. 2005.
- [35] D. Zhang, G. Luo, X. Ding, and C. Lu, "Preclinical experimental models of drug metabolism and disposition in drug discovery and development," *Acta Pharm. Sin. B*, vol. 2, no. 6, pp. 549–561, Dec. 2012.
- [36] X. Yang, Y. A. Gandhi, D. B. Duignan, and M. E. Morris, "Prediction of Biliary Excretion in Rats and Humans Using Molecular Weight and Quantitative Structure-Pharmacokinetic Relationships," *AAPS J.*, vol. 11, no. 3, pp. 511–525, Sep. 2009.
- [37] S. Fowler and H. Zhang, "In Vitro Evaluation of Reversible and Irreversible Cytochrome P450 Inhibition: Current Status on Methodologies and their Utility for Predicting Drug-Drug Interactions," *AAPS J.*, vol. 10, no. 2, pp. 410–424, Aug. 2008.
- [38] V. Chu, H. J. Einolf, R. Evers, G. Kumar, D. Moore, S. Ripp, J. Silva, V. Sinha, M. Sinz, and A. Skerjanec, "In Vitro and in Vivo Induction of Cytochrome P450: A Survey of the Current Practices and Recommendations: A Pharmaceutical Research and Manufacturers of America Perspective," *Drug Metab. Dispos.*, vol. 37, no. 7, pp. 1339–1354, Jul. 2009.
- [39] V. Vasiliou, K. Vasiliou, and D. W. Nebert, "Human ATP-binding cassette (ABC) transporter family," *Hum. Genomics*, vol. 3, no. 3, p. 281, Apr. 2009.
- [40] K. P. Locher, "Structure and mechanism of ATP-binding cassette transporters," *Philos. Trans. R. Soc. B Biol. Sci.*, vol. 364, no. 1514, pp. 239–245, Jan. 2009.

- [41] P. J. Verrier, D. Bird, B. Burla, E. Dassa, C. Forestier, M. Geisler, M. Klein, Ü. Kolukisaoglu, Y. Lee, E. Martinoia, A. Murphy, P. A. Rea, L. Samuels, B. Schulz, E. P. Spalding, K. Yazaki, and F. L. Theodoulou, "Plant ABC proteins – a unified nomenclature and updated inventory," *Trends Plant Sci.*, vol. 13, no. 4, pp. 151–159, Apr. 2008.
- [42] M. Dean, Y. Hamon, and G. Chimini, "The human ATP-binding cassette (ABC) transporter superfamily," *J. Lipid Res.*, vol. 42, no. 7, pp. 1007–1017, Jul. 2001.
- [43] "Guideline on the Investigation of Drug Interactions," European Medicines Agency, CPMP/EWP/560/95/Rev.1 Corr, Jun. 2012.
- [44] T. Lin, O. Islam, and K. Heese, "ABC transporters, neural stem cells and neurogenesis – a different perspective," *Cell Res.*, vol. 16, no. 11, pp. 857–871, Nov. 2006.
- [45] L. He, K. Vasiliou, and D. W. Nebert, "Analysis and update of the human solute carrier (SLC) gene superfamily," *Hum. Genomics*, vol. 3, no. 2, pp. 195–206, Jan. 2009.
- [46] T. Fujita, T. J. Urban, M. K. Leabman, K. Fujita, and K. M. Giacomini, "Transport of drugs in the kidney by the human organic cation transporter, OCT2 and its genetic variants," *J. Pharm. Sci.*, vol. 95, no. 1, pp. 25–36, Jan. 2006.
- [47] O. Zolk, T. F. Solbach, J. König, and M. F. Fromm, "Functional Characterization of the Human Organic Cation Transporter 2 Variant p.270Ala>Ser," *Drug Metab. Dispos.*, vol. 37, no. 6, pp. 1312–1318, Jun. 2009.
- [48] K. Higashi, M. Imamura, S. Fudo, T. Uemura, R. Saiki, T. Hoshino, T. Toida, K. Kashiwagi, and K. Igarashi, "Identification of Functional Amino Acid Residues Involved in Polyamine and Agmatine Transport by Human Organic Cation Transporter 2," *PLoS ONE*, vol. 9, no. 7, p. e102234, Jul. 2014.
- [49] R. M. Pelis, X. Zhang, Y. Dangprapai, and S. H. Wright, "Cysteine Accessibility in the Hydrophilic Cleft of Human Organic Cation Transporter 2," *J. Biol. Chem.*, vol. 281, no. 46, pp. 35272–35280, Nov. 2006.
- [50] H. E. M. zu Schwabedissen, C. Verstuyft, H. K. Kroemer, L. Becquemont, and R. B. Kim, "Human multidrug and toxin extrusion 1 (MATE1/SLC47A1) transporter: functional characterization, interaction with OCT2 (SLC22A2), and single

- nucleotide polymorphisms," *Am. J. Physiol. - Ren. Physiol.*, vol. 298, no. 4, pp. F997–F1005, Apr. 2010.
- [51] X. Zhang, X. He, J. Baker, F. Tama, G. Chang, and S. H. Wright, "Twelve Transmembrane Helices Form the Functional Core of Mammalian MATE1 (Multidrug and Toxin Extruder 1) Protein," *J. Biol. Chem.*, vol. 287, no. 33, pp. 27971–27982, Aug. 2012.
- [52] H. Motohashi and K. Inui, "Multidrug and toxin extrusion family SLC47: Physiological, pharmacokinetic and toxicokinetic importance of MATE1 and MATE2-K," *Mol. Aspects Med.*, vol. 34, no. 2–3, pp. 661–668, Apr. 2013.
- [53] Z. Wang, C. E. C. A. Hop, K. H. Leung, and J. Pang, "Determination of in vitro permeability of drug candidates through a Caco-2 cell monolayer by liquid chromatography/tandem mass spectrometry," *J. Mass Spectrom.*, vol. 35, no. 1, pp. 71–76, Jan. 2000.
- [54] C. J. Bode, H. Jin, E. Rytting, P. S. Silverstein, A. M. Young, and K. L. Audus, "In Vitro Models for Studying Trophoblast Transcellular Transport," *Methods Mol. Med.*, vol. 122, pp. 225–239, 2006.
- [55] C. for D. E. and Research, "Drug Interactions & Labeling - Drug Development and Drug Interactions: Table of Substrates, Inhibitors and Inducers." [Online]. Available: <http://www.fda.gov/Drugs/DevelopmentApprovalProcess/DevelopmentResources/DrugInteractionsLabeling/ucm093664.htm#major>. [Accessed: 12-Aug-2012].
- [56] J. Rautio, J. E. Humphreys, L. O. Webster, A. Balakrishnan, J. P. Keogh, J. R. Kunta, C. J. Serabjit-Singh, and J. W. Polli, "In vitro p-glycoprotein inhibition assays for assessment of clinical drug interaction potential of new drug candidates: a recommendation for probe substrates," *Drug Metab. Dispos. Biol. Fate Chem.*, vol. 34, no. 5, pp. 786–792, May 2006.
- [57] J. A. Cook, B. Feng, K. S. Fenner, S. Kempshall, R. Liu, C. Rotter, D. A. Smith, M. D. Troutman, M. Ullah, and C. A. Lee, "Refining the in vitro and in vivo critical parameters for P-glycoprotein, [1]/IC50 and [12]/IC50, that allow for the exclusion of drug candidates from clinical digoxin interaction studies," *Mol. Pharm.*, vol. 7, no. 2, pp. 398–411, Apr. 2010.

- [58] M. Culot, S. Lundquist, D. Vanuxeem, S. Nion, C. Landry, Y. Delplace, M.-P. Dehouck, V. Berezowski, L. Fenart, and R. Cecchelli, "An in vitro blood-brain barrier model for high throughput (HTS) toxicological screening," *Toxicol. In Vitro*, vol. 22, no. 3, pp. 799–811, Apr. 2008.
- [59] S. Forster, A. E. Thumser, S. R. Hood, and N. Plant, "Characterization of Rhodamine-123 as a Tracer Dye for Use In In vitro Drug Transport Assays," *PLoS ONE*, vol. 7, no. 3, p. e33253, Mar. 2012.
- [60] S. Wada, T. Kano, S. Mita, Y. Idota, K. Morimoto, F. Yamashita, and T. Ogihara, "The role of inter-segmental differences in P-glycoprotein expression and activity along the rat small intestine in causing the double-peak phenomenon of substrate plasma concentration," *Drug Metab. Pharmacokinet.*, vol. 28, no. 2, pp. 98–103, 2013.
- [61] C. J. Endres, P. Hsiao, F. S. Chung, and J. D. Unadkat, "The role of transporters in drug interactions," *Eur. J. Pharm. Sci.*, vol. 27, no. 5, pp. 501–517, Apr. 2006.
- [62] A. B. Shapiro, K. Fox, P. Lee, Y. D. Yang, and V. Ling, "Functional intracellular P-glycoprotein," *Int. J. Cancer*, vol. 76, no. 6, pp. 857–864, Jun. 1998.
- [63] T. Nabekura, "Overcoming Multidrug Resistance in Human Cancer Cells by Natural Compounds," *Toxins*, vol. 2, no. 6, pp. 1207–1224, May 2010.
- [64] E. Wang, C. N. Casciano, R. P. Clement, and W. W. Johnson, "Cholesterol Interaction with the Daunorubicin Binding Site of P-Glycoprotein," *Biochem. Biophys. Res. Commun.*, vol. 276, no. 3, pp. 909–916, Oct. 2000.
- [65] P. Acharya, M. P. O'Connor, J. W. Polli, A. Ayrton, H. Ellens, and J. Bentz, "Kinetic Identification of Membrane Transporters That Assist P-glycoprotein-Mediated Transport of Digoxin and Loperamide through a Confluent Monolayer of MDCKII-hMDR1 Cells," *Drug Metab. Dispos.*, vol. 36, no. 2, pp. 452–460, Feb. 2008.
- [66] M. F. Fromm, R. B. Kim, C. M. Stein, G. R. Wilkinson, and D. M. Roden, "Inhibition of P-Glycoprotein-Mediated Drug Transport A Unifying Mechanism to Explain the Interaction Between Digoxin and Quinidine," *Circulation*, vol. 99, no. 4, pp. 552–557, Feb. 1999.
- [67] G. J. E. J. Hooiveld, J. Heegsma, J. E. van Montfoort, P. L. M. Jansen, D. K. F. Meijer, and M. Muller, "Stereoselective transport of hydrophilic quaternary drugs by

- human MDR1 and rat Mdr1b P-glycoproteins," *Br. J. Pharmacol.*, vol. 135, no. 7, pp. 1685–1694, Apr. 2002.
- [68] H. Kusuvara, H. Suzuki, T. Terasaki, A. Kakee, M. Lemaire, and Y. Sugiyama, "P-Glycoprotein Mediates the Efflux of Quinidine across the Blood-Brain Barrier," *J. Pharmacol. Exp. Ther.*, vol. 283, no. 2, pp. 574–580, Nov. 1997.
- [69] A. A. Lumen, L. Li, J. Li, Z. Ahmed, Z. Meng, A. Owen, H. Ellens, I. J. Hidalgo, and J. Bentz, "Transport Inhibition of Digoxin Using Several Common P-gp Expressing Cell Lines Is Not Necessarily Reporting Only on Inhibitor Binding to P-gp," *PLoS ONE*, vol. 8, no. 8, p. e69394, Aug. 2013.
- [70] I. Tamai and A. R. Safa, "Azidopine noncompetitively interacts with vinblastine and cyclosporin A binding to P-glycoprotein in multidrug resistant cells.," *J. Biol. Chem.*, vol. 266, no. 25, pp. 16796–16800, Sep. 1991.
- [71] R. B. Kirn, C. Wandel, B. Leake, M. Cvetkovic, M. F. Fromm, P. J. Dempsey, M. M. Roden, F. Belas, A. K. Chaudhary, D. M. Roden, A. J. J. Wood, and G. R. Wilkinson, "Interrelationship Between Substrates and Inhibitors of Human CYP3A and P-Glycoprotein," *Pharm. Res.*, vol. 16, no. 3, pp. 408–414, Mar. 1999.
- [72] E. Wang, K. Lew, C. N. Casciano, R. P. Clement, and W. W. Johnson, "Interaction of Common Azole Antifungals with P Glycoprotein," *Antimicrob. Agents Chemother.*, vol. 46, no. 1, pp. 160–165, Jan. 2002.
- [73] G. Pietig, T. Mehrens, J. R. Hirsch, I. Çetinkaya, H. Piechota, and E. Schlatter, "Properties and Regulation of Organic Cation Transport in Freshly Isolated Human Proximal Tubules," *J. Biol. Chem.*, vol. 276, no. 36, pp. 33741–33746, Sep. 2001.
- [74] M. J. Wilmer, M. A. Saleem, R. Masereeuw, L. Ni, T. J. van der Velden, F. G. Russel, P. W. Mathieson, L. A. Monnens, L. P. van den Heuvel, and E. N. Levtchenko, "Novel conditionally immortalized human proximal tubule cell line expressing functional influx and efflux transporters," *Cell Tissue Res.*, vol. 339, no. 2, pp. 449–457, Feb. 2010.
- [75] M. Belzer, M. Morales, B. Jagadish, E. A. Mash, and S. H. Wright, "Substrate-Dependent Ligand Inhibition of the Human Organic Cation Transporter OCT2," *J. Pharmacol. Exp. Ther.*, vol. 346, no. 2, pp. 300–310, Aug. 2013.
- [76] J. W. Jonker, E. Wagenaar, S. van Eijl, and A. H. Schinkel, "Deficiency in the Organic Cation Transporters 1 and 2 (Oct1/Oct2 [Slc22a1/Slc22a2]) in Mice Abolishes

- Renal Secretion of Organic Cations," *Mol. Cell. Biol.*, vol. 23, no. 21, pp. 7902–7908, Nov. 2003.
- [77] N. Asavapanumas, S. Kittayaruksakul, P. Meetam, C. Muanprasat, V. Chatsudthipong, and S. Soodvilai, "Fenofibrate Down-regulates Renal OCT2-mediated Organic Cation Transport *via* PPAR $\alpha$ -independent Pathways," *Drug Metab. Pharmacokinet.*, vol. 27, no. 5, pp. 513–519, 2012.
- [78] J. J. Salomon, S. Endter, G. Tachon, F. Falson, S. T. Buckley, and C. Ehrhardt, "Transport of the fluorescent organic cation 4-(4-(dimethylamino)styryl)-N-methylpyridinium iodide (ASP+) in human respiratory epithelial cells," *Eur. J. Pharm. Biopharm.*, vol. 81, no. 2, pp. 351–359, Jun. 2012.
- [79] H. Koepsell, "The SLC22 family with transporters of organic cations, anions and zwitterions," *Mol. Aspects Med.*, vol. 34, no. 2–3, pp. 413–435, Apr. 2013.
- [80] Z.-J. Wang, O. Q. P. Yin, B. Tomlinson, and M. S. S. Chow, "OCT2 polymorphisms and in-vivo renal functional consequence: studies with metformin and cimetidine:," *Pharmacogenet. Genomics*, vol. 18, no. 7, pp. 637–645, Jul. 2008.
- [81] T. Nakanishi, T. Haruta, Y. Shirasaka, and I. Tamai, "Organic Cation Transporter-Mediated Renal Secretion of Ipratropium and Tiotropium in Rats and Humans," *Drug Metab. Dispos.*, vol. 39, no. 1, pp. 117–122, Jan. 2011.
- [82] Y. Wang and N. Behler, "In Vitro Characterization of Renal Transporters OAT1, OAT3, and OCT2," in *Optimization in Drug Discovery*, G. W. Caldwell and Z. Yan, Eds. Humana Press, 2014, pp. 417–429.
- [83] J. Biermann, D. Lang, V. Gorboulev, H. Koepsell, A. Sindic, R. Schröter, A. Zvirbliene, H. Pavenstädt, E. Schlatter, and G. Ciarimboli, "Characterization of regulatory mechanisms and states of human organic cation transporter 2," *Am. J. Physiol. - Cell Physiol.*, vol. 290, no. 6, pp. C1521–C1531, Jun. 2006.
- [84] M. A. Nagle, D. M. Truong, A. V. Dnyanmote, S.-Y. Ahn, S. A. Eraly, W. Wu, and S. K. Nigam, "Analysis of Three-dimensional Systems for Developing and Mature Kidneys Clarifies the Role of OAT1 and OAT3 in Antiviral Handling," *J. Biol. Chem.*, vol. 286, no. 1, pp. 243–251, Jan. 2011.
- [85] D. S. Miller, "Nucleoside Phosphonate Interactions with Multiple Organic Anion Transporters in Renal Proximal Tubule," *J. Pharmacol. Exp. Ther.*, vol. 299, no. 2, pp. 567–574, Nov. 2001.

- [86] A. G. Aslamkhan, D. M. Thompson, J. L. Perry, K. Bleasby, N. A. Wolff, S. Barros, D. S. Miller, and J. B. Pritchard, "The flounder organic anion transporter fOat has sequence, function, and substrate specificity similarity to both mammalian Oat1 and Oat3," *Am. J. Physiol. - Regul. Integr. Comp. Physiol.*, vol. 291, no. 6, pp. R1773–R1780, Dec. 2006.
- [87] M. Takeda, S. Khamdang, S. Narikawa, H. Kimura, M. Hosoyamada, S. H. Cha, T. Sekine, and H. Endou, "Characterization of Methotrexate Transport and Its Drug Interactions with Human Organic Anion Transporters," *J. Pharmacol. Exp. Ther.*, vol. 302, no. 2, pp. 666–671, Aug. 2002.
- [88] C. C. Wong, N. P. Botting, C. Orfila, N. Al-Maharik, and G. Williamson, "Flavonoid conjugates interact with organic anion transporters (OATs) and attenuate cytotoxicity of adefovir mediated by organic anion transporter 1 (OAT1/SLC22A6)," *Biochem. Pharmacol.*, vol. 81, no. 7, pp. 942–949, Apr. 2011.
- [89] B. Astorga, T. M. Wunz, M. Morales, S. H. Wright, and R. M. Pelis, "Differences in the substrate binding regions of renal organic anion transporters 1 (OAT1) and 3 (OAT3)," *Am. J. Physiol. - Ren. Physiol.*, vol. 301, no. 2, pp. F378–F386, Aug. 2011.
- [90] Y. Huh, R. F. Keep, and D. E. Smith, "Impact of Lipopolysaccharide-Induced Inflammation on the Disposition of the Aminocephalosporin Cefadroxil," *Antimicrob. Agents Chemother.*, vol. 57, no. 12, pp. 6171–6178, Dec. 2013.
- [91] M. Takeda, A. Tojo, T. Sekine, M. Hosoyamada, Y. Kanai, and H. Endou, "Role of organic anion transporter 1 (OAT1) in cephaloridine (CER)-induced nephrotoxicity," *Kidney Int.*, vol. 56, no. 6, pp. 2128–2136, Dec. 1999.
- [92] G. Burckhardt, "Drug transport by Organic Anion Transporters (OATs)," *Pharmacol. Ther.*, vol. 136, no. 1, pp. 106–130, Oct. 2012.
- [93] A. R. Erdman, L. M. Mangravite, T. J. Urban, L. L. Lagpacan, R. A. Castro, M. de la Cruz, W. Chan, C. C. Huang, S. J. Johns, M. Kawamoto, D. Stryke, T. R. Taylor, E. J. Carlson, T. E. Ferrin, C. M. Brett, E. G. Burchard, and K. M. Giacomini, "The human organic anion transporter 3 (OAT3; SLC22A8): genetic variation and functional genomics," *Am. J. Physiol. - Ren. Physiol.*, vol. 290, no. 4, pp. F905–F912, Apr. 2006.
- [94] Y. Shibayama, K. Ushinohama, R. Ikeda, Y. Yoshikawa, T. Motoya, Y. Takeda, and K. Yamada, "Effect of methotrexate treatment on expression levels of multidrug resistance protein 2, breast cancer resistance protein and organic anion

- transporters Oat1, Oat2 and Oat3 in rats," *Cancer Sci.*, vol. 97, no. 11, pp. 1260–1266, Nov. 2006.
- [95] T. Sekine, S. H. Cha, and H. Endou, "The multispecific organic anion transporter (OAT) family," *Pflüg. Arch.*, vol. 440, no. 3, pp. 337–350, Jul. 2000.
- [96] S. A. Eraly, "Organic anion transporter 3 inhibitors as potential novel antihypertensives," *Pharmacol. Res.*, vol. 58, no. 5–6, pp. 257–261, Nov. 2008.
- [97] Y. C. Kim, I.-B. Kim, C.-K. Noh, H. P. Quach, I.-S. Yoon, E. C. Y. Chow, M. Kim, H.-E. Jin, K. H. Cho, S.-J. Chung, K. S. Pang, and H.-J. Maeng, "Effects of  $1\alpha,25$ -Dihydroxyvitamin D<sub>3</sub>, the Natural Vitamin D Receptor Ligand, on the Pharmacokinetics of Cefdinir and Cefadroxil, Organic Anion Transporter Substrates, in Rat," *J. Pharm. Sci.*, vol. 103, no. 11, pp. 3793–3805, Nov. 2014.
- [98] S.-Y. Ahn and S. K. Nigam, "Toward a Systems Level Understanding of Organic Anion and Other Multispecific Drug Transporters: A Remote Sensing and Signaling Hypothesis," *Mol. Pharmacol.*, vol. 76, no. 3, pp. 481–490, Sep. 2009.
- [99] A. Gupta, Y. Zhang, J. D. Unadkat, and Q. Mao, "HIV Protease Inhibitors Are Inhibitors but Not Substrates of the Human Breast Cancer Resistance Protein (BCRP/ABCG2)," *J. Pharmacol. Exp. Ther.*, vol. 310, no. 1, pp. 334–341, Jul. 2004.
- [100] F. Staud and P. Pavek, "Breast cancer resistance protein (BCRP/ABCG2)," *Int. J. Biochem. Cell Biol.*, vol. 37, no. 4, pp. 720–725, Apr. 2005.
- [101] C. W. Scharenberg, "The ABCG2 transporter is an efficient Hoechst 33342 efflux pump and is preferentially expressed by immature human hematopoietic progenitors," *Blood*, vol. 99, no. 2, pp. 507–512, Jan. 2002.
- [102] G. Merino, A. I. Álvarez, M. M. Pulido, A. J. Molina, A. H. Schinkel, and J. G. Prieto, "Breast Cancer Resistance Protein (bcrp/Abcg2) Transports Fluoroquinolone Antibiotics and Affects Their Oral Availability, Pharmacokinetics, and Milk Secretion," *Drug Metab. Dispos.*, vol. 34, no. 4, pp. 690–695, Apr. 2006.
- [103] I. S. Haslam, J. A. Wright, D. A. O'Reilly, D. J. Sherlock, T. Coleman, and N. L. Simmons, "Intestinal ciprofloxacin efflux: the role of breast cancer resistance protein (ABCG2)," *Drug Metab. Dispos. Biol. Fate Chem.*, vol. 39, no. 12, pp. 2321–2328, Dec. 2011.

- [104] L. A. Doyle and D. D. Ross, "Multidrug resistance mediated by the breast cancer resistance protein BCRP (ABCG2)," *Oncogene*, vol. 22, no. 47, pp. 7340–7358, Oct. 2003.
- [105] X. Wang, T. Furukawa, T. Nitanda, M. Okamoto, Y. Sugimoto, S.-I. Akiyama, and M. Baba, "Breast cancer resistance protein (BCRP/ABCG2) induces cellular resistance to HIV-1 nucleoside reverse transcriptase inhibitors," *Mol. Pharmacol.*, vol. 63, no. 1, pp. 65–72, Jan. 2003.
- [106] A. Boumendjel, J. Boutonnat, and J. Robert, *ABC Transporters and Multidrug Resistance*. John Wiley & Sons, 2009.
- [107] Z. Ni, Z. Bikadi, M. F. Rosenberg, and Q. Mao, "Structure and Function of the Human Breast Cancer Resistance Protein (BCRP/ABCG2)," *Curr. Drug Metab.*, vol. 11, no. 7, pp. 603–617, Sep. 2010.
- [108] X. Wang, *Transporter-mediated Flavonoid-drug Interactions: In Vitro and in Vivo*. ProQuest, 2007.
- [109] P. A. Pham, C. J. L. la Porte, L. S. Lee, R. van Heeswijk, J. P. Sabo, M. M. Elgadi, P. J. Piliero, P. Barditch-Crovo, E. Fuchs, C. Flexner, and D. W. Cameron, "Differential Effects of Tipranavir plus Ritonavir on Atorvastatin or Rosuvastatin Pharmacokinetics in Healthy Volunteers," *Antimicrob. Agents Chemother.*, vol. 53, no. 10, pp. 4385–4392, Oct. 2009.
- [110] J. Weiss, J. Rose, C. H. Storch, N. Ketabi-Kiyanvash, A. Sauer, W. E. Haefeli, and T. Efferth, "Modulation of human BCRP (ABCG2) activity by anti-HIV drugs," *J. Antimicrob. Chemother.*, vol. 59, no. 2, pp. 238–245, Feb. 2007.
- [111] T. Yasujima, K. Ohta, K. Inoue, M. Ishimaru, and H. Yuasa, "Evaluation of 4',6-Diamidino-2-phenylindole as a Fluorescent Probe Substrate for Rapid Assays of the Functionality of Human Multidrug and Toxin Extrusion Proteins," *Drug Metab. Dispos.*, vol. 38, no. 4, pp. 715–721, Apr. 2010.
- [112] A. Yonezawa and K. Inui, "Importance of the multidrug and toxin extrusion MATE/SLC47A family to pharmacokinetics, pharmacodynamics/toxicodynamics and pharmacogenomics," *Br. J. Pharmacol.*, vol. 164, no. 7, pp. 1817–1825, Dec. 2011.
- [113] M. B. Wittwer, A. A. Zur, N. Khuri, Y. Kido, A. Kosaka, X. Zhang, K. M. Morrissey, A. Sali, Y. Huang, and K. M. Giacomini, "Discovery of Potent, Selective Multidrug and

- Toxin Extrusion Transporter 1 (MATE1, SLC47A1) Inhibitors Through Prescription Drug Profiling and Computational Modeling," *J. Med. Chem.*, vol. 56, no. 3, pp. 781–795, Feb. 2013.
- [114] L. J. Martínez-Guerrero and S. H. Wright, "Substrate-Dependent Inhibition of Human MATE1 by Cationic Ionic Liquids," *J. Pharmacol. Exp. Ther.*, vol. 346, no. 3, pp. 495–503, Sep. 2013.
- [115] Y. Tanihara, S. Masuda, T. Sato, T. Katsura, O. Ogawa, and K.-I. Inui, "Substrate specificity of MATE1 and MATE2-K, human multidrug and toxin extrusions/H(+)-organic cation antiporters," *Biochem. Pharmacol.*, vol. 74, no. 2, pp. 359–371, Jul. 2007.
- [116] A. Yonezawa, S. Masuda, S. Yokoo, T. Katsura, and K. Inui, "Cisplatin and Oxaliplatin, but Not Carboplatin and Nedaplatin, Are Substrates for Human Organic Cation Transporters (SLC22A1–3 and Multidrug and Toxin Extrusion Family)," *J. Pharmacol. Exp. Ther.*, vol. 319, no. 2, pp. 879–886, Nov. 2006.
- [117] G. You and M. E. Morris, *Drug Transporters: Molecular Characterization and Role in Drug Disposition*. John Wiley & Sons, 2014.
- [118] J. Grottker, A. Rosenberger, G. Burckhardt, and Y. Hagos, "Interaction of human multidrug and toxin extrusion 1 (MATE1) transporter with antineoplastic agents," *Drug Metabol. Drug Interact.*, vol. 26, no. 4, pp. 181–189, 2011.
- [119] F. Tang, H. Ouyang, J. Z. Yang, and R. T. Borchardt, "Bidirectional transport of rhodamine 123 and Hoechst 33342, fluorescence probes of the binding sites on P-glycoprotein, across MDCK-MDR1 cell monolayers," *J. Pharm. Sci.*, vol. 93, no. 5, pp. 1185–1194, May 2004.
- [120] M. Fontaine, W. F. Elmquist, and D. W. Miller, "Use of rhodamine 123 to examine the functional activity of P-glycoprotein in primary cultured brain microvessel endothelial cell monolayers," *Life Sci.*, vol. 59, no. 18, pp. 1521–1531, Sep. 1996.
- [121] G. Ciarimboli, C. S. Lancaster, E. Schlatter, R. M. Franke, J. A. Sprowl, H. Pavenstädt, V. Massmann, D. Guckel, R. H. J. Mathijssen, W. Yang, C.-H. Pui, M. V. Relling, E. Herrmann, and A. Sparreboom, "Proximal Tubular Secretion of Creatinine by Organic Cation Transporter OCT2 in Cancer Patients," *Clin. Cancer Res.*, vol. 18, no. 4, pp. 1101–1108, Feb. 2012.

- [122] M. Huls, C. D. A. Brown, A. S. Windass, R. Sayer, J. J. M. W. van den Heuvel, S. Heemskerk, F. G. M. Russel, and R. Masereeuw, "The breast cancer resistance protein transporter ABCG2 is expressed in the human kidney proximal tubule apical membrane," *Kidney Int.*, vol. 73, no. 2, pp. 220–225, Oct. 2007.
- [123] Y. Su, P. Hu, S.-H. Lee, and P. J. Sinko, "Using novobiocin as a specific inhibitor of breast cancer resistant protein to assess the role of transporter in the absorption and disposition of topotecan," *J. Pharm. Pharm. Sci. Publ. Can. Soc. Pharm. Sci. Société Can. Sci. Pharm.*, vol. 10, no. 4, pp. 519–536, 2007.
- [124] O. Zolk, T. F. Solbach, J. König, and M. F. Fromm, "Structural determinants of inhibitor interaction with the human organic cation transporter OCT2 (SLC22A2)," *Naunyn. Schmiedebergs Arch. Pharmacol.*, vol. 379, no. 4, pp. 337–348, Apr. 2009.
- [125] G. Da Violante, N. Zerrouk, I. Richard, G. Provot, J. C. Chaumeil, and P. Arnaud, "Evaluation of the cytotoxicity effect of dimethyl sulfoxide (DMSO) on Caco2/TC7 colon tumor cell cultures," *Biol. Pharm. Bull.*, vol. 25, no. 12, pp. 1600–1603, Dec. 2002.
- [126] M. F. Fromm, R. B. Kim, C. M. Stein, G. R. Wilkinson, and D. M. Roden, "Inhibition of P-Glycoprotein–Mediated Drug Transport A Unifying Mechanism to Explain the Interaction Between Digoxin and Quinidine," *Circulation*, vol. 99, no. 4, pp. 552–557, Feb. 1999.
- [127] L.-F. Blume, M. Denker, F. Gieseler, and T. Kunze, "Temperature corrected transepithelial electrical resistance (TEER) measurement to quantify rapid changes in paracellular permeability," *Pharm.*, vol. 65, no. 1, pp. 19–24, Jan. 2010.
- [128] J. B. Dressman and C. Reppas, *Oral Drug Absorption: Prediction and Assessment, Second Edition*. CRC Press, 2010.
- [129] Y. Kido, P. Matsson, and K. M. Giacomini, "Profiling of a prescription drug library for potential renal drug-drug interactions mediated by the organic cation transporter 2," *J. Med. Chem.*, vol. 54, no. 13, pp. 4548–4558, Jul. 2011.
- [130] R. Borchardt, E. Kerns, C. Lipinski, D. Thakker, and B. Wang, *Pharmaceutical Profiling in Drug Discovery for Lead Selection*. Springer Science & Business Media, 2005.

- [131] H. Zhang, F. Tasnim, J. Y. Ying, and D. Zink, "The impact of extracellular matrix coatings on the performance of human renal cells applied in bioartificial kidneys," *Biomaterials*, vol. 30, no. 15, pp. 2899–2911, May 2009.
- [132] R. Masereeuw and F. G. M. Russel, "Therapeutic implications of renal anionic drug transporters," *Pharmacol. Ther.*, vol. 126, no. 2, pp. 200–216, May 2010.
- [133] K.V.Lemley, "Anatomy of the renal interstitium," *Kidney Int*, vol. 39, no. 3, pp. 370–381, Mar. 1991.
- [134] B. Kaissling and M. Le Hir, "The renal cortical interstitium: morphological and functional aspects," *Histochem. Cell Biol.*, vol. 130, no. 2, pp. 247–262, Aug. 2008.
- [135] F. Strutz and M. Zeisberg, "Renal Fibroblasts and Myofibroblasts in Chronic Kidney Disease," *J. Am. Soc. Nephrol.*, vol. 17, no. 11, pp. 2992–2998, Nov. 2006.
- [136] F. Genovese, A. A. Manresa, D. J. Leeming, M. A. Karsdal, and P. Boor, "The extracellular matrix in the kidney: a source of novel non-invasive biomarkers of kidney fibrosis?," *Fibrogenesis Tissue Repair*, vol. 7, no. 1, p. 4, 2014.
- [137] "nephron (anatomy)," *Encyclopedia Britannica*. [Online]. Available: <http://www.britannica.com/EBchecked/topic/409282/nephron>. [Accessed: 26-Nov-2014].
- [138] J. Goldberg, *Human Nephron*. [Online]. Available: [http://www.goldiesroom.org/Multimedia/Bio\\_Images/13%20Human%20Other/14%20Nephron.jpg](http://www.goldiesroom.org/Multimedia/Bio_Images/13%20Human%20Other/14%20Nephron.jpg). [Accessed: 26-Nov-2014].
- [139] D. R. Abrahamson and V. Leardkamolkarn, "Development of kidney tubular basement membranes," *Kidney Int.*, vol. 39, no. 3, pp. 382–393, Mar. 1991.
- [140] J. H. Miner, "Renal basement membrane components," *Kidney Int.*, vol. 56, no. 6, pp. 2016–2024, Dec. 1999.
- [141] J. Davies, "The kidney development database." . [Online]. Available: <http://golgi.ana.ed.ac.uk/kidhome.html>. [Accessed: 03-Jan-2015].
- [142] M. A. Gawad, "Proximal renal tubule physiology," October. 2012. [Online]. Available: <http://www.slideshare.net/MohammedGawad/renal-physiology-iii-renal-tubular-processing>. [Accessed: 04-Mar-2015].
- [143] C. L. Triplitt, "Understanding the kidneys' role in blood glucose regulation," *Am. J. Manag. Care*, vol. 18, no. 1 Suppl, pp. S11–16, Jan. 2012.

- [144] D. E. Golan, A. H. Tashjian, and E. J. Armstrong, *Principles of Pharmacology: The Pathophysiologic Basis of Drug Therapy*. Lippincott Williams & Wilkins, 2011.
- [145] K. Ishibashi, F. C. Rector, and C. A. Berry, "Role of Na-dependent Cl/HCO<sub>3</sub> exchange in basolateral Cl transport of rabbit proximal tubules," *Am. J. Physiol.*, vol. 264, no. 2 Pt 2, pp. F251–258, Feb. 1993.
- [146] D. B. Mount and G. Gamba, "Renal potassium-chloride cotransporters," *Curr. Opin. Nephrol. Hypertens.*, vol. 10, no. 5, pp. 685–691, Sep. 2001.
- [147] M. Castañeda-Bueno, J. P. Arroyo, and G. Gamba, "Independent regulation of Na<sup>+</sup> and K<sup>+</sup> balance by the kidney," *Med. Princ. Pract. Int. J. Kuwait Univ. Health Sci. Cent.*, vol. 21, no. 2, pp. 101–114, 2012.
- [148] D. Manski, "Physiology of the kidney: Tubular reabsorption," in *Urology online*, vol. 7, .
- [149] D. C. Dawson, D. J. Wilkinson, and N. W. Richards, "Chapter 6 Basolateral Potassium Channel Noise: Signals from the Dark Side," in *Current Topics in Membranes and Transport*, vol. 37, F. Bronner, Ed. Academic Press, 1990, pp. 191–212.
- [150] R. W. Schrier, *Atlas of Diseases of the Kidney*. Wiley, 1999. [Online]. Available: <http://www.kidneyatlas.org/>.
- [151] F. Cioppi, L. Taddei, M. L. Brandi, and E. Croppi, "Idiopathic hypercalciuria and calcium renal stone disease: our cases," *Clin. Cases Miner. Bone Metab.*, vol. 6, no. 3, pp. 251–253, 2009.
- [152] O. W. Moe, P. A. Preisig and R. J. Alpern, "Cellular model of proximal tubule NaCl and NaHCO<sub>3</sub> absorption," *Kidney Int*, vol. 38, no. 4, pp. 605–611, Oct. 1990.
- [153] A. C. Brown, "Renal Physiology: Water regulation." 2004. [Online]. Available: <http://www.acbrown.com/kidney/Lectures/RnWatr/RnWatrIndx.htm>. [Accessed: 03-Mar-2015].
- [154] M. Baum and R. Quigley, "Proximal tubule water transport-lessons from aquaporin knockout mice," *Am. J. Physiol. Renal Physiol.*, vol. 289, no. 6, pp. F1193–1194, Dec. 2005.
- [155] M. W. Taal, G. M. Chertow, P. A. Marsden, K. Skorecki, A. S. L. Yu, and B. M. Brenner, *Brenner and Rector's The Kidney*. Elsevier Health Sciences, 2011.

- [156] J. M. Anderson and C. M. V. Itallie, "Physiology and Function of the Tight Junction," *Cold Spring Harb. Perspect. Biol.*, vol. 1, no. 2, p. a002584, Aug. 2009.
- [157] M. Furuse, "Molecular Basis of the Core Structure of Tight Junctions," *Cold Spring Harb. Perspect. Biol.*, vol. 2, no. 1, Jan. 2010.
- [158] M. Peckham, A. Knibbs, and S. Paxton, "The histology guide." [Online]. Available: [http://www.histology.leeds.ac.uk/tissue\\_types/epithelia/epi\\_cell\\_junctions.php](http://www.histology.leeds.ac.uk/tissue_types/epithelia/epi_cell_junctions.php). [Accessed: 30-Nov-2014].
- [159] W. M. Haschek, C. G. Rousseaux, and M. A. Wallig, *Fundamentals of Toxicologic Pathology*. Academic Press, 2009.
- [160] A. Atala, R. Lanza, J. A. Thomson, and R. Nerem, *Principles of Regenerative Medicine*. Academic Press, 2010.
- [161] A. S. Dusso, A. J. Brown, and E. Slatopolsky, "Vitamin D," *Am. J. Physiol. - Ren. Physiol.*, vol. 289, no. 1, pp. F8–F28, Jul. 2005.
- [162] B. Koeppen and B. Stanton, *Schematic of an epithelial cell illustrating the various adhering junctions. The tight junction separates the apical membrane from the basolateral membrane*. 2008.
- [163] Solvo, *Transporters in the human renal barrier*. [Online]. Available: <http://www.solvobiotech.com/barriers/renal-barrier>. [Accessed: 12-Nov-2014].
- [164] D. W. Johnson, B. K. Brew, P. Poronnik, D. I. Cook, A. Z. Györy, M. J. Field, and C. A. Pollock, "Transport characteristics of human proximal tubule cells in primary culture," *Nephrology*, vol. 3, no. 2, pp. 183–194, Apr. 1997.
- [165] G. Chung, S. Billington, N. Soomoro, and C. Brown, "Development and characterisation of rat primary proximal tubule cells," presented at the 37th Congress of IUPS, Birmingham, 2013.
- [166] "Human Proximal Tubular Cells as an In Vitro Model- for Drug Screening and Mechanistic Toxicology," [Online]. Available: <http://www.alttox.org/human-proximal-tubular-cells-as-an-in-vitro-model-for-drug-screening-and-mechanistic-toxicology/> [Accessed: 12-Nov-2014].
- [167] Y. Li, Z. Y. Oo, S. Y. Chang, P. Huang, K. G. Eng, J. L. Zeng, A. J. Kaestli, B. Gopalan, K. Kandasamy, F. Tasnim, and D. Zink, "An in vitro method for the prediction of renal proximal tubular toxicity in humans," *Toxicol. Res.*, vol. 2, no. 5, pp. 352–365, Aug. 2013.

- [168] C. D. A. Brown, R. Sayer, A. S. Windass, I. S. Haslam, M. E. De Broe, P. C. D’Haese, and A. Verhulst, “Characterisation of human tubular cell monolayers as a model of proximal tubular xenobiotic handling,” *Toxicol. Appl. Pharmacol.*, vol. 233, no. 3, pp. 428–438, Dec. 2008.
- [169] L. H. Lash, D. A. Putt, and H. Cai, “Drug metabolism enzyme expression and activity in primary cultures of human proximal tubular cells,” *Toxicology*, vol. 244, no. 1, pp. 56–65, Feb. 2008.
- [170] D. A. Vesey, W. Qi, X. Chen, C. A. Pollock, and D. W. Johnson, “Isolation and Primary Culture of Human Proximal Tubule Cells,” in *Kidney Research*, G. J. Becker and T. D. Hewitson, Eds. Humana Press, 2009, pp. 19–24.
- [171] D. A. Herzlinger, T. G. Easton, and G. K. Ojakian, “The MDCK epithelial cell line expresses a cell surface antigen of the kidney distal tubule,” *J. Cell Biol.*, vol. 93, no. 2, pp. 269–277, May 1982.
- [172] P. Thomas and T. G. Smart, “HEK293 cell line: A vehicle for the expression of recombinant proteins,” *J. Pharmacol. Toxicol. Methods*, vol. 51, no. 3, pp. 187–200, May 2005.
- [173] M. J. Ryan, G. Johnson, J. Kirk, S. M. Fuerstenberg, R. A. Zager, and B. Torok-Storb, “HK-2: an immortalized proximal tubule epithelial cell line from normal adult human kidney,” *Kidney Int.*, vol. 45, no. 1, pp. 48–57, Jan. 1994.
- [174] C. S. Bathula, S. H. Garrett, X. D. Zhou, M. A. Sens, D. A. Sens, and S. Somji, “Cadmium, Vectorial Active Transport, and MT-3–Dependent Regulation of Cadherin Expression in Human Proximal Tubular Cells,” *Toxicol. Sci.*, vol. 102, no. 2, pp. 310–318, Apr. 2008.
- [175] L. C. Racusen, C. Monteil, A. Sgrignoli, M. Lucskay, S. Marouillat, J. G. Rhim, and J. P. Morin, “Cell lines with extended in vitro growth potential from human renal proximal tubule: characterization, response to inducers, and comparison with established cell lines,” *J. Lab. Clin. Med.*, vol. 129, no. 3, pp. 318–329, Mar. 1997.
- [176] C. M. Kowolik, S. Liang, Y. Yu, and J.-K. Yee, “Cre-mediated reversible immortalization of human renal proximal tubular epithelial cells,” *Oncogene*, vol. 23, no. 35, pp. 5950–5957, Aug. 2004.
- [177] M. Wieser, G. Stadler, P. Jennings, B. Streubel, W. Pfaller, P. Ambros, C. Riedl, H. Katinger, J. Grillari, and R. Grillari-Voglauer, “hTERT alone immortalizes epithelial

- cells of renal proximal tubules without changing their functional characteristics,” *Am. J. Physiol. - Ren. Physiol.*, vol. 295, no. 5, pp. F1365–F1375, Nov. 2008.
- [178] K. Narayanan, K. M. Schumacher, F. Tasnim, K. Kandasamy, A. Schumacher, M. Ni, S. Gao, B. Gopalan, D. Zink, and J. Y. Ying, “Human embryonic stem cells differentiate into functional renal proximal tubular-like cells,” *Kidney Int.*, vol. 83, no. 4, pp. 593–603, Apr. 2013.
- [179] A. Q. Lam, B. S. Freedman, R. Morizane, P. H. Lerou, M. T. Valerius, and J. V. Bonventre, “Rapid and efficient differentiation of human pluripotent stem cells into intermediate mesoderm that forms tubules expressing kidney proximal tubular markers,” *J. Am. Soc. Nephrol. JASN*, vol. 25, no. 6, pp. 1211–1225, Jun. 2014.
- [180] N. Cartier, R. Lacave, V. Vallet, J. Hagege, R. Hellio, S. Robine, E. Pringault, F. Cluzeaud, P. Briand, and A. Kahn, “Establishment of renal proximal tubule cell lines by targeted oncogenesis in transgenic mice using the L-pyruvate kinase-SV40 (T) antigen hybrid gene,” *J. Cell Sci.*, vol. 104, no. 3, pp. 695–704, Mar. 1993.
- [181] M. Ni, J. C. M. Teo, M. S. B. Ibrahim, K. Zhang, F. Tasnim, P.-Y. Chow, D. Zink, and J. Y. Ying, “Characterization of membrane materials and membrane coatings for bioreactor units of bioartificial kidneys,” *Biomaterials*, vol. 32, no. 6, pp. 1465–1476, Feb. 2011.
- [182] Y. Sugiyama and B. Steffansen, *Transporters in Drug Development: Discovery, Optimization, Clinical Study and Regulation*. Springer Science & Business Media, 2013.
- [183] Y. Arima and H. Iwata, “Effects of surface functional groups on protein adsorption and subsequent cell adhesion using self-assembled monolayers,” *J. Mater. Chem.*, vol. 17, no. 38, pp. 4079–4087, Sep. 2007.
- [184] L. Pastewka and M. O. Robbins, “Contact between rough surfaces and a criterion for macroscopic adhesion,” *Proc. Natl. Acad. Sci.*, vol. 111, no. 9, pp. 3298–3303, Mar. 2014.
- [185] F. Poncin-Epaillard, T. Vrlicin, D. Debarnot, M. Mozetic, A. Coudreuse, G. Legeay, B. El Moualij, and W. Zorzi, “Surface treatment of polymeric materials controlling the adhesion of biomolecules,” *J. Funct. Biomater.*, vol. 3, no. 3, pp. 528–543, 2012.

- [186] S. Michaelis, R. Robelek, and J. Wegener, "Studying cell-surface interactions in vitro: a survey of experimental approaches and techniques," *Adv. Biochem. Eng. Biotechnol.*, vol. 126, pp. 33–66, 2012.
- [187] J. A. Hubbell, "Chapter 21 - Matrix Effects," in *Principles of Tissue Engineering (Fourth Edition)*, R. L. L. Vacanti, Ed. Boston: Academic Press, 2014, pp. 407–421.
- [188] N. A. Hoenich, "Cellulose for medical applications: Past, present and future," *BioResources*, vol. 1, no. 2, pp. 270–280, Aug. 2007.
- [189] H. Klinkmann and J. Vienken, "Membranes for dialysis," *Casopis Lékařů Českých*, vol. 133, no. 11, pp. 323–329, May 1994.
- [190] A. Saito, K. Sawada, and S. Fujimura, "Present status and future perspectives on the development of bioartificial kidneys for the treatment of acute and chronic renal failure patients," *Hemodial. Int.*, vol. 15, no. 2, pp. 183–192, 2011.
- [191] M. J. El-Hibri, "Polymers Containing Sulfur, Polysulfones," in *Kirk-Othmer Encyclopedia of Chemical Technology*, John Wiley & Sons, Inc., 2000.
- [192] Z. Y. Oo, K. Kandasamy, F. Tasnim, and D. Zink, "A novel design of bioartificial kidneys with improved cell performance and haemocompatibility," *J. Cell. Mol. Med.*, vol. 17, no. 4, pp. 497–507, 2013.
- [193] H. Ueda, J. Watanabe, T. Konno, M. Takai, A. Saito, and K. Ishihara, "Asymmetrically functional surface properties on biocompatible phospholipid polymer membrane for bioartificial kidney," *J. Biomed. Mater. Res. A*, vol. 77, no. 1, pp. 19–27, Apr. 2006.
- [194] P. Y. W. Dankers, J. M. Boomker, A. H. der Vlag, F. M. M. Smedts, M. C. Harmsen, and M. J. A. van Luyn, "The Use of Fibrous, Supramolecular Membranes and Human Tubular Cells for Renal Epithelial Tissue Engineering: Towards a Suitable Membrane for a Bioartificial Kidney," *Macromol. Biosci.*, vol. 10, no. 11, pp. 1345–1354, 2010.
- [195] K. Khulbe, C. Feng and T. Matsura, "Synthetic Polymeric Membranes - Characterization by Atomic Force Microscopy", 1<sup>st</sup> ed. Springer-Verlag Berlin Heidelberg, 2008.
- [196] K. Stana-Kleinschek, T. Kreze, V. Ribitsch, and S. Strnad, "Reactivity and electrokinetical properties of different types of regenerated cellulose fibres," *Colloids Surf. Physicochem. Eng. Asp.*, vol. 195, no. 1–3, pp. 275–284, Dec. 2001.

- [197] C. Yamane, T. Aoyagi, M. Ago, K. Sato, K. Okajima, and T. Takahashi, "Two Different Surface Properties of Regenerated Cellulose due to Structural Anisotropy," *Polym. J.*, vol. 38, no. 8, pp. 819–826, Jul. 2006.
- [198] F. A. Müller, L. Müller, I. Hofmann, P. Greil, M. M. Wenzel, and R. Staudenmaier, "Cellulose-based scaffold materials for cartilage tissue engineering," *Biomaterials*, vol. 27, no. 21, pp. 3955–3963, Jul. 2006.
- [199] H. Y. Erbil and R. A. Meriç, "Determination of surface free energy components of polymers from contact angle data using nonlinear programming methods," *Colloids Surf.*, vol. 33, pp. 85–97, 1988.
- [200] E.-R. Kenawy, J. M. Layman, J. R. Watkins, G. L. Bowlin, J. A. Matthews, D. G. Simpson, and G. E. Wnek, "Electrospinning of poly(ethylene-co-vinyl alcohol) fibers," *Biomaterials*, vol. 24, no. 6, pp. 907–913, Mar. 2003.
- [201] C. López-de-Dicastillo, M. Gallur, R. Catalá, R. Gavara, and P. Hernandez-Muñoz, "Immobilization of  $\beta$ -cyclodextrin in ethylene-vinyl alcohol copolymer for active food packaging applications," *J. Membr. Sci.*, vol. 353, no. 1–2, pp. 184–191, May 2010.
- [202] P. J. Martens, S. J. Bryant, and K. S. Anseth, "Tailoring the Degradation of Hydrogels Formed from Multivinyl Poly(ethylene glycol) and Poly(vinyl alcohol) Macromers for Cartilage Tissue Engineering," *Biomacromolecules*, vol. 4, no. 2, pp. 283–292, 2003.
- [203] X. Gao, Y. Tanaka, Y. Sugii, K. Mawatari, and T. Kitamori, "Basic structure and cell culture condition of a bioartificial renal tubule on chip towards a cell-based separation microdevice," *Anal. Sci. Int. J. Jpn. Soc. Anal. Chem.*, vol. 27, no. 9, pp. 907–912, 2011.
- [204] W. R. Bowen and R. J. Cooke, "Properties of microfiltration membranes: Computer automated determination of the electrokinetic properties of polycarbonate membranes," *J. Colloid Interface Sci.*, vol. 141, no. 1, pp. 280–287, Jan. 1991.
- [205] J. Basu, C. W. Genheimer, E. A. Rivera, R. Payne, K. Mihalko, K. Guthrie, A. T. Bruce, N. Robbins, D. McCoy, N. Sangha, R. Ilagan, T. Knight, T. Spencer, B. J. Wagner, M. J. Jayo, D. Jain, J. W. Ludlow, and C. Halberstadt, "Functional Evaluation of Primary Renal Cell/Biomaterial Neo-Kidney Augment Prototypes for Renal Tissue Engineering," *Cell Transplant.*, vol. 20, no. 11–12, pp. 1771–1790, Nov. 2011.

- [206] Y. Zhu, C. Gao, X. Liu, and J. Shen, "Surface Modification of Polycaprolactone Membrane via Aminolysis and Biomacromolecule Immobilization for Promoting Cytocompatibility of Human Endothelial Cells," *Biomacromolecules*, vol. 3, no. 6, pp. 1312–1319, 2002.
- [207] E. Bilensoy, C. Sarisozen, G. Esendağlı, A. L. Doğan, Y. Aktaş, M. Şen, and N. A. Mungan, "Intravesical cationic nanoparticles of chitosan and polycaprolactone for the delivery of Mitomycin C to bladder tumors," *Int. J. Pharm.*, vol. 371, no. 1–2, pp. 170–176, Apr. 2009.
- [208] M. A. Woodruff and D. W. Hutmacher, "The return of a forgotten polymer— Polycaprolactone in the 21st century," *Prog. Polym. Sci.*, vol. 35, no. 10, pp. 1217–1256, Oct. 2010.
- [209] S. Dumitriu and V. I. Popa, *Polymeric Biomaterials: Medicinal and Pharmaceutical Applications*. CRC Press, 2011.
- [210] D. Mazia, G. Schatten, and W. Sale, "Adhesion of cells to surfaces coated with polylysine. Applications to electron microscopy.," *J. Cell Biol.*, vol. 66, no. 1, pp. 198–200, Jul. 1975.
- [211] P. M. Crapo, T. W. Gilbert, and S. F. Badylak, "An overview of tissue and whole organ decellularization processes," *Biomaterials*, vol. 32, no. 12, pp. 3233–3243, Apr. 2011.
- [212] R. Katari, A. Peloso, J. P. Zambon, S. Soker, R. J. Stratta, A. Atala, and G. Orlando, "Renal Bioengineering with Scaffolds Generated from Human Kidneys," *Nephron Exp. Nephrol.*, vol. 126, no. 2, pp. 119–119, 2014.
- [213] G. Orlando, C. Booth, Z. Wang, G. Totonelli, C. L. Ross, E. Moran, M. Salvatori, P. Maghsoudlou, M. Turmaine, G. Delario, Y. Al-Shraideh, U. Farooq, A. C. Farney, J. Rogers, S. S. Iskandar, A. Burns, F. C. Marini, P. De Coppi, R. J. Stratta, and S. Soker, "Discarded human kidneys as a source of ECM scaffold for kidney regeneration technologies," *Biomaterials*, vol. 34, no. 24, pp. 5915–5925, Aug. 2013.
- [214] A. Hoppensack, C. C. Kazanecki, D. Colter, A. Gosiewska, J. Schanz, H. Walles, and K. Schenke-Layland, "A Human In Vitro Model That Mimics the Renal Proximal Tubule," *Tissue Eng. Part C Methods*, vol. 20, no. 7, pp. 599–609, Jul. 2014.

- [215] B. Kunst and S. Sourirajan, "Development and performance of some porous cellulose acetate membranes for reverse osmosis desalination," *J. Appl. Polym. Sci.*, vol. 14, no. 10, pp. 2559–2568, 1970.
- [216] M. Ulbricht, "Advanced functional polymer membranes," *Polymer*, vol. 47, no. 7, pp. 2217–2262, Mar. 2006.
- [217] E. Boland D., "Electrospinning collagen and elastin: preliminary vascular tissue engineering," *Front. Biosci.*, vol. 9, no. 1–3, p. 1422, 2004.
- [218] F. Yang, R. Murugan, S. Wang, and S. Ramakrishna, "Electrospinning of nano/micro scale poly(l-lactic acid) aligned fibers and their potential in neural tissue engineering," *Biomaterials*, vol. 26, no. 15, pp. 2603–2610, May 2005.
- [219] H. Yoshimoto, Y. M. Shin, H. Terai, and J. P. Vacanti, "A biodegradable nanofiber scaffold by electrospinning and its potential for bone tissue engineering," *Biomaterials*, vol. 24, no. 12, pp. 2077–2082, May 2003.
- [220] J. Zeng, X. Xu, X. Chen, Q. Liang, X. Bian, L. Yang, and X. Jing, "Biodegradable electrospun fibers for drug delivery," *J. Controlled Release*, vol. 92, no. 3, pp. 227–231, Oct. 2003.
- [221] D. S. Katti, K. W. Robinson, F. K. Ko, and C. T. Laurencin, "Bioresorbable nanofiber-based systems for wound healing and drug delivery: Optimization of fabrication parameters," *J. Biomed. Mater. Res. B Appl. Biomater.*, vol. 70B, no. 2, pp. 286–296, 2004.
- [222] T. J. Sill and H. A. von Recum, "Electrospinning: Applications in drug delivery and tissue engineering," *Biomaterials*, vol. 29, no. 13, pp. 1989–2006, May 2008.
- [223] N.-N. Bui, M. L. Lind, E. M. V. Hoek, and J. R. McCutcheon, "Electrospun nanofiber supported thin film composite membranes for engineered osmosis," *J. Membr. Sci.*, vol. 385–386, pp. 10–19, Dec. 2011.
- [224] R. Gopal, S. Kaur, Z. Ma, C. Chan, S. Ramakrishna, and T. Matsuura, "Electrospun nanofibrous filtration membrane," *J. Membr. Sci.*, vol. 281, no. 1–2, pp. 581–586, Sep. 2006.
- [225] J. F. Moulder, W. F. Stickle, P. Sobol, and K. D. Bomben, *Handbook of X-ray photoelectron spectroscopy*, vol. 40. Eden Prairie, MN: Perkin Elmer, 1992.

- [226] M. Hayama, K. Yamamoto, F. Kohori, and K. Sakai, "How polysulfone dialysis membranes containing polyvinylpyrrolidone achieve excellent biocompatibility?," *J. Membr. Sci.*, vol. 234, no. 1–2, pp. 41–49, May 2004.
- [227] J. C. M. Teo, R. R. G. Ng, C. P. Ng, and A. W. H. Lin, "Surface characteristics of acrylic modified polysulfone membranes improves renal proximal tubule cell adhesion and spreading," *Acta Biomater.*, vol. 7, no. 5, pp. 2060–2069, May 2011.
- [228] A. Higuchi, K. Shirano, M. Harashima, B. O. Yoon, M. Hara, M. Hattori, and K. Imamura, "Chemically modified polysulfone hollow fibers with vinylpyrrolidone having improved blood compatibility," *Biomaterials*, vol. 23, no. 13, pp. 2659–2666, Jul. 2002.
- [229] P. S. Singh, K. Parashuram, S. Maurya, P. Ray, and A. V. R. Reddy, "Structure-performance-fouling studies of polysulfone microfiltration hollow fibre membranes," *Bull. Mater. Sci.*, vol. 35, no. 5, pp. 817–822, Oct. 2012.
- [230] "Effects of heat treatment and poly(vinylpyrrolidone) (PVP) polymer on electrocatalytic activity of polyhedral Pt nanoparticles towards their methanol oxidation - Springer."
- [231] "Adhesion of cells to polystyrene surfaces," *J. Cell Biol.*, vol. 97, no. 5, pp. 1500–1506, Nov. 1983.
- [232] M. Mulder, *Basic Principles of Membrane Technology*. Springer Science & Business Media, 1996.
- [233] Y. Koc, A. J. de Mello, G. McHale, M. I. Newton, P. Roach, and N. J. Shirtcliffe, "Nano-scale superhydrophobicity: suppression of protein adsorption and promotion of flow-induced detachment," *Lab. Chip*, vol. 8, no. 4, pp. 582–586, Apr. 2008.
- [234] J. Berthier and K. Brakke, *The Physics of Microdroplets*. John Wiley & Sons, 2012.
- [235] R. M. Boom, I. M. Wienk, T. van den Boomgaard, and C. A. Smolders, "Microstructures in phase inversion membranes. Part 2. The role of a polymeric additive," *J. Membr. Sci.*, vol. 73, no. 2–3, pp. 277–292, Oct. 1992.
- [236] S. H. Yoo, J. H. Kim, J. Y. Jho, J. Won, and Y. S. Kang, "Influence of the addition of PVP on the morphology of asymmetric polyimide phase inversion membranes: effect of PVP molecular weight," *J. Membr. Sci.*, vol. 236, no. 1–2, pp. 203–207, Jun. 2004.

- [237] H. Shearer, M. J. Ellis, S. P. Perera, and J. B. Chaudhuri, "Effects of common sterilization methods on the structure and properties of poly(D,L lactic-co-glycolic acid) scaffolds," *Tissue Eng.*, vol. 12, no. 10, pp. 2717–2727, Oct. 2006.
- [238] M. J. Ellis and J. B. Chaudhuri, "Poly(lactic-co-glycolic acid) hollow fibre membranes for use as a tissue engineering scaffold," *Biotechnol. Bioeng.*, vol. 96, no. 1, pp. 177–187, Jan. 2007.
- [239] I. Martin, D. Wendt, and M. Heberer, "The role of bioreactors in tissue engineering," *Trends Biotechnol.*, vol. 22, no. 2, pp. 80–86, Feb. 2004.
- [240] G. Guglielmi, D. Chiarani, S. J. Judd, and G. Andreottola, "Flux criticality and sustainability in a hollow fibre submerged membrane bioreactor for municipal wastewater treatment," *J. Membr. Sci.*, vol. 289, no. 1–2, pp. 241–248, Feb. 2007.
- [241] M. A. Mehaia and M. Cheryan, "Hollow fibre bioreactor for ethanol production: Application to the conversion of lactose by *Kluyveromyces fragilis*," *Enzyme Microb. Technol.*, vol. 6, no. 3, pp. 117–120, Mar. 1984.
- [242] J. D. Brotherton and P. C. Chau, "Modeling of Axial-Flow Hollow Fiber Cell Culture Bioreactors," *Biotechnol. Prog.*, vol. 12, no. 5, pp. 575–590, 1996.
- [243] Q. A. Rafiq, K. M. Brosnan, K. Coopman, A. W. Nienow, and C. J. Hewitt, "Culture of human mesenchymal stem cells on microcarriers in a 5 l stirred-tank bioreactor," *Biotechnol. Lett.*, vol. 35, no. 8, pp. 1233–1245, Aug. 2013.
- [244] G. Vunjak-Novakovic, L. E. Freed, R. J. Biron, and R. Langer, "Effects of mixing on the composition and morphology of tissue-engineered cartilage," *AIChE J.*, vol. 42, no. 3, pp. 850–860, Mar. 1996.
- [245] N. Plunkett and F. J. O'Brien, "Bioreactors in tissue engineering," *Technol. Health Care Off. J. Eur. Soc. Eng. Med.*, vol. 19, no. 1, pp. 55–69, 2011.
- [246] A. W. Nienow, "Hydrodynamics of Stirred Bioreactors," *Appl. Mech. Rev.*, vol. 51, no. 1, pp. 3–32, Jan. 1998.
- [247] J. S. Temenoff and A. G. Mikos, "Review: tissue engineering for regeneration of articular cartilage," *Biomaterials*, vol. 21, no. 5, pp. 431–440, Mar. 2000.
- [248] A. B. Yeatts and J. P. Fisher, "Bone tissue engineering bioreactors: Dynamic culture and the influence of shear stress," *Bone*, vol. 48, no. 2, pp. 171–181, Feb. 2011.
- [249] F. dos Santos, P. Z. Andrade, M. M. Abecasis, J. M. Gimble, L. G. Chase, A. M. Campbell, S. Boucher, M. C. Vemuri, C. L. da Silva, and J. M. S. Cabral, "Toward a

- clinical-grade expansion of mesenchymal stem cells from human sources: a microcarrier-based culture system under xeno-free conditions," *Tissue Eng. Part C Methods*, vol. 17, no. 12, pp. 1201–1210, Dec. 2011.
- [250] G. Vunjak-Novakovic, I. Martin, B. Obradovic, S. Treppo, A. J. Grodzinsky, R. Langer, and L. E. Freed, "Bioreactor cultivation conditions modulate the composition and mechanical properties of tissue-engineered cartilage," *J. Orthop. Res. Off. Publ. Orthop. Res. Soc.*, vol. 17, no. 1, pp. 130–138, Jan. 1999.
- [251] R. L. Carrier, M. Papadaki, M. Rupnick, F. J. Schoen, N. Bursac, R. Langer, L. E. Freed, and G. Vunjak-Novakovic, "Cardiac tissue engineering: cell seeding, cultivation parameters, and tissue construct characterization," *Biotechnol. Bioeng.*, vol. 64, no. 5, pp. 580–589, Sep. 1999.
- [252] H. W. Rhee, H. E. Zhou, S. Pathak, A. S. Multani, S. Pennanen, T. Visakorpi, and L. W. Chung, "Permanent phenotypic and genotypic changes of prostate cancer cells cultured in a three-dimensional rotating-wall vessel," *In Vitro Cell. Dev. Biol. Anim.*, vol. 37, no. 3, pp. 127–140, Mar. 2001.
- [253] L. L. Licato, V. G. Prieto, and E. A. Grimm, "A novel preclinical model of human malignant melanoma utilizing bioreactor rotating-wall vessels," *Vitro Cell. Dev. Biol. - Anim.*, vol. 37, no. 3, pp. 121–126, Mar. 2001.
- [254] S. Saini and T. M. Wick, "Concentric cylinder bioreactor for production of tissue engineered cartilage: effect of seeding density and hydrodynamic loading on construct development," *Biotechnol. Prog.*, vol. 19, no. 2, pp. 510–521, Apr. 2003.
- [255] V. I. Sikavitsas, G. N. Bancroft, and A. G. Mikos, "Formation of three-dimensional cell/polymer constructs for bone tissue engineering in a spinner flask and a rotating wall vessel bioreactor," *J. Biomed. Mater. Res.*, vol. 62, no. 1, pp. 136–148, Oct. 2002.
- [256] T.-W. Wang, H.-C. Wu, H.-Y. Wang, F.-H. Lin, and J.-S. Sun, "Regulation of adult human mesenchymal stem cells into osteogenic and chondrogenic lineages by different bioreactor systems," *J. Biomed. Mater. Res. A*, vol. 88, no. 4, pp. 935–946, Mar. 2009.
- [257] D. Matziolis, J. Tuischer, G. Matziolis, G. Kasper, G. Duda, and C. Perka, "Osteogenic Predifferentiation of Human Bone Marrow-Derived Stem Cells by Short-Term Mechanical Stimulation," *Open Orthop. J.*, vol. 5, pp. 1–6, Jan. 2011.

- [258] C. Y. L. Woon, A. Kraus, S. S. Raghavan, B. C. Pridgen, K. Megerle, H. Pham, and J. Chang, "Three-Dimensional-Construct Bioreactor Conditioning in Human Tendon Tissue Engineering," *Tissue Eng. Part A*, vol. 17, no. 19–20, pp. 2561–2572, Oct. 2011.
- [259] G. H. Altman, H. H. Lu, R. L. Horan, T. Calabro, D. Ryder, D. L. Kaplan, P. Stark, I. Martin, J. C. Richmond, and G. Vunjak-Novakovic, "Advanced bioreactor with controlled application of multi-dimensional strain for tissue engineering," *J. Biomech. Eng.*, vol. 124, no. 6, pp. 742–749, Dec. 2002.
- [260] V. I. Sikavitsas, G. N. Bancroft, H. L. Holtorf, J. A. Jansen, and A. G. Mikos, "Mineralized matrix deposition by marrow stromal osteoblasts in 3D perfusion culture increases with increasing fluid shear forces," *Proc. Natl. Acad. Sci.*, vol. 100, no. 25, pp. 14683–14688, Dec. 2003.
- [261] M. J. Helmedag, S. Weinandy, Y. Marquardt, J. M. Baron, N. Pallua, C. V. Suschek, and S. Jockenhoevel, "The Effects of Constant Flow Bioreactor Cultivation and Keratinocyte Seeding Densities on Prevascularized Organotypic Skin Grafts Based on a Fibrin Scaffold," *Tissue Eng. Part A*, vol. 21, no. 1–2, pp. 343–352, Jan. 2015.
- [262] R. M. Tostões, S. B. Leite, M. Serra, J. Jensen, P. Björquist, M. J. T. Carrondo, C. Brito, and P. M. Alves, "Human liver cell spheroids in extended perfusion bioreactor culture for repeated-dose drug testing," *Hepatology*, vol. 55, no. 4, pp. 1227–1236, 2012.
- [263] T. Kofidis, A. Lenz, J. Boublik, P. Akhyari, B. Wachsmann, K. Mueller-Stahl, M. Hofmann, and A. Haverich, "Pulsatile perfusion and cardiomyocyte viability in a solid three-dimensional matrix," *Biomaterials*, vol. 24, no. 27, pp. 5009–5014, Dec. 2003.
- [264] D. Pazzano, K. A. Mercier, J. M. Moran, S. S. Fong, D. D. DiBiasio, J. X. Rulfs, S. S. Kohles, and L. J. Bonassar, "Comparison of Chondrogenesis in Static and Perfused Bioreactor Culture," *Biotechnol. Prog.*, vol. 16, no. 5, pp. 893–896, 2000.
- [265] S. Partap, N. Plunkett, and F. J. O'Brien, "Bioreactors in Tissue Engineering," *InTech*, 2010.
- [266] A. S. Goldstein, T. M. Juarez, C. D. Helmke, M. C. Gustin, and A. G. Mikos, "Effect of convection on osteoblastic cell growth and function in biodegradable polymer foam scaffolds," *Biomaterials*, vol. 22, no. 11, pp. 1279–1288, Jun. 2001.

- [267] T. Davisson, R. L. Sah, and A. Ratcliffe, "Perfusion increases cell content and matrix synthesis in chondrocyte three-dimensional cultures," *Tissue Eng.*, vol. 8, no. 5, pp. 807–816, Oct. 2002.
- [268] J.-K. Park and D.-H. Lee, "Bioartificial liver systems: current status and future perspective," *J. Biosci. Bioeng.*, vol. 99, no. 4, pp. 311–319, Apr. 2005.
- [269] J. C. Gerlach, K. Zeilinger, and J. F. Patzer li, "Bioartificial liver systems: why, what, whither?," *Regen. Med.*, vol. 3, no. 4, pp. 575–595, Jul. 2008.
- [270] E. Schmelzer, K. Mutig, P. Schrade, S. Bachmann, J. C. Gerlach, and K. Zeilinger, "Effect of human patient plasma ex vivo treatment on gene expression and progenitor cell activation of primary human liver cells in multi-compartment 3D perfusion bioreactors for extra-corporeal liver support," *Biotechnol. Bioeng.*, vol. 103, no. 4, pp. 817–827, 2009.
- [271] K. Zeilinger, T. Schreiter, M. Darnell, T. Söderdahl, M. Lübberstedt, B. Dillner, D. Knobloch, A. K. Nüssler, J. C. Gerlach, and T. B. Andersson, "Scaling Down of a Clinical Three-Dimensional Perfusion Multicompartment Hollow Fiber Liver Bioreactor Developed for Extracorporeal Liver Support to an Analytical Scale Device Useful for Hepatic Pharmacological In Vitro Studies," *Tissue Eng. Part C Methods*, vol. 17, no. 5, pp. 549–556, May 2011.
- [272] W. Neuhaus, R. Lauer, S. Oelzant, U. P. Fringeli, G. F. Ecker, and C. R. Noe, "A novel flow based hollow-fiber blood-brain barrier in vitro model with immortalised cell line PBMEC/C1-2," *J. Biotechnol.*, vol. 125, no. 1, pp. 127–141, Aug. 2006.
- [273] O. Lacombe, O. Videau, D. Chevillon, A.-C. Guyot, C. Contreras, S. Blondel, L. Nicolas, A. Ghetas, H. Bénech, E. Thevenot, A. Pruvost, S. Bolze, L. Krzaczkowski, C. Prévost, and A. Mabondzo, "In Vitro Primary Human and Animal Cell-Based Blood–Brain Barrier Models as a Screening Tool in Drug Discovery," *Mol. Pharm.*, vol. 8, no. 3, pp. 651–663, Jun. 2011.
- [274] H. Ye, D. B. Das, J. T. Triffitt, and Z. Cui, "Modelling nutrient transport in hollow fibre membrane bioreactors for growing three-dimensional bone tissue," *J. Membr. Sci.*, vol. 272, no. 1–2, pp. 169–178, Mar. 2006.
- [275] J. E. Prenosil and P. E. Villeneuve, "Automated production of cultured epidermal autografts and sub-confluent epidermal autografts in a computer controlled bioreactor," *Biotechnol. Bioeng.*, vol. 59, no. 6, pp. 679–683, Sep. 1998.

- [276] R. M. Sutherland, J. A. McCredie, and W. R. Inch, "Growth of Multicell Spheroids in Tissue Culture as a Model of Nodular Carcinomas," *J. Natl. Cancer Inst.*, vol. 46, no. 1, pp. 113–120, Jan. 1971.
- [277] L. A. McMahon, A. J. Reid, V. A. Campbell, and P. J. Prendergast, "Regulatory effects of mechanical strain on the chondrogenic differentiation of MSCs in a collagen-GAG scaffold: experimental and computational analysis," *Ann. Biomed. Eng.*, vol. 36, no. 2, pp. 185–194, Feb. 2008.
- [278] D. A. Buffington, A. J. Westover, K. A. Johnston, and H. D. Humes, "The bioartificial kidney," *Transl. Res.*, vol. 163, no. 4, pp. 342–351, Apr. 2014.
- [279] T. K. Ip, P. Aebischer, and P. M. Galletti, "Cellular control of membrane permeability. Implications for a bioartificial renal tubule," *ASAIO Trans. Am. Soc. Artif. Intern. Organs*, vol. 34, no. 3, pp. 351–355, Sep. 1988.
- [280] H. D. Humes, W. H. Fissell, W. F. Weitzel, D. A. Buffington, A. J. Westover, S. M. MacKay, and J. M. Gutierrez, "Metabolic replacement of kidney function in uremic animals with a bioartificial kidney containing human cells," *Am. J. Kidney Dis. Off. J. Natl. Kidney Found.*, vol. 39, no. 5, pp. 1078–1087, May 2002.
- [281] H. D. Humes, D. A. Buffington, S. M. MacKay, A. J. Funke, and W. F. Weitzel, "Replacement of renal function in uremic animals with a tissue-engineered kidney," *Nat. Biotechnol.*, vol. 17, no. 5, pp. 451–455, May 1999.
- [282] W. H. Fissell, D. B. Dyke, W. F. Weitzel, D. A. Buffington, A. J. Westover, S. M. MacKay, J. M. Gutierrez, and H. D. Humes, "Bioartificial kidney alters cytokine response and hemodynamics in endotoxin-challenged uremic animals," *Blood Purif.*, vol. 20, no. 1, pp. 55–60, 2002.
- [283] W. H. Fissell, L. Lou, S. Abrishami, D. A. Buffington, and H. D. Humes, "Bioartificial kidney ameliorates gram-negative bacteria-induced septic shock in uremic animals," *J. Am. Soc. Nephrol. JASN*, vol. 14, no. 2, pp. 454–461, Feb. 2003.
- [284] G. M. Chertow and S. S. Waikar, "Toward the Promise of Renal Replacement Therapy," *J. Am. Soc. Nephrol.*, vol. 19, no. 5, pp. 839–840, May 2008.
- [285] M. Essig and G. Friedlander, "Tubular shear stress and phenotype of renal proximal tubular cells," *J. Am. Soc. Nephrol. JASN*, vol. 14 Suppl 1, pp. S33–35, Jun. 2003.

- [286] Y. Fujita, T. Kakuta, M. Asano, J. Itoh, K. Sakabe, T. Tokimasa, and A. Saito, "Evaluation of Na<sup>+</sup> active transport and morphological changes for bioartificial renal tubule cell device using Madin-Darby canine kidney cells," *Tissue Eng.*, vol. 8, no. 1, pp. 13–24, Feb. 2002.
- [287] N. Ozgen, M. Terashima, T. Aung, Y. Sato, C. Isoe, T. Kakuta, and A. Saito, "Evaluation of long-term transport ability of a bioartificial renal tubule device using LLC-PK1 cells," *Nephrol. Dial. Transplant. Off. Publ. Eur. Dial. Transpl. Assoc. - Eur. Ren. Assoc.*, vol. 19, no. 9, pp. 2198–2207, Sep. 2004.
- [288] C. P. Ng, Y. Zhuang, A. W. H. Lin, and J. C. M. Teo, "A Fibrin-Based Tissue-Engineered Renal Proximal Tubule for Bioartificial Kidney Devices: Development, Characterization and *In Vitro* Transport Study," *Int. J. Tissue Eng.*, vol. 2013, p. e319476, Nov. 2012.
- [289] K.-J. Jang, H. S. Cho, D. H. Kang, W. G. Bae, T.-H. Kwon, and K.-Y. Suh, "Fluid-shear-stress-induced translocation of aquaporin-2 and reorganization of actin cytoskeleton in renal tubular epithelial cells," *Integr. Biol.*, vol. 3, no. 2, p. 134, 2011.
- [290] R. j. Shipley, A. j. Davidson, K. Chan, J. b. Chaudhuri, S. . Waters, and M. j. Ellis, "A strategy to determine operating parameters in tissue engineering hollow fiber bioreactors," *Biotechnol. Bioeng.*, vol. 108, no. 6, pp. 1450–1461, 2011.
- [291] L. J. Kelsey, M. R. Pillarella, and A. L. Zydney, "Theoretical analysis of convective flow profiles in a hollow-fiber membrane bioreactor," *Chem. Eng. Sci.*, vol. 45, no. 11, pp. 3211–3220, 1990.
- [292] N. S. Abdullah and D. B. Das, "Modelling nutrient transport in hollow fibre membrane bioreactor for growing bone tissue with consideration of multi-component interactions," *Chem. Eng. Sci.*, vol. 62, no. 21, pp. 5821–5839, Nov. 2007.
- [293] A. Apelblat, A. Katzir-Katchalsky, and A. Silberberg, "A mathematical analysis of capillary-tissue fluid exchange," *Biorheology*, vol. 11, no. 1, pp. 1–49, Jan. 1974.
- [294] W. J. Bruining, "A general description of flows and pressures in hollow fiber membrane modules," *Chem. Eng. Sci.*, vol. 44, no. 6, pp. 1441–1447, 1989.
- [295] G. Kretzmer and K. Schügerl, "Response of mammalian cells to shear stress," *Appl. Microbiol. Biotechnol.*, vol. 34, no. 5, pp. 613–616, Feb. 1991.

- [296] C. Heath and G. Belfort, "Immobilization of suspended mammalian cells: Analysis of hollow fiber and microcapsule bioreactors," in *Vertebrate Cell Culture I*, Springer Berlin Heidelberg, 1987, pp. 1–31.
- [297] N. S. Abdullah, D. R. Jones, and D. B. Das, "Nutrient transport in bioreactors for bone tissue growth: Why do hollow fibre membrane bioreactors work?," *Chem. Eng. Sci.*, vol. 64, no. 1, pp. 109–125, Jan. 2009.
- [298] P. D. Hay, A. R. Veitch, M. D. Smith, R. B. Cousins, and J. D. Gaylor, "Oxygen transfer in a diffusion-limited hollow fiber bioartificial liver," *Artif. Organs*, vol. 24, no. 4, pp. 278–288, Apr. 2000.
- [299] Y. Kawazoe, S. Eguchi, N. Sugiyama, Y. Kamohara, H. Fujioka, and T. Kanematsu, "Comparison between bioartificial and artificial liver for the treatment of acute liver failure in pigs," *World J. Gastroenterol. WJG*, vol. 12, no. 46, pp. 7503–7507, Dec. 2006.
- [300] S. L. Nyberg, J. Hardin, B. Amiot, U. A. Argikar, R. P. Rimmel, and P. Rinaldo, "Rapid, large-scale formation of porcine hepatocyte spheroids in a novel spheroid reservoir bioartificial liver," *Liver Transplant. Off. Publ. Am. Assoc. Study Liver Dis. Int. Liver Transplant. Soc.*, vol. 11, no. 8, pp. 901–910, Aug. 2005.
- [301] J. F. Patzer, "Oxygen consumption in a hollow fiber bioartificial liver--revisited," *Artif. Organs*, vol. 28, no. 1, pp. 83–98, Jan. 2004.
- [302] T. D. Sielaff, S. L. Nyberg, M. D. Rollins, M. Y. Hu, B. Amiot, A. Lee, F. J. Wu, W. S. Hu, and F. B. Cerra, "Characterization of the three-compartment gel-entrapment porcine hepatocyte bioartificial liver," *Cell Biol. Toxicol.*, vol. 13, no. 4–5, pp. 357–364, Jul. 1997.
- [303] J. P. Sullivan, D. R. Harris, and A. F. Palmer, "Convection and hemoglobin-based oxygen carrier enhanced oxygen transport in a hepatic hollow fiber bioreactor," *Artif. Cells. Blood Substit. Immobil. Biotechnol.*, vol. 36, no. 4, pp. 386–402, 2008.
- [304] M. Wurm, C. Woess, K. Libiseller, B. Beer, and M. Pavlic, "Challenging small human hepatocytes with opiates: further characterization of a novel prototype bioartificial liver," *Tissue Eng. Part A*, vol. 16, no. 3, pp. 807–813, Mar. 2010.
- [305] Q. Zhang, X. Lu, and L. Zhao, "Preparation of Polyvinylidene Fluoride (PVDF) Hollow Fiber Hemodialysis Membranes," *Membranes*, vol. 4, no. 1, pp. 81–95, 2014.

- [306] H. Chang and Y. Wang, "Cell responses to surface and architecture of tissue engineering scaffolds," in *Regenerative Medicine and Tissue Engineering- Cells and Biomaterials*, vol. 27, InTech, 2011, pp. 569–588.
- [307] D. Schop, R. van Dijkhuizen-Radersma, E. Borgart, F. W. Janssen, H. Rozemuller, H.-J. Prins, and J. D. de Bruijn, "Expansion of human mesenchymal stromal cells on microcarriers: growth and metabolism," *J. Tissue Eng. Regen. Med.*, vol. 4, no. 2, pp. 131–140, Feb. 2010.
- [308] M. Hay, D. W. Thomas, J. L. Craighead, C. Economides, and J. Rosenthal, "Clinical development success rates for investigational drugs," *Nat. Biotechnol.*, vol. 32, no. 1, pp. 40–51, Jan. 2014.
- [309] T.-S. Chung, Z.-L. Xu, and W. Lin, "Fundamental understanding of the effect of air-gap distance on the fabrication of hollow fiber membranes," *J. Appl. Polym. Sci.*, vol. 72, no. 3, pp. 379–395, Apr. 1999.
- [310] M. Neunlist, F. Toumi, T. Oreschkova, M. Denis, J. Leborgne, C. L. Laboisse, J.-P. Galmiche, and A. Jarry, "Human ENS regulates the intestinal epithelial barrier permeability and a tight junction-associated protein ZO-1 via VIPergic pathways," *Am. J. Physiol. Gastrointest. Liver Physiol.*, vol. 285, no. 5, pp. G1028–1036, Nov. 2003.
- [311] T. Duff, S. Carter, G. Feldman, G. McEwan, W. Pfaller, P. Rhodes, M. Ryan, and G. Hawksworth, "Transepithelial resistance and inulin permeability as endpoints in in vitro nephrotoxicity testing," *Altern. Lab. Anim. ATLA*, vol. 30 Suppl 2, pp. 53–59, Dec. 2002.

# Appendices

## 1. List of Equipment

- Agilent 2100 bioanalyzer; Agilent Technologies, UK
- Contact angle system; Dataphysics Instruments, Germany
- CM-0045 CO<sub>2</sub> meter; CO<sub>2</sub> Meter Inc, USA
- Delta 20BM spin coater; BLE Laboratory Equipment, Germany
- Emitech SC7640 Sputter Coater; Quorum Technologies, UK
- Eppendorf 5804 centrifuge; Eppendorf, UK
- FEGSEM; Carl Zeiss, Germany
- Fluostar Omega; BMG Labtech, Germany
- Galaxy 170r Incubator; New Brunswick Scientific, UK
- Grant 24L unstirred water bath; Thermo Scientific, UK
- Heraeus HERAcell 150 CO<sub>2</sub> Incubator; Thermo Scientific, UK
- Herasafe KS Class II Biosafety Cabinet; Thermo Scientific, UK
- K-Alpha™ X-ray photon spectrometer system, Thermo Scientific, UK
- Magnetic Stirrer 11-102-17S; Thermo Scientific, UK
- MilliQ ultrafiltration unit, Millipore, UK
- Nanodrop 2000c, Thermo Scientific, UK
- Nikon Eclipse Ti Fluorescence Microscope; Nikon Instruments, UK
- Nikon TS-100 Inverted Microscope; Nikon Instruments, UK
- NucleoCounter NC-100 mammalian cell counter; Chemometec, Denmark
- NucleoCounter NC-3000 mammalian cell counter; Chemometec, Denmark
- PHD Ultra syringe pump; Harvard Apparatus, USA
- Polarstar Omega, BMG Labtech, Germany
- REMS Autosampler, World Precision Instruments, USA
- Sanyo MIR-S100C Flask Shaker Platform; Sanyo Biomedical, UK
- StepOne plus RT-PCR system; Applied Technologies, UK
- Systec VX-95 autoclave, Systec, Germany
- Veeco Explorer atomic force microscope, Veeco Instruments, USA

## 2. List of Equations

### 2.1. Equation 1: Cell Counting and viability

$$(1) Cx(\bar{v}) = Cx(c) / 4$$

$$(2) Cx(\bar{v})/mL = Cx(\bar{v}) * df$$

$$(3) Cx(v) = Cx(\bar{v})/mL * V(0)$$

$$(4) V(f) = Cx(v) / SD$$

Where:  $Cx(\bar{v})$  is the average viable cells,  $Cx(c)$  is the cell count on the haemocytometer,  $Cx(\bar{v})/mL$  is the average viable cells per mL,  $df$  is the dilution factor of trypan blue to sample,  $Cx(v)$  is the total viable cells,  $V(0)$  is the cell suspension volume,  $V(f)$  is the resuspension volume and  $SD$  is seeding density.

### 2.2. Equation 2: Population Doublings

$$\text{Population doubling} = 3.32 * (\log Cx(t) - \log Cx(0)) + x$$

Where  $Cx(t)$  is the cell yield,  $Cx(0)$  is the initial cell number and  $x$  is the previous number of cell doublings.

### 2.3. Equation 3: Transepithelial electrical resistance (TEER $\Omega/cm^2$ )

$$TEER = (TEER(\bar{s}) - TEER(\bar{b})) / SA$$

Where:  $TEER(\bar{s})$  is the average TEER measurement of the sample well,  $TEER(\bar{b})$  is the average TEER measurement of the blank well and  $SA$  is the surface area of the transwell insert.

#### 2.4. Equation 4: Apparent Permeability ( $P_{app} \times 10^6 / \text{cm}^2$ )

$$P_{app} = (dQ/dt) * V / A * C_0$$

Where:  $dQ/dt$  is the rate of drug transport ( $\text{nmol L}^{-1}/\text{min}$ ),  $V$  is the volume of the receiver compartment (mL),  $A$  is the surface area of the membrane ( $\text{cm}^2$ ) and  $C_0$  is the initial donor concentration (nmol/L)

#### 2.5. Equation 5: Efflux Ratio

$$\text{Efflux ratio} = P_{app} (B \rightarrow A) / P_{app} (A \rightarrow B)$$

Where:  $P_{app} (B \rightarrow A)$  is the apparent permeability in the basolateral to apical direction and  $P_{app} (A \rightarrow B)$  is the apparent permeability in the apical to basolateral direction.

#### 2.6. Equation 6: Fibre porosity (%)

$$\varepsilon = (((W_w - W_d) / \rho_w) / ((W_w - W_d) / \rho_w) + \rho_p) * 100\%$$

Where:  $W_w$  is the mass of the wet membrane (g),  $W_d$  is the mass of the dry membrane (g),  $\rho_w$  is the density of water ( $1.0 \text{ g/cm}^3$ ) and  $\rho_p$  is the density of the membrane ( $\text{g/cm}^3$ ).

#### 2.7. Equation 7: Volumetric water flux ( $\text{m}^3/\text{m}^2 \cdot \text{s}$ )

$$J = V_p / tA$$

Where:  $V_p$  is the volume of permeate collected,  $t$  is time (h) and  $A$  is membrane surface area ( $\text{m}^2$ ).

#### 2.8. Equation 8: Hydraulic permeability ( $\text{Pa m}^3/\text{m}^2 \cdot \text{s}$ )

$$L_p = J / \Delta P$$

Where:  $J$  is the volumetric water flux ( $\text{m}^3/\text{m}^2 \cdot \text{s}$ ) and  $\Delta P$  is the transmembrane pressure (Pa)

### 3. Development of MDCKII cell growth in transwells

To ascertain culture conditions for MDCKII growth on the porous transwell inserts due to poor visibility through the membrane insert, cells were seeded at a range of cell densities and cultured over a period of 7 days on 12 well transwell inserts (0.4µm, 1.12cm<sup>2</sup> insert area). LY permeation percentages were obtained daily from day 3 onwards. The seeding densities:  $1 \times 10^5$ ,  $5 \times 10^5$ ,  $1 \times 10^6$ ,  $2 \times 10^6$  and  $5 \times 10^6$  were calculated at cells per well, and medium was changed on day 2 after seeding. It was noted that the wells seeded at  $2 \times 10^6$  and  $5 \times 10^6$  contained detached cells in the medium indicative of an excess of cells, at seeding on the day 2 medium change.

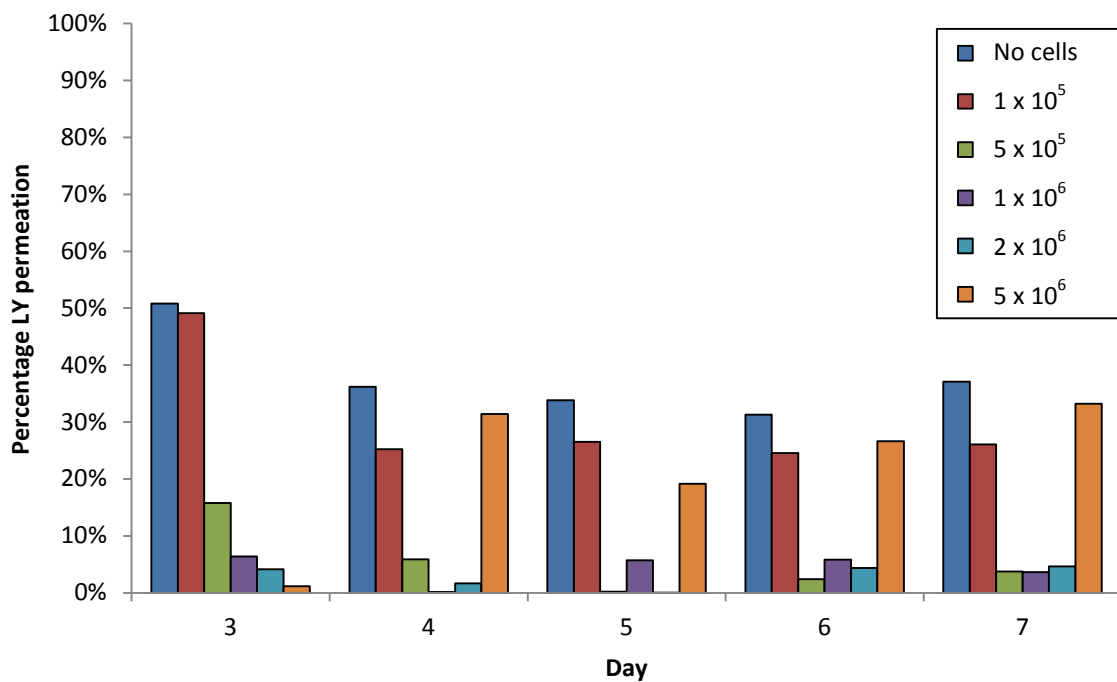


**Figure 51:** LY permeation over 7 days in monolayers of MDCKII seeded at a range of seeding densities (n=1)

#### 4. Rhodamine 123 transport in MDCK-MDR1 and MDCKII cells

TEERs were measured before the Rho123 assays as an indication of monolayer integrity by using an automated TEER reader (REMS Autosampler, WPI, USA). Briefly, electrodes were placed in the insert and well of the transwell plate, and the resistance of the monolayer was measured. The values were then divided by the insert area ( $0.11\text{cm}^2$ ) to determine the TEERs. TEERs of above  $500\Omega/\text{cm}^2$  were deemed as viable and used in the Rho123 assay.

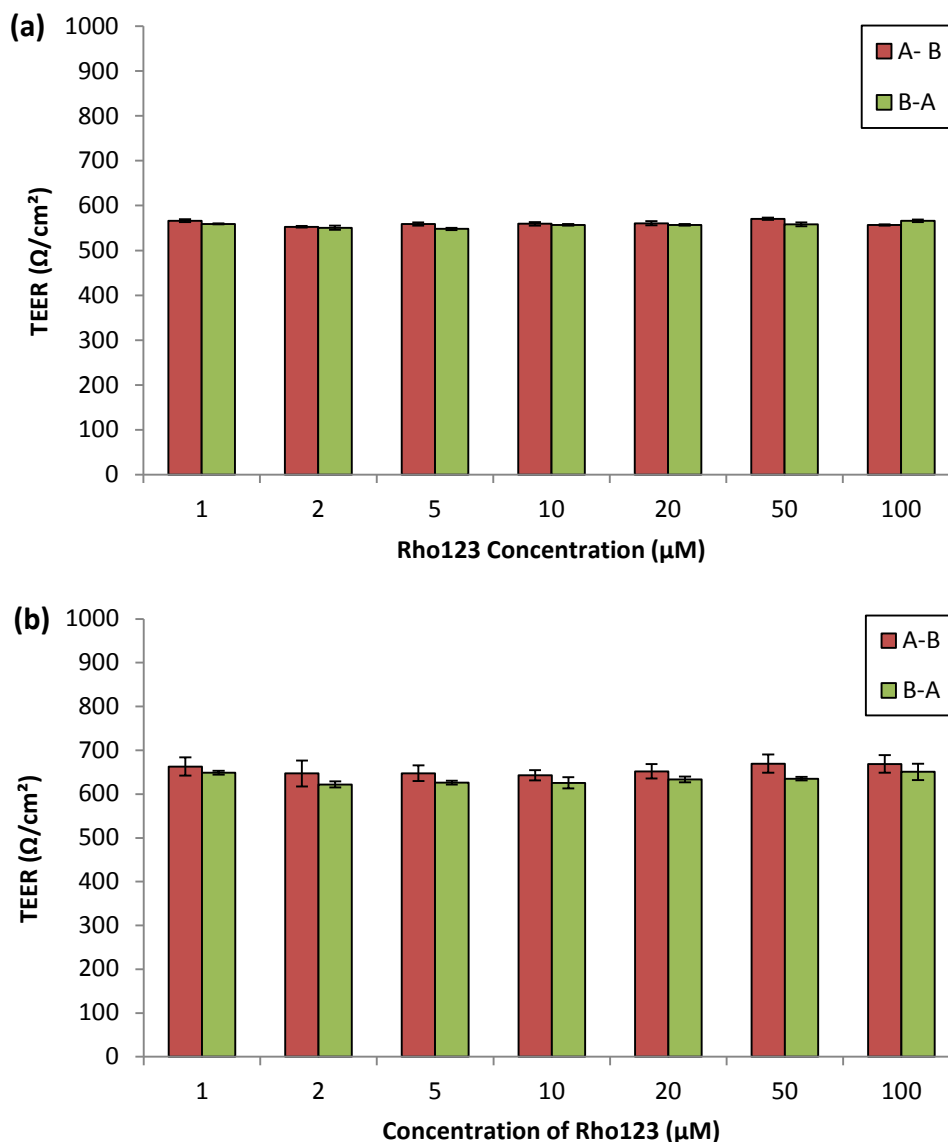


**Figure 52:** TEER values at a range of concentrations of Rho123 between  $1\mu\text{M}$  and  $100\mu\text{M}$  before the bidirectional transport assay in (a) MDCKII and (b) MDCK-MDR1 cell monolayers (Mean value  $\pm$  SEM,  $n=3$ )

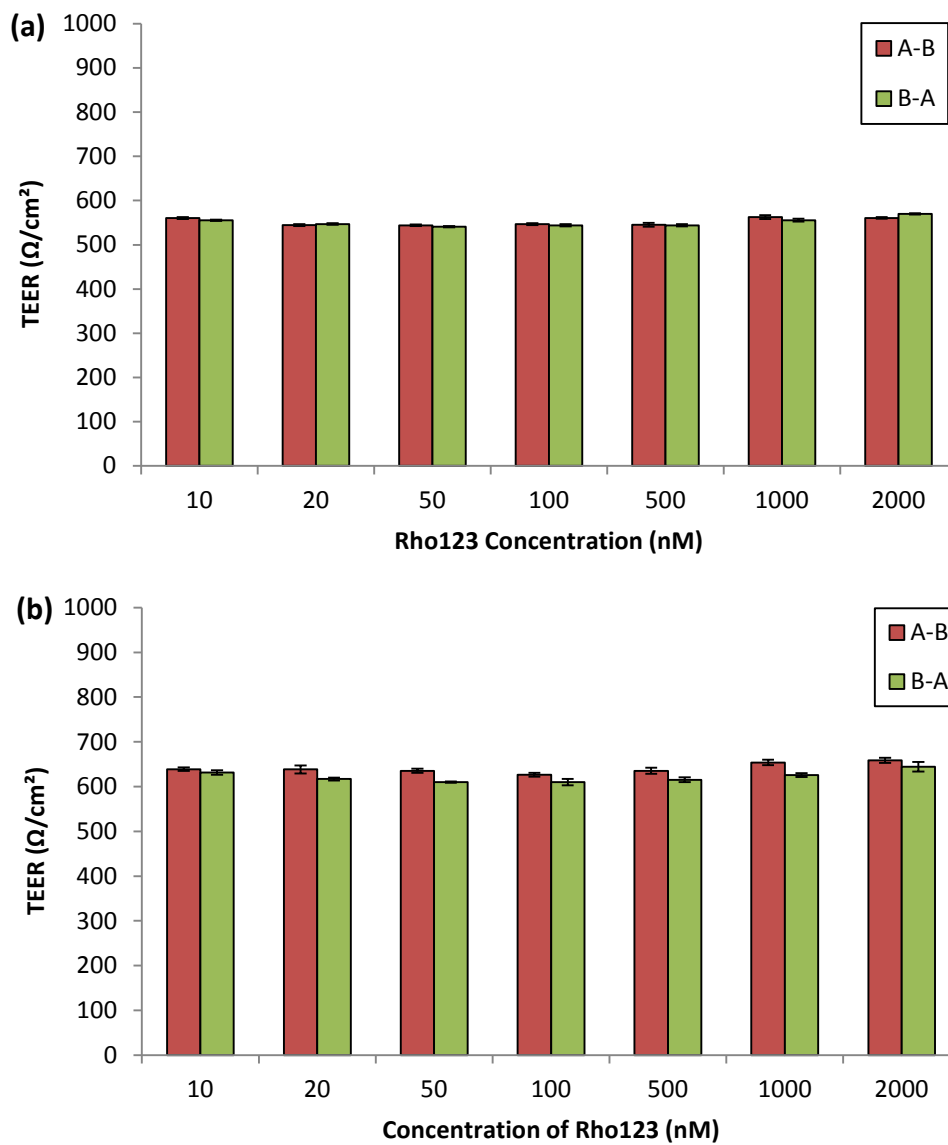


**Figure 53:** TEER values at a range of concentrations of Rho123 between 10nM and 2000nM before the bidirectional transport assay in (a) MDCKII and (b) MDCK-MDR1 cell monolayers (Mean value  $\pm$  SEM, n=3)

### 5. Calcein-AM efflux in the presence of P-gp inhibitors in MDC-MDR1 cells

MDCK-MDR1 cells were incubated with Calcein-AM in the presence and absence of the P-gp inhibitors Quinidine, Verapamil (Figure 54a) and Ketoconazole (Figure 54b). The fluorescence over the 71 cycles are shown below.

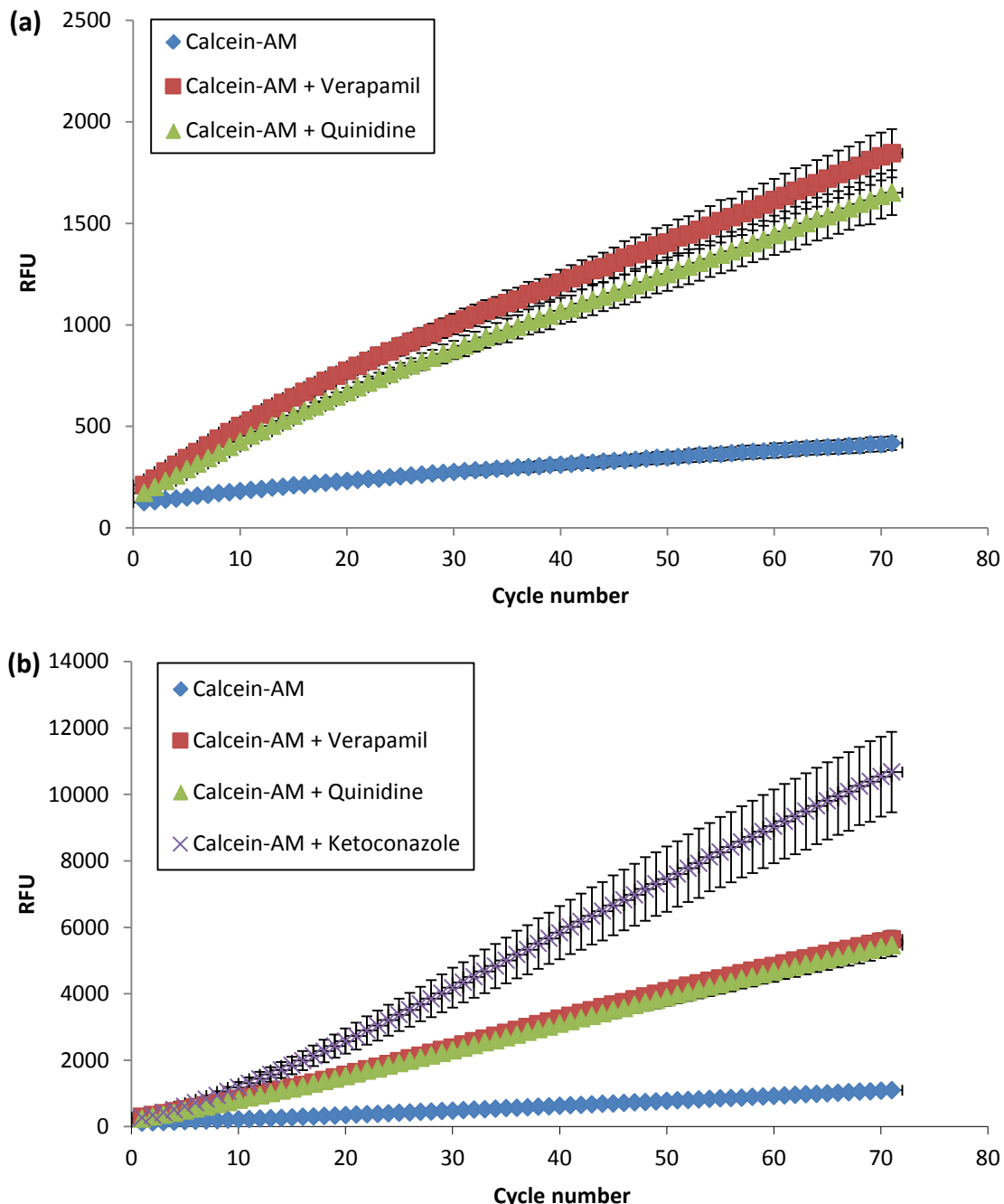


**Figure 54:** Calcein-AM fluorescence in MDCK-MDR1 cells in the presence and absence of the P-gp inhibitors Quinidine, Verapamil (a) and Ketoconazole (b) over 71 cycles (approximately 60 minutes) (Mean value  $\pm$  SD, n=9)

## 6. Calcein-AM degradation and its effect on fluorescence

As with other substrates, Calcein-AM was diluted from its desiccated form in DMSO to a stock concentration, and then diluted in transport buffer for the assay. The recommended storage conditions are for 2 weeks at -5°C to -30°C (Life Technologies product manual). However, following the use of Calcein-AM diluted in DMSO within the specified period in a repeat of the above assay, there was evidence that this period might not be sufficient to prevent Calcein-AM degradation.

During the cycles, the Calcein-AM fluorescence did not change in the absence of an inhibitor, and started off at cycle 1 at a relatively high reading of 406 RFU. Compared to the previous 2 experiments, this starting value was approximately 4 times higher. This was also seen in the presence of 2 inhibitors Verapamil and Ketoconazole at approximately the same RFU values throughout the cycles. This suggests the degradation of the Calcein-AM forms a complex which is fluorescent, but is either not affected by esterases within the cells, or cannot be transported through to the cells. In the presence of Quinidine, the fluorescence values were noticeably higher than any other state. However the same steady levels in fluorescence throughout the cycles, at approximately 1000 RFU, indicated this is an artefact from the Quinidine and Calcein-AM rather than any effects from the cell. This raises the question of the suitability of the inhibitors to their corresponding transporter in the presence of specific fluorophores, and whether the substrate and inhibitors form fluorescent complexes independent of the cell (Figure 55).

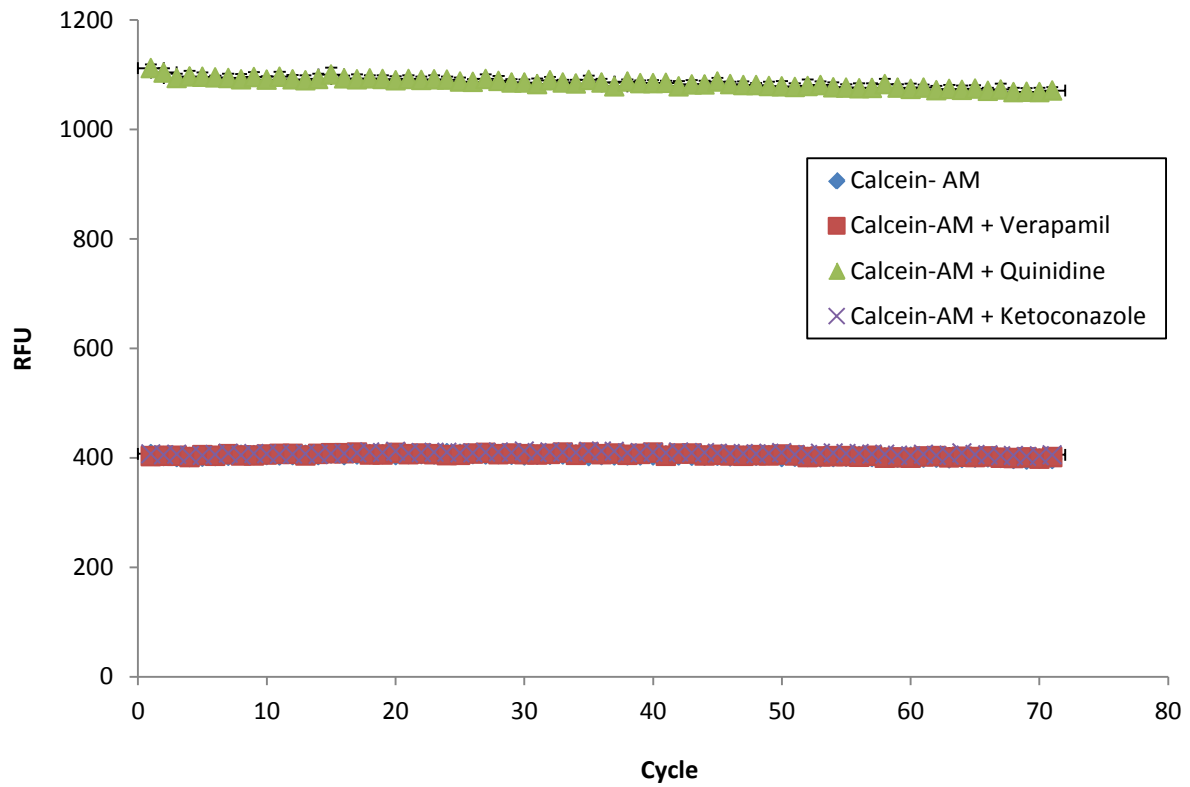


**Figure 55:** Calcein-AM fluorescence in MDCK-MDR1 cells in the presence and absence of the P-gp inhibitors Ketoconazole, Verapamil and Quinidine over 71 cycles (approximately 60 minutes) (Mean value  $\pm$  SD, n=9)

## 7. Hoechst 33342 concentration assessment for efflux assay

MDCK-BCRP cells were incubated with varying concentrations of Hoechst 33342 in the presence and absence of the BCRP inhibitors Novobiocin and Ko143 (Figure 56). 20 $\mu$ M H33342 demonstrated the highest fluorescence in the presence of inhibitors and was repeated (Figure 57). The fluorescence over the 71 cycles are shown below.

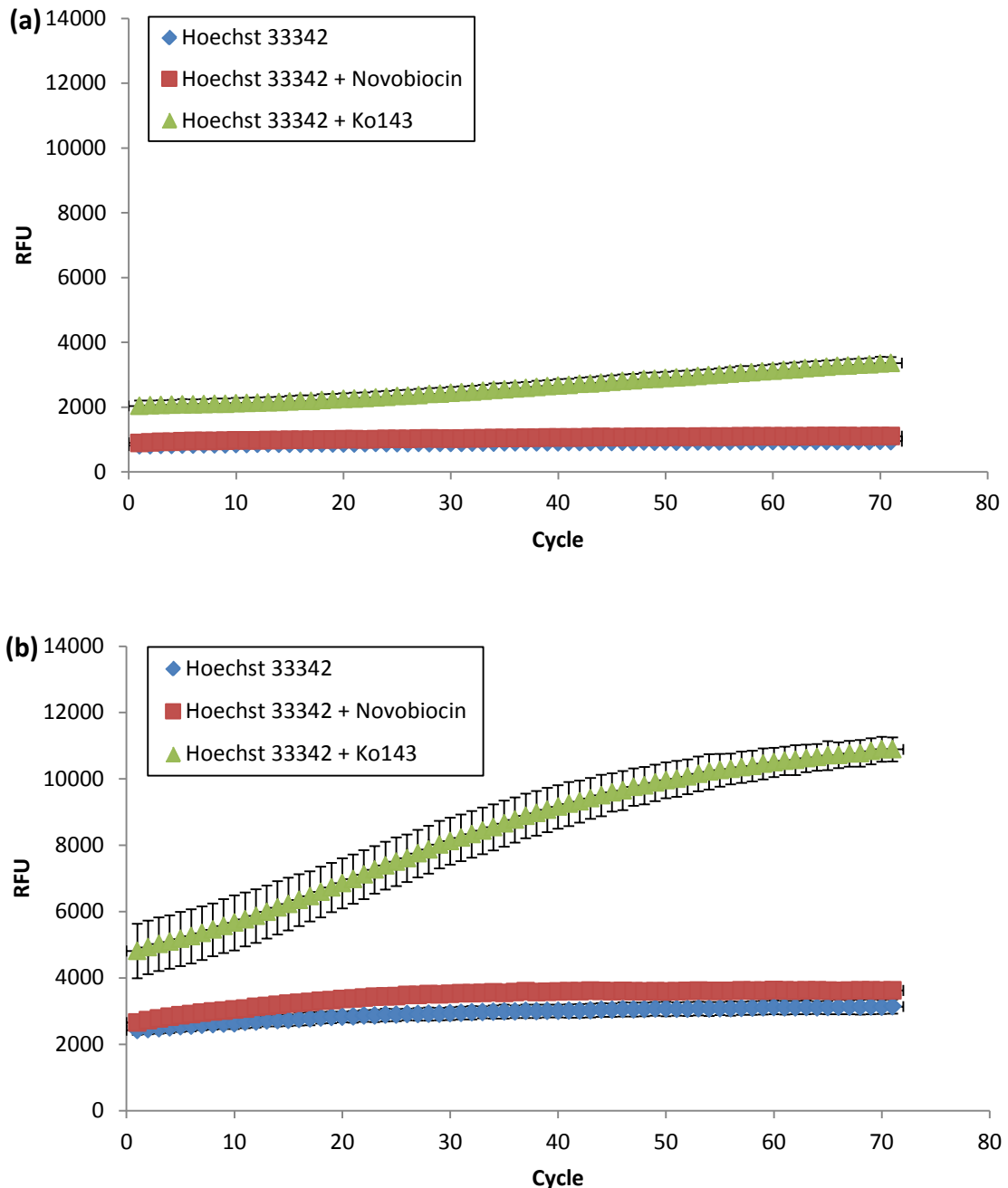


**Figure 56:** Fluorescence of Hoechst 33342 at (a) 1 $\mu$ M and (b) 5 $\mu$ M in MDCK-BCRP cells in

the presence and absence of the BCRP inhibitors Novobiocin and Ko143 throughout 71 cycles (approximately 60 minutes) (Mean value  $\pm$  SD, n=8)

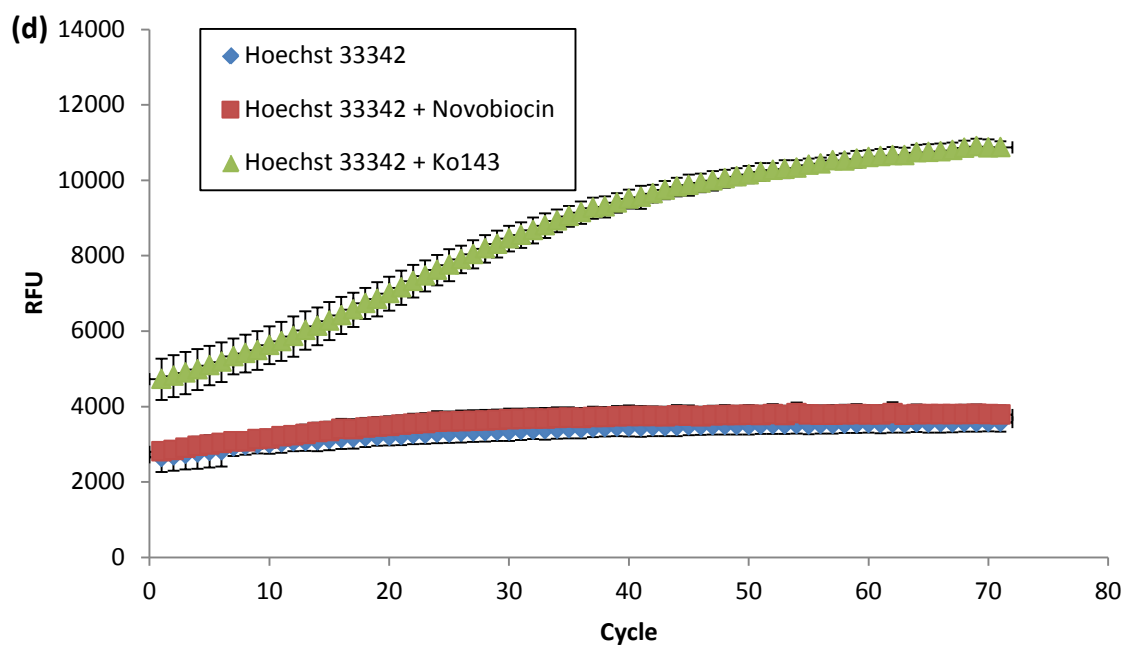
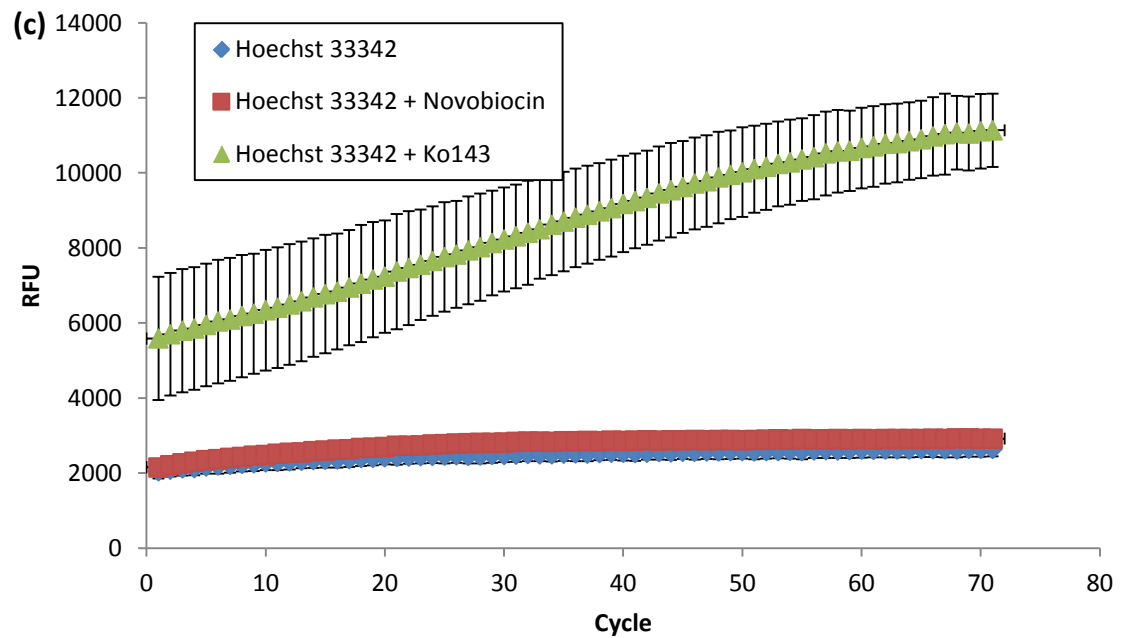


**Figure 56 continued:** Fluorescence of Hoechst 33342 at (c) 10 $\mu$ M and (d) 20 $\mu$ M in MDCK-BCRP cells in the presence and absence of the BCRP inhibitors Novobiocin and Ko143 throughout 71 cycles (approximately 60 minutes) (Mean value  $\pm$  SD, n=8)

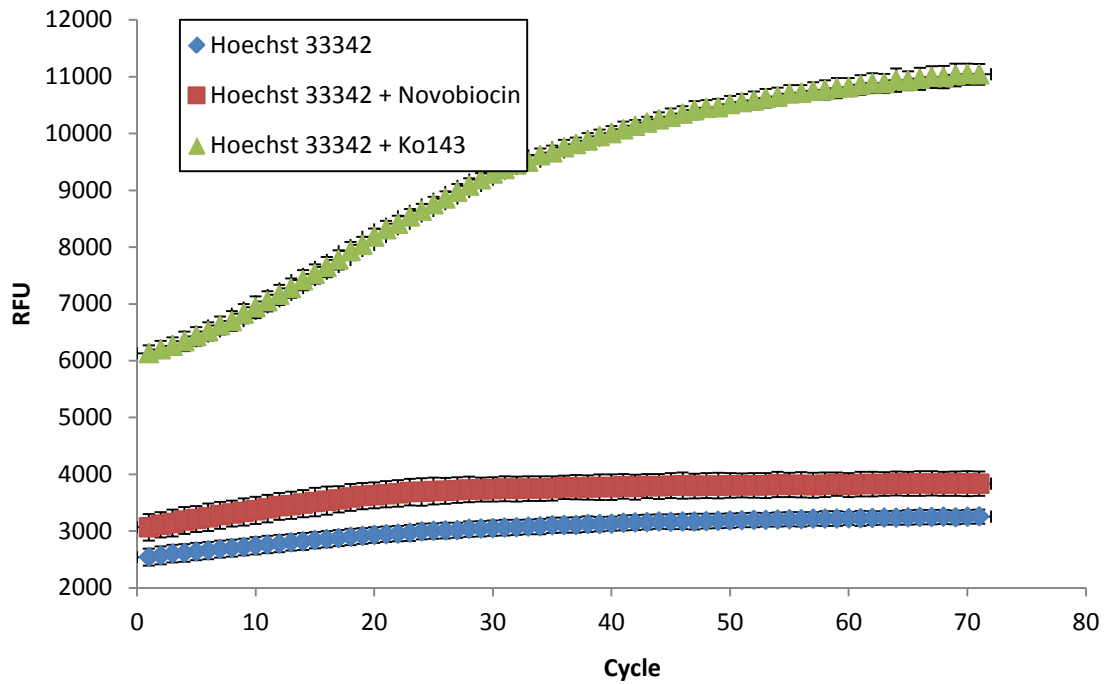


**Figure 57:** Fluorescence of Hoechst 33342 at 20µM in MDCK-BCRP cells in the presence and absence of the BCRP inhibitors Novobiocin and Ko143 throughout 71 cycles (approximately 60 minutes) (Mean value  $\pm$  SD, n=18)

## 8. RPTEC growth profile

The culture of RPTECs to produce a growth curve was done over a 16 day period. RPTEC cell counts were performed over various time points to establish the cumulative population doubling over time. The equation was then used to calculate the doublings of cells cultured for 0 (Pd=0), 7 (Pd=5), 14 (Pd=7) and 24 (Pd=9) days for experimental use. Initially cells up to the guaranteed doubling by the manufacturer (Pd=15) were going to be used, however the length of time and consumables needed for cell culture was too large.

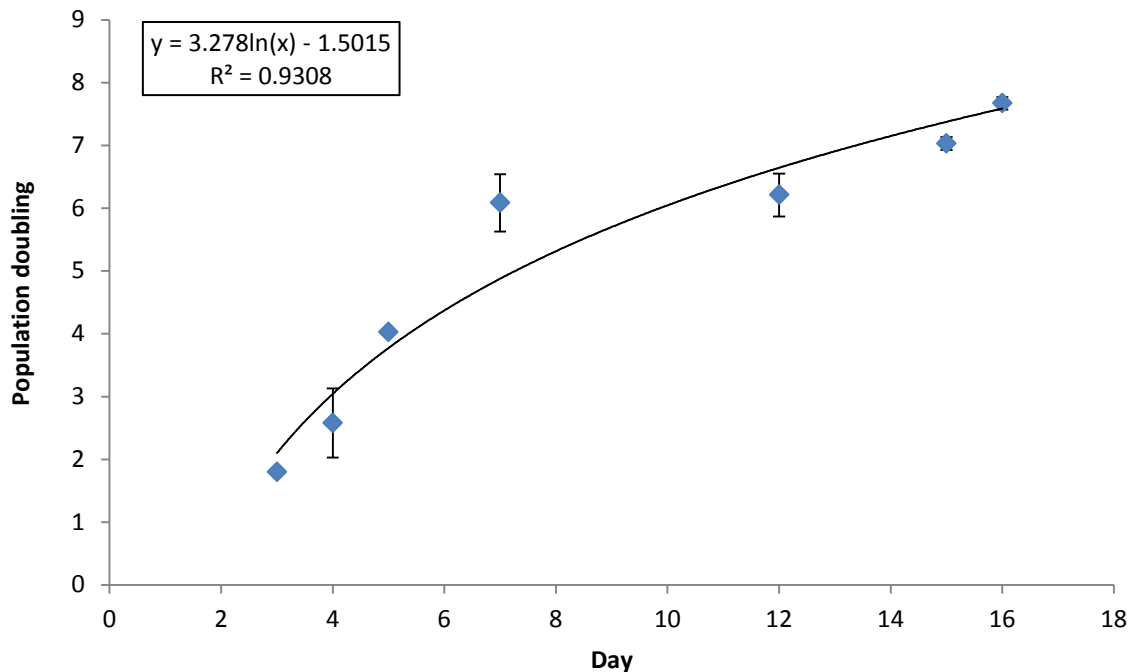


**Figure 58:** Growth curve of RPTECs over 16 days (Mean value  $\pm$  SEM, n=3)

## 9. RNA integrity assessment

RNA stock solutions were run on the Agilent 2100 bioanalyzer to assess RNA integrity. All sample and ladder electropherograms displayed the typical peaks exhibited in eukaryotic cells i.e. a marker peak (2 small peaks) and two ribosomal peaks (18S and 28S) (Figure 59).

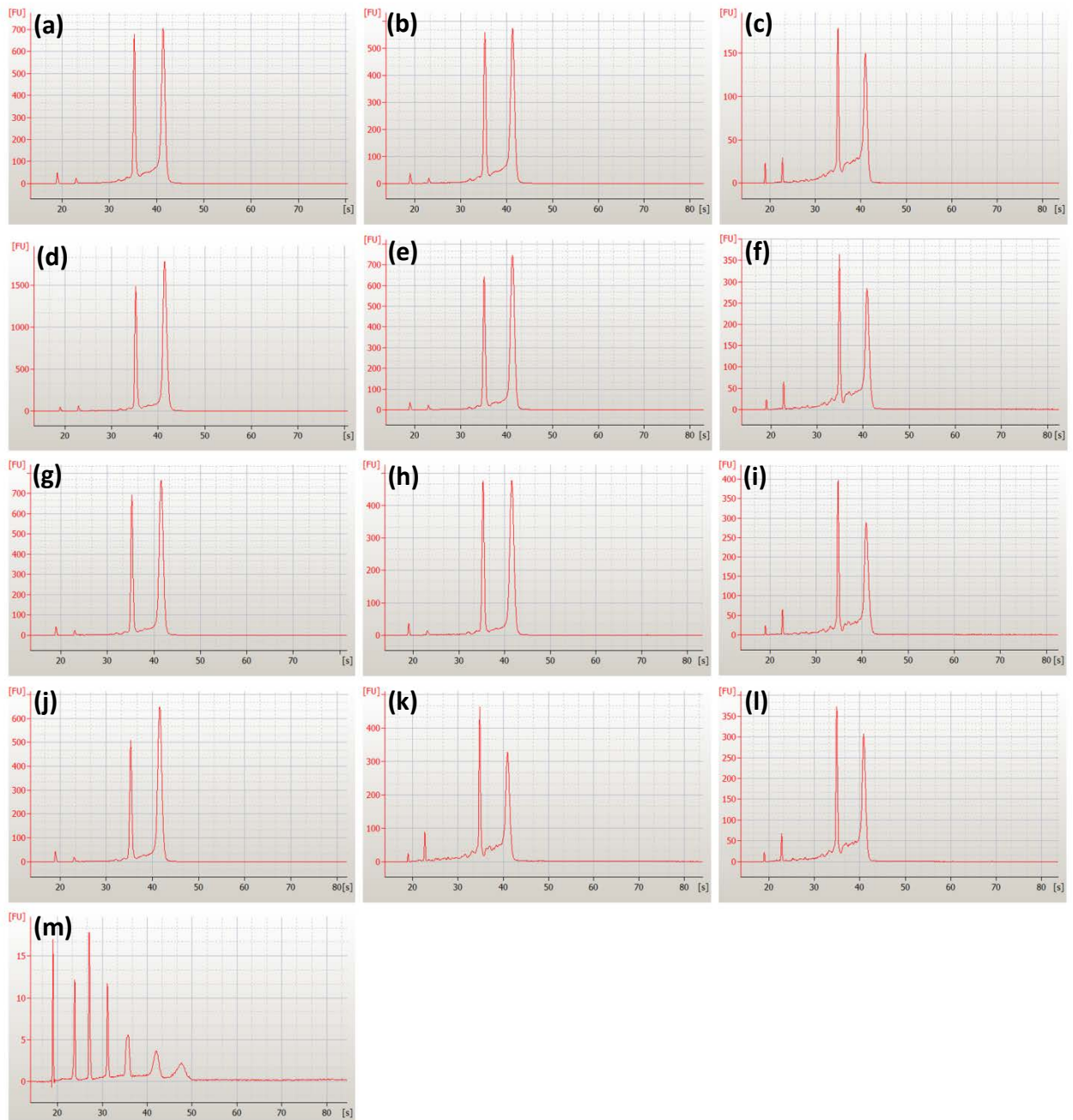


**Figure 59:** Electropherograms showing successful RNA runs in terms of integrity (a-c) 0, (d-f) 5, (g-l) 9 doublings with the reference ladder (m)

### 10. Calcein-AM efflux assay in RPTECs at various population doublings

Calcein-AM was incubated with RPTECs seeded at doublings 0, 5, 7 and 9 in the presence and absence of Verapamil and Ketoconazole to assess P-gp functionality.

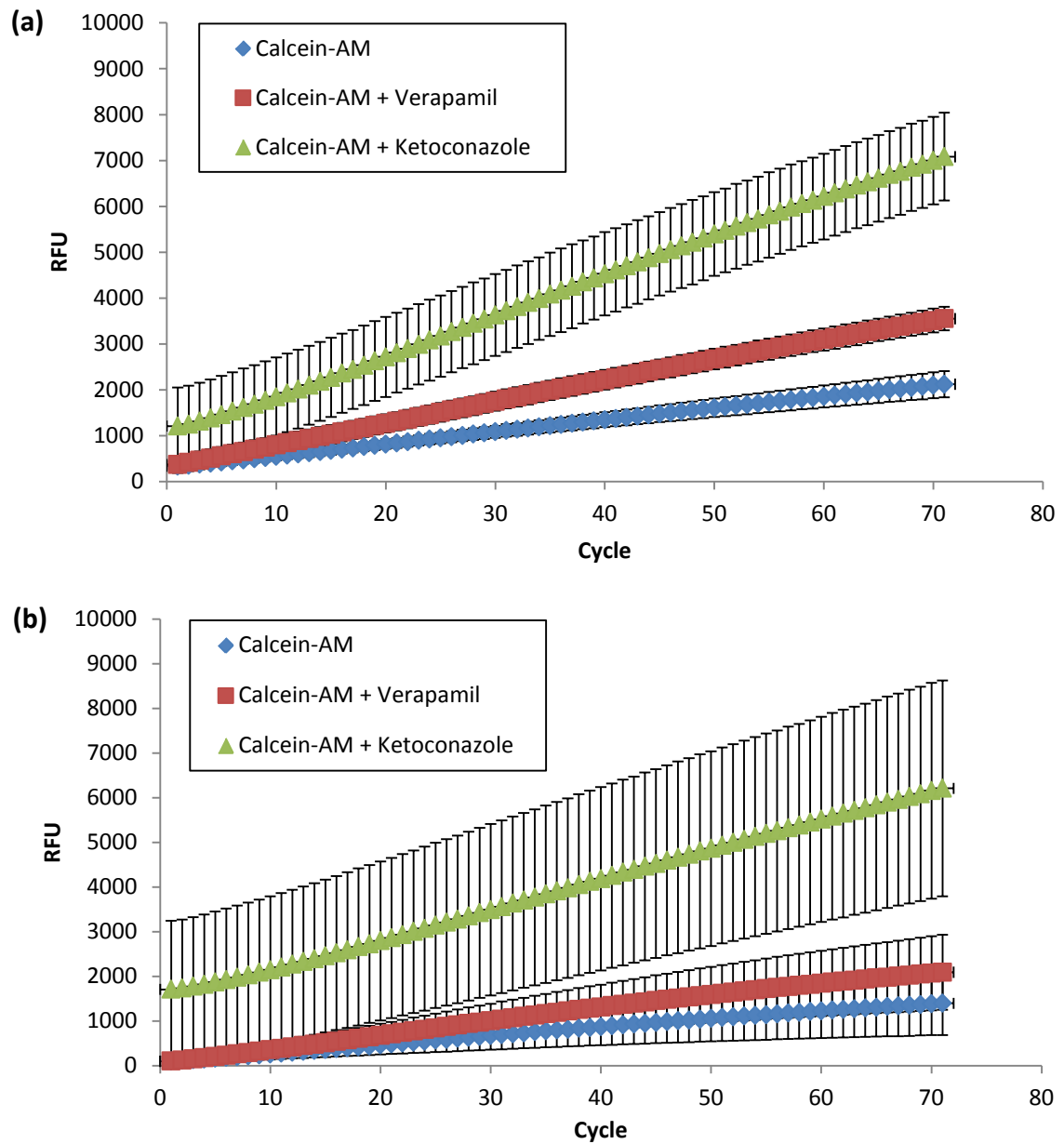


**Figure 60:** Calcein-AM fluorescence in RPTECs seeded at (a) 0 and (b) 5 doublings in the presence and absence of the P-gp inhibitors Verapamil and Ketoconazole over 71 cycles (approximately 60 minutes) (Mean value  $\pm$  SD, n=36)

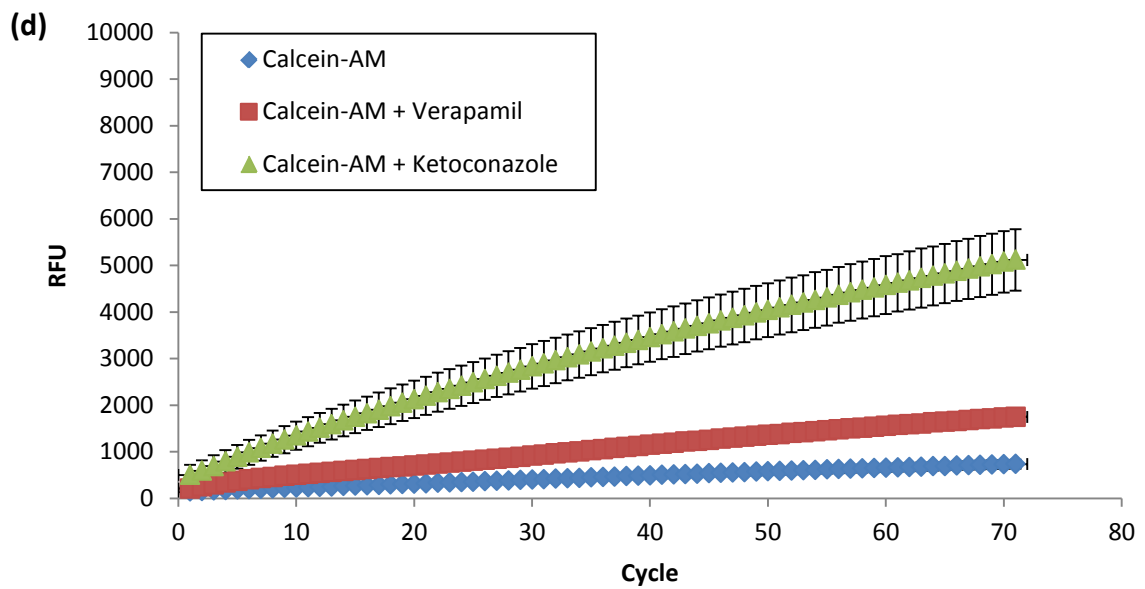
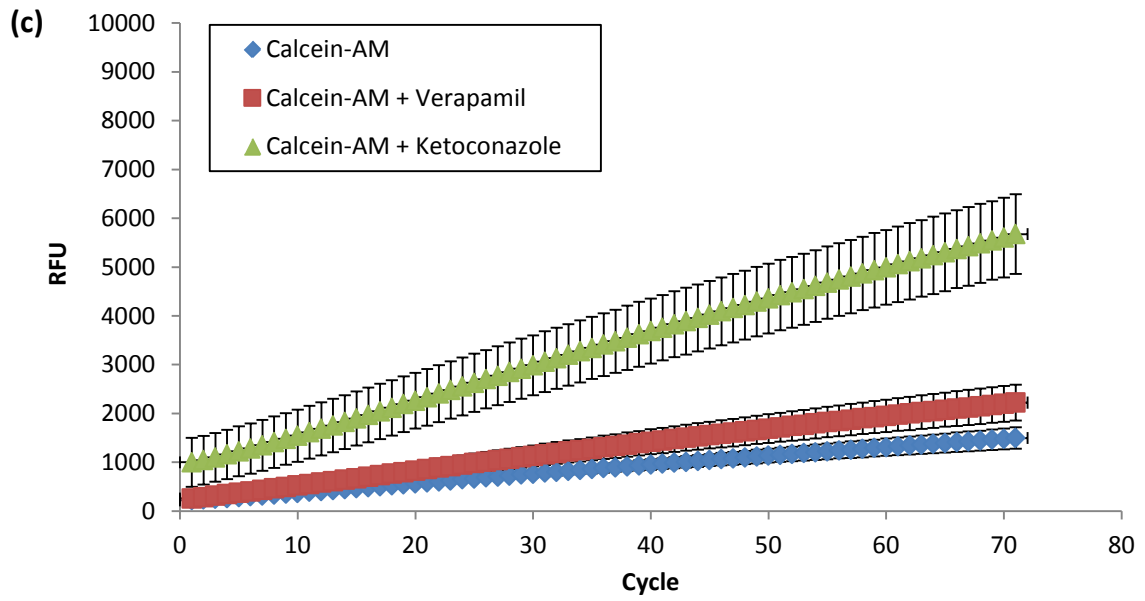


**Figure 60 (continued):** Calcein-AM fluorescence in RPTeCs seeded at (c) 7 and (d) 9 doublings in the presence and absence of the P-gp inhibitors Verapamil and Ketoconazole over 71 cycles (approximately 60 minutes) (Mean value  $\pm$  SD, n=36)

## 11. Hoechst 33342 efflux assay in RPTECs at various population doublings

Hoechst 33342 was incubated with RPTECs seeded at doublings 0, 5, 7 and 9 in the presence and absence of Novobiocin and Ko143 to assess BCRP functionality.

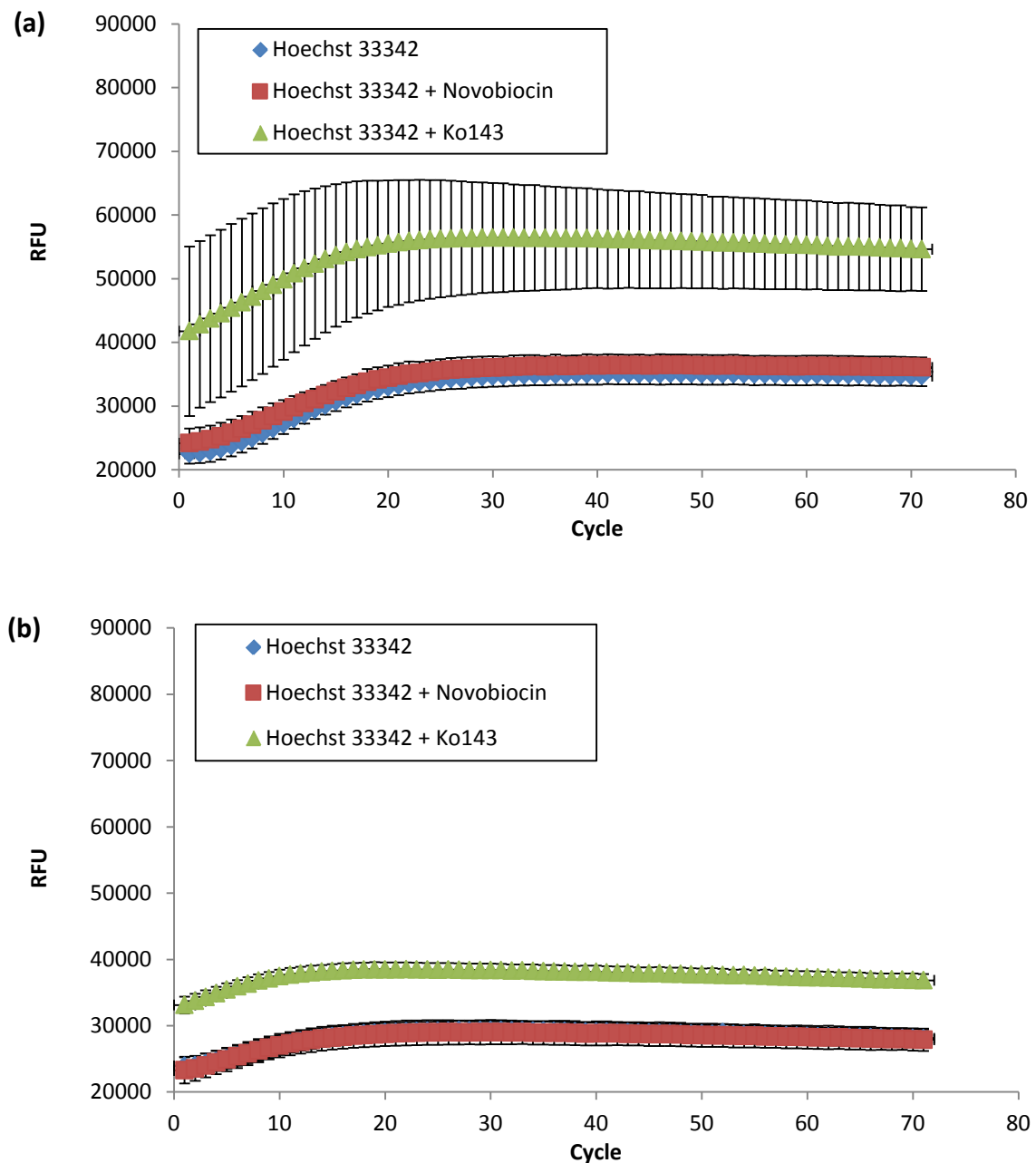


**Figure 61:** Hoechst 33342 fluorescence in RPTECs seeded at (a) 0 and (b) 5 doublings in the presence and absence of the BCRP inhibitors Novobiocin and Ko143 over 71 cycles (approximately 60 minutes) (Mean value  $\pm$  SD, n=36)

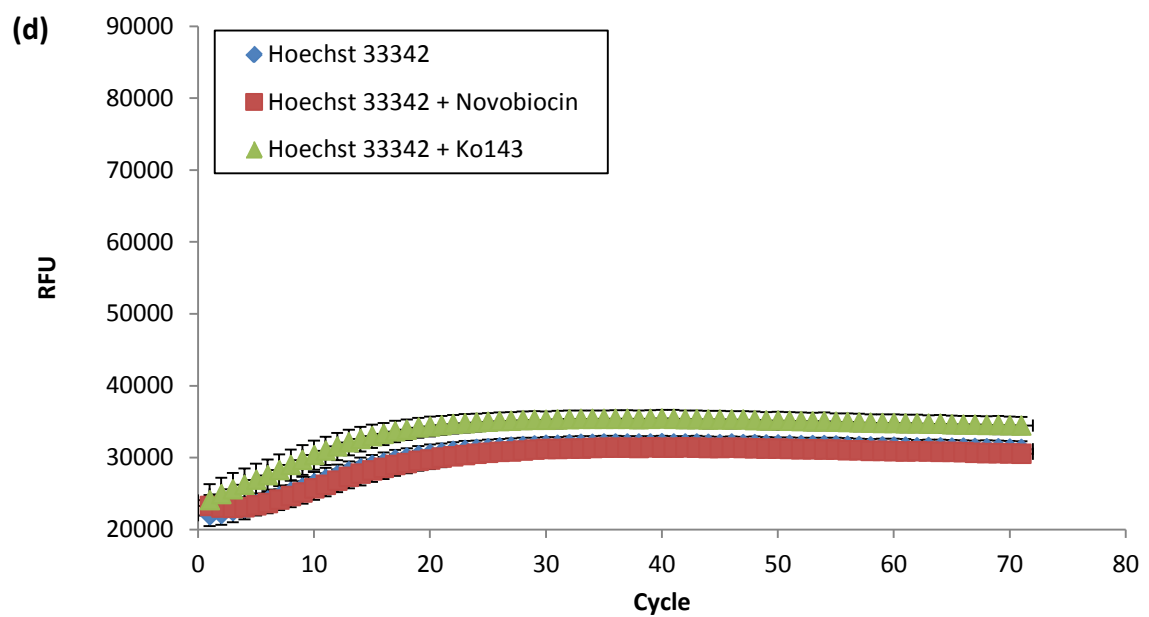
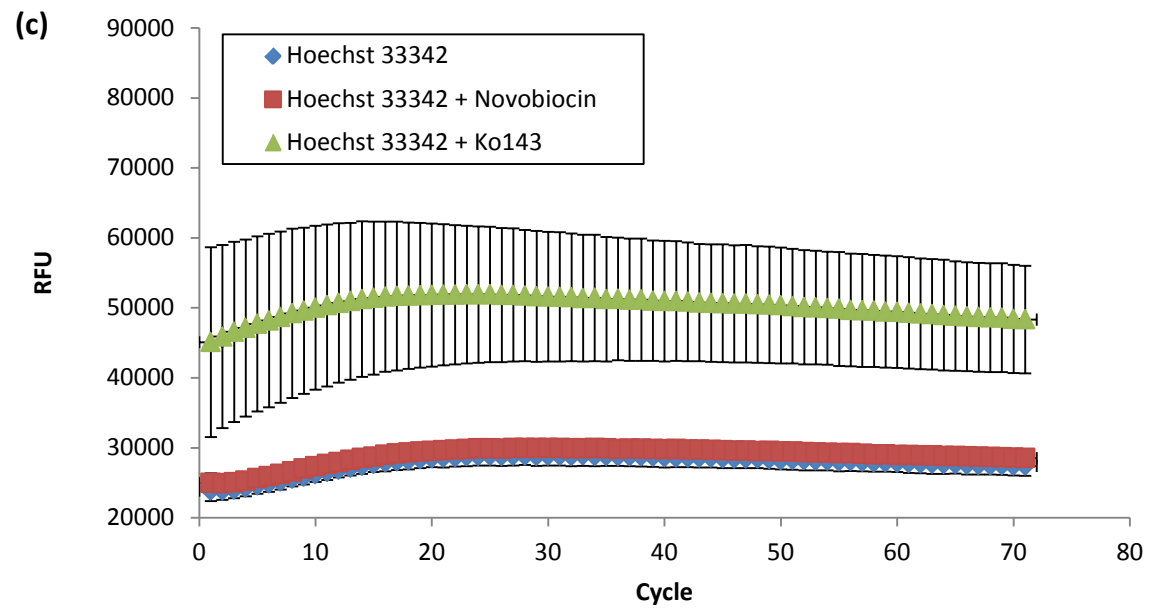


**Figure 61 (continued):** Hoechst 33342 fluorescence in RPTeCs seeded at (c) 7 and (d) 9 doublings in the presence and absence of the BCRP inhibitors Novobiocin and Ko143 over 71 cycles (approximately 60 minutes) (Mean value  $\pm$  SD, n=36)

## 12. RPTEC culture in transwell plates

RPTEC culture was initially attempted in static plates on polycarbonate transwell inserts as performed in literature [168] at a seeding density of  $3.13 \times 10^5$  cells/cm<sup>2</sup> (Figure 62). LY permeation was assessed on days 4, 6 and 8, with a higher percentage of LY permeating than the initial threshold ( $\leq 1\%$ ). On day 6 LY permeation was within the raised threshold (2-3%). RPTEC culture was then trialled at a higher seeding density ( $4.46 \times 10^5$  cells/cm<sup>2</sup>) with cells incubated for 1 day in static conditions before culture on a shaker platform at 90rpm. LY permeation was assessed on days 2, 4 and 6. The LY percentage permeation on days 2 and 4 were both within the higher threshold, with day 4 displaying the lowest percentage (2.28%).

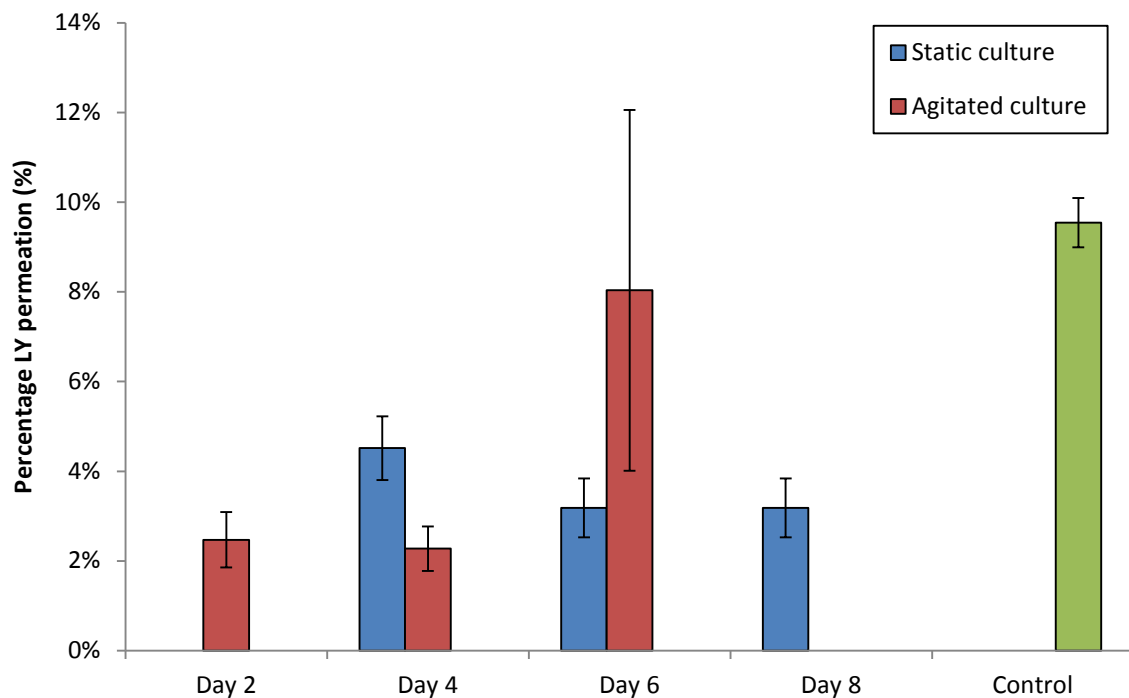


**Figure 62:** LY percentage permeation through RPTEC monolayers cultured in static and agitated conditions over 8 days against a no cell control. (Mean value  $\pm$  SEM, n=4)

### 13. Presto Blue assay calibration curves

The Presto Blue assay was used to assess the metabolic activity of RPTECs on fibres in static and flow conditions over time (described in Section 4.4.7.2. and 5.4.6. respectively). Calibration curves were generated to equate fluorescence with the number of metabolically active cells present. Cells were seeded in a 48 well plate at varying cell densities for the membrane and fibre curves respectively. The cells were left to attach for four hours before carrying out the assay, where medium was aspirated from each well and replaced with the Presto Blue reagent at a 1:10 dilution. Cells were incubated for 40 minutes at 37°C before sampling three times and reading on the microplate reader. Cells were then removed from the wells and counted. The cell numbers were plotted against RFU of the samples (Figure 63).

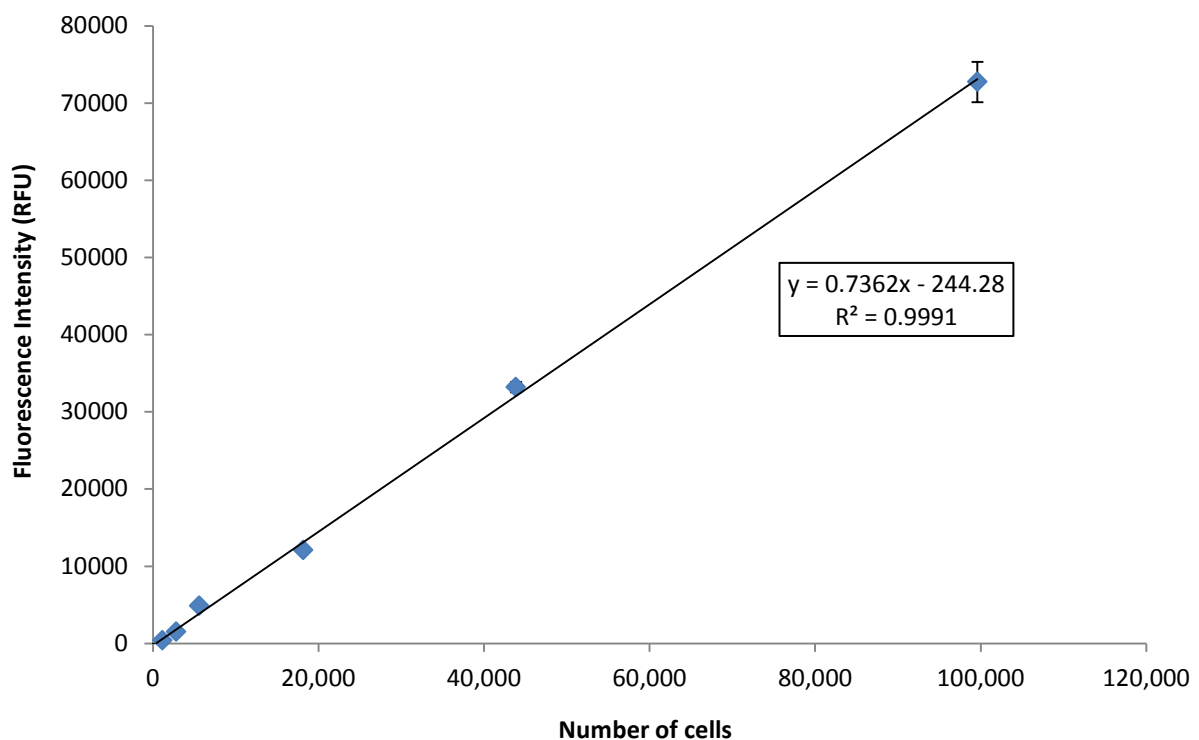


**Figure 63:** Presto blue calibration curve with recovered cells from the well against fluorescence intensity (RFU). (Mean value  $\pm$  SEM, n=3)

## 14. Membrane sterilisation

Membrane sterilisation was investigated by measuring the OD of incubated nutrient broth (Figure 64) and performing spread plates (Figure 65). Membrane discs were incubated for 48 hours in nutrient broth before analysis.

The OD was measured at both 600nm and 660nm to investigate both bacterial and fungal growth. Fresh broth incubated for 48 hours was used as the blank for all samples. All samples displayed ODs similar to the blank, with only two samples showing a slight increase in ODs at 660nm (autoclaved PSF and IMS sterilised PSF+PVP). However, when comparing this to the positive *E.coli* K-12 control incubated for 24 hours and the spread plates, the increase indicates machine error. The spread plates were all clear except for antibiotic sterilised PSF and autoclaved PSF+GA. However as only 1 colony was present on each of the plates, whereas the positive control had too many colonies to count, the contamination was assumed to be due to operator technique.

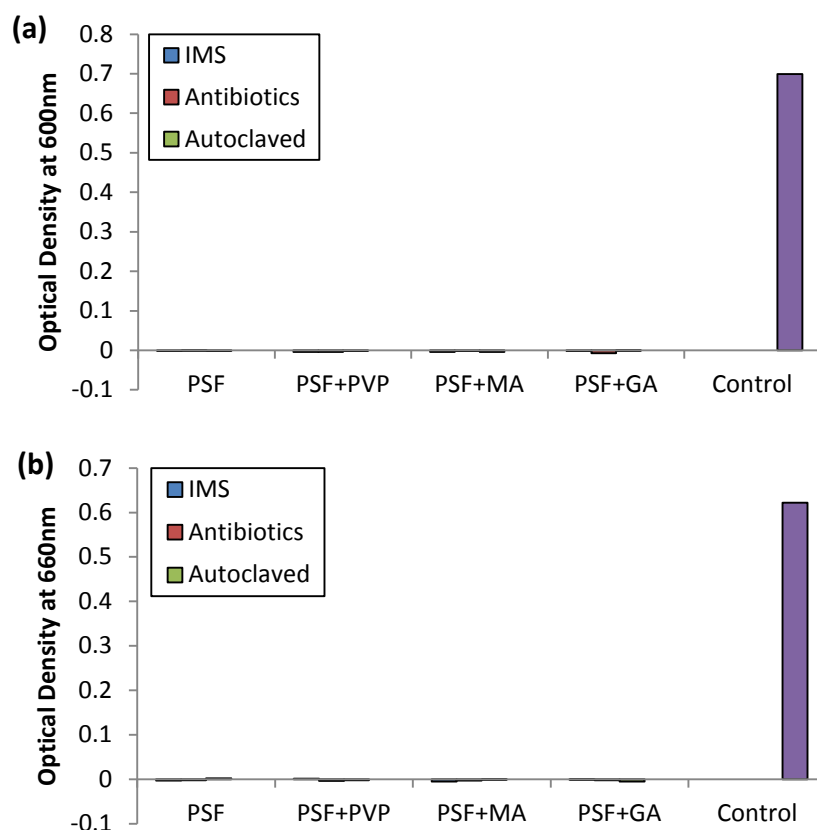


**Figure 64:** The optical density at 600nm (a) and 660nm (b) of nutrient broth incubated for 48 hours with sterilised membranes: PSF, PSF+PVP, PSF+MA and PSF+GA against a positive *E.coli* control

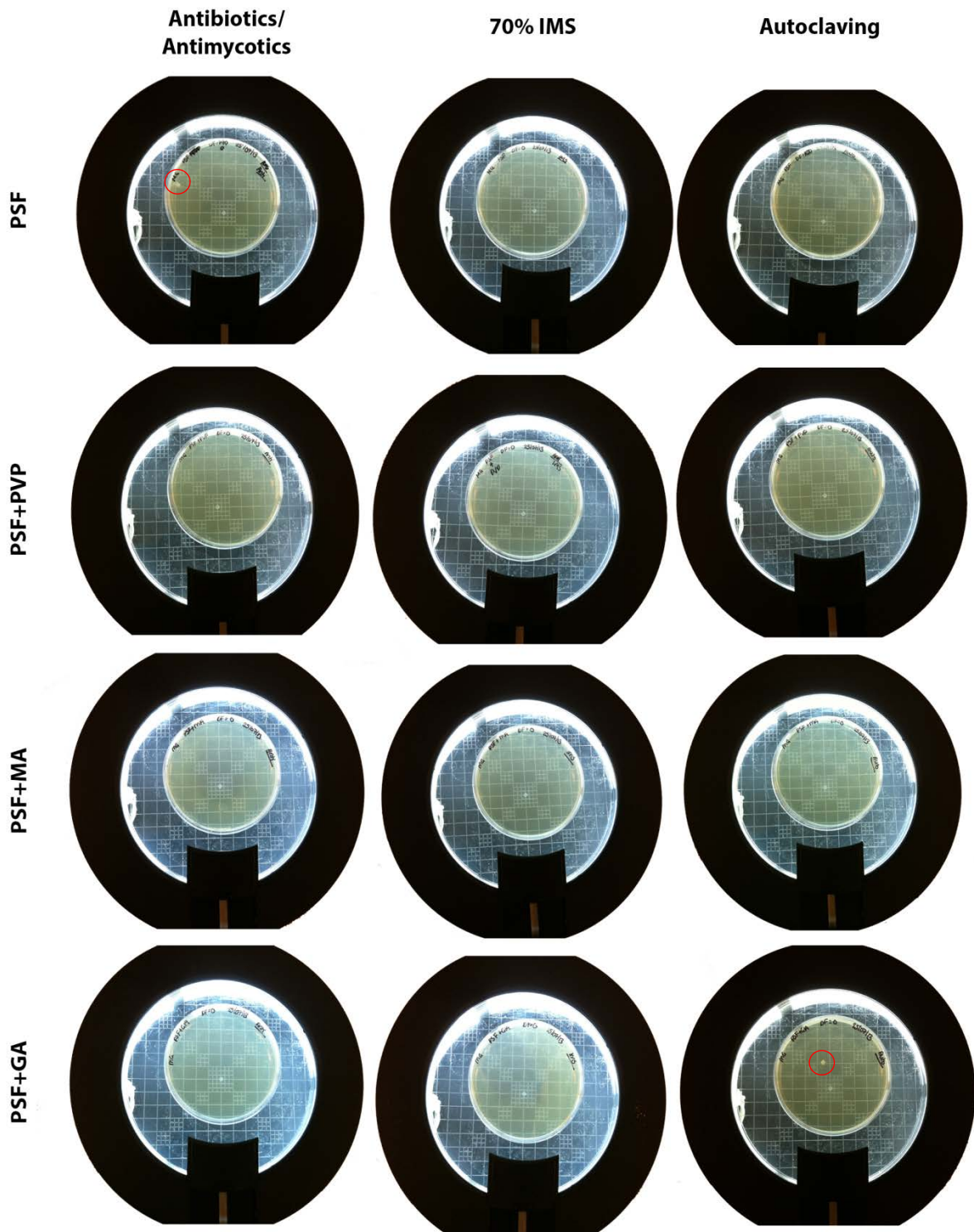


**Figure 65:** Images of spread plates incubated with nutrient broth from PSF, PSF+PVP, PSF+MA and PSF+GA membranes after sterilisation with IMS, antibiotics and autoclaving with a positive and negative control plate. Red circles indicate the presence of a bacterial colony on the plates.

## 15. Membrane sterilisation images

Flat sheet membranes were sterilised as described in Section 4.3.7. Membrane cross sections were then imaged via SEM. During processing membrane cross sections were damaged, although the macrovoid structure can be seen in some images.

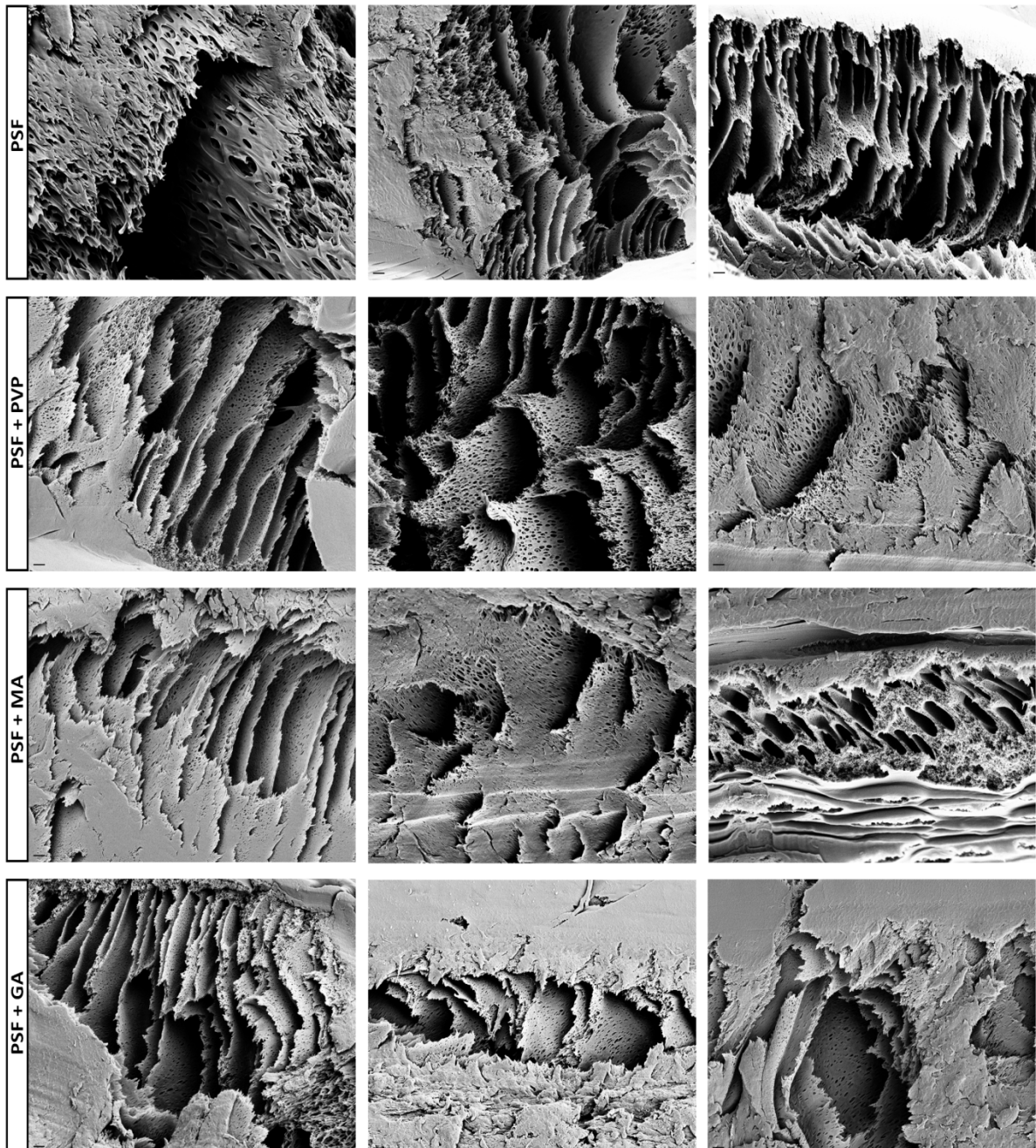


**Figure 66:** Cross sections of PSF, PSF+PVP, PSF+MA and PSF+GA membranes sterilised using 70% IMS (a-c), Antibiotic/ antimycotics (d-f) and autoclaving (g-i). Scale bars = 2µm

## 16. Bioreactor setup

An incubation chamber was originally designed to house the pumps and modules during RPTEC culture in the HFBs. The chamber was assembled with a clear polycarbonate lid on top of a baseplate containing holders for the pumps, modules and cables (Figure 67). The heater and CO<sub>2</sub> meter were attached to the sides of the lid and controlled externally by the settings box and laptop respectively.

Although this setup allowed a simplistic layout of the pumps, modules and bottles, various issues arose leading to the use of an incubator for RPTEC culture instead. The CO<sub>2</sub> concentration could not be controlled by the meter (CM-0045; CO<sub>2</sub> meter, USA) as the flow rate from the gas cylinder was too high. When a flow meter was applied to the system, the flow rate was reduced and the CO<sub>2</sub> percentage was controlled for a few hours at 5% before increasing to 12%. Alongside the unstable CO<sub>2</sub> concentrations within the box the application of heat and/or CO<sub>2</sub> caused the suspected leaching of plasticisers from the PCT lid or polyvinyl chloride cable tidy which resulted in a ‘burning plastic’ smell being emitted overnight. As the effect of this phenomenon on the cells was unknown, the chamber was discarded.

## 17. Hydraulic permeability

The hydraulic permeability for modules containing batch 2 fibres were ascertained once but could not be repeated due to fibre breakage (Table 22).

**Table 22:** Transmembrane pressure, water flux and hydraulic permeability of modules incorporating batch 2 fibres

Module	Transmembrane pressure (mbar)	Water flux (J) (m <sup>3</sup> /m <sup>2</sup> ·s)	Hydraulic permeability (L <sub>(p)</sub> ) (10 <sup>9</sup> Pa m <sup>3</sup> /m <sup>2</sup> ·s)
1	10.4	1.55 x 10 <sup>-8</sup>	265.5
2	14.2	2.05 x 10 <sup>-8</sup>	143.8
3	11	3.42 x 10 <sup>-8</sup>	310.17

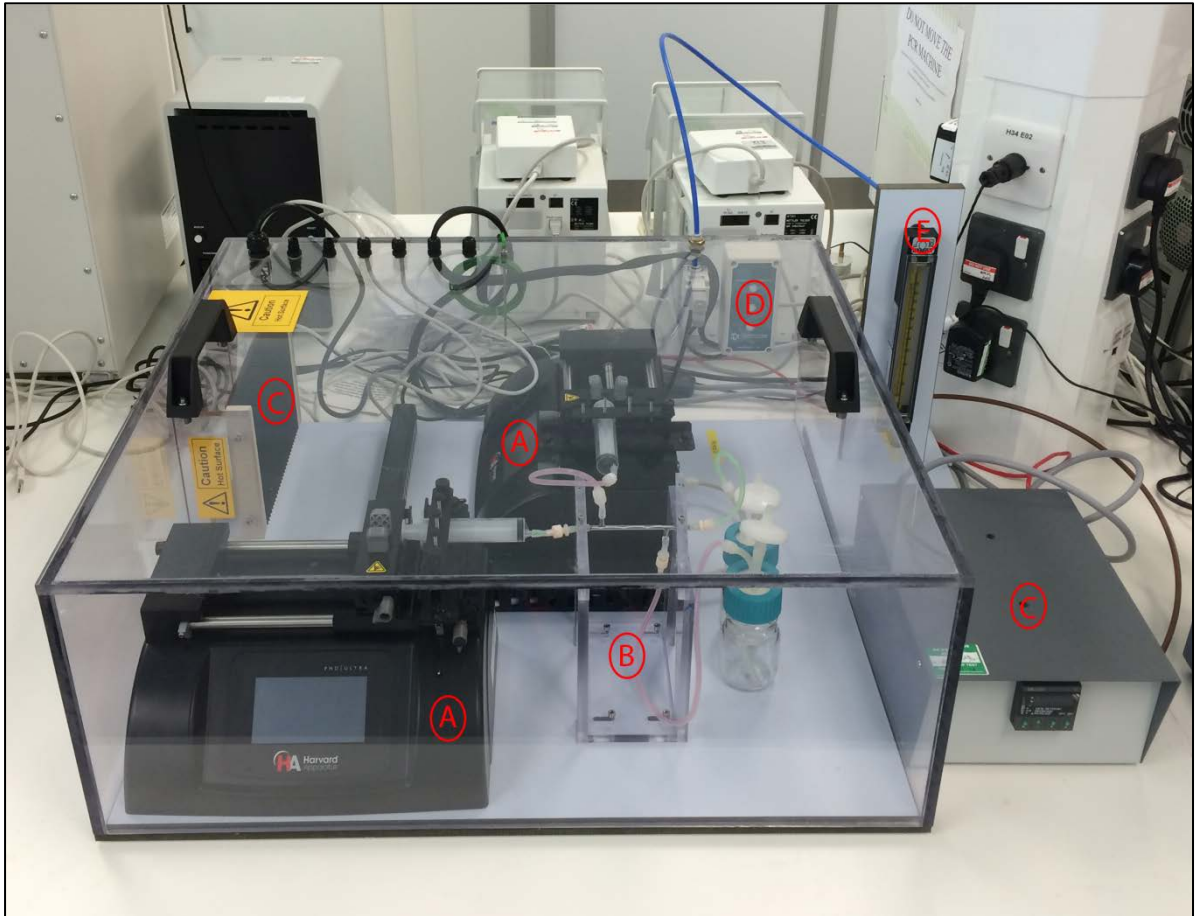


**Figure 67:** Image of the incubation chamber assembled initially for RPTEC culture in single hollow fibre bioreactors. A= Syringe pumps, B= Module holder, C= Heater and control unit), D= CO<sub>2</sub> controller, E= CO<sub>2</sub> Flow meter. The module is shown in position with the ECS (red) and lumen (green) loops highlighted

### 18. Surface topography of hollow fibres

AFM was performed on the interior and exterior of the hollow fibres using contact mode on a 20µm x 20µm area.

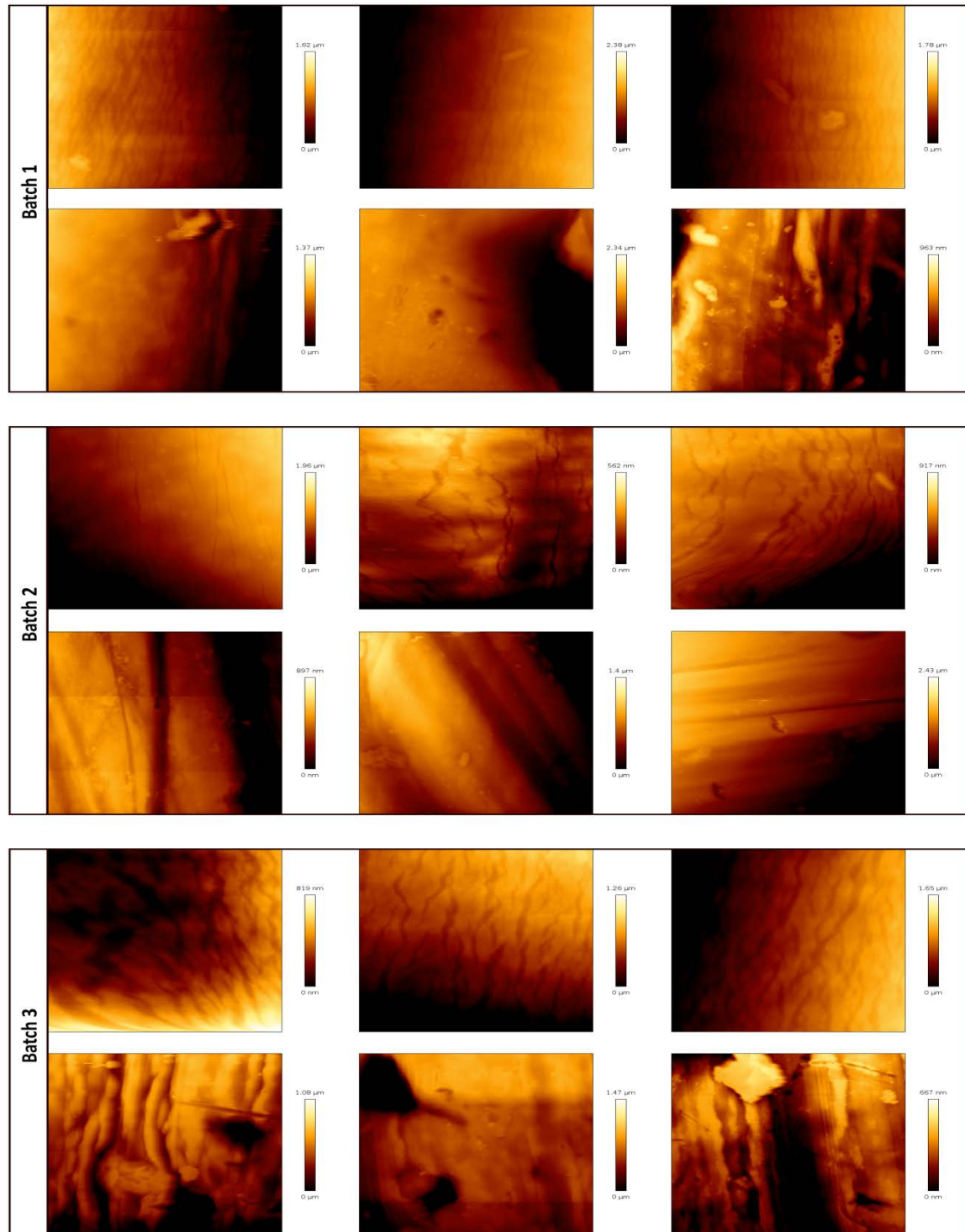


**Figure 68:** AFM images of the Lumen (top rows) and Exterior (bottom rows) of batch 1, 2 and 3 fibres

## 19. Module sterilisation

Medium incubated in modules sterilised by autoclaving after assembly showed no clear signs of infection after 2 days. However, medium incubated in modules sterilised by 70% IMS showed typical signs of infection in the lumen and ECS after 2 days.

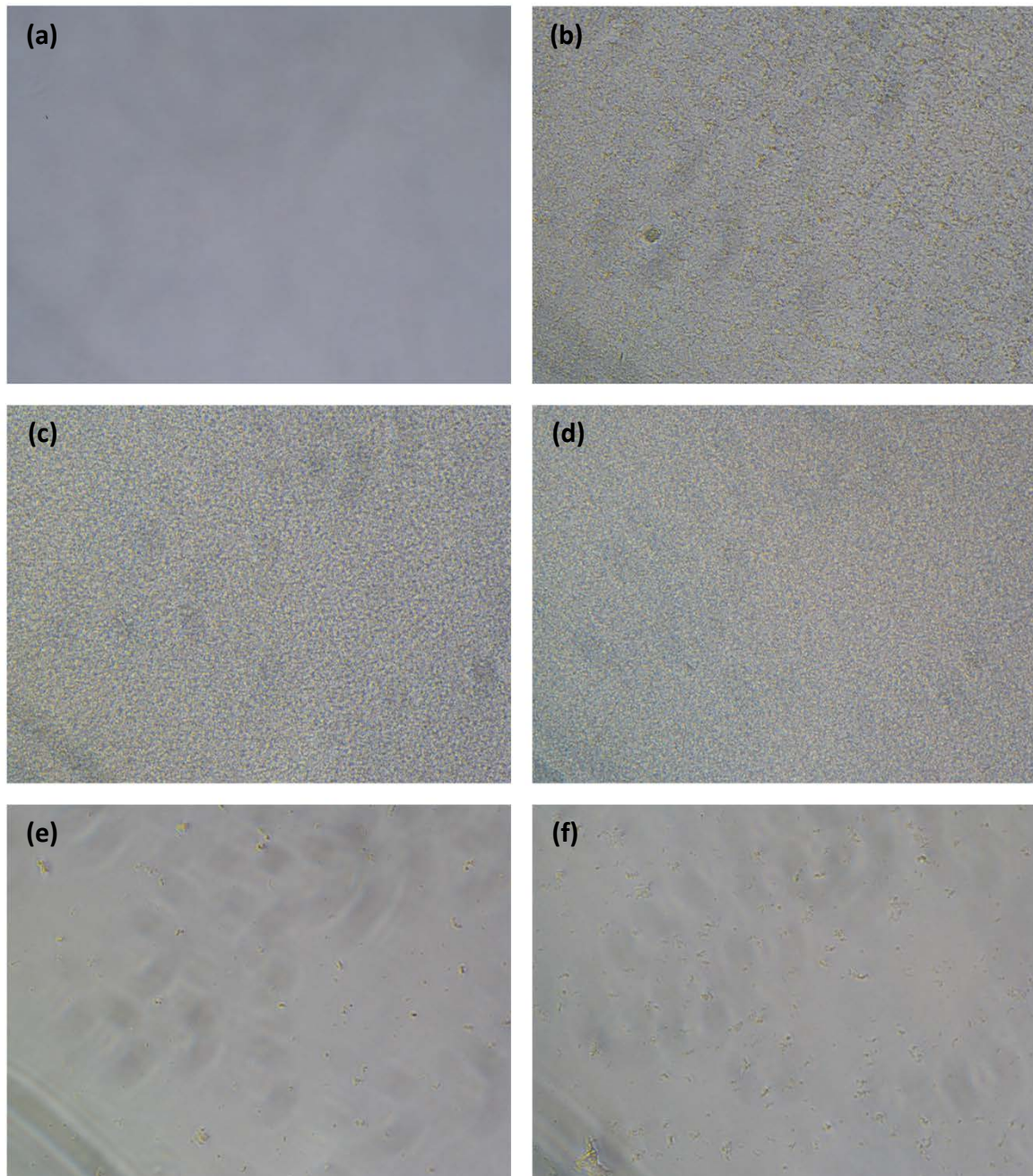


**Figure 69:** Images of medium from modules sterilised with 70% IMS (lumen (c), ECS (d)) and autoclaving (lumen (e), ECS (f)) with negative (a) and positive (b) infection controls

## 20. Cell performance in hollow fibre bioreactors

One module incorporating batch 2 fibres was intact when seeded with cells. The resultant Presto Blue (indicating metabolic activity) and nutrient metabolite data indicate a growth and proliferation of cells within the device during culture. The data also indicates that a longer culture period may be required to generate a confluent monolayer of cells within the fibre.

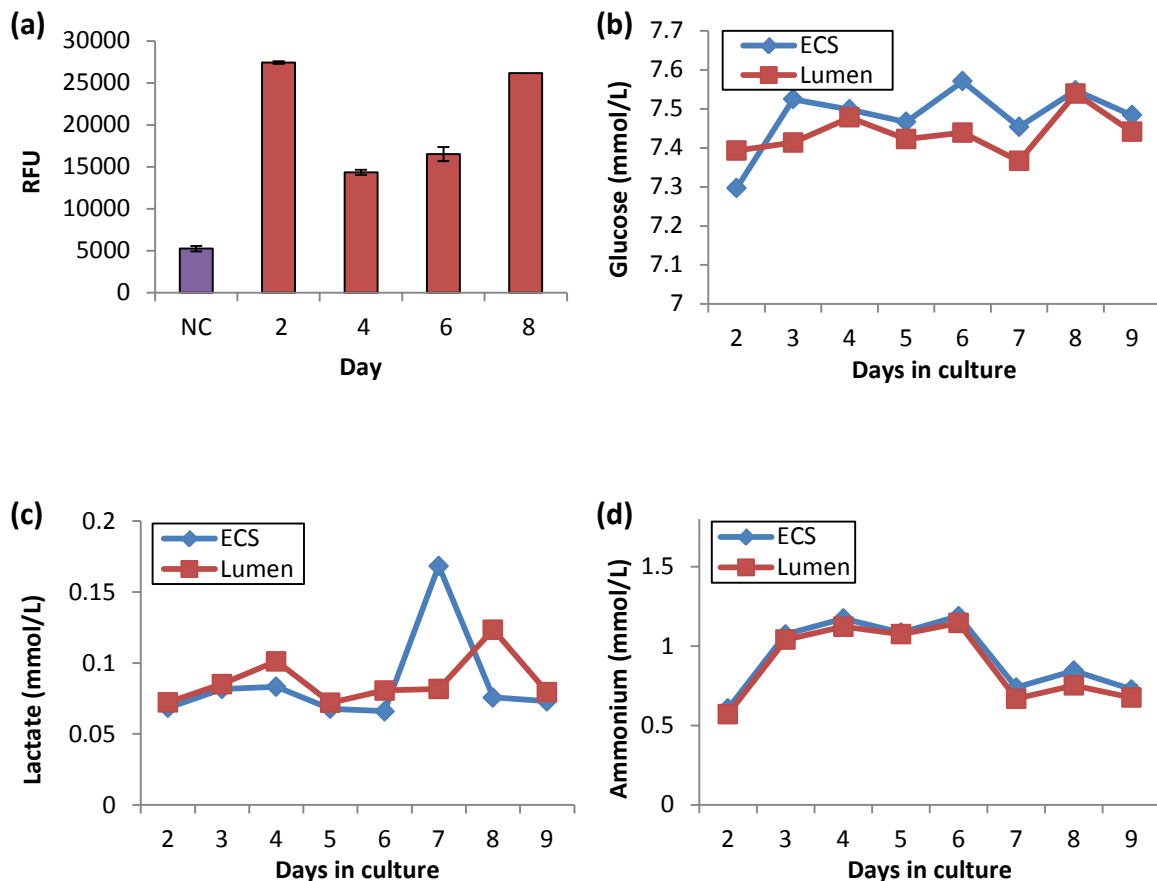


**Figure 70:** The (a) Presto Blue fluorescence and (b) glucose (c) lactate and (d) ammonium concentrations of RPTECs during 8 days of culture under flow conditions